Planktonic contact and predation rates: Studies on saltatory foraging strategy and prey perception by hydromechanical means

Thesis submitted in accordance with the requirements of
the University of Liverpool for the degree of Doctor in Philosophy
by
Saminu Iliyasu Bala

JUNE 2009

Abstract

In this thesis, the connection between a planktonic predator's perception field and its predation strategy is investigated. In addition, the impacts of small-scale turbulence, prevalent in most planktonic environments on the predator's optimal mode of foraging for prey are also investigated. To this end, the predator's perception field was modeled as a conical shaped with a semi-vertex angle α. Larval fish, such as the Atlantic cod, do not swim continuously but forage following an intermittent locomotion pattern, consisting of bursts of relatively high speed swimming movements, interspersed with pauses when they scan the water column for prey. This behaviour is known as saltatory feeding strategy. Using the theoretical model and series of kinematic simulations, this thesis demonstrates that saltatory predation does indeed remain the optimal foraging strategy over a considerable range of turbulence and temperature regimes, and that the narrowness of the larva's perception field is fundamental reason why it adopts this sort of behaviour. Extensions of these modeling ideas were also done to examine for the first time the predation rates models where both the predator and prey (of different sizes) are swimming in a turbulent flow. Despite the complexities involved in the formulation, the model developed produces reliable and encouraging results. A numerical model that examines planktonic encounter rates by means of hydromechanical signals in a small-scale turbulent flow was also formulated. The results add to the evidences that planktonic perception fields are not spherically symmetric.

Publications and Presentations

Most of the materials in Chapter 4 and 5 are based on the following publications:

1. D.M. Lewis, S.I. Bala. "Plankton predation rates in turbulence: A study of the limitations imposed on a predator with a non-spherical field of sensory perception." `Journal of Theoretical Biology Volume 242 pages 44-61, 2006.`

2. D. M. Lewis, S. I. Bala. "An examination of saltatory predation strategies employed by fish larvae foraging in a variety of different turbulent regimes." `Mar Ecol Prog Ser`, Volume 359, pages 261-274, 2008.

The following presentation have been given based on some of the materials in this thesis:

1. "Effects Of Turbulence On Planktonic Contact And Predation Rates", S.I. Bala, Annual applied Maths. PhD symposium, University of Liverpool May 2005.

2. "Prey perception by hydromechanical signals", S.I. Bala, Annual applied Maths. PhD symposium, University of Liverpool May 23, 2006.

3. "An examination of saltatory predation strategies employed by fish larvae foraging in a variety of different turbulent regimes", S.I. Bala, Annual applied Maths. PhD symposium, University of Liverpool May 22 2007.

4. "An examination of saltatory predation strategies employed by fish larvae foraging in a variety of different turbulent regimes", S.I. Bala, Euro Mech conference, Liverpool May 2007.

Table of Contents

List of Figures

List of Tables

Acknowledgement

I am grateful to God who spares my life to undertake my studies up to the PhD level. First, I wish to thank my supervisor, Dr David Mark Lewis, for his continues support, patient and understanding. He introduced me into the field of fluid dynamics and computer simulations; he made me a better programmer. I also thank my second supervisor Professor Vadim Viktashev and the entire members of staff in the department of mathematical sciences, university of Liverpool.

My profound gratitude also goes to Professor Muhammad Yahuza Bello for all his assistance and the management of Bayero University Kano, Nigeria for funding me through the McArthur Grant. The past four and half years or so, have some important implications in my life. It was during this time, my youngest daughter, Zainab was born. It was during the same period that she lost both eyes due to malignant cancer of the eye, `RETINOBLASTOMA`. It was indeed a very traumatic period for me and my family. I must not forget those who assisted me during the difficult moment of Zainab's lost of sight. Special thanks also goes to Clic sargent, the world friendship fund, the methodist overseas fund, Dr Sani Aliyu, family support fund, Retinoblastoma team of Birmingham children hospital and the oncology unit of Alder Hey Children hospital, Liverpool. Special thanks also go to Muhammad Sulaiman and his family, Muhammad Jameel and family, Abeeb Salaam and family.

I must mention my parents, Bala Sani and Zainab Bala who were not even alive to see the commencement of my PhD. I cherished whatever they have done for me in their life time. I am also indebted to a number of people who assisted me in several ways. These people are too numerous to make list of. But I should mention a few. Alhaji Sabo Mangu, Muhammad Khamis Bala, Hassan Shitu, Habeeb Saleh, Abdulazeez Hassan, Sani Bala, Sani Garba, Sani Adams, Bala Dauda, Ibrahim Idris, Faruk Sarkinfada, Abubakar Alhassan and Rilwanu Ibrahim, Fawaz Alharbi. I am indeed grateful to all of them.

Finally, I wish to mention people who are very dear to my heart. Asiya, Harira, Wasila, Maryam, Abdulqawiy, Raihan, Abdulhakeem, Aisha, Abdulazeez and Zainab, I cannot forget their valuable support and understanding without which, this dream may not be accomplished. These are people who had to cope with my long absence. They shared the good and the bad moments with me.

Dedication

Zainab, who lost her sight during this work and the entire members of my family.

Chapter 1

General introduction

1.1 Preamble

The abundance and the composition of plankton (tiny open-water plants, animals or bacteria) in the ocean are greatly influenced by predation. Planktonic predators are generally larger than their prey and swim much faster. The presence of a nearby prey can be detected by visual, hydromechanical or some other means. Identifying the decisive factors controlling predation in the planktonic communities will help in constructing realistic models of predator-prey interactions. In this thesis, attention will be focussed on interactions between planktonic predators and their prey in the oceanic environment. To begin with, the general background will be reviewed.

1.2 Plankton

The oceanic environment is broadly divided into the pelagic and the benthic environments. The surface of the ocean to the bottom is referred to as the pelagic environment and the animals inhabiting this realm are called the pelagic animals. The bottom of the sea is called the benthic environment and the animals inhabiting it are collectively called the benthos. The most basic marine organisms found in the pelagic environment are the plankton and nekton. The nekton are generally much larger than the plankton and have fully developed swimming abilities example of which include fish, sharks and squid.

The planktonic microorganisms vary in size from microscopic bacteria to larger animals such as jellyfish and live in the top 100 m or so where sunlight can penetrate efficiently. Generally, they have limited or no swimming capabilities and are transported through the water by advection. This group is further divided into phytoplankton and zooplankton according as whether they are plants or animals respectively. Most planktonic species are microscopic in size with the zooplankton typically being larger (Lalli & Parsons 2002). The phytoplankton synthesize energy through the process of

photosynthesis and are therefore confined to the photic zone. The photic zone, also called the euphotic zone, is the depth of the water in a lake or ocean that is exposed to sufficient sunlight for photosynthesis to occur. Generally the zooplankton population sustains itself by grazing on the phytoplankton.

1.2.1 A note on Copepods

Copepods belong to the class of animals forming a significant sub-group of the zooplankton. They are also classified as holoplankton because they spend their entire life as plankton. They are found almost everywhere where water is available and make up the largest source of protein in the oceans (see Lalli & Parsons (2002)). They are an important link in the food web between the primary-producing phytoplankton and other animals feeding on plankton such as fish larvae, example the Atlantic herring and cod (MacKenzie et al. (1994)). Most of the economically important fish species feeds on copepods. Free-living copepods can feed only on small food items like bacteria, diatoms or other unicellular microorganisms. The first larvae of copepods are called nauplii. They are very small and are found in very different habitats. There are several different groups of copepods and each group is called an order. The order Calanoida is one of the most predominant and is made up of about 1850 species (Lalli & Parsons 2002). Examples of copepods from different orders include; `Oithona similis, Acartia tonsa, temora longicornis, Diapotamus sicils, Calanus finmarchicus.`

1.2.2 Why is the plankton population important?

Plankton forms the basis of the marine food web; moreover phytoplankton consumes the greenhouse gas carbon dioxide during photosynthesis. The uptake of carbon dioxide by phytoplankton across the vast expanses of the oceans reduces the level of the rising carbon dioxide in the atmosphere. Phytoplankton form the foundation of oceanic food chain. This means that the aquatic food web depend on them to a large extent (see Saiz et al. (2003)). Zooplankton such as shrimp, fish larvae and krill feed on plankton and they are in turn eaten by larger organisms. Without phytoplankton, the oceans would soon become barren marine deserts.

The oceans occupies over 71% (Hays et al. 2005) of the earth. It is therefore necessary for us to understand and address how changes in the climatic condition will affect the marine environment. For example, reports from 43 years studies off the coast of California by Roemmich & McGowan (1995) show that the surface layer has warmed by 1.5 ^{o}C over the said period, and this warming has resulted in the decline of some zooplankton species by 80%. Since fish feed mainly on zooplankton, climate impacts on the oceans might have widespread economical implications.

1.2.3 Factors affecting plankton biomass in the marine environments

Temperature

Temperature is one of the most important physical properties of the marine environment as it influences many physical, chemical and biological events such as metabolism and growth. Variations in temperature and salinity in the ocean combine to determine the density of sea water, which in turn determine the vertical movements of materials in the water column. These vertical movements have importance consequence for biological processes. The motility of microorganisms in aquatic environments depends on both internal processes and physical condition of the fluid environment (see von Herbing et al. (2001), von Herbing (2002)). The locomotory organs are strongly influenced both physically and physiologically by temperature. Sea surface temperatures vary with latitude, and can exceed 30 ^{o}C in the tropical waters and can be as low as the freezing point in the polar region (see Stefan. et al. (2003)). The inverse relation between temperature and kinematic viscosity implies that changes in temperature of the ambient fluid will affect the life of small fish larvae both mechanically and physiologically. For example, higher temperature reduces the viscosity and density of the water, which makes it difficult for plankton to remain afloat in the surface layers. Temperature changes also affect the physics of the flow field and have important consequences on swimming and feeding strategies of small fish larvae whose surroundings is dominated by viscous hydrodynamic regimes (Podolsky & Emlet 1993, Bolton & Havenhand 2005, von Herbing 2002).

Light

Sunlight is crucial element in the life of marine animals. Part of the light from solar radiation penetrating into the sea is absorbed by phytoplankton for use in photosynthesis. The water itself absorbs some of the light from solar radiation and converts it into internal heat. This process is very important as it establishes the oceanic temperature regimes. Plankton are found throughout the oceans, seas and lakes of Earth. However, the local abundance of plankton varies horizontally, vertically and seasonally, depending upon suitable conditions. One of these conditions is the availability of light. All plankton ecosystems are driven by the input of solar energy and this confines primary production to surface waters where light is abundant. In addition many planktonic microorganisms rely on visual cues to locate food, mate or escape from predators.

Predator-prey interactions: Visual perception

Predation is a major driving force governing the dynamics and structure of the planktonic communities. Understanding the process by which planktonic species interact

with each other and how they perceive their environment is important in plankton trophodynamics.[1] In this work the act of predation is summarised into two distinct events: **Encounter** and **Capture**.

Following Gerritsen & Strickler (1977) one can define a planktonic encounter between predator and prey as an event when the two microorganisms move to within a fixed distance from each other. From this definition, it is assumed that once they are within this fixed distance (termed the contact radius), the predator will detect the presence of the prey and make a capture attempt. Similarly, the prey may detect the presence of the predator and exhibit escape behaviour. The detection technique could be visual, as in fish larvae (see Galbraith et al. (2004)), or chemical and hydromechanical signals (see Fields & Yen (1997), Kiørboe et al. (1999), Kiørboe & Visser (1999)). Whichever detection technique is employed, encounter rates play a central role in population and community dynamics, by determining which and how many individuals, populations and species can interact with each other at a specific location. A food particle[2] that has not been encountered cannot be eaten. Therefore, the dynamics of encounter play a central role in foraging theory. Indeed, physical encounter is the first step of any ecological predator-prey interactions.

For a visual encounter, explicit geometrical representations of encounter scenarios such as positioning of the perception field (detection region) together with some physical insights into the encounter process (velocity and size of interacting particles) allow for the development of encounter rates equations. Gerritsen & Strickler (1977) developed the first encounter rate model. Since then, encounter rate models have been extended and improved conceptually (Rothschild & Osborn 1988, Lewis & Pedley 2000, 2001). Estimates of encounter rates (NT^{-1}, where N is number and T is time) by means of encounter rate equation depends upon four elements :

- Projected cross-sectional area perpendicular to the predator's direction of movement. If the predator is assumed to be moving in a relative velocity velocity frame of reference in which its direction of motion coincides with the $z-$ axis, then this refers to the area one would see projected onto the xy plane by the predator's perception field (see Figure 4.2). If there no flow, the centre line of its perception field will coincide with $z-$ axis which is the predators's swimming direction. However, the presence of the flow field will tend to deflect the predator's intended swimming direction from its actual swimming direction of motion. Consequently it will be assumed that the predator's swimming direction (and line of sight) lies at an angle γ to the $z-$ axis. If in addition the perception field is assumed to be spherical, then the area projected by the perception field onto the xy - plane

[1] Refers to the study of inter-relations between animals with respect to energy transfer

[2] By particle we mean a body having finite mass and internal structure but negligible dimensions and does not influence the fluid flow

will be a circle, irrespective of the angle γ. Any potential prey (assumed to be stationary in the relative velocity frame of reference) which impacts on this surface area as the predator move by is assumed to be encountered. However, the situation is much more complicated in the presence of the flow coupled with the assumption that the perception field is not spherical (see Figures 4.2,4.3 also see the appendix of Lewis (2003)).

- Density of prey or predators (NL^{-3}, L is length).
- Mean encounter speed (LT^{-1}) measured as the relative velocity vector of the body doing the encountering with respect to the body being encountered.
- Identification of the geometry of the encounter situation.

In this manner, it is possible that one can determine how density, relative velocities, detection radius and specific geometries of the perception field can influence the encounter rates.
Explicit formulation of the encounter rate equations depends on the kind of motility of the predator and prey considered. There are basically two main forms of motion: straight line and irregular motility patterns. Naturally, the motion of planktonic microorganisms can include several combinations of these behaviours, and the resulting encounter rate arises from the combinations of these simplified behaviours (Rothschild & Osborn 1988, Lewis & Pedley 2000, 2001). Several models have been developed that investigate the role of encounter rates in the feeding behaviour of zooplankton. These models depend on velocity through the fluid and the sensory perception field.

Gerritsen and Strickler (GS) Encounter Rates Model for constant swimming speeds

The GS model is a simple model devoid of the effects of turbulence. In the development of this model, the following assumptions are made

- The perception field of the predator is spherical in shape. That is any prey particle coming into a spherical region of radius R surrounding the predator is assumed to be in contact, see Figure 1.1.
- The organisms are dimensionless points in space.
- The organisms are swimming in random directions with uniform speeds
- The distribution of the animals is random
- The organisms are swimming constantly in straight lines.

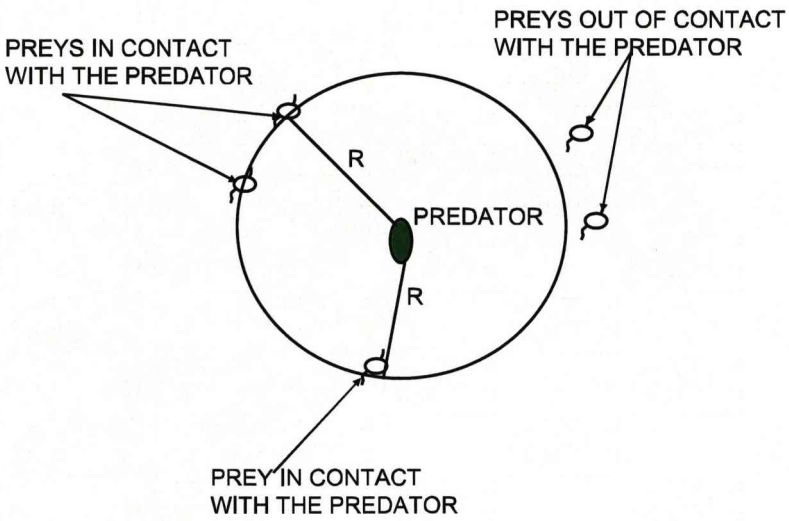

Figure 1.1: Schematic diagram for the perception field of a predator with spherical geometry,having a contact radius R.

Consider microorganisms with subscripts H for prey and P for predator. Let $\mathbf{v}_{\mathrm{P}}$ and $\mathbf{v}_{\mathrm{H}}$ be the swimming velocities of the predator and prey respectively, $\mathbf{U}$ be the velocity of the predator relative to the prey. Then the speed of the predator relative to the can be written as

$$U = \sqrt{v_{\mathrm{P}}^2 + v_{\mathrm{H}}^2 - 2v_{\mathrm{P}}v_{\mathrm{H}}\cos\theta}, \tag{1.2.1}$$

where $v_{\mathrm{P}} = |\mathbf{v}_{\mathrm{P}}|$ and $v_{\mathrm{H}} = |\mathbf{v}_{\mathrm{H}}|$, represent the speed of the predator and prey respectively, θ is the angle between $\mathbf{v}_{\mathrm{P}}$ and $\mathbf{v}_{\mathrm{H}}$. The number of prey which cross into the contact sphere per unit time, is given by the perpendicular projected cross-sectional area, times the prey density assumed to be uniform, times the speed on entering the contact sphere, times the probability of moving with such speed. Integrating over all velocity and angle variables gives the total contact rate (CR) for a single predator as

$$CR = \frac{R^2\rho_{\mathrm{H}}}{4}\int_0^{\pi}\int_0^{2\pi}\int_{v_{\mathrm{P}}}\int_{v_{\mathrm{H}}} U p_{\mathrm{P,H}}(v_{\mathrm{P}}, v_{\mathrm{H}})\sin\theta dv_{\mathrm{P}}dv_{\mathrm{H}}d\phi d\theta. \tag{1.2.2}$$

Here $p_{\mathrm{P,H}}(v_{\mathrm{P}}, v_{\mathrm{H}})$ is the probability density function of the predator and prey velocities respectively, ρ_{H} is the constant prey density and R is the perception distance or contact radius. In the analytical derivation of the GS model, the authors further assumed that the predators and prey population are moving with certain average speed $\langle v_{\mathrm{P}}\rangle$ and $\langle v_{\mathrm{H}}\rangle$

respectively. By this assumption, the probability distribution in equation (1.2.2) is constant and the equation can be written as

$$CR = \frac{R^2\rho_{\mathrm{H}}}{4}\int_0^{\pi}\int_0^{2\pi} U\sin\theta d\phi d\theta. \tag{1.2.3}$$

With U defined as in equation (1.2.1) the integral in equation (1.2.3) is evaluated to give the contact rate for constant swimming speed in still fluid as (CR_S^{Cons}) as

$$CR_S^{Cons} = \begin{cases} \frac{\pi R^2\rho_{\mathrm{H}}\left(3\langle v_{\mathrm{P}}\rangle^2+\langle v_{\mathrm{H}}\rangle^2\right)}{3\langle v_{\mathrm{P}}\rangle}, & \langle v_P\rangle \geq \langle v_H\rangle, \\ \frac{\pi R^2\rho_{\mathrm{H}}\left(3\langle v_{\mathrm{H}}\rangle^2+\langle v_{\mathrm{P}}\rangle^2\right)}{3\langle v_{\mathrm{H}}\rangle}, & \langle v_H\rangle \geq \langle v_P\rangle. \end{cases} \tag{1.2.4}$$

Equation (1.2.4) gives the idea behind the still fluid contact rate model due to GS assuming that the predator and prey are moving constantly in straight lines. The Gerritsen & Strickler (1977) model is plausible for still fluid. The question then is how is this modified in turbulent flow?

1.2.4 Rothschild and Osborn (RO) model

The theoretical work of Rothschild & Osborn (1988), sparked considerable theoretical and experimental research efforts towards the understanding of how planktonic and other small microorganisms in the ocean interact with each other and their coping strategy in a turbulent environment. Example of these studies include: Yamazaki et al. (1991), Ki⊘rboe & Saiz (1995), Galbraith et al. (2004). Others are, Lewis & Pedley (2000, 2001), Lewis (2003), and Lewis & Bala (2006). To investigate the effect of turbulence on planktonic encounter rates, Rothschild & Osborn (1988) modified the Gerritsen & Strickler (1977) model by incorporating a turbulence contribution to the relative speed between the predator and prey. The RO formulation is based on estimate of turbulence velocity scale (w_{RO}^2). The turbulent velocity scale is define as the difference between the average of the square turbulent velocity $\mathbf{w}(\mathbf{x},t)$ at a point $\mathbf{x}$ at time t, and its correlation with velocity at a position a distance $\mathbf{r}$ away . Mathematically, this is define as

$$\begin{aligned} w_{\mathrm{RO}}^2 &= \langle \mathbf{w}(\mathbf{x}+\mathbf{r},t)\rangle^2 - \langle \mathbf{w}(\mathbf{x}+\mathbf{r},t)\cdot\mathbf{w}(\mathbf{x},t)\rangle \\ &= \frac{3S_c}{2}\langle\epsilon\rangle^{2/3}r^{2/3}. \end{aligned} \tag{1.2.5}$$

Here, $\langle\rangle$ denote ensemble averaging (average taking over large sample, see section 2.3), $\langle\epsilon\rangle$ is the average rate at which the turbulent energy is being converted into heat and S_c is constant called the structure constant function whose values lie in the range 2 to 2.5 (see Lewis & Pedley (2000)). With the turbulent velocity scale given by equation (1.2.5), RO modified the GS model by replacing $\langle v_{\mathrm{P}}\rangle$ with $\sqrt{\langle v_{\mathrm{P}}\rangle^2 + w_{\mathrm{RO}}^2}$

and $\langle v_{\mathrm{H}} \rangle$ with $\sqrt{\langle v_{\mathrm{H}} \rangle^2 + w_{\mathrm{RO}}^2}$ in equation (1.2.4). Thus, the contact rate formula for constant swimming in turbulent flow ($CR_{\mathrm{T}}^{\mathrm{Cons}}$) reduces to

$$CR_{\mathrm{T}}^{\mathrm{Cons}} = \frac{\pi \rho_{\mathrm{H}} R^2 \left(3\langle v_P \rangle^2 + \langle v_H \rangle^2 + 4 w_{\mathrm{RO}}^2 \right)}{3(\langle v_P \rangle^2 + w_{\mathrm{RO}}^2)^{\frac{1}{2}}}, \quad \langle v_P \rangle \geq \langle v_H \rangle. \tag{1.2.6}$$

In fact, this novel idea formed a cornerstone in the development of planktonic predator-prey interactions. However, the increase in particle encounter may adversely affect capture efficiency. This is because turbulence sweeps away prey particles from the detection zone before the predator has a chance to capture them. Another detrimental effect of turbulence is that it interferes with the structure and the efficiency of the feeding current as well as the detection abilities of the microorganisms to hydromechanical signals. These effects mean that there is an optimum level of turbulence which enhances feeding. This is confirmed by the report of Ki⊘rboe & Saiz (1995), that low levels of turbulence are beneficial to small zooplankton such as fish larvae in contrast to intermediate levels.

1.2.5 Lewis and Pedley 2001 model

Another model of planktonic encounter rates in turbulence was formulated by Lewis & Pedley (2001). This model incorporate more realistic predator and prey swimming behaviour based on the assumption that the swimming speeds (v_P, v_H) follow isotropic Gaussian distributions with mean zero and standard deviations σ_P and σ_H, where

$$\sigma_{P,H} = \sqrt{\frac{\pi}{8}} v_{P,H}. \tag{1.2.7}$$

The analysis in that paper show that the contact rate due to Gaussian swimming in turbulent flow ($CR_{\mathrm{T}}^{\mathrm{Gauss}}$) reduces to the following

$$CR_{\mathrm{T}}^{\mathrm{Gauss}} = 4\rho_{\mathrm{H}} R^2 \sqrt{\frac{\pi}{2}} \sigma_U(R), \tag{1.2.8}$$

where

$$\begin{aligned} \sigma_U^2(R) &= \frac{4}{3} \int_0^\infty E(k,t) \left(1 - \frac{\sin(kR)}{kR} \right) dk + \sigma_P^2 + \sigma_H^2 \\ &= w_T^2(R) + \sigma_P^2 + \sigma_H^2. \end{aligned} \tag{1.2.9}$$

Here k is a wavenumber (inverse of wave length) and $E(k,t)$ represent the distribution of turbulent energy over k and $w_T^2(R)$ is the turbulent velocity scale.

The definition of encounter rates advanced by Gerritsen & Strickler (1977) has some underlying implications: (a) Regardless of the perception technique employed, the perception capabilities of a predator are spherically symmetric (see Figure 1.1). This

means that all prey particles are initially perceived at a contact distance R. The distance R varies with species but typical values are within 1 - 40 mm (Lewis & Pedley 2000) for the cruising[3] predator, herring larvae. (b) The definition also means that a predator with this isotropic perception field can maximize its encounter rates by swimming constantly at its maximum speed. However, both theoretical and experimental studies contradict these assumptions. For instance, Bundy et al. (1998) conducted an experiment to study prey perception by hydromechanical signals using `Diaptomus sicilis` as the predator and 50 μm polystyrene beads as prey. The copepod was observed to attack the beads by swimming at relatively slow speed ($\approx$ 1 mm s^{-1}) with many changes in swimming directions. The report also shows that it formulates attack posture (when a prey is perceived) at a range of different separations distances (0.97 -2.1 mm) and narrow angular range. The various angles at which the copepod attack the beads were recorded by the authors of that paper and are reproduced here in form of angular frequencies depicted on Figure 1.2. These results show that the perception capabilities of the planktonic predators are far from being spherically symmetric. The

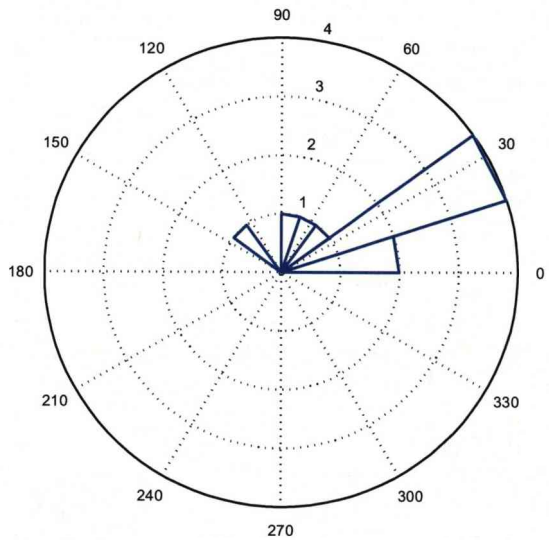

Figure 1.2: Angular frequencies showing contact distances as recorded by Bundy et al. (1998), who performed an experiment to study the the process of prey detection by `Diaptomus sicilis` using polystyrene beads as prey. The authors recorded the orientation angles of the predator with respect to the prey when contact occur. The results are presented here in form of angular frequencies.

video observations and analysis by Galbraith et al. (2004) of the foraging behaviour of Atlantic cod larvae show that they adopt a 'pause - travel' strategy by alternating periods of relatively fast swim (2-12 mm s^{-1} for $\approx 2s$) with pauses ($\approx 1s$) in which they change their orientation as they search for prey. Svensen & Kiørboe (2000) reported

[3]cruising is associated with a predator adopting a continuous swimming as it searches for prey

that the copepod `Oithona similis` feeding mainly on `Gymbnodium dominas` follow the 'sit and wait' (ambush) strategy, where it lies motionless in the water column relying on hydromechanical signals to detect a prey in close proximity. Detection occurs over a range of distances. These observations do not corroborate with the idea that planktonic predation strategy involves a combination of fast straight line swimming coupled with initial prey perception at a fixed distance R. These body of evidences compelled researchers to begin to consider predators with non spherical field of perception.

Lewis 2003 model

Encounter problem for a predator with a restricted field of perception was studied by Lewis (2003). He modelled the perception field as a right circular cone with semi-vertex angle α augmented by a corresponding segment of a sphere of contact radius R. This kind of perception field is depicted in Figure 1.3. The narrow perception field involves more parameters than the spherical field and it is insuperable to analytic

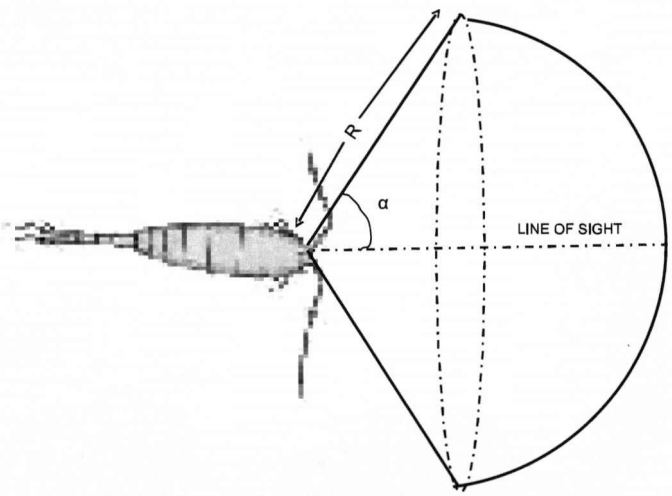

Figure 1.3: Schematic diagram of the restricted perception of a predator modelled by Lewis (2003). The perception field is conical in shaped with a semi vertical angle α.

solution in general. Lewis (2003) derived the exact results for the expected number of prey encounters based on assumption that the microorganisms swim constantly in straight lines for a time T and speed $\langle U(R)\rangle$. This is equivalent to the volume of a cylinder of radius R and length $T\langle U(R)\rangle$. But Planktonic microorganisms seldom follow a straight line path for long. They exhibit a wide variety of swimming patterns, examples of which are: run-tumble, hop-sink, helical motion (Visser & Kiørboe 2006, Svensen & Kiørboe 2000). Consequently, he modified the model using the idea of

volume fraction to account for irregular trajectory.

To estimate the effect of n direction changes after time $\tau < T$, he defined the volume fraction

$$\langle f_v\left[U_R, R, n, \tau, \alpha\right]\rangle = \frac{\langle \text{volume mapped}\rangle}{\left[(n+1)\pi R^2(\alpha)U_R\tau + 2\pi\frac{R^3(\alpha)(1-\cos\alpha)}{3}\right]}, \tag{1.2.10}$$

where

$$R(\alpha) = \begin{cases} R\sin\alpha, & \alpha < \frac{\pi}{2}, \\ R, & \alpha \geq \frac{\pi}{2}. \end{cases}$$

The $\langle$volume mapped$\rangle$ is the volume predator would map out following an irregular path. The term in the denominator represent the volume it would map out following a straight line trajectory. The parameters U_R and τ that appear in the volume fraction need to be explained.

U_R is a relative velocity scale defined such that

$$U_R = \frac{CR(\alpha, r = R)}{\pi\rho_H R^2(\sin\alpha)^2} \tag{1.2.11}$$

where $CR(\alpha, r = R)$ is equivalent to the contact rate for a predator encountering preys at distance R (see equation (1.2.7) for definition of σ_P). The author also defined χ_{U} as the ratio of U_R when $\sigma_P \to 0$ to U_R for $\sigma_P \neq 0$. Mathematically, this can be written as

$$\chi_{\text{U}} = \frac{U_R(\sigma_P \to 0)}{U_R(\sigma_P)} \in [0, 1]. \tag{1.2.12}$$

The parameter encapsulate the dominant influence between the predator's swimming behaviour and the flow.

The parameter τ measures the effective time interval for a predator to change its direction of motion. This time scale depend on the relative strength of the flow field and the motility pattern of a predator. Suppose a hypothetical predator decides to change its direction of motion after a time τ_{sight}. Then for straight line swimming (no direction changes) Lewis (2003) defined $\tau_{\text{sight}} = \infty$. However, if the swimming motion is made up of rapid direction changes, he defined $\tau_{\text{sight}} \to 0$.

The author then defined the effective time scale for a predator to change its swimming direction as

$$\begin{aligned} \tau &= \left(\chi_{\text{U}}^2\tau_{\text{LC}} + (1+\chi_{\text{U}}^2)\tau_{\text{sight}}\right)\exp\left(-\chi_{\text{U}}\tau_{\text{sight}}/\tau_{\text{LC}}\right) \\ &+ \left(1 - \exp\left(-\chi_{\text{U}}\tau_{\text{sight}}/\tau_{\text{LC}}\right)\right)\tau_{\text{LC}}/\chi_{\text{U}}. \end{aligned} \tag{1.2.13}$$

Here τ_{LC} is a property of the flow field called Lagrangian contact time scale (see Lewis & Pedley (2000)). Equation (1.2.13) is composed of two terms. For predator moving constantly in a straight line without change of direction, $\tau_{\text{sight}} \to \infty$ and the first term vanishes. The trajectory of the predator is

$$\begin{cases} \text{linear}, & \chi_{\text{U}} \ll 1, \tau \to \infty, \\ \text{irregular}, & \chi_{\text{U}} \approx 1, \tau \to \tau_{LC}. \end{cases}$$

On the other hand if the predator makes rapid direction changes $\tau_{\text{sight}} \to 0$ the second term vanishes and only the first term applies. The comparative strength of the predator's swimming motion and the flow capsulised in χ_U will govern the trajectory followed.

The ⟨volume mapped⟩ was calculated using Monte Carlo simulation. This consists of tracking a planktonic particle with contact radius R around a cubic domain containing grid points for a period T. During this time, the number of points that falls within a cylindrical region surrounding the predator as it moves and turns are counted. The volume mapped out is proportional to the counted grid points and from this result the volume fraction was calculated as the ratio of the volume mapped out to the volume that would have been encompassed if the predator had moved in a straight line.

One of the conclusions drawn from that study is that predators with narrow fields of perception will encounter prey at a range of different distances, not just at R as had been assumed previously. This conclusion calls for revision of capture rate models that advocates all round perception field. It will also be potentially something new to extend this encounter rate to study the predation rates.

Predator-prey interactions: Hydromechanical perception

A body whether self propelled or passively moving with the flow generates hydromechanical disturbance in the ambient fluid. The magnitude of this disturbance may depend on the size and speed of the moving body. Experimental and theoretical investigations have shown that the ability to detect and react to these disturbances is well developed in copepods (Ki⊘rboe et al. 1999, Ki⊘rboe & Visser 1999, Hwang & Strickler 2001, Fields & Yen 1997). Their first antennae are adorned with array of hair-like setae which are highly sensitive to fluid motion (Visser 2001, Hwang & Strickler 2001) and can sense the flow disturbance generated by other bodies in close proximity. A response behaviour is initiated when the flow disturbance is sufficient to cause the mechanoreceptory setae to bend (Yen et al. 1992, Ki⊘rboe et al. 1999). The mechanical bending of the setae alerts the copepod to the presence of impending friend, food or foe.

In practice, small microorganisms in the ocean not only experience the hydromechanical signals generated by other organisms in the flow, but also myriad of other disturbances associated with the physical forcing of their environment. This might mean that the microorganisms have developed some sort of pattern recognition enabling them to distinguish the flow disturbances emanating from their own activities and those coming from other sources.

The distances at which a body in the flow can be detected depends upon the copepod's sensitivity to hydrodynamic signals, brought about by changes in the characteristics of the surrounding flow field when they are in close proximity. Typically, a relative velocity of about 20 μm s^{-1} is enough to elicit a neurophysiological response (Yen et al.

1992).

Copepods not only perceive signals from moving bodies but also from inert particles as well. Observation by Bundy et al. (1998) show that `D. sicilis` can detect beads that are located outside the influence of its feeding current even before contact with the sensory structures are made. This indicates that, the signal might have been perceived as a result of the deformation of the flow streamlines as the copepods and beads are close together. Although there exists a lot of evidence in support of the fact that copepods respond behaviourally to hydromechanical signals, it is not very clear which components of the fluid disturbance (fluid velocity, velocity gradient, fluid acceleration, drag force or other flow characteristics) they respond to. Jiang et al. (1999) used viscous dissipation as the relevant signal strength to study the hydrodynamic interactions between copepods of the same size. Kiørboe & Saiz (1995) reported that for predators perceiving prey, the relevant signal strength is the absolute magnitude of the velocity. It appears that if one is to investigate encounter rates by hydromechanical perception, one has a variety of choice for the components of fluid disturbance to use. One possibility of studying hydromechanical perception theoretically is to examine the problem of two spheres in Stokes flow.

Two spheres in Stokes flow

Numerous studies have been undertaken over the years using bispherical coordinates into the hydrodynamic interactions that arise in Stokes flow between a solid of revolution and another object. One of the earliest of such studies was Stimson & Jeffery (1926) who considered the flow in the vicinity of two spheres rotating about their line of centres. Lin et al. (1970), investigated the motion of two spheres in a shear field. Davis (1969) analyzed the translation and rotation of two unequal spheres in a viscous fluid. Goldman et al. (1966) investigated the motion of two identical and arbitrarily oriented spheres through a viscous fluid. The problem of computing the trajectories of two spherical bodies has applications in meteorology, colloid chemistry and viscosity of moderately concentrated suspension of spherical particles (Goldman et al. 1966, Davis 1969). In this thesis the applications of two spheres in Stokes flow will be extended to study planktonic predator-prey relation.

Why two spheres?

The flow field around a copepod is ecologically significant because it brings food to the copepod and transmits signals to the mechanoreceptive satae of the copepod. Aside feeding benefit, information from the surrounding flow field helps the copepod to avoid predators and also to find mates. When two copepods or a copepod and another body are in close proximity, the flow field around each of them is different. The extent

to which one influence the other largely depends on the separations. One important parameter in planktonic encounter rate theory is the distance over which a predator can detect the presence of the prey or the other way round. Using bispherical coordinates, it is convenient to study resulting distortion of the flow field in the vicinity of two spheres by varying their separation. Therefore, to study the flow field-difference arising from the hydrodynamic interactions of a relatively large predator and its relatively small prey in close proximity, it is convenient to use two spheres of different sizes. By assuming that the bodies are spherical in shape, substantial complexities can be overcome. Moreover, the existence of a natural coordinates system where the boundary conditions on the spheres can be satisfied simultaneously is an added advantage.

1.3 A note on fish larvae

Larval fish are visual predators (see Peck et al. (2006)). Majority of the species feeds on the developmental stages of copepods (eggs, Nauplii, copepodites) and are mostly found in the wind mixed-layer where sunlight can penetrate efficiently. This layer is one of the most turbulent parts of the ocean as a result of wind forcing and tidal currents. Larval fish exhibit complicated vertical and horizontal movements which invariably expose them to varying turbulent conditions caused by fluctuations in wind speed and proximity to the surface of the water. They meet diverse environmental and physical conditions at sea, and their growth and chances of survival depend on a compromising response to environmental variability.

Newly hatched larvae are usually small in size (2-9 mm long, see Werner et al. (2001)) with high mortality rate per day. Mortality occurs as a result of starvation, predation, pollution and other causes. They have evolved sophisticated behaviour to enhance feeding and to avoid being eaten by others. The Atlantic Herring (`Clupea harengus`) and cod larvae (`Gadus morhua`) have evolved different prey searching strategies. Herring larvae are cruise predators as they are observed to forage continuously without pausing in between search events (MacKenzie et al. 1994, MacKenzie & Kiørboe 1995). The Atlantic cod do not swim continuously but forage following an intermittent locomotion pattern, consisting of bursts of relatively high speed swimming movements, interspersed with pauses when they scan the water column for prey. Predators that pause for brief periods before moving at discrete units of time are referred to as saltatory predators. Thus, the dynamics of their intermittent locomotion consist of movement in discrete units of time along with pauses, by means of which they adjust their behaviour to changing circumstances. It is not immediately clear why this type of behaviour is exhibited. Given that these predators have a wedge-shaped perception field (Galbraith et al. 2004), one would like to know whether there is any connection between this type of strategy and the perception field of the larvae. It is however hypothesized in

literature that the following are some reasons for saltatory behaviour.

- Partial recovery from fatigue can be achieved during pauses leading to increase in endurance.
- Perception benefit can be achieved because pauses allow the sensory system to detect the relevant stimuli more efficiently by stabilizing the visual field.
- Pausing during the course of intermittent locomotion reduces the probability of detection of both the prey and predator (Kramer & Mclaughlin 2001).

This study will explain another reason why saltatory foraging is pursue.
Experimentally, larval fish are observed to perform saltatory foraging strategy. Example of larval species following the pause travel strategy include the white crappie (`pomoxis annularis`), the Golden shiner (`Notemigonous Crysolecus`), the Atlantic cod larvae (`Gadus morhua`), see Browman & O'Brain (1992), von Herbing & Gallager (2000), von Herbing et al. (2001), Galbraith et al. (2004), Kramer & Mclaughlin (2001), MacKenzie & Ki⌀rboe (1995) for details. The question of whether saltatory predators perceive their prey during pauses or travels appear to be contentious. MacKenzie & Ki⌀rboe (1995) believe that these predators search for prey only during pauses. von Herbing et al. (2001) observed that prey are perceived during both pausing and travels. These observations should not be viewed to be in conflict because the strategy is influenced by environmental variability.
The rate at which turbulent kinetic energy from large to small scale is dissipated into internal heat (see section 2.6) is an inherent component of marine environment and hence this will impact on the optimum foraging strategy that should be adopted. Variations in this dissipation will play a significant role in larval trophodynamics. Planktonic microorganisms in the ambient fluid are observed to respond both passively and actively to fluctuations in turbulent energy dissipation. These inherent natural variations in dissipation rates can lead to a large difference in contact rates and swimming speeds of larval fish and its prey (MacKenzie & Leggett 1991).
The findings that encounter rates are enhanced by turbulence were extended to suggest that this has overall beneficial effects on predation rates (see Sundby & Fossum (1990), MacKenzie & Leggett (1991)). This extension does not reflect the effects of turbulence on post encounter events. MacKenzie et al. (1994) investigated the predation rates of cruising larval fish by including the effects of turbulence on post encounter events. One of the conclusions from that paper was that predation rate is a dome-shaped function of swimming speeds.
The swimming speed which maximizes the foraging performance is important because it is strongly linked to the viscosity of the flow regime. For small fish larvae, this implies that viscosity have a dominant effect on its feeding process. Considering the broad knowledge available on the importance of water viscosity, and given that temperature

can modify performance of aquatic microorganisms, it is really unclear why its effect have been ignored in encounter and predation rate models. It is therefore useful to explore the biological implications of environmental viscosity associated with temperature changes. Larval fish recruitment relies to some extent on predator prey interaction. This has triggered major efforts to build models of larval feeding that integrates their searching behaviour and reliable sensory field of perception. The contributions that will be made in this work are to improve the basic formulations of interactions between larval fish and their prey by looking at more realistic perception field and investigating specific search strategies.

Numerous theoretical studies have shown that fish can swim more efficiently by using the pause-travel pattern (see Weihs (1980), Videler & Weihs (1982), Stocker & Weihs (2001)). The analysis presented by these authors revealed that this strategy is associated with large energy savings of over 50% as compared to continuous movement and that the advantage increases with size.

According to these reports, fish larvae do not share the advantage of pause-travel swimming, due to the dominant influence of water viscosity at small Reynolds numbers. However, this conclusion fundamentally deviates from experimental studies which show that pause-travel is commonly observed in numerous species of larval fish. The fundamental assumption made by these authors in their formulations is that the Reynolds numbers base on the animals scale is above 1000. This actually corresponds to a fish with size 5 cm swimming at 2 cm s^{-1} in the viscosity regime characterised by $\nu = 1.0$ m^2 s^{-1}. With this assumption, their models are formulated for the energy expenditure needed to overcome drag at high Reynolds number which is independent of viscosity.

Larval fish differ from adults in their interaction with the physical environment and their small size makes them to experience water mainly as viscous medium (see Peck et al. (2006)). Verhagen (2004) has shown that fish larva of about 5-15 mm in length can accelerate from rest to a high velocity in such a short time scale that viscous forces are negligible in comparison with inertial forces during the initial acceleration stage of the locomotion. The result of this observation means that the dynamics of pause-travel involves both inertial and viscous components.

1.4 Statement of the problem

Plankton are important components of marine environment as they formed the base of oceanic food chain and by absorbing carbon dioxide during respiration, they reduced the level of green house gasses from the atmosphere. Sustainable growth of fisheries industries requires an improved knowledge basis that predicts optimal conditions for larval fish feeding behaviours which is directly linked to recruitment into the adult stage. To this end, numerous models of planktonic predation rates have been devel-

oped with the assumption that their perception fields are spherically symmetric.
Overwhelming evidences from recent literature studies presented in the previous sections show that planktonic perception fields are far from spherical as previously assumed. These calls for revisions of encounter and predation rates models that advocate all round perception fields.
The mathematical equations for encounter rates for non-spherical field of perception are in general complicated and not amenable to analytical treatment. For example, the Lewis (2003) encounter rate model for general value of $\alpha \in [0, \frac{\pi}{2}]$ is so complicated that it can only be linked to predation rates when the capture probability is 100%. Experiments and field observations have shown planktonic predators capture rate is much lower than 100% (see Buskey (1994), Kiørboe & Saiz (1995)).
It is well documented that viscosity has a profound influence on swimming speeds of small fish larva. This means that viscosity is an important environmental factor that should play central role in any larval fish foraging model. Low environmental temperatures (high viscosities) are linked to decline of swimming speeds (see Fuiman & Batty (1997), von Herbing (2002)). Because of their small size all the crucial activities of fish larvae occur in both the viscous and intermediate Reynolds number regimes (see Müller et al. (2008)).
Theoretical models that describe how pause-travel swimming style can be energetically more advantageous over continuous swimming in fish were developed by Weihs (1980), Stocker & Weihs (2001), Videler & Weihs (1982). These models assumed that the Reynolds number base on the fish size must be greater than 1000. Since pause-travel is also commonly observed in larval fish, it will be useful to formulate a corresponding model on larval scale. The parameters that may play significant role in the model include size of the larva and viscosity of the flow regime.
The purposes of this work are

1. To examine for the first time the combined problems of encounter and predation rates for planktonic predators with restricted perception field in a turbulent flow using a realistic probability capture function. The model will then be used to study the efficiency or otherwise of cruising and saltatory feeding strategies of fish larvae in various turbulent and viscosity regimes. The predation rate is usually expressed as the product of encounter and the capture probability function. For

$\alpha = \frac{\pi}{2}$ the analysis in Lewis (2003) paper reduces to the following integrals

$$\begin{aligned} CR_2(\alpha) &= \frac{\pi\rho_H R^2}{2}\int_{\mathbf{V}}\int_{\mathbf{U}}(1+\cos\gamma)U(R) \\ &\times\ p_{UV}(\mathbf{U},\mathbf{V}|R)d\mathbf{U}d\mathbf{V}, \qquad \gamma \leq \frac{\pi}{2}, r = R, \end{aligned} \tag{1.4.1}$$

$$\begin{aligned} CR_3(\alpha) &= \frac{\pi\rho_H R^2}{2}\int_{\mathbf{V}}\int_{\mathbf{U}}(1+\cos\gamma)U(R) \\ &\times\ p_{UV}(\mathbf{U},\mathbf{V}|R)d\mathbf{U}d\mathbf{V}, \qquad \gamma > \frac{\pi}{2}, r = R, \end{aligned} \tag{1.4.2}$$

$$\begin{aligned} CR_6(\alpha) &= 2\pi\rho_H\int_0^R\int_{\mathbf{V}}\int_{\mathbf{U}}(-\cos\gamma)rU(r) \\ &\times\ p_{UV}(\mathbf{U},\mathbf{V}|r)d\mathbf{U}d\mathbf{V}, \qquad \gamma > \frac{\pi}{2}, r < R. \end{aligned} \tag{1.4.3}$$

Here $p_{UV}(\mathbf{U},\mathbf{V}|R)$ is the conditional joint probability distribution of the predator and prey swimming velocities encapsulated in $\mathbf{U},\mathbf{V}$ at contact distance R. U is the speed of the predator relative to the prey, γ is the angle which the predators swimming direction makes with the vertical axis. The encounter rate model from that paper are made up of six integrals CR_{1-6} depending on the angle γ and the distance at which contacts occurred. Those contacts which occurred at distances $r < R$ are called closed encounters. From the six integrals, only those mentioned above are non zero when $\alpha = \frac{\pi}{2}$. Note that equations (1.4.1) to (1.4.3) could be interpreted as the predation rates if capture probability is assumed to equal 100%. For a restricted perception field the capture function depends upon the prey entry point and the orientation of the perception field. This means that simple multiplication of equations (1.4.1), (1.4.2) and (1.4.3) with a capture function will not suffice.

2. Theoretical energy saving function (Ratio of the energy expenditure during pause-travel swimming style to the energy expenditure for continuous swimming with the same average speed) for fish is usually written the in the form

$$E_{\text{ratio}} = \frac{E_{\text{sal}}}{E_{\text{cru}}}, \tag{1.4.4}$$

where E_{sal} is energy expended during pause-travel and E_{cru} is the corresponding energy expended by continuous swimming. To evaluate equation (1.4.4) numerically, it is required to be written in terms of the times spent and distances covered during the pause and the travel phases. These are obtained using the relevant conditions by solving the equation of motion of the form

$$M\frac{dv_P(t)}{dt} + C_D f(t) = T_{\text{crit}}, \tag{1.4.5}$$

where M is mass, T_{crit} is the maximum sustained thrust and C_D is the drag coefficient and $f(t)$ is function of swimming speed.
Therefore the goals are

- To re-formulate the encounter rate equations and to postulate a realistic capture probability function so that the products will define realistic formulae for the predation rates.
- To formulate a new energy saving function on fish larval scale that will involve the viscosity of the flow regime as a parameter.

The research will help answer some questions such as

- Given the commonness with which saltatory strategy is practice, what are the energetic benefits associated with this particular type of behaviour?
- How does the geometry of the perception field influence the pause-travel foraging strategy?
- Under what range of swimming speeds and pause-travel combinations is the strategy most beneficial to the animals? Planktonic habitat is subjected to frequent changes associated with temperature and other physical forcing such as wind-driven turbulence. Is the strategy robust across these regimes?
- Can we use theory and simulation to explain experimental and field observations?

1.5 Methodology

Due to the complexity of the task, analytical treatment of the problems is restricted to a few situations. Kinematic simulations have been used profusely in the investigations that follow.

1.6 Organisation of the rest of the chapters

The thesis is made up of nine Chapters that are organised as follows. In Chapter 2, a review of basic concepts in turbulent flow is tackled. These include introduction to the governing equations of motion, the statistical treatment of turbulence and turbulent kinetic energy spectrum.
Chapter 3 deals with the main methodology employed in this thesis. In this Chapter we looked at the construction of the simulation flow fields using two forms of turbulent kinetic energy spectrum. Descriptions of the various simulations were subsequently presented.
In Chapter 4, analytical formulation of the predation rates model for planktonic predators with hemispherical perception field is presented. Subsequently, simulations and predictions are conducted for various perceptions angles.
Chapter 5 serves as an extension of Chapter 4, where predation rates under varying

turbulent and viscosity regimes were investigated.

In Chapter 6 planktonic predation rates for saltatory predators feeding on mobile prey was formulated.

In Chapter 7 a new model that compares the energetic advantages of pause-travel with cruise searching strategies was formulated.

Chapter 8 involves prey perception by hydromechanical means using two spheres of arbitrary sizes and speeds.

Chapter 9 is the last chapter where future directions were discussed.

Chapter 2

A review of Turbulence

2.1 Introduction

The word turbulence is used to describe certain motion in fluids and gasses that is associated with random velocity fluctuations and wide range of different length and time scales. There is no succinct and clear definition of fluid turbulence and for this reason, the meaning of the term would be explained by its characteristics in the next section. Turbulence has been studied for more than 100 years, when it was discovered that at velocities exceeding a certain threshold, frictional losses became independent of velocity in pipes used in city sewerage. One of the pioneers in the study of turbulence, Osborn Reynolds concluded that the phenomenon occurred as a result of random velocity fluctuations. Reynolds himself called this motion "sinuous motion" (see Hinze (1959)), as the term turbulence was not connected to this type of fluid flow at the time. Turbulence can be generated by processes such as fluid layers moving or passing over one another at different velocities, by frictional force as fluid moves over a fixed boundary and by wind forcing, tide and currents in the ocean (see Kiørboe & Saiz (1995), Hinze (1959)). Because of the irregular nature of turbulence, it is not amenable to rigorous mathematical treatment. It is, however, possible to study its characteristics by statistical laws.

In this work, attention will be focused on the flow of an incompressible Newtonian fluid with constant density and viscosity. It will be further assume that the fluid is not acted upon by any body forces. With this assumption, the velocity and pressure fields satisfy the Navier-Stokes equations

$$\frac{\partial u_i}{\partial t} + \underbrace{u_j \frac{\partial u_i}{\partial x_j}}_{\text{Inertial term}} = -\frac{1}{\rho}\frac{\partial P}{\partial x_i} + \underbrace{\nu \frac{\partial^2 u_i}{\partial x_j \partial x_j}}_{\text{Viscous term}}, \tag{2.1.1}$$

and continuity

$$\frac{\partial u_i}{\partial x_i} = 0, \tag{2.1.2}$$

where $u_i \equiv u_i(\mathbf{x}, t), P \equiv P(\mathbf{x}, t)$ are velocity and pressure fields, $x_{i,j}$ are cartesian spatial coordinates, ρ and ν are the density and kinematic viscosity of the fluid respectively. The kinematic viscosity is often written in terms of dynamic viscosity μ, as $\nu = \frac{\mu}{\rho}$. Here the summation convention applies for repeated subscripts. The non-linear inertial term in the equation of motion quantifies the momentum transport by the flow and is fundamental to understanding the nature of the turbulent flows. The ratio of inertial forcing to the viscous forcing, for a given flow is called the Reynolds number, which encapsulates the relative importance of these two types of forces for the particular flow in question. Mathematically, the Reynolds number can be defined as

$$Re = \frac{\rho U L}{\mu}, \tag{2.1.3}$$

where U and L are characteristic velocity and length scales of the flow respectively. It is generally used to classify different flow regimes as either laminar or turbulent, depending upon whether the inertial forces dominate the viscous forces, or vice-versa. It is one of the most important dimensionless numbers found in fluid dynamics. Transition to turbulence results when instabilities of the laminar flow merge together at intermediate Reynolds numbers. Further increases in Reynolds number result in the non-linear inertial term dominating the viscous term, resulting in the flow taking on irregular character. Turbulence is not completely random but has random characteristics as $Re \to \infty$.

2.2 Nature and characteristics of Turbulence

Turbulent flows exhibit continuous instabilities which makes a deterministic approach of the turbulence problems impossible. In the study of such flows, it would be useful if a concise definition of the subject can be given. However, it is very difficult to give a short and precise definition of a turbulent flow. Perhaps the meaning of turbulence can be best encapsulated by a description of its inherent characteristics, which includes dissipation of kinetic energy, irregularity, rapid mixing, and high levels of fluctuating vorticity (a measure of local rotation in a fluid flow). In the following subsections, the characteristics of turbulence are expanded in more detail.

Diffusion

One of the consequence of turbulence is the mixing of materials, which is important in industrial processes and in dilution of pollutant in the environment. The advection (inertial) terms in the equation of motion (2.1.1) accelerate greatly the process of turbulent diffusion. This effectively leads to rapid mixing, increased rate of momentum, heat and mass transfer. Quantitatively, turbulent diffusion is several order bigger than

molecular diffusion (see Tennekes & Lumley (1972)). The diffusive nature of turbulence is one of its most important features and has a direct effect on any ongoing biological processes occurring in the turbulent regime.

High Reynolds number

Turbulence is the result of the merging of instabilities that are generated in laminar flow (orderly flow) as the relative strength of the non-linear inertial term increases. By definition this occur as the Reynolds number gets large, typically $Re \approx 100$ or so. For small Reynolds number, equation (2.1.1) is mathematically nice, the non-linearities are small, and the equation can be solved. As the Reynolds number are turn up, the non-linearities become important, and the flow is no longer steady, but erratic.

Rotational

One of the most important characteristics of turbulent flow is the fact that they are rotational and three dimensional, resulting in high level of fluctuating vorticity. The vorticity fluctuations can only maintain themselves if the velocity fluctuation is three dimensional. A very important mechanism for vorticity maintenance is the vortex stretching (deformation of a column that contains a vortex), which is absent in two dimensions. Vorticity dynamics is therefore central in the role of turbulent descriptions.

Irregularity

Turbulent flows takes on pseudo-random character as the relative strength of the non-linear inertial term increases limiting one's ability to make a prediction. However, even at very high Reynolds numbers $Re \gg 10000$, there remains a precise statistical structure to the correlations between velocity values at different points in space and time. This statistical structure allows one to characterise the nature of a particular turbulent flow.

Dissipative

One clear distinction between turbulence theory and standard statistical mechanics is that turbulence is dissipative (see Tennekes & Lumley (1972)). Even at high Reynolds number, the effect of viscosity cannot be neglected. This is because it act to dissipate the energy driving the flow, ensuring (so it is believed, see Hinze (1959),Tennekes & Lumley (1972)) that the solution to Navier-Stokes equations can never diverge to infinity. Energy fed into the flow on large scales is converted into internal heat at small scales through the process of dissipation. For a turbulent flow to be sustained, a continuous supply of energy is required to overcome energy losses due to viscous dissipation.

Without such a constant energy supply, turbulent flows will die off rapidly. The rate at which this energy dissipation process occurs is one of the most important ways of characterising a turbulent flow and is usually denoted by ϵ. Another important aspect of the viscous effects on turbulence is that it makes the flow more homogeneous and reduces the dependence on directions particularly under small length and time scales. If the statistical properties of the turbulence are the same throughout the flow and it does not depend on any direction, the turbulence is said to be homogeneous and isotropic. Usually on relatively small scales, turbulent flows are, to a good approximation, homogeneous and isotropic (they have a universal structure). This makes them easier to deal with and can be used as a basis for practical predictions.

2.3 The statistical Description of Turbulent motion

For more than a century, considerable effort has been devoted to turbulent flow investigations, but so far no general methodology for tackling general turbulent flow problems exists. The unpredictable nature of turbulence means that it is often useful to express its characteristics by statistical means. Because it is not possible to describe the flow at any given realization, researchers resort to describing the statistical ensemble properties of the flow over many realisations. If the flow is statistically stationary, one can define statistical averages by considering samples over large period of time (or space). Thus, the flow can be characterised by averaged quantities such as the mean velocity. However, adopting the statistical approach in an effort to solve the governing equations always results in a situation where the unknowns out-number the equations. This is called the closure problem of turbulence theory. There are at least three different ways in which the averaging is performed. These are time average $\langle u_i \rangle_t$, space average $\langle u_i \rangle_x$ and ensemble average $\langle u_i \rangle_e$. The various averaging are defined as (see Tennekes & Lumley (1972), Hinze (1959)),

$$\langle u_i \rangle_t = \lim_{T \to \infty} \frac{1}{2T} \int_{-T}^{T} u_i dt, \tag{2.3.1}$$

$$\langle u_i \rangle_x = \lim_{X \to \infty} \frac{1}{2X} \int_{-X}^{X} u_i dx, \tag{2.3.2}$$

$$\langle u_i \rangle_e = \lim_{N \to \infty} \frac{1}{N} \sum_{i=1}^{N} u_i. \tag{2.3.3}$$

Here 'T' is time, X is a large volume of space and N is large number of identical samples. Equations (2.3.1), (2.3.2) and (2.3.3) are only practically useful if T, X and N are finite. If the flow is homogeneous and statistically stationary, the three averaging process are assumed to be the same and can be denoted by $\langle u_i \rangle$. Henceforth the equality of the three averaging will be implied whenever average is mentioned.

In the statistical description of turbulence, the velocity u_i and pressure field P are decomposed into mean $\langle u_i \rangle, \langle P \rangle$ and fluctuating $\widetilde{u}_i, \widetilde{P}$ components as (see Tritton (1988))

$$u_i = \langle u_i \rangle + \widetilde{u}_i \tag{2.3.4}$$

$$P = \langle P \rangle + \widetilde{P}. \tag{2.3.5}$$

The averaging process satisfies the following axioms,

$$\begin{aligned}
\langle \lambda u_i \rangle &= \lambda \langle u_i \rangle, \quad \lambda \text{ is a constant} , \\
\langle u_i + u_j \rangle &= \langle u_i \rangle + \langle u_j \rangle, \\
\langle \langle u_i \rangle \rangle &= \langle u_i \rangle, \\
\langle u_i \rangle &= \langle \langle u_i \rangle + \widetilde{u}_i \rangle = \langle u_i \rangle + \langle \widetilde{u}_i \rangle \Rightarrow \langle \widetilde{u}_i \rangle = 0, \\
\langle \langle u_i \rangle \widetilde{u}_i \rangle &= \langle u_i \rangle \langle \widetilde{u}_i \rangle = 0, \\
\langle u_i u_j \rangle &= \langle \langle u_i \rangle + \widetilde{u}_i \rangle \langle \langle u_j \rangle + \widetilde{u}_j \rangle = \langle u_i \rangle \langle u_j \rangle + \langle \widetilde{u}_i \widetilde{u}_j \rangle.
\end{aligned} \tag{2.3.6}$$

Since the velocity field of the flow depends on spatial position ($\mathbf{x}$) and time (t), must satisfy differential equations (2.1.1) and (2.1.2), one frequently needs to calculate averages over derivatives. By using the linearity relation one can write

$$\frac{\langle u_i (\mathbf{x} + h) - u_i (\mathbf{x}) \rangle}{h} = \frac{\langle u_i (\mathbf{x} + h) \rangle - \langle u_i (\mathbf{x}) \rangle}{h}. \tag{2.3.7}$$

As $h \to 0$

$$\left\langle \frac{\partial u_i}{\partial x_j} \right\rangle = \frac{\partial \langle u_i \rangle}{\partial x_j}. \tag{2.3.8}$$

Incompressibility condition implies

$$\nabla \cdot \mathbf{u} = 0 \Leftrightarrow \frac{\partial \langle u_i \rangle}{\partial x_i} + \frac{\partial \widetilde{u}_i}{\partial x_i} = 0. \tag{2.3.9}$$

Taking the average of the continuity equation yields,

$$\frac{\partial \langle u_i \rangle}{\partial x_i} = 0, \tag{2.3.10}$$

one must have

$$\frac{\partial \widetilde{u}_i}{\partial x_i} = 0. \tag{2.3.11}$$

It follows that both the mean flow and the fluctuations satisfy the incompressibility condition (continuity equation).

2.4 The equation governing the mean flow $\langle \mathbf{u} \rangle$

In terms of mean and fluctuating quantities, equation (2.1.1) can be written as,

$$\frac{\partial (\langle u_i \rangle + \widetilde{u}_i)}{\partial t} + (\langle u_j \rangle + \widetilde{u}_j) \frac{\partial (\widetilde{u}_i + \langle u_i \rangle)}{\partial x_j} = -\frac{1}{\rho} \frac{\partial (\langle P \rangle + \widetilde{P})}{\partial x_i} + \nu \frac{\partial^2 (\widetilde{u}_i + \langle u_i \rangle)}{\partial x_j \partial x_j}. \tag{2.4.1}$$

Carrying out the averaging on equation (2.4.1) and using equation (2.3.8) one obtains,

$$\frac{\partial\langle u_i\rangle}{\partial t} + \langle u_j\rangle\frac{\partial\langle u_i\rangle}{\partial x_j} = -\frac{1}{\rho}\frac{\partial\langle P\rangle}{\partial x_i} + \nu\frac{\partial^2\langle u_i\rangle}{\partial x_j\partial x_j} - \left\langle \widetilde{u}_j\frac{\partial\widetilde{u}_i}{\partial x_j}\right\rangle. \tag{2.4.2}$$

The equation of the mean flow differs from the laminar flow equation by the addition of the last term which represents the action of velocity fluctuations on the mean flow. In view of equation (2.3.11) one can write this term as

$$\left\langle \widetilde{u}_j\frac{\partial\widetilde{u}_i}{\partial x_j}\right\rangle = \frac{\partial\langle\widetilde{u}_i\widetilde{u}_j\rangle}{\partial x_j}. \tag{2.4.3}$$

Now $\frac{\partial\langle u_j\rangle}{\partial x_j} = 0 \Leftrightarrow \frac{\partial}{\partial x_j}\left(\frac{\partial\langle u_j\rangle}{\partial x_i}\right)$ so that the equation of the mean flow becomes

$$\frac{\partial\langle u_i\rangle}{\partial t} + \langle u_j\rangle\frac{\partial\langle u_i\rangle}{\partial x_j} = \frac{1}{\rho}\frac{\partial}{\partial x_j}\left(-\langle P\rangle\delta_{ij} + \mu\left(\frac{\partial\langle u_i\rangle}{\partial x_j} + \frac{\partial\langle u_j\rangle}{\partial x_i}\right) - \rho\langle\widetilde{u}_i\widetilde{u}_j\rangle\right), \tag{2.4.4}$$

where $\nu = \mu/\rho$. Equation (2.4.4) is often written as (see Hinze (1959))

$$\frac{\partial\langle u_i\rangle}{\partial t} + \langle u_j\rangle\frac{\partial\langle u_i\rangle}{\partial x_j} = \frac{1}{\rho}\frac{\partial\sigma_{ij}}{\partial x_j}, \tag{2.4.5}$$

where

$$\sigma_{ij} = -P\delta_{ij} + \mu S_{ij} - \rho\langle\widetilde{u}_i\widetilde{u}_j\rangle, \tag{2.4.6}$$

is the complete mean stress tensor, δ_{ij} is the Kronecker delta function defined by

$$\delta_{ij} = \begin{cases} 1, & i = j, \\ 0, & i \neq j, \end{cases} \tag{2.4.7}$$

and

$$S_{ij} = \frac{1}{2}\left(\frac{\partial\langle u_i\rangle}{\partial x_j} + \frac{\partial\langle u_j\rangle}{\partial x_i}\right) \tag{2.4.8}$$

is the rate of strain tensor. The term $-\rho\langle\widetilde{u}_i\widetilde{u}_j\rangle$ physically corresponds to transport of momentum due to turbulence fluctuations and is called the Reynolds stress, in recognition of the original developer of the theory (see Hinze (1959)) and is denoted by

$$\tau^r_{ij} = -\rho\langle\widetilde{u}_i\widetilde{u}_j\rangle. \tag{2.4.9}$$

It is the appearance of the Reynolds stress in equation (2.4.4) which makes turbulence problem extremely difficult because it introduces additional unknowns into the equation of the mean flow. Thus, the averaged equations are not closed. This is called the closure problem of turbulence. Considerable insight into the characteristics of turbulence can be provided by studying the Reynolds stresses, but their presence in equations like (2.4.4) acts as an insuperable barrier for the computation of large scale turbulent flows. Most of the progress made in closing the turbulence equations involves the introduction

of plausible, but artificial relations between the Reynolds stress and the mean flow. In 1877 Boussinesq introduced the concept of relating the Reynolds stress to the shear strain rate viz,

$$\tau_{ij}^{r} = A\frac{\partial\langle u_i\rangle}{\partial x_j}. \tag{2.4.10}$$

A is constant of proportionality called the eddy viscosity, which depends on the type and scale of the motion considered.

2.5 Characteristic scales of Turbulence

Turbulent flows are characterized by the coexistence of variety of different length scales which play specific role in the dynamics of the flow. The sizes of these scales are regulated by both dimensions of the domain of the flow field and the size and extent of the forces driving the flow. The largest scales are called the integral length and time scales. Turbulent flows generate large and unstable eddies (overturning motions) which give rise to progressively smaller and smaller eddies. The viscous term in the Navier-Stokes equations hampers the propagation of infinitely small scale fluctuations by dissipating small scale energy into heat. The smallest scales at which the dissipation takes place are called the Kolmogorov scales (see Tennekes & Lumley (1972), Tritton (1988), Hinze (1959)). These scales are governed by; viscosity (ν)[$\mathrm{L}^2\ \mathrm{T}^{-1}$] and the rate of energy dissipation per unit mass (ϵ)[Energy/time $=$ $\mathrm{L}^2/\mathrm{T}^3$]. This parameter will henceforth be called rate of energy dissipation. By using dimensional analysis, the Kolmogorov length (η_k), velocity (v_k) and time (τ_k) scales can be determined. For instance, the Kolmogorov length scale is given by

$$\begin{aligned} \eta_k &= \nu^x \epsilon^y \\ [\,\mathrm{L}\,] &= [\,\mathrm{L}^2\ \mathrm{T}^{-1}]^x [\,\mathrm{L}^2/\ \mathrm{T}^3]^y \Rightarrow x = \frac{3}{4}, y = -\frac{1}{4} \text{ and} \\ \eta_k &= \left(\frac{\nu^3}{\epsilon}\right)^{\frac{1}{4}}. \end{aligned} \tag{2.5.1}$$

Similarly, the velocity and time scales can be obtained as

$$v_k = (\nu\epsilon)^{\frac{1}{4}}, \tag{2.5.2}$$

$$\tau_k = \left(\frac{\nu}{\epsilon}\right)^{\frac{1}{2}}. \tag{2.5.3}$$

Another important turbulent length scale one frequently finds in literature is the Taylor microscale. It marks the transition between the inertial and the dissipative ranges. This length scale is defined by (see McComb (1991))

$$\lambda = \left(\frac{\epsilon}{15\nu W^2}\right)^{-\frac{1}{2}} \tag{2.5.4}$$

where W is the turbulent intensity defined by $W = \sqrt{u_1^2 + u_2^2 + u_3^2}$, u_1, u_2 and u_3 are the turbulent velocity component in x, y and z coordinates. So Reynolds number based on microscale can also be defined as

$$Re_\lambda = \frac{W\lambda}{\nu}. \tag{2.5.5}$$

2.6 Energy spectrum

Fourier analysis is a very important mathematical tool, that has wide applications in science, engineering, signal processing, medical imaging and quantum mechanics. It can be used to decompose functions into their sinusoidal components. The decomposed functions can be reconstructed using the inverse transform. For homogeneous isotropic turbulence, it is extremely useful to work in Fourier space. Results can be obtained which gives physical interpretations of energy transfer mechanism between the different scales of the turbulence and the energy associated with a particular eddy scale. Let $F(\mathbf{x})$ be a function of spatial location $\mathbf{x}$. Then its Fourier transform is

$$F(\mathbf{k}) = \frac{1}{(2\pi)^3}\int_{-\infty}^{\infty}\int_{-\infty}^{\infty}\int_{-\infty}^{\infty}\exp(-i\mathbf{k}\,.\,\mathbf{x})F(\mathbf{x})d\mathbf{x}, \tag{2.6.1}$$

where $\mathbf{k}$ is a wave vector. The inverse is defined as,

$$F(\mathbf{x}) = \int_{-\infty}^{\infty}\int_{-\infty}^{\infty}\int_{-\infty}^{\infty}\exp(i\mathbf{k}\,.\,\mathbf{x})F(\mathbf{k})d\mathbf{k}. \tag{2.6.2}$$

For a homogeneous turbulence the velocity correlation tensor $R_{ij}(\mathbf{r})$ for velocities measured at positions $\mathbf{x}$ and $\mathbf{x}+\mathbf{r}$ can be defined as (see Lesieur (2008))

$$R_{ij}(\mathbf{r}) = \langle\widetilde{u}_i(\mathbf{x},t)\widetilde{u}_j(\mathbf{x}+\mathbf{r},t)\rangle. \tag{2.6.3}$$

A measure of correlation between $\widetilde{u}_i$ and $\widetilde{u}_j$ is given by the correlation coefficient, which is defined as (see Tennekes & Lumley (1972)),

$$C_{ij}(\mathbf{r}) = \frac{R_{ij}(\mathbf{r})}{W^2}. \tag{2.6.4}$$

If $\widetilde{u}_i$ and $\widetilde{u}_j$ are independent (far apart), $C_{ij} \to 0$ and the variables are said to be uncorrelated. Perfect correlation is said to occur if $C_{ij} = 1$ when $\mathbf{r} = 0$. Now let us define the spectral function $\Phi_{ij}(\mathbf{k})$ as a Fourier transform of $R_{ij}(\mathbf{r})$

$$\Phi_{ij}(\mathbf{k}) = \frac{1}{(2\pi)^3}\int_{-\infty}^{\infty}\int_{-\infty}^{\infty}\int_{-\infty}^{\infty}\exp(-i\mathbf{k}\,.\,\mathbf{r})R_{ij}(\mathbf{r})d\mathbf{r}. \tag{2.6.5}$$

The inverse transform of the spectral function is then

$$R_{ij}(\mathbf{r}) = \int_{-\infty}^{\infty}\int_{-\infty}^{\infty}\int_{-\infty}^{\infty}\exp(i\mathbf{k}\,.\,\mathbf{r})\Phi_{ij}(\mathbf{k})d\mathbf{k}. \tag{2.6.6}$$

Frequently, attention is usually devoted to the same component of fluid velocity at separations either perpendicular or parallel to that velocity component. If $\mathbf{r} = \mathbf{0}$ and $i = j$, then we have (see Tennekes & Lumley (1972)),

$$\frac{1}{2}\langle \widetilde{u}_i \widetilde{u}_i \rangle = \frac{1}{2} R_{ii}(\mathbf{0}) = \frac{1}{2} \int_{-\infty}^{\infty} \int_{-\infty}^{\infty} \int_{-\infty}^{\infty} \Phi_{ii}(\mathbf{k}) d\mathbf{k}. \tag{2.6.7}$$

Equation (2.6.7) shows that the turbulent kinetic energy is expressible as an integral over the Fourier space $\mathbf{k}$. The function $\Phi_{ii}(\mathbf{k})$ is interpreted as a distribution of turbulent kinetic energy over different wave numbers. For homogeneous isotropic and statistically stationary turbulence, which possesses a spherical symmetry the energy spectrum is conventionally defined as (see Mathieu & Scott (2000))

$$E(k) = 2\pi k^2 \Phi_{ij}(\mathbf{k}). \tag{2.6.8}$$

This energy spectrum is extremely important in the theory of turbulence. It is a function of wavenumber $k = 2\pi/\lambda_e$ where λ_e is the wave length of the eddies.

2.7 Inertial subrange (IS)

In the past, several functional form of the energy spectrum over the various scales have been proposed by researchers (see Hinze (1959), Pao (1965), Martinez et al. (1997)). However, over a certain range of wave numbers called the inertial subrange, the energy spectrum shows a universal form. This is briefly discussed here.

This universal form of energy spectrum was first derived by Kolmogorov using dimensional arguments. The wave number (k) is inversely proportional to the wave length, which in turn is proportional the eddy size ℓ. Hence $k \propto \frac{1}{\ell}$. "Large energy containing eddies" are associated with large ℓ and small k and energy is transported in spectral space (wave number space) to small scales (associated with large k and small ℓ) through the intermediate scales. At large scales, energy is extracted or inserted from the forcing terms driving the flow. At small scales energy is dissipated as heat. At intermediate scales (Inertial sub-range), energy is transferred from large scales to small scales (see Figure 2.1). Ultimately, all the energy extracted at large scales must be dissipated at small scales. Hence, the rate of energy extraction (which depends purely on large scale structure of the flow) must equal the rate of dissipation which depends on small scale parameters. The matching of these two numbers at intermediate scales when neither large nor small scale parameters are relevant implies a universal structure to the way energy is transferred in a sort of energy cascade process. The form of the energy spectrum in the IS first derived by Kolmogorov is (see Hinze (1959))

$$E(k) = \alpha_k \epsilon^{\frac{2}{3}} k^{-\frac{5}{3}}, \tag{2.7.1}$$

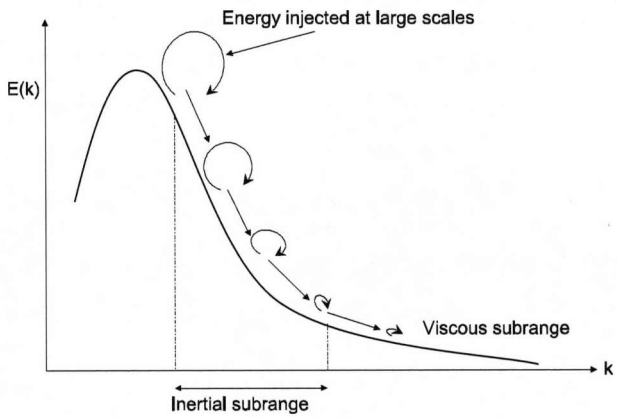

Figure 2.1: Schematic diagram showing turbulent energy cascade where $E(k)$ is the energy spectrum and k is the wave number. Also shown is the hierarchy of eddies from the production stage, via the inertial subrange to the dissipative subrange where viscosity finally dominates the flow.

where α_k is a constant. This form of energy spectrum in the IS is termed universal because it is independent of external conditions. Experimental investigations both in the laboratory and the ocean confirm this important result first obtained by Kolmogorov (see Hinze (1959)).

2.8 Turbulence in the Ocean

In the interior of the ocean, turbulence generated by wind forcing or tidal currents may transport phytoplankton from the well-lit, but frequently nutrient-poor surface water to deeper waters which are dark but potentially high in nutrients (Lalli & Parsons (2002)). Investigations into the variations of vertical and horizontal turbulent mixing processes so generated are fundamental to the understanding of the distribution and population dynamics of phytoplankton, which form the basis of the oceanic food chain. Turbulence also affects marine life through its effect on irradiance variability. In the upper ocean, phytoplankton are transported through a light field that exhibits exponential decay with depth from the sea surface (see Baird & Emsley (1999)). This process significantly affects the physical and physiological life of those organisms at the lowest level of oceanic food chain (Lalli & Parsons (2002)). Understanding the mechanism of turbulence and mixing in the ocean is important for many reasons. One important area that has blossomed in current research is the study of interactions between ocean physics and biology, especially interactions at small scales. Two very important problems relates to

the influence of turbulence on encounter and predation rates of planktonic predators foraging for their prey, and its influence on the ability of male copepods to track down a suitable mate. To begin to understand these problems there is the need to classify the level of turbulence as it pertains on the relevant small scales.

2.8.1 Energy dissipation rates in the ocean

Turbulence energy dissipation rate is known to vary with depth and the average value is usually defined in terms of the velocity fluctuation as (see Mathieu & Scott (2000))

$$\langle \epsilon \rangle = \nu \left\langle \frac{\partial \widetilde{u}_i}{\partial x_j} \left(\frac{\partial \widetilde{u}_i}{\partial x_j} + \frac{\partial \widetilde{u}_j}{\partial x_i} \right) \right\rangle . \tag{2.8.1}$$

Typically, estimates (direct measurement is not possible) of dissipation rates are obtained by experimental measurements. Direct measurement of turbulent energy dissipation, require measurement of all the terms in the equation (2.8.1) which is the appropriate term for general turbulent flow. However, not all terms can be measured in the laboratory (see Hinze (1959)). For homogeneous turbulence $\nu \left\langle \frac{\partial \widetilde{u}_i}{\partial x_j} \frac{\partial \widetilde{u}_j}{\partial x_i} \right\rangle = \nu \left\langle \frac{\partial \widetilde{u}_i}{\partial x_i} \frac{\partial \widetilde{u}_j}{\partial x_j} \right\rangle = 0$ and the equation for the rate of energy dissipation becomes

$$\langle \epsilon \rangle = \nu \left\langle \frac{\partial \widetilde{u}_i}{\partial x_j} \frac{\partial \widetilde{u}_i}{\partial x_j} \right\rangle . \tag{2.8.2}$$

To determine the value of $\langle \epsilon \rangle$, Klebanoff (see Hinze (1959)) measured only $\left\langle \left(\frac{\partial \widetilde{u}_1}{\partial x_1} \right)^2 \right\rangle$, $\left\langle \left(\frac{\partial \widetilde{u}_2}{\partial x_1} \right)^2 \right\rangle$, $\left\langle \left(\frac{\partial \widetilde{u}_3}{\partial x_1} \right)^2 \right\rangle$, $\left\langle \left(\frac{\partial \widetilde{u}_1}{\partial x_2} \right)^2 \right\rangle$ and $\left\langle \left(\frac{\partial \widetilde{u}_1}{\partial x_3} \right)^2 \right\rangle$. He then assumed isotropic relation for the following

$$\begin{aligned}
\left\langle \left(\frac{\partial \widetilde{u}_3}{\partial x_2} \right)^2 \right\rangle &= \left\langle \left(\frac{\partial \widetilde{u}_1}{\partial x_2} \right)^2 \right\rangle = \left\langle \left(\frac{\partial \widetilde{u}_2}{\partial x_1} \right)^2 \right\rangle , \\
\left\langle \left(\frac{\partial \widetilde{u}_2}{\partial x_2} \right)^2 \right\rangle &= \frac{1}{2} \left\langle \left(\frac{\partial \widetilde{u}_1}{\partial x_2} \right)^2 \right\rangle , \\
\left\langle \left(\frac{\partial \widetilde{u}_2}{\partial x_3} \right)^2 \right\rangle &= \left\langle \left(\frac{\partial \widetilde{u}_1}{\partial x_3} \right)^2 \right\rangle = \left\langle \left(\frac{\partial \widetilde{u}_3}{\partial x_1} \right)^2 \right\rangle , \\
\left\langle \left(\frac{\partial \widetilde{u}_3}{\partial x_3} \right)^2 \right\rangle &= \frac{1}{2} \left\langle \left(\frac{\partial \widetilde{u}_1}{\partial x_2} \right)^2 \right\rangle .
\end{aligned} \tag{2.8.3}$$

Klebanof also obtained the relation $\left\langle \left(\frac{\partial \widetilde{u}_2}{\partial x_1} \right)^2 \right\rangle = 2 \left\langle \left(\frac{\partial \widetilde{u}_1}{\partial x_1} \right)^2 \right\rangle$. Using this and equation (2.8.3), equation (2.8.2) reduces to

$$\langle \epsilon \rangle = \nu \left(4 \left\langle \left(\frac{\partial \widetilde{u}_1}{\partial x_2} \right)^2 \right\rangle + \frac{7}{2} \left\langle \left(\frac{\partial \widetilde{u}_1}{\partial x_3} \right)^2 \right\rangle \right) . \tag{2.8.4}$$

Assuming for isotropic turbulence,

$$\left\langle \left(\frac{\partial \widetilde{u}_1}{\partial x_2} \right)^2 \right\rangle \approx \left\langle \left(\frac{\partial \widetilde{u}_1}{\partial x_3} \right)^2 \right\rangle, \tag{2.8.5}$$

then equation (2.8.4) becomes

$$\langle \epsilon \rangle = \frac{15\nu}{2} \left\langle \left(\frac{\partial \widetilde{u}_1}{\partial x_3} \right)^2 \right\rangle. \tag{2.8.6}$$

Values of $\langle \epsilon \rangle$ varies with depth (z). At lower depths, $\langle \epsilon \rangle$ is generally much smaller than at the surface. The lower ocean is generally inaccessible and is characterized by huge pressure and relatively weak turbulence with small dissipation rates (10^{-10} m^2 s^{-3}, see Thorpe (2004)). The upper ocean is highly turbulent and is characterised by high values of dissipation rates. A relation for $\langle \epsilon \rangle$ was derived by MacKenzie & Leggett (1993). This is based on the assumption that wind-induced shear is the dominant mechanism responsible for generating turbulence given $\langle \epsilon \rangle$ as,

$$\langle \epsilon \rangle = \frac{5.82 \times 10^{-6} \langle U_w \rangle^3}{z} \tag{2.8.7}$$

where $\langle U_w \rangle$ and z are the average wind speed and sampling depth respectively. Generally speaking, turbulent dissipation rates in the upper 1 to 1.5 m are much higher than those predicted by equation (2.8.7) (see MacKenzie & Leggett (1993)).

2.8.2 Ocean Layers characterised by $\langle \epsilon \rangle$

Scientists have divided the ocean layers into zones, extending from the surface to the most extreme depths where light can no longer penetrate. As the depth increases the temperature drops and the pressure increases. The divisions are mainly based on temperature or turbulent regimes. Based on the value of $\langle \epsilon \rangle$ the ocean can be divided into layers (see Table 2.1). Two layers of considerable importance in this work, the thermocline and the mixed layer are described below.

Ocean layer	$\langle \epsilon \rangle$(m^2 s^{-3})	η_k (m)	τ_k(s)	v_k(m^2 s^{-1})
Thermocline	$10^{-10} - 10^{-8}$	$10^{-2} - 3 \times 10^{-3}$	$100 - 10$	$10^{-4} - 3 \times 10^{-4}$
Mixed layer	$10^{-8} - 10^{-6}$	$3 \times 10^{-3} - 10^{-3}$	$10 - 1$	$3 \times 10^{-4} - 10^{-3}$
Coastal zone	$10^{-7} - 10^{-4}$	$2 \times 10^{-3} - 10^{-4}$	$3 - 0.1$	$5 \times 10^{-4} - 3 \times 10^{-3}$

Table 2.1: The table shows typical range of values of energy dissipation rates and Kolmogorov scale at various ocean layers (see Yamazaki et al. (1991) for more details).

The surface mixed layer

The upper region of the ocean is referred to as the surface mixed layer and has a thickness that varies almost from 10 to 100 metres (see Suga & Hanawa (1990)) depending on the sea state and local heat flux arising from solar radiation. The surface layer of the ocean is also known as the sunlight zone because this is where most of the visible light exists. Solar heat is directly responsible for the wide range of temperatures that occur in this zone. This mixed layer is a key component in studies of climate, biological productivity and marine pollution. It serves as an interface between the atmosphere and deep ocean and directly affects the exchange of heat, gas and momentum between the sea and the atmosphere. Moreover, turbulent flows in the mixed layer affect biological productivity by controlling both the supply of nutrients from the deep ocean and by regulating the time phytoplankton spend in this region and the amount of sunlight they require. The temperature in this region in nearly uniform.

The thermocline

The thermocline is the region of the ocean sandwiched between the mixed layer at the top, and the deep sea beneath. The temperature in this region decreases rapidly with depth. The top of the thermocline is affected by seasonal fluctuations and the depth depends upon the geographical location. The value of $\langle \epsilon \rangle$ depends upon the ocean layer. It is therefore, expected that those biological responses that are sensitive to turbulence will generally vary to reflect the changes in the dissipation rates. Some zooplankton species are frequently observed leaving the surface ocean to the thermocline to avoid high turbulence level (see MacKenzie & Leggett (1993)). Typical values of the dissipation rates are given in Table 2.1. Variations in the values of the dissipation rates with the ocean layers give rise to variety of length, time and velocity scales.

2.9 Conclusions

In this Chapter, general overview of turbulent flow and its inherent characteristics was reviewed. Specifically, attention was focussed on homogeneous isotropic turbulence. This assumption is reasonable on small scales. For a flow to be classified as turbulent, it must posses certain distinctive features which include energy dissipation, high Reynolds number and randomness. Statistical approaches are mostly used in solving turbulent flow problems. However, this approach always leads to system of equations that are not closed. Consequently, heuristic modellings are needed to close and solve the equations. The rate of turbulent energy dissipation is an important quantity characterising the flow, the difficulty associated with the measurement of this quantity means that it is often modelled. The variation of this parameter with ocean depth may play a major role

in determining the levels of interactions and vertical distribution of zooplankton and their phytoplankton prey. Those animals that live near the surface would experience high level of turbulence which might influence their feeding behaviour. Near the surface, high turbulent level coupled with light abundance may give rise to a different habitat from the lower depth which is less turbulent with low level of solar irradiance.
Understanding of how turbulence is generated, its nature and effects in the ocean is a subject of considerable importance and practical application.
The inaccessibility of turbulence flows to general analytical treatment implies that it is often tackled through numerical simulations. This is the subject of the next Chapter.

Chapter 3

Kinematic Simulations

3.1 Introduction

Almost any naturally occurring flow is turbulent, and hence it is important to be able to model turbulent flows as accurately as possible. In the present age of large scale computer resources one may think that the full set of Navier-Stokes equations can be solved using numerical integration. However, except in certain highly idealise situations, the computational complexity of the basic problem limits the utility of this approach. Approximations to Navier-Stokes equations can be found much more easily by means of simulations.

A simulation is a representation of some physical process, state of affairs, or biological activity. The act of simulation generally entails imitation of certain key features or behaviour of a physical or abstract system. The development of modern computers, which have the ability to store large amount of data and to perform rapid calculations, enables researchers to develop sophisticated techniques for simulating turbulent flow fields. These compliment experimental observations and in some cases may even replace them because it reduces the cost of design and developmental phases (Mathieu & Scott 2000). To this end, simulation has long been an important tool for designers and is a relatively valuable and versatile method in areas where analytical solutions are not possible. Computations of turbulent flows in engineering and other applications sometimes rely on simple descriptions. That is, in lieu of the solution of the Navier-Stokes equations, the statistical evolution of the overall flow field is sought by means of simulation. A number of turbulent simulation techniques are in use, Direct Numerical Simulation (DNS), Reynolds-averaged Navier-Stokes (RANS) equations, Large Eddy Simulation (LES) and Kinematic Simulation (KS).

3.1.1 DNS

Researchers are making attempt to solve the full set of Navier-Stokes equations using the DNS. However, the inherent computational effort required to directly calculate turbulent flows from the full set of Navier-Stokes equations is so great that it makes the method for most applications impractical. In DNS, the full set of Navier-Stokes equations (2.1.1) are solved numerically without any closure assumption. Because DNS attempts to solve all time and spatial scales, the results are potentially very accurate but computationally unrealisible. This is because the width of the spatial and temporal scales increases with Reynolds number which in turn implies that enormous computer time and storage are required. Thus, DNS is limited to studying flows over small relative simple domain (usually cuboid, see Yamazaki et al. (1991)) ranges and requires large computing time. To appreciate the computational demand of DNS, example will be provided through the study of turbulent diffusion by Chatwin & Paul (1993). Their applications requires the solution of the advection diffusion - equation

$$\frac{\partial \Gamma(x,t)}{\partial t} + Y\dot{\nabla}\Gamma = \kappa\nabla^2\gamma. \tag{3.1.1}$$

Here $\Gamma(x,t)$ is the concentration of dispersing contaminant, $Y = Y(x,t)$ is fluid velocity and κ is the diffusivity coefficient. Because Y is required to satisfy the Navier-Stokes equations, the difficulty of obtaining a solution via the DNS can be summarised in the words of Chatwin & Paul (1993),

"Real mastery of the closure problem will probably occur only when a future generation of computers is large enough and fast enough to allow full 3D and unsteady solutions of (3.1.1) to be directly calculated to adequate accuracy, which requires, in particular, a satisfactory resolution of all length scales down to the conduction cut-off length ($\approx 10^{-4}$)*, and of all time scales. In addition, enough solutions must be generated for each ensemble of velocity fields to permit direct estimation of the statistical properties of* $\Gamma(x,t)$ *to within acceptable limits which will, of course, require a large enough sample size. What evidence there is (Thomson, 1990) suggests that the number of solutions will need to be at least* 10^4 *(and perhaps larger than* 10^5*) for the estimation of statistical properties as simple as velocity variance, this requires a sampling of order* $10^4 - 10^5$*, way beyond current computational resources."*

The inherent computational difficulties limit practical applicability of DNS because it is very expensive to conduct. The method is often used in the development of large scale turbulence models. That is, results from DNS are used as input to other turbulence models such as RANS or results from such models are compared with DNS (see Lewis & Pedley (2000)). At relatively low range of Reynolds numbers, DNS remains a unique computational method that provides information about a number of quantities inaccessible in a laboratory (see Fung & Perkins (2008)). However, alternative approaches are needed for numerical simulations of relatively high Reynolds number flows.

3.1.2 RANS

As the name implies, RANS equations are basically the time-averaged Navier-Stokes equations. In this procedure, approximations are usually done to model the Reynolds stresses and to close the equations. The basic tool required in RANS is the Reynolds decomposition (see Chapter 2). The RANS equations are given by equation (2.4.4). In RANS only representative solutions, typically the mean and variance of the random velocity field are obtained. The advantage of this method is that it does not require enormous computing time. However, the results obtained by this method are often unreliable (see Speziale (1991)).
However, by supplying only mean turbulence quantities, the RANS approach significantly limits the ability to study spatio-temporal structures in turbulent flows.

Some RANS closure schemes

From the equation of the mean flow (2.4.4), it is not generally possible to determine the mean filed without knowing the Reynolds stress $-\langle \widetilde{u}_i \widetilde{u}_j \rangle$. One of the most popular closure scheme was developed by Boussinesq. This procedure is usually done by connecting the Reynolds stress with the mean flow as (see McComb (1991))

$$-\langle \widetilde{u}_i \widetilde{u}_j \rangle = -\frac{2}{3}\langle q^2 \rangle \delta_{ij} + \nu_T \left(\frac{\partial \langle u_i \rangle}{\partial x_j} + \frac{\partial \langle u_j \rangle}{\partial x_i} \right), \tag{3.1.2}$$

where $\langle q^2 \rangle = 1/2 \langle \widetilde{u}_i \widetilde{u}_i \rangle$ is the mean turbulent energy per unit mass and $\nu_T(\mathbf{x}, t)$ is the turbulent eddy viscosity. This closure scheme has several draw backs because it does not reflect the properties of most flow when compared with experimental results (see McComb (1991)). To employ the closure scheme given by (3.1.2), one needs to have an expression for $\nu_T(\mathbf{x}, t)$ which depends on the particular flow in question. Typically, the eddy viscosity is usually model as $\nu_T(\mathbf{x}, t) = \frac{\ell_0^2}{\tau_0}$ where ℓ_0 and τ_0 (see Speziale (1991)) are the turbulent length and time scales respectively.
A better closure scheme than the eddy viscosity type is the so-called $k - \epsilon$ method. In this scheme, the eddy viscosity ν_T is written as the function of turbulent kinetic energy $\langle q^2 \rangle$ and the mean turbulent energy dissipation rate $\langle \epsilon \rangle$. The $k - \epsilon$ method differ from eddy viscosity model because in addition to ν_T, heuristic approximations are also done that produces adjustable constants which will match a given experimental result. In this scheme, the eddy viscosity is approximated by (see Mathieu & Scott (2000))

$$\nu_T = C_\mu \frac{K^2}{\epsilon}, \tag{3.1.3}$$

where C_μ is a constant and $K = \langle q^2 \rangle$. As it stands, equation (3.1.3) cannot be used immediately because K and ϵ are unknown. For homogeneous turbulence, the evolution

equations for these variable are given by (see Lesieur (2008), Mathieu & Scott (2000))

$$\frac{dK}{dt} = \Upsilon - \epsilon, \tag{3.1.4}$$

$$\frac{d\epsilon}{dt} = C_{\epsilon 1}\frac{\epsilon}{K}\Upsilon - C_{\epsilon 2}\frac{\epsilon^2}{K}, \tag{3.1.5}$$

where $\Upsilon = \frac{\nu_T}{2}\left(\frac{\partial\langle u_i\rangle}{\partial x_j} + \frac{\partial\langle u_j\rangle}{\partial x_i}\right)\left(\frac{\partial\langle u_i\rangle}{\partial x_j} + \frac{\partial\langle u_j\rangle}{\partial x_i}\right)$, $C_{\epsilon 1}$ and $C_{\epsilon 2}$ are numerical parameters of the model.

One of the major inadequacies of the standard $k-\epsilon$ model lies in its over reliance on eddy-viscosity model for the Reynolds-stress tensor. Eddy-viscosity models are known to produce poor results in some flows (see Speziale (1991)).

3.1.3 LES

LES is a numerical method for solving the Navier-Stokes equations. The method was first formulated by Joseph Smagorinsky in 1963. In this procedure, the governing equations are solved directly only on relatively large scales. However, the dynamics of turbulence is such that all scales are important. LES seeks to directly solve large spatial scales, while modelling the smaller scales. There are two reasons for doing this. First, the larger scales carry the bulk of the energy, and hence are usually more important. Secondly, the smaller scales have been found to be more universal, and hence are more easily modelled. The resulting methodology involves filtering the Navier-Stokes equations to separate those scales which will be modelled from those which will be solved for directly. The smaller scales which cannot be resolved directly have to be modelled by addition of terms to the equation of motion called the subgrid terms.

Mathematically, the velocity field is separated into a resolved and subgrid part. By doing this the Navier-Stoke equations (2.1.1) is modified to read (see Smagorinsky (1963))

$$\frac{\partial\overline{u_i}}{\partial t} + \overline{u_j}\frac{\partial\overline{u_i}}{\partial x_j} = -\frac{1}{\rho}\frac{\overline{P}}{\partial x_i} + \frac{\partial}{\partial x_j}\left([\nu + \nu_s]\frac{\partial\overline{u_i}}{\partial x_j}\right), \tag{3.1.6}$$

$$\frac{\partial\overline{u_i}}{\partial x_i} = 0, \tag{3.1.7}$$

where $\overline{u_i}$ and $\overline{P}$ are the resolved velocity and pressure fields respectively and ν_s is the subgrid scale eddy viscosity. A standard Smagorinsky subgrid viscosity is given by (see McComb (1991))

$$\nu_s = (c_s\delta)^2\left(\left(\frac{\partial\overline{u_i}}{\partial x_j} + \frac{\partial\overline{u_j}}{\partial x_i}\right)\left(\frac{\partial\overline{u_i}}{\partial x_j} + \frac{\partial\overline{u_j}}{\partial x_i}\right)\right)^{\frac{1}{2}}, \tag{3.1.8}$$

$c_s\delta$ is a length scale that is usually chosen to be of the order of the numerical resolution. What is usually done in LES is that an arbitrary wave number k_c is chosen ($k_c \ll \frac{1}{\eta_k}$).

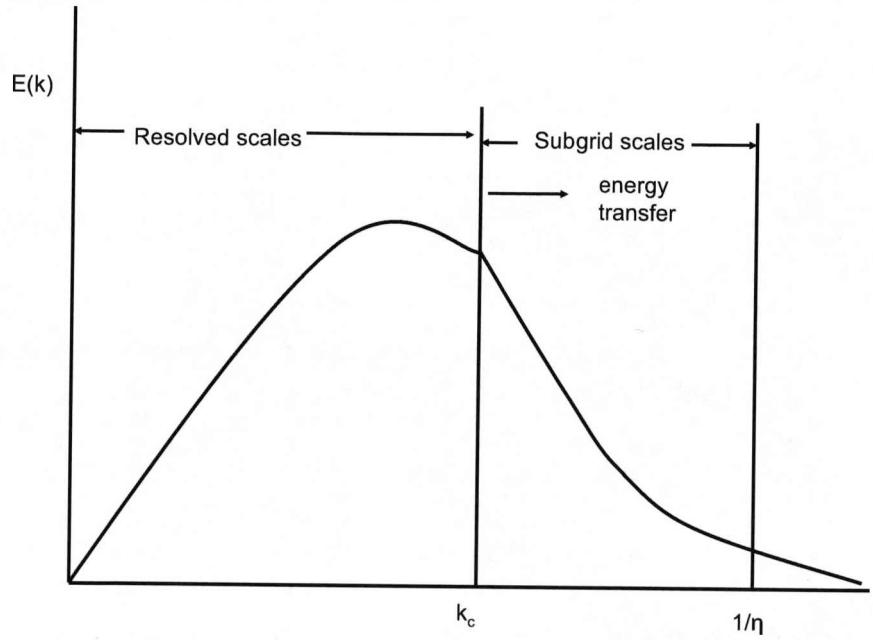

Figure 3.1: A schematic diagram of LES technique showing the cut-off ponit k_c the ranges of resolved and unresolved scales. $E(k)$ is the turbulent energy spectrum.

All modes for which $k > k_c$, which marks the boundary of the desired resolution are neglected. Untreated consequence of this is that energy would accumulate at the cut off (k_c). This is because the mechanism by which energy is transferred beyond k_c has been artificially removed. Subgrid terms are then added to account for the effect of transfer to wave numbers beyond k_c. This process is depicted in Figure 3.1.

The advantages of LES over RANS is that it is more easier to model flows over diverse domains because the various boundary conditions form an inherent part of the large scale motion. Also, RANS provides average results while LES can provide instantaneous characteristics of the flow structure (see McComb (1991)). LES require more computational effort than RANS. The computational demand increases in the vicinity of a wall and often exceed the limit of supercomputer. LES is specially suitable for studying environmental flows such as the dynamics of the mixed layer. DNS is more accurate than LES and is intrinsically capable of producing information about the smallest scales of the flow at a given computational cost. However, higher Reynolds number can be achieved with LES as compared to DNS. As with DNS, LES require large mainframe computers and large amounts of computing time.

An alternative approach, based on an idea of Kraichnan (1970), is to simulate the kinematics of the velocity field without solving the dynamical equations. This technique

is known as Kinematic simulation, which is the method employed in this thesis and is describe in greater detail below.

3.2 Kinematic Simulation (KS)

KS is a Lagrangian model that can be used to track individual particles by following their trajectories. In this method, the turbulent flow is assumed to be homogeneous and isotropic and the velocity fields are simulated using a large number of Fourier modes which vary spatially and with time. The method was first introduced by Kraichnan to study turbulent dispersion (see Kraichnan (1970)). Modified versions are available and are used to study planktonic interactions in the flow (see Lewis & Pedley (2000, 2001)). The flow fields are constructed to satisfy the incompressibility condition but it is not require to satisfy the Navier-Stokes equations. Rather, it seeks to generate flow regimes which mimic universal properties of turbulent flow on small scales without reference to any boundary condition that drive it. KS does not have the full properties of actual turbulent flow as the the structures are quantitatively inaccurate (Malik & Vassilicos 1999). In particular it does not have the mechanism of energy transfer from large to small scales (Lewis & Pedley 2000, Fung et al. 1992). Consequently, turbulence simulated in this way will differ from the actual hydrodynamic turbulence. However, the flow structures have many features of turbulent flow such as eddying, straining and streaming (Malik & Vassilicos 1999). A number of advantages for using KS are

- Considerable reduction of computer time necessary to calculate the velocity field at each time step.
- Computational simplicity allows extra simulations to be carried out in order to track many particles over larger domain sizes.
- Very large inertial subrange are accessible in KS even with moderate computer resources.
- Turbulent flows simulated by this method to study turbulent dispersion have been found to give good agreement with corresponding results from DNS (see Malik & Vassilicos (1999)).

KS turns out to be a powerful tool to study issues of planktonic interactions in turbulent flows.

3.3 Flow Field Parameters

To construct the KS velocity field, certain parameter values are needed. The main input parameters are as follows: For a given wave number $k^{(n)}$, one needs the frequencies $\omega^{(n)}$

which determines how fast an eddy of a particular size overturns and the distribution of the turbulent kinetic energy spectrum $E(k)$. In this dissertation, two forms of energy spectrum are used. Namely, the Inertial subrange (E_{IS}, see Lewis & Pedley (2000, 2001)) and the spectrum function of Mei & Adrian (1995) (E_{MA}, see Mei & Adrian (1995), Lewis & Bala (2006)). These spectrum functions are respectively given as

$$E_{\mathrm{IS}}(k) = \begin{cases} 0, & k \in \left[0, \frac{\check{\alpha}}{\ell}\right), \\ \frac{3}{2}\check{\beta}\frac{W^2}{\ell^{\frac{2}{3}}}k^{-\frac{5}{3}}, & k \in \left[\frac{\check{\alpha}}{\ell}, \frac{1}{\eta_k}\right], \\ 0, & k > \frac{1}{\eta_k} \end{cases} \tag{3.3.1}$$

$$E_{\mathrm{MA}}(k) = \frac{1.5CW^2k^4\ell^5\exp\left(-k^2\eta_k^2\right)}{\left(1+k^2\ell^2\right)^{\frac{17}{6}}}, \quad k \in \left[\frac{1}{4\ell}, \frac{2}{\eta_k}\right] \tag{3.3.2}$$

where $\check{\alpha}, C$, and $\check{\beta}$ are normalisation constants, W is the turbulent intensity, ℓ is a representative scale of the largest eddy. As reported by Yamazaki et al. (1991) the standard value of the buoyancy frequency ($\aleph$) is 0.01 s^{-1}. The authors also reported that this value can be used to calculate the large eddy size and the turbulent intensity respectively using the formulae

$$\ell = \left(\frac{\langle\epsilon\rangle}{\aleph^3}\right)^{\frac{1}{2}}, \tag{3.3.3}$$

$$W = \left(\frac{\langle\epsilon\rangle}{\aleph}\right)^{\frac{1}{2}}. \tag{3.3.4}$$

The normalisation constant $\check{\beta}$ is given by

$$\check{\beta} = \frac{1}{(1-1.5/(\ell^{2/3}))}, \tag{3.3.5}$$

while $\check{\alpha} = 1.5^{1.5}$ see Lewis & Pedley (2000), Lewis (2003). For the Mei & Adrian (1995) spectrum function, the normalisation constant can be calculated using the formula (see appendix of Mei & Hu (1999))

$$C^{-1} = \int_0^\infty \frac{\ell^5k^4\exp\left(-n_k^2k^2\right)}{\left(1+(k\ell)^2\right)^{17/6}}dk. \tag{3.3.6}$$

The integral in (3.3.6) dies off quickly for small and large values of k hence the limits of integration used in calculating C in this work lies in the range $k \in [1/(4\ell), 2]$.

Fluctuating properties of turbulent flow contain energy across a wide range of wave numbers. This feature of the flow is mimicked by the spectrum functions (3.3.2) and (3.3.1) and demonstrated in Figures 3.2 and 3.3. The Figures are for the turbulent energy dissipation rates $\langle\epsilon\rangle = 5.53 \times 10^{-6}$ m^2 s^{-3} for two different kinematic viscosities, $\nu = 1, 1.5 \times 10^{-6}$ $\mathrm{m}^2\mathrm{s}^{-1}$. With the values of $\langle\epsilon\rangle$ and ν the Kolmogorov length, time

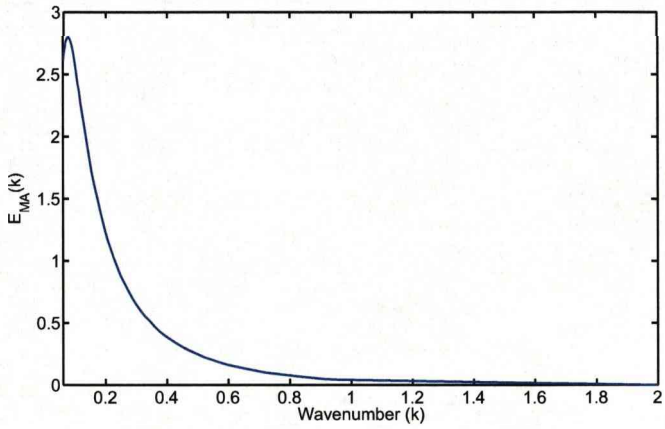

(a) $\nu = 1.0 \times 10^{-6}$ m^{2}s^{-1}

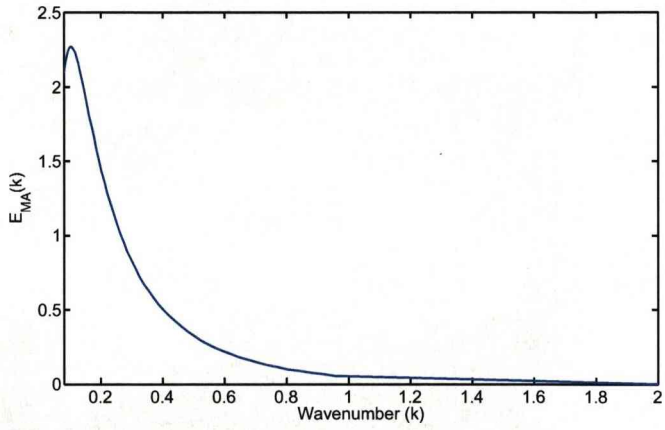

(b) $\nu = 1.5 \times 10^{-6}$ m^{2}s^{-1}

Figure 3.2: A plot of Mei & Adrian (1995) spectrum function (E_{MA}) with $\langle\epsilon\rangle = 5.53 \times 10^{-6}$ m^2 s^{-3} for two different kinematic viscosities. The normalisation constant was calculated using equation (3.3.6) to give $C = 1.303$, ℓ and W were calculated according to equations (3.3.3) and (4.6.2) respectively. (a) With $\nu = 1.0 \times 10^{-6}$ m^{2}s^{-1}, and (b) With $\nu = 1.5 \times 10^{-6}$ m^{2}s^{-1}.

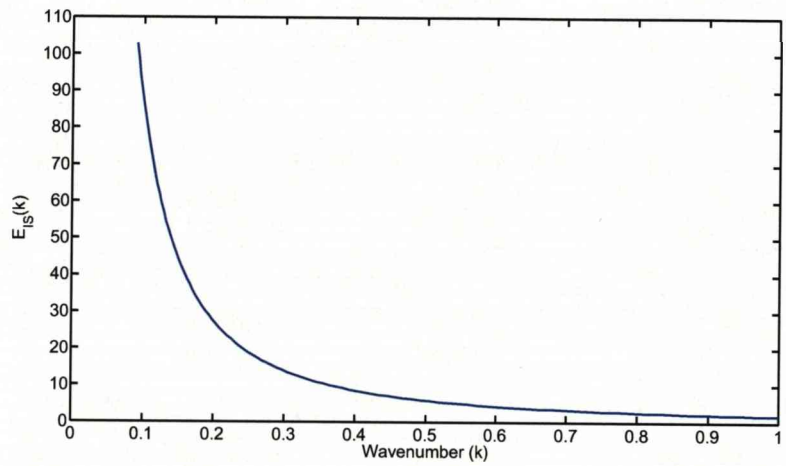

(a) $\nu = 1.0 \times 10^{-6}$ m^{2}s^{-1}

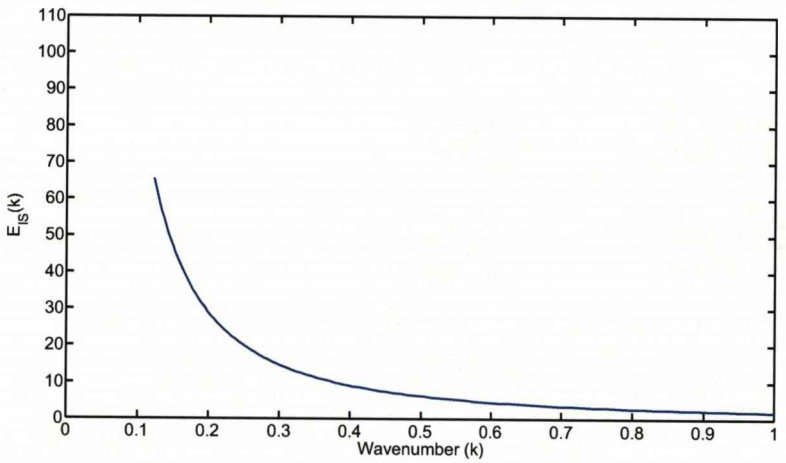

(b) $\nu = 1.5 \times 10^{-6}$ m^{2}s^{-1}

Figure 3.3: A plot of Inertial subrange spectrum function (E_{IS}) with $\langle\epsilon\rangle = 5.53 \times 10^{-6}$ m^2 s^{-3} for two different kinematic viscosities, ℓ and W were calculated according to equations (3.3.3) and (4.6.2) respectively. (a) With $\nu = 1.0 \times 10^{-6}$ m^{2}s^{-1}. (b) With $\nu = 1.5 \times 10^{-6}$ m^{2}s^{-1}.

and velocity scale were calculated by means of equations (2.5.1) and (2.5.3). These are used in non-dimensionalising the remaining variable. For instance, all length scales are non-dimensionalised by dividing with the Kolmogorov length scale (η_k). Similarly the velocity and time scale are non-dimensionalised using the Kolmogorov velocity (ν_k) and time (v_k) respectively. For full account of the simulation parameters and their flow field values see Tables 4.1 and 4.2.

At very high wave numbers, Mei & Adrian (1995) function decreases exponentially as viscosity damps the flow. The Figures show that energy peak occurs at low wave numbers characterising the largest eddies established by the forcing boundary conditions of the flow. This reflects the transfer of energy from large to small scales where it is dissipated by viscosity into heat. Looking at Figures 3.2 and 3.3 one can see that the spectral distribution of energy between the two functions varies slightly. However, the contact/predation rates results using these functions do not differ much. Providing one function is used consistently in a given runs of simulation, realistic estimates of the results are obtainable.

Similarly, one should notice the consequence of altering the viscosity scale. Increasing the viscosity tends to reduce the peak energy as can be observed from Figures 3.2(a) and 3.2(b). This trend is also reflected on Figures 3.3(a) and 3.3(b). It appears that the inertial subrange function is more sensitive to changes in viscosity than the Mei & Adrian (1995) function. For instance, a 50% increase in viscosity produces a net reduction in peak energy of 37% in the former but only 18% in the latter.

Looking at equation (3.3.2), one can see that for low wave numbers, $(k\ell)^2 \ll 1$ and the spectrum function behaves like k^4 (increasing function). At higher wave numbers $(k\ell)^2 \gg 1$ and the spectrum function behaves like $k^{-5/3}$ (decreasing function) which is the expected behaviour at the inertial subrange. The contrasting behaviour of this function at low and high wave numbers results in peak energy as can be seen on Figure 3.2. The k^4 behaviour only applies to homogeneous isotropic turbulence (see Batchelor (1967)). In real environmental flows it is usually impossible to distinguished the true behaviour of $E(k)$ at very low wave numbers.

3.4 Construction of the flow field

Kinematic simulation gives simplified, but realistic representation of turbulence flow structure across a large number of Fourier modes. In this method, the velocity field $(\mathbf{w}(\mathbf{x},t))$ representation is given as a truncated Fourier series

$$\begin{aligned}\mathbf{w}(\mathbf{x},t) &= \sum_{n=1}^{N_k}[(\mathbf{a}^{(n)} \times \widehat{\mathbf{k}}^{(n)}) \cos(\mathbf{k}^{(n)} \cdot \mathbf{x} + \omega^{(n)} t) \\ &+ (\mathbf{b}^{(n)} \times \widehat{\mathbf{k}}^{(n)}) \sin(\mathbf{k}^{(n)} \cdot \mathbf{x} + \omega^{(n)} t)]. \qquad (3.4.1)\end{aligned}$$

Here $\mathbf{k}^{(n)} = k^{(n)}\widehat{\mathbf{k}}^{(n)}$ are randomly directed wave vectors, $\widehat{\mathbf{k}}^{(n)}$ are random unit vectors, $k^{(n)}$ are components of the wave modes and $\omega^{(n)}$ are angular frequency modes. N_k is the number of modes in the simulation. The wave vectors and the angular frequencies both depend on the energy spectrum $E(k)$. The directions of the random coefficients $\mathbf{a}^{(n)}$ and $\mathbf{b}^{(n)}$ must be normal to $\widehat{\mathbf{k}}^{(n)}$ to guarantee the flow field is incompressible (continuity equation is satisfied). The magnitudes of $\mathbf{a}^{(n)}$ and $\mathbf{b}^{(n)}$ are chosen to satisfy equation (3.4.2), in addition to ensure each wave mode contains the correct amount of energy.

$$|\mathbf{a}^{(n)}|^2 = |\mathbf{b}^{(n)}|^2 = 2E(k^{(n)})\delta k^{(n)}. \tag{3.4.2}$$

This choice guarantees that the flow field is incompressible by construction (continuity equation is satisfied). To show that the choice of the random vectors above enables the continuity equation is satisfied, we proceed as follows.
The cross products of two arbitrary vectors $\acute{\mathbf{A}} = (\acute{a}_1, \acute{a}_2, \acute{a}_3)$ and $\acute{\mathbf{B}} = (\acute{a}_1, \acute{a}_2, \acute{a}_3)$ in three dimension can be written as

$$\acute{\mathbf{A}} \times \acute{\mathbf{B}} = \left(\acute{a}_2\acute{b}_3 - \acute{a}_3\acute{b}_2\right)\mathbf{i} + \left(\acute{a}_3\acute{b}_1 - \acute{a}_1\acute{b}_3\right)\mathbf{j} + \left(\acute{a}_1\acute{b}_2 - \acute{a}_2\acute{b}_1\right)\mathbf{k}. \tag{3.4.3}$$

Let

$$\acute{\mathbf{D}} = \mathbf{k}^{(n)} \cdot \mathbf{x} + \omega^{(n)}t = k^{(n)}\left(\widehat{k}_1^{(n)}x_1 + \widehat{k}_2^{(n)}x_2 + \widehat{k}_3^{(n)}x_3\right) + \omega^{(n)}t. \tag{3.4.4}$$

Then

$$\frac{\partial \acute{\mathbf{D}}}{\partial x_i} = k^{(n)}\widehat{k}_i^{(n)}. \tag{3.4.5}$$

In view of equations (3.4.3) and (3.4.4), the velocity field (3.4.1) can be written as

$$\mathbf{w}(\mathbf{x}, t) = \sum_{n=1}^{N_k}\left[(f_1\mathbf{i} + f_2\mathbf{j} + f_3\mathbf{k})\cos\acute{\mathbf{D}} + (g_1\mathbf{i} + g_2\mathbf{j} + g_3\mathbf{k})\sin\acute{\mathbf{D}}\right]. \tag{3.4.6}$$

Here

$$f_1 = \left(a_2^{(n)}\widehat{k}_3^{(n)} - a_3^{(n)}\widehat{k}_2^{(n)}\right), \quad f_2 = \left(a_3^{(n)}\widehat{k}_1^{(n)} - a_1^{(n)}\widehat{k}_3^{(n)}\right), \quad f_3 = \left(a_1^{(n)}\widehat{k}_2^{(n)} - a_2^{(n)}\widehat{k}_1^{(n)}\right)$$

and

$$g_1 = \left(b_2^{(n)}\widehat{k}_3^{(n)} - b_3^{(n)}\widehat{k}_2^{(n)}\right), \quad g_2 = \left(b_3^{(n)}\widehat{k}_1^{(n)} - b_1^{(n)}\widehat{k}_3^{(n)}\right), \quad g_3 = \left(b_1^{(n)}\widehat{k}_2^{(n)} - b_2^{(n)}\widehat{k}_1^{(n)}\right).$$

Here $a_i^{(n)}$, $\widehat{k}_i^{(n)}$, $b_i^{(n)}$, $i = 1, 2, 3$ are components of $\mathbf{a}^{(n)}$, $\widehat{\mathbf{k}}^{(n)}$, $\mathbf{b}^{(n)}$ respectively. Using equation (3.4.5), we have

$$\begin{aligned}\frac{\partial w_1}{\partial x_1} + \frac{\partial w_2}{\partial x_2} + \frac{\partial w_3}{\partial x_3} &= -k^{(n)}\left(\widehat{k}_1^{(n)}f_1 + \widehat{k}_2^{(n)}f_2 + \widehat{k}_3^{(n)}f_3\right)\sin\acute{\mathbf{D}} \\ &+ k^{(n)}\left(\widehat{k}_1^{(n)}g_1 + \widehat{k}_2^{(n)}g_2 + \widehat{k}_3^{(n)}g_3\right)\cos\acute{\mathbf{D}}. \end{aligned} \tag{3.4.7}$$

Here w_i, are components of $\mathbf{w}$. The sums inside the parenthesis in equation (3.4.7) vanishes. Hence, the incompressibility condition is satisfied.
The $\delta k^{(n)}$ are given by Lewis & Pedley (2000)

$$\delta k^{(n)} = \begin{cases} (k^{(2)} - k^{(1)})/2 & n = 1, \\ (k^{(n+1)} - k^{(n-1)})/2 & n = 2, 3 \cdots N_k - 1, \\ (k^{(N_k)} - k^{(N_k-1)})/2 & n = N_k \end{cases} \tag{3.4.8}$$

and

$$k^{(n)} = \begin{cases} \frac{\check{\alpha}}{\ell} & n = 1, \\ k^{(1)} \left(\frac{k^{(N_k)}}{k^{(1)}}\right)^{((n-1)/(N_k-1))} & n = 2, 3 \cdots N_k - 1, \\ \frac{1}{\eta_k} & n = N_k. \end{cases} \tag{3.4.9}$$

Typically 50 to 100 modes (N_k) are adequate to cover the full range of eddies in a fully turbulent flow when the Reynolds number is of order 104 (Fung et al. (1992), Fung & Perkins (2008)). Following Lewis & Pedley (2000) the frequency modes are chosen to satisfy

$$\omega^{(n)} = 0.4\sqrt{(k^{(n)})^3 E(k^{(n)})}. \tag{3.4.10}$$

This choice is motivated by the fact that large eddies with more energy (low $k^{(n)}$) tend to over turn at slower rate than smaller eddies (high $k^{(n)}$).

3.5 Conclusions

In this Chapter some methods of simulating turbulent flow were reviewed. These methods are the DNS, RANS, LES and KS. Of all the methods, DNS is the most accurate but suffers from severe inaccessibility due to enormous computational demand. RANS is relatively more accessible but the results are often unreliable. LES is some what between DNS and RANS in terms of computational demand and is relatively less accurate than DNS. It is more particularly suited to the study of complex situation such as the dynamics of the mixed layers. KS is found to be more accessible and can be used with relatively modest computer. The relatively smaller computational effort means that one can track several planktonic particles in a cubic using the method. This is the methodology that will be employed in this thesis.

Chapter 4

Plankton predation rates for a predator with limited sensory field of perception

4.1 Introduction

Given that the perception field of a planktonic predator is not spherically symmetric as previously assumed, it is important to formulate a new model of planktonic interactions using more realistic geometry. A conical perception field appears to be a good choice because this is closer to real life situation. However, this kind of geometry involves more than one parameter and consequently it is much more complicated to devise theoretical predictions than in the spherically symmetric case. In this Chapter the perception field of a planktonic predator is assumed to be conical in shape, with semi-vertex angle α (see Figure 4.1). If $\alpha = \pi$, the perception field becomes the traditional spherical geometry. For $\alpha = \frac{\pi}{2}$, the perception field become a hemisphere. The conical perception field gives rise to a variety of prey entry points into the perception field. Based on the different relative orientations of the perception field presented to the prey, encounter rate formulae will be derived for a predator following a straight line trajectory. The assumption of the straight line trajectory is important because it simplifies the formulations. Estimates of predation rate for such predators will then be derived by assigning a capture probability function to each encounter that occurs. However, planktonic predators seldom move in straight lines for long. Consequently, modifications to the model will be made to obtain more realistic estimates of the predation rates when the predator changes its direction of swimming rapidly. In this thesis, the derivation of the predation rates for the perception angle $\alpha = \frac{\pi}{2}$ will be presented. But it should be emphasised that predation rates estimates for arbitrary values of $\alpha \in [0, \frac{\pi}{2}]$ have been derived.

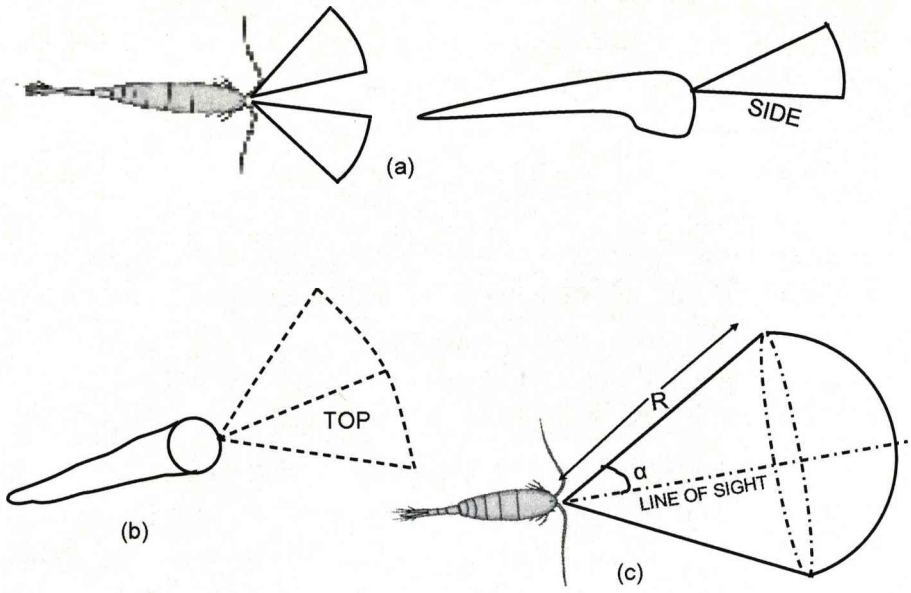

Figure 4.1: Schematic diagrams of the perception field of (**a**) copepod, (**b**) the wedge shape perception field of cod larvae and (**c**) The right circular perception field with semi-vertex angle α for the idealized predator used in this work.

4.2 Initial assumptions

To begin with, it is necessary to draw attention to the distinction between two important terminologies used in this thesis. When it is stated that a planktonic predator follow a straight line trajectory, this means its path is always a straight line irrespective of the flow field present. On the other hand, when it is stated that a predator is pursuing a straight line swimming motion, this means that it is attempting to swim in a straight line, but because its path is also influenced by the flow field the resulting path taken could be very irregular. In the analytical work that follows it is assume that, the predator follows a straight line trajectory and that its field of perception is conical shaped, centred on its head and is characterised by contact radius R, and a semi-vertical angle α as depicted in Figure 4.1. It will be further assumed that the predator's line of sight lies along it swimming direction $\mathbf{v}_{\mathrm{P}}$.

Suppose two microorganisms a predator and prey swimming in a turbulent flow at positions $\mathbf{x}$ and $\mathbf{x}+\mathbf{r}$ respectively at some initial time t. The predator will henceforth be labelled with subscript P and the prey with subscript H. Suppose further that

$$\mathbf{V}_{\mathrm{P}}(\mathbf{x},t) = \mathbf{v}_{\mathrm{P}}(t)+\mathbf{w}(\mathbf{x},t), \tag{4.2.1}$$

$$\mathbf{V}_{\mathrm{H}}(\mathbf{x}+\mathbf{r},t) = \mathbf{v}_{\mathrm{H}}(t)+\mathbf{w}(\mathbf{x}+\mathbf{r},t), \tag{4.2.2}$$

where $\mathbf{V}_{P,H}$ represent the total swimming velocities of the microorganisms comprising of contributions from their own swimming motions $\mathbf{v}_{P,H}$ and a contribution from uncorrelated flow field $\mathbf{w}(\mathbf{x}, t)$. In a coordinate system moving with the prey, the relative straight line velocity $\mathbf{U}$ between the predator and the prey is given by

$$\mathbf{U} = \mathbf{V}_P(\mathbf{x}, t) - \mathbf{V}_H(\mathbf{x} + \mathbf{r}, t). \tag{4.2.3}$$

It will be assumed without loss of generality, that the relative speed is directed along the z-axis as in Figure 4.2(**a**). From the modelling view point, we assumed that $\mathbf{U}$ has a constant direction with random magnitude. This means that, it is not completely random. Modifications will be done later to account for directions changes. If there is no flow and the prey are non-swimming, $\mathbf{v}_P$ will coincide with $\mathbf{U}$. However, the presence of the flow field will cause $\mathbf{v}_P$ to deviate from $\mathbf{U}$ so that the perception field is rotated (see Figure 4.2). The extent of the rotation will depend upon the angle γ which the line of sight makes with the vertical. It will further be assumed that the line of sight lies in the yz- plane. Based on these assumptions, two scenarios can be depicted depending upon the size of angle γ. If γ is small, then it would be expected that $\mathbf{v}_P$ and $\mathbf{U}$ are correlated to some extent. In this scenario, $\gamma \leq \frac{\pi}{2}$ and lies in the yz- plane as in Figure 4.2(**a**). The perception field in this case allows all prey particles to be perceived entering the hemisphere at a distance R, some exit at distance R away from the predator (see the left part of Figure 4.2(**a**)), with others exiting through the spherical base of the hemisphere (at distance less than R as in the right part of Figure 4.2(**a**)).

The second scenario is depicted in Figure 4.2(**b**), when the angle $\gamma > \frac{\pi}{2}$. This situation in Figure 4.2(**b**) is different to 4.2(**a**)) because some prey can be encountered entering the hemisphere through the circular base (distance less than R as in the right part of the Figure) and exiting through the curved surface at a distance R away. However, some prey still enter at a distance R (entering the perception field through the spherical surface, see the left part of the Figure) and exiting at a distance R away from the predator. The act of predation can be broken down into a set of sequentially executed behavioural activities. For the purpose of this work, predation is broken down into two events, `Encounter` and `Capture`. Mathematically speaking, predation rate can be defined as

$$\text{predation rate} = \text{ Encounter rate } \times \text{ Capture probability.} \tag{4.2.4}$$

The predation events are described in some detail below.

Due to the variations in the entry and exit points, which occur mainly because the size of the angle γ, it would be helpful to categorise the predation rates accordingly. The conglomeration of these categories will form the total predation rate. To begin with, the following four simplifying assumptions will be made. After the initial encounter between a predator and prey

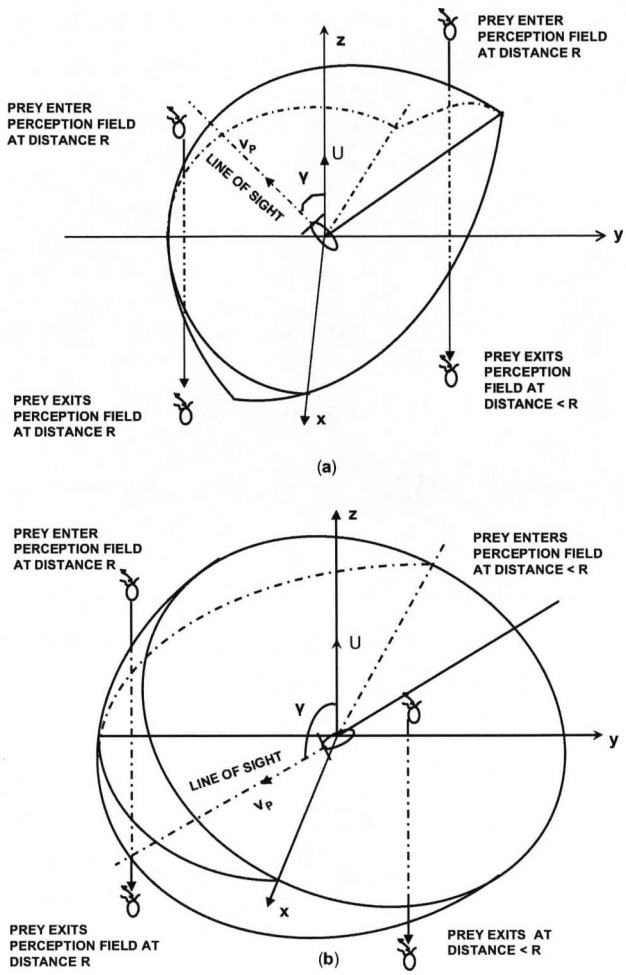

Figure 4.2: Geometry of the encounter process between predator and prey for hemispherical field of perception. (**a**) when the line of sight makes and angle $\gamma \leq \frac{\pi}{2}$ with the vertical, (**b**) when the line of sight makes and angle $\gamma > \frac{\pi}{2}$ with the vertical. The dashes on the Figure represent the the areas outside the perception field.

- the predator continues on its straight line trajectory with relative speed U along the z-axis making no attempt to capture the prey.
- The prey will take a straight line path parallel to the z-axis across the perception field. This assumption is important because knowing the prey entry point, we can calculate the exit point and hence the distance travelled across the perception field.
- Since prey attack and capture by planktonic predators varies with species (see section 4.4), it is therefore unrealistic to model all the responses in detail. It will be assumed that a simple capture probability function exist. This function would expectedly sum up all post-encounter behaviour.
- For each predator species, a particular reaction time T_R exist, which encapsulate

the average time it takes an individual to react, fixate (pursue) and capture its prey and may also incorporate prey escape capabilities.

Some of these assumptions are unrealistic in real life. But given the complexities of the process involved, these will help in making the problem amenable to analytical treatment.

4.3 Mathematical formulation of the predation rate for a planktonic predator with a hemispherical perception field following a straight line trajectory

The predation rates for arbitrary perception field α will result into complicated formulae, hence only derivation of the perception field $\alpha = \frac{\pi}{2}$ will be given here. For this value of α is equivalent to hemispherical perception field and the predation rates formulae for this perception field is presented below. The equations are formulated based on the two situations considered in Figure 4.2. These formulae depend on the scenarios presented by the perception cone which depends on the angle γ which the predators line of sight makes with the vertical (see Lewis (2003)). Therefore the formulation is divided into cases $\gamma \leq \frac{\pi}{2}$ and $\gamma \geq \frac{\pi}{2}$. To do this, the perception field will be transformed into a rotated coordinates system that sends vectors to corresponding vectors rotated about an axis by the angle γ using a rotation matrix. Strictly speaking, rotation matrices are not unique but they are generally required to satisfy the following properties.

- A rotation matrix $\mathbf{Q}$ is a real square matrix with the following properties (see Wikipedia).
  - $\det(\mathbf{Q}) = 1$, where det stand for the determinant.
  - $\mathbf{Q}^T = \mathbf{Q}^{-1}$, where ^{T} and $^{-1}$ stand for transpose and inverse respectively.
  - the sum of squares of the elements in any row or column of $\mathbf{Q}$ is 1.

A rotation matrix $\mathbf{Q}$ about the $x-$axis through an angle γ can be defined as

$$\mathbf{Q} = \begin{pmatrix} 1 & 0 & 0 \\ 0 & \cos\gamma & -\sin\gamma \\ 0 & \sin\gamma & \cos\gamma \end{pmatrix}. \tag{4.3.1}$$

4.3.1 Case 1: $\gamma \leq \frac{\pi}{2}$

In spherical polar coordinates, the position vector of an arbitrary point lying on a hemisphere of radius R can be represented as,

$$\mathbf{s} = R\left(\sin\chi\cos\phi, \sin\chi\sin\phi, \cos\chi\right), \tag{4.3.2}$$

where $\chi \in [0, \frac{\pi}{2}]$ is the angle to the vertical and $\phi \in [0, 2\pi]$ is the azimuthal angle. By rotating the hemisphere through an angle $\gamma \leq \frac{\pi}{2}$, we can find a set of points representing entry points into the perception hemisphere. Consider such rotation in an anticlockwise manner about the x-axis, so that the predator's line of sight lies along its swimming direction $\mathbf{v}_P$ as in Figure 4.2(**a**). Then we have,

$$\mathbf{r}_{in} = \mathbf{Qs} = R \begin{pmatrix} \sin\chi\cos\phi \\ \sin\chi\sin\phi\cos\gamma - \sin\gamma\cos\chi \\ \sin\chi\sin\phi\sin\gamma + \cos\gamma\cos\chi \end{pmatrix}. \tag{4.3.3}$$

Here $\mathbf{r}_{in}$ stands for the potential prey entry point into the perception field. The elemental area projected onto the xy-plane by the curved surface mapped out by the vector $\mathbf{r}_{in}$ is given by,

$$\left| \frac{\partial \mathbf{r}_{inxy}}{\partial \chi} \times \frac{\partial \mathbf{r}_{inxy}}{\partial \phi} \right| d\phi d\chi = R^2 \sin\chi |\cos\gamma\cos\chi + \sin\chi\sin\phi\sin\gamma| d\phi d\chi \tag{4.3.4}$$

where,

$$\mathbf{r}_{inxy} = R(\sin\chi\cos\phi, \sin\chi\sin\phi\cos\gamma - \sin\gamma\cos\chi, 0). \tag{4.3.5}$$

Now define

$$A_{Proj} = \sin\chi|\cos\gamma\cos\chi + \sin\chi\sin\phi\sin\gamma|. \tag{4.3.6}$$

The total predation rate is given by equation (4.2.4). The encounter rate is equal to the prey density ρ_H(which is assumed to be constant throughout this thesis) times the elemental cross-sectional area (CA), times relative speed at constant distance R, times the probability of moving with such speed. Mathematically, the elemental predation rate is given as,

$$\delta PR = \rho_H \times CA \times U(R) \times p_{\text{cap}}(\chi, \phi, \gamma | R) \times p_{P,H}(\mathbf{V}_P, \mathbf{V}_H | R) \mathbf{dV}_P \mathbf{dV}_H \tag{4.3.7}$$

where, $p_{P,H}(\mathbf{V}_P, \mathbf{V}_H|R)$ represent the joint probability distribution of the velocities of the predator and prey separated by the distance R, $U(R)$ is the relative speed at contact distance R apart and $p_{\text{cap}}(\chi, \phi, \gamma|R)$ is the capture probability function. The capture probability function shall be assigned later (section 4.4.3). Because of the appearance of U in the right hand of equation (4.3.7), it is useful to make the following change of variables (see Lewis & Pedley (2000, 2001)),

$$\mathbf{U}(\mathbf{x}, \mathbf{r}, t) = \mathbf{V}_{\text{P}}(\mathbf{x}, t) - \mathbf{V}_{\text{H}}(\mathbf{x} + \mathbf{r}, t), \tag{4.3.8}$$

$$\mathbf{V}(\mathbf{x}, \mathbf{r}, t) = \frac{\sigma^2_{V_{\text{P}}} \mathbf{V}_{\text{H}}(\mathbf{x} + \mathbf{r}, t) + \sigma^2_{V_{\text{H}}} \mathbf{V}_{\text{P}}(\mathbf{x}, t)}{\sigma^2_{V_{\text{P}}} + \sigma^2_{V_{\text{H}}}}, \tag{4.3.9}$$

where,

$$\sigma^2_{V_{\text{i}}} = \frac{1}{3} \left(\langle \mathbf{V}_i \cdot \mathbf{V}_i \rangle - \langle \mathbf{V}_i \rangle \cdot \langle \mathbf{V}_i \rangle \right), \tag{4.3.10}$$

for i = H,P .

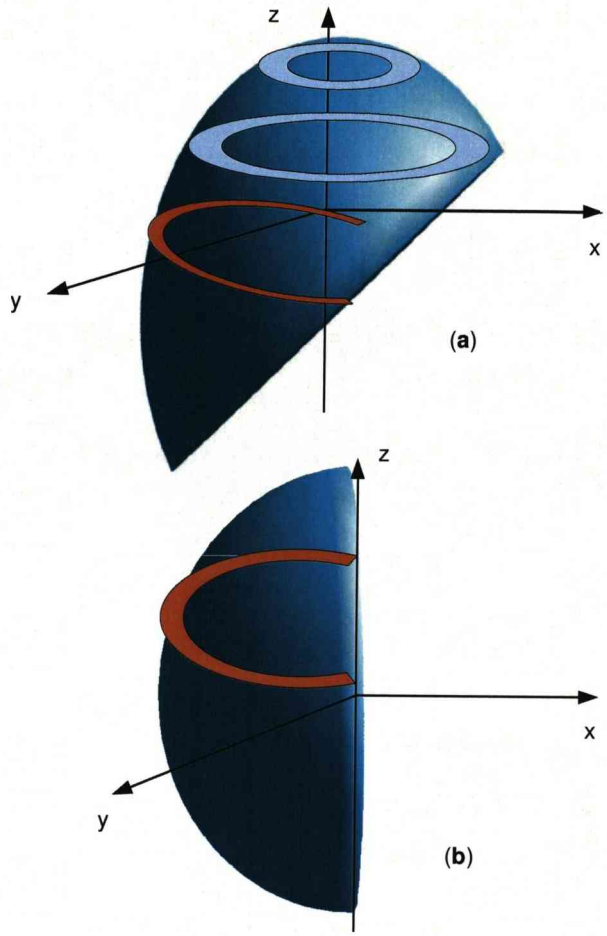

Figure 4.3: Schematic diagrams of the rotated perception hemisphere. This shows that slicing the hemisphere produces either a full (blue) or fraction (orange colored) of a ring depending upon where the hemisphere is sliced and the rotation angle. (a) When rotated by an angle $< \frac{\pi}{2}$. In this both full and incomplete rings are obtainable. (b) When the hemisphere is rotated by an angle equal to $\frac{\pi}{2}$. In this case it can seen that the elemental area is only half a ring.

The limit of ϕ

It is necessary to obtain the limits of integration for all the variables that will appear in the predation rates integrals. Particularly, the limits of ϕ are more complicated because of the rotation of the perception field. The perception field can be divided into a series of horizontal rings (that is parallel to the xy- axes), each defined by a polar angle χ. Some of the rings are complete, some are broken. Complete rings are defined by an azimuthal angle ϕ running the full range from 0 to 2π. The broken rings have a restricted range of ϕ, with some angles excluded. The angles excluded depend

upon by how much the hemisphere has been pivoted around the x-axis (the line of sight angle γ). Full rings always have an angle $\chi < \frac{\pi}{2} - \gamma$. Broken rings only occur when $\chi > \frac{\pi}{2} - \gamma$. The reason for the break is that part of the broken ring is inaccessible to a prey particle moving down the z-axis without encountering another part of the perception field first. Hence it can never make 'first contact' in this part of the ring, and that is why it does not feature. If $\gamma = \frac{\pi}{2}$ exactly as in Figure 4.3 (b) then $\frac{\pi}{2} - \gamma = 0$ and all the rings are broken as $\chi > 0$ (the broken rings in this case are just semi-circles as shown). If the hemisphere is not rotated then the elemental area will always be a full ring. It is therefore necessary to define the limits of ϕ to reflect these restrictions. The requirement that $\cos\gamma\cos\chi + \sin\chi\sin\phi\sin\gamma \geq 0$ (see equation (4.3.6)) implies that $\sin\phi \geq -\cot\gamma\cot\chi$. It makes sense to look at two limiting cases.

- $0 \leq \chi \leq \left(\frac{\pi}{2} - \gamma\right)$:
  In this case
  $$\lim_{\chi \to 0} \cot\chi \to \infty$$
  which means $\cot\gamma\cot\chi \to \infty$. On the other hand
  $$\lim_{\chi \to \left(\frac{\pi}{2} - \gamma\right)} \cot\chi \to \tan\gamma$$
  so that $\cot\gamma\cot\chi \to 1$. These conditions mean that $\sin\phi \geq -\cot\gamma\cot\chi \in [-\infty, -1]$ which in turn implies that $\sin\phi \geq -1$ and that ϕ is free to take any value in the range $[0, 2\pi]$.

- $\left(\frac{\pi}{2} - \gamma\right) < \chi \leq \frac{\pi}{2}$:
  In this case
  $$\lim_{\chi \to \frac{\pi}{2}} \cot\chi \to 0$$
  which means $\cot\gamma\cot\chi \to 0$. This condition imply that $\sin\phi \geq -\cot\gamma\cot\chi \in (-1, 0]$ which in turn implies that $\sin\phi \geq 0$.

The analysis presented above show that in the region where $\arcsin(\cot\gamma\cot\chi) \to \frac{\pi}{2}$, the elemental area is close to a full ring. In the region where $\arcsin(\cot\gamma\cot\chi) \to 0$ the elemental area is closer to half a ring. In between these regions, there is a gradual transition from half to full ring as $\arcsin(\cot\gamma\cot\chi)$ increases. In a nutshell, the conditions restrict

$$\phi \in [0, \pi + \zeta_+] \bigcup [2\pi - \zeta_+, 2\pi], \tag{4.3.11}$$

where $\zeta_\pm(\chi, \gamma) = \arcsin(\pm\cot\gamma\cot\chi) \in [0, \frac{\pi}{2})$. Notice when $\gamma = \frac{\pi}{2}$ as in Figure 4.3 (b), $\zeta_+ = 0$ and hence the range of ϕ is limited to lie between 0 and π (the second interval just becomes the single point 2π) and so all the rings are semicircles irrespective of the value of χ, as is clear from the diagram.

By integrating equation (4.3.7) the total predation rate for $\gamma \leq \frac{\pi}{2}$ reduces to the equation below.

$$\begin{aligned} PR_2(\alpha = \frac{\pi}{2}, \gamma \leq \frac{\pi}{2}) &= \rho_H R^2 \int_{\mathbf{V}} \int_{\mathbf{U}} \int_0^{\frac{\pi}{2}} \int_0^{\pi+\varpi} U(R) p_{UV}(\mathbf{U}, \mathbf{V}|R) \\ &\times A_{Proj} p_{\text{cap}}(\chi, \phi, \gamma|R) d\phi d\chi d\mathbf{U} d\mathbf{V} \\ &+ \rho_H R^2 \int_{\mathbf{V}} \int_{\mathbf{U}} \int_0^{\frac{\pi}{2}} \int_{\pi+H(\chi-(\frac{\pi}{2}-\gamma))\pi-\varpi}^{2\pi} U(R) p_{UV}(\mathbf{U}, \mathbf{V}|R) \\ &\times A_{Proj} p_{\text{cap}}(\chi, \phi, \gamma|R) d\phi d\chi d\mathbf{U} d\mathbf{V}, \end{aligned} \tag{4.3.12}$$

where, $\varpi = H[\chi - (\frac{\pi}{2} - \gamma)] \arcsin(\pm \cot\gamma \cot\chi)$ and $H(x)$ is the Heaviside unit step function defined by,

$$H(x) = \begin{cases} 0 & \text{if } x < 0 \\ 1 & \text{if } x \geq 0. \end{cases}$$

4.3.2 Case 2: $\gamma > \frac{\pi}{2}$

The scenario is depicted in the left part of Figure 4.2(**b**) and can be further divided into two cases. That is, those encounters occurring at a distance R away and those at a distance less than R.

Contact at distance R away.

In this instance when the prey microorganism are initially perceived at a distance R, the prey entry point $\mathbf{r}_{in}(\chi, \phi)$ into the perception hemisphere is restricted to lie in a narrow range of angles. In analogy to that derived in equation (4.3.12) the predation rate is then given by

$$\begin{aligned} PR_3(\alpha = \frac{\pi}{2}, \gamma > \frac{\pi}{2}) &= \rho_H R^2 \int_{\mathbf{V}} \int_{\mathbf{U}} \int_{\gamma-\frac{\pi}{2}}^{\frac{\pi}{2}} \int_{\zeta_-}^{\pi-\zeta_-} U(R) p_{UV}(\mathbf{U}, \mathbf{V}|R) \\ &\times A_{Proj} p_{\text{cap}}(\chi, \phi, \gamma|R) d\phi d\chi d\mathbf{U} d\mathbf{V}. \end{aligned} \tag{4.3.13}$$

$\gamma > \frac{\pi}{2}$ (Close encounters)

The second scenario involved is what could be termed as the close encounters (see Lewis (2003)). This involves prey being perceived at a distance less than R away (right part of Figure 4.2(**b**), that is when prey enter the circular base of the perception field). This is a consequence of the predator's non-isotropic perception field. For a predator looking along the z-axis the entry point can be defined by the vector

$$\mathbf{r}_{in} = r(\cos\phi, \cos\gamma \sin\phi, \sin\phi \sin\gamma), \quad r \in [0, R], \quad \phi \in [0, 2\pi]. \tag{4.3.14}$$

The corresponding elemental cross-sectional area projected onto the xy- plane is given by

$$B_{Proj} = \left| \frac{\partial \mathbf{r}_{inxy}}{\partial r} \times \frac{\partial \mathbf{r}_{inxy}}{\partial \phi} \right| d\phi dr. \tag{4.3.15}$$

The predation rate is obtained in analogous fashion to equation (4.3.12) and (4.3.13) as

$$PR_6(\alpha = \frac{\pi}{2}, \gamma > \frac{\pi}{2}) = \rho_H \int_{\mathbf{V}} \int_{\mathbf{U}} \int_0^R \int_0^{2\pi} U(r) p_{UV}(\mathbf{U}, \mathbf{V}|r) \times B_{Proj} p_{\text{cap}}(r, \phi, \gamma|R) d\phi dr d\mathbf{U} d\mathbf{V}. \quad (4.3.16)$$

For a predator with a hemispherical perception field following straight line trajectory, the total predation rate is given by the sum of equations (4.3.12), (4.3.13) and (4.3.16). It should be noted that predation rates equations are also derived for arbitrary perception angles $\alpha \leq \frac{\pi}{2}$. These cumbersome formulae are omitted here. The notation $PR_n(\alpha = \frac{\pi}{2}, \gamma \leq \frac{\pi}{2})$ needs some explaining. In Lewis (2003) appendix for the general case $\alpha \leq \frac{\pi}{2}$, the resulting encounter rates is made op of 6 integrals denoted by PR_{1-6}. In the particular case $\alpha = \frac{\pi}{2}$, integrals $PR_1 = PR_4 = PR_5 = 0$. Hence the notation used in equations (4.3.12), (4.3.13) and (4.3.16) corresponds to those used in the appendix of the paper.

4.4 Capture Probability function

From information gathered from literature studies, probability of capture depends upon a wide variety of different parameters such as

- The species.
- Predation strategy employed.
- Prey size and speed.

Due to these differences in behaviour between the species, rather than modelling a particular behaviour, a relatively simple but plausible capture probability function that may have wide applicability shall be used. The key parameter is the predators reaction time (T_R) which encapsulates how long on average it takes a predator to react, fixate, pursue, and capture the prey. Typical values of the reaction time can be estimated from studies for most species found in the literature. In addition to the parameters listed above it may also depend on environmental factors. For instance, zooplankton that inhabits quiescent environment are known to react faster than those living in more violent ones (see Yen et al. (1992)). So with this one, single parameter, it should then be possible to model the results of a wide variety of different attack responses. The capture probability function is then modelled according to equation (4.4.1).
Consider a prey particle moving a with relative speed $U(p)$ within the perception field of the predator. Here p is distance. The prey will disappear from the perception field after a time t_{TRA} has elapsed. Thus, probability of capture can be written as

$$p_{\text{cap}} = \frac{\langle t_{TRA} \rangle^\beta}{\langle t_{TRA} \rangle^\beta + T_R^\beta} \quad \beta > 1. \quad (4.4.1)$$

Here $\langle t_{TRA} \rangle$ represents an estimate of the average time the prey spends traversing the predator's perception field assuming the latter makes no capture attempt. And β is a non-dimensional parameter. From equation (4.4.1) and Figure 4.4, it is clearly seen

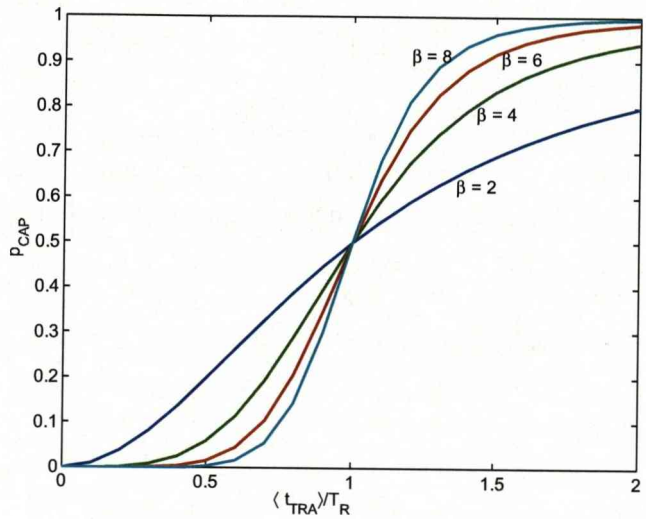

Figure 4.4: Variation of the capture probability function for different values of of shape parameter β. This Figure is plotted using equation (4.4.1). $\langle t_{\mathrm{TRA}} \rangle$ and T_R are the average time take by prey to traverse the perception field and the predators reaction time respectively. For large β, the function behaves more like a step function. To get the Figure, we divided the top and the bottom of equation (4.4.1) by T_R and then used assumed values for $\frac{\langle t_{\mathrm{TRA}} \rangle}{T_R}$ in the range [0,2].

that capture is very difficult if $T_R \gg \langle t_{TRA} \rangle$ and is most likely when $T_R \ll \langle t_{TRA} \rangle$. To get the Figure, we divided the top and the bottom of equation (4.4.1) by T_R and then used assumed values for $\frac{\langle t_{\mathrm{TRA}} \rangle}{T_R}$ in the range [0, 2]. The Figure also portrays the behaviour of the capture function for different values of β. For $T_R \gg \langle t_{TRA} \rangle$, the $\beta = 2$ curve predicts higher capture probability than the other curves in contrast to the case when $T_R \ll \langle t_{TRA} \rangle$. The variation in the capture function with β is effectively modest, hence any reasonable choice should not give rise to radically different results. In this thesis $\beta = 2$ is going to be used throughout.

In order to utilise this capture function in any theoretical predictions it is necessary to estimate the average value of $\langle t_{TRA} \rangle$. For a predator following a straight line trajectory such an estimate can be made using the following procedures.

4.5 Estimation of the time taken $\langle t_{TRA} \rangle$ by the prey to traverse the perception field if the predator follows a straight line trajectory

The distance travelled by the prey across the perception field depends on the entry point and the angle γ. One of the fundamental assumptions initially made was that the prey follows a straight line trajectory parallel to the z-axis across the perception field and the predator make no attempt to capture the prey. The assumptions became necessary in order to simplify the problem (in practice, the planktonic prey seldom follow a straight line path for a long time). This implies that knowing the prey entry points into the perception field (equations (4.3.3) and (4.3.14)), we can determine the values of s and θ that determine its exit point.

4.5.1 Prey exit at distance $s < R$ and $\gamma \leq \frac{\pi}{2}$

In this orientation all prey microorganism are perceived entering the perception field through the curved surface with some exiting through the base (right half of Figure 4.2(**a**)) at a distance $s < R$. The general position vector of points describing the circular base of the cone can be written as

$$\mathbf{p}_{out} = s(\cos\theta, \sin\theta, 0) \quad s \in [0, R], \quad \theta \in [0, 2\pi]. \tag{4.5.1}$$

If the perception field is rotated anticlockwise about the x-axis through an angle $\gamma \leq \frac{\pi}{2}$ the exit point ($\mathbf{r}_{out}$) is

$$\mathbf{r}_{out} = \begin{pmatrix} 1 & 0 & 0 \\ 0 & \cos\gamma & -\sin\gamma \\ 0 & \sin\gamma & \cos\gamma \end{pmatrix} \mathbf{p}_{out} = s \begin{pmatrix} \cos\theta \\ \sin\theta\cos\gamma \\ \sin\theta\sin\gamma \end{pmatrix}. \tag{4.5.2}$$

Since prey are assumed to traverse the perception field in straight line, the x, y coordinates of the prey path remain the same but the z coordinates changes. Therefore, the values of s and θ are the solutions of the x, y parts of equations (4.3.3) and (4.5.2)

$$s\cos\theta = R\sin\chi\cos\phi \tag{4.5.3}$$

$$s\sin\theta\cos\gamma = R(\sin\chi\sin\phi\cos\gamma - \cos\chi\sin\gamma), \tag{4.5.4}$$

which yields,

$$s = R\big(\sin^2\chi - \sin 2\chi\sin\phi\tan\gamma + \cos^2\chi\tan^2\gamma\big)^{\frac{1}{2}}, \quad s \leq R, \tag{4.5.5}$$

and

$$\theta = \begin{cases} \arccos\left(\frac{R\sin\chi\cos\phi}{s}\right), & \sin\chi\cos\phi\cos\gamma - \sin\gamma\cos\chi > 0, \\ 2\pi - \arccos\left(\frac{R\sin\chi\cos\phi}{s}\right), & \text{otherwise.} \end{cases} \tag{4.5.6}$$

Upon substituting equations (4.5.5) and (4.5.6) in (4.5.2) the coordinates of the exit point are obtained. The values of s defined by equation (4.5.5) may not always lie in the range $[0, R]$. If values of $s > R$ are obtained, then the prey exit the perception field through the curve surface (left part of Figure 4.2(**a**)). Symmetrically, the exit point ($\mathbf{r}_{out}$) is the entry point with the sign of the z coordinate changed.

$$\mathbf{r}_{out}(\chi, \phi) = R \begin{pmatrix} \sin\chi\cos\phi \\ \sin\chi\sin\phi\cos\gamma - \sin\gamma\cos\chi \\ -(\sin\chi\sin\phi\sin\gamma + \cos\chi\cos\gamma) \end{pmatrix}. \tag{4.5.7}$$

4.5.2 Prey entry through the base and $\gamma > \frac{\pi}{2}$

From the right part of Figure 4.2(**b**), prey entering the perception field through the base (distance $< R$) will always exit at a distance R (through the curved surface). For a straight line path parallel to the z - axis, the x, y coordinates remain the same but the z- coordinate must alter to give a vector of magnitude R. Since the entry point depends on r and ϕ, (see equation (4.3.14)) then

$$\mathbf{r}_{out} = \begin{pmatrix} r_{inx} \\ r_{iny} \\ -\sqrt{R^2 - r_{inx}^2 - r_{iny}^2} \end{pmatrix} = \begin{pmatrix} r\cos\phi \\ r\sin\phi\cos\gamma \\ -\sqrt{R^2 - (r\cos\phi)^2 - (r\sin\phi\cos\gamma)^2} \end{pmatrix} \tag{4.5.8}$$

To estimate the time taken by the prey in the predator's perception field, we can define a function $\mathbf{p}$ that parameterises the prey trajectory across the perception field as follows

$$\mathbf{p}(\zeta) = (1 - \zeta)\mathbf{r}_{in} + \zeta\mathbf{r}_{out}, \quad \zeta \in [0, 1]. \tag{4.5.9}$$

It is of interest to note here that the function $\mathbf{p}$ delineates the prey-predator separations as the former traverses the perception field in contrast to $\mathbf{r}, \mathbf{R}$ which depicts their separation as the prey enters the perception field. So, the average time taken by the prey across the perception field $\langle t_{TRA} \rangle$ =(distance covered)/(average speed). The distance travelled is the length of the arc described by $\mathbf{p}$ from $\zeta = 0$ to $\zeta = 1$. Hence, $\langle t_{TRA} \rangle$ can be defined as

$$\langle t_{TRA} \rangle = \int_0^1 \frac{1}{\langle U(p(\zeta)) \rangle} \left| \frac{d\mathbf{p}}{d\zeta} \right| d\zeta = \left(\frac{2}{\pi}\right)^{\frac{1}{2}} \int_0^1 \frac{1}{\sigma_U(p(\zeta))} \left| \frac{d\mathbf{p}}{d\zeta} \right| d\zeta, \tag{4.5.10}$$

where $\sigma_U^2, \langle U^{-1} \rangle$ are defined as (see Lewis & Pedley (2001))

$$\sigma_U^2 = \frac{\langle \mathbf{U} \cdot \mathbf{U} \rangle - \langle \mathbf{U} \rangle \cdot \langle \mathbf{U} \rangle}{3}, \qquad \langle U^{-1} \rangle = \frac{1}{\sigma_U} \left(\frac{2}{\pi}\right)^{\frac{1}{2}}.$$

σ_U^2 is the ensemble average variance of the components of $\mathbf{U}$.

4.6 Evaluation of the predation rate integrals

Having specified the form of the probability capture function, the next step in the evaluation of the predation rate integrals given by equations (4.3.12), (4.3.13) and (4.3.16) is to specify the probability distribution $p_{UV}(\mathbf{U},\mathbf{V}|r)$. Unfortunately, there is no general information on what the distribution function might be. However, for a homogeneous isotropic turbulence, it is possible to postulate a relatively simple form of this distribution. Here the six-dimensional binormal distribution (see Lewis & Pedley (2000, 2001), Lewis (2003)) will be employed

$$\begin{aligned} p_{UV} &= \frac{1}{\left(2\pi\sigma_U\sigma_V(1-\zeta^2)^{\frac{1}{2}}\right)^3} \times \exp\left[\left(-\frac{1}{2(1-\zeta)^2}\right)\right. \\ &\times \left.\left(\frac{(\mathbf{V}-\langle\mathbf{V}\rangle)^2}{\sigma_V^2}+\frac{(\mathbf{U}-\langle\mathbf{U}\rangle)^2}{\sigma_U^2}-\frac{2\zeta(\mathbf{V}-\langle\mathbf{V}\rangle)\cdot(\mathbf{U}-\langle\mathbf{U}\rangle)}{\sigma_U\sigma_V}\right)\right], \end{aligned} \tag{4.6.1}$$

where the function $\zeta(r)$ is the correlation coefficient of the pair $(\mathbf{U},\mathbf{V})$ and is defined by $\zeta(r)=\frac{(\mathbf{U}\cdot\mathbf{V})}{3\sigma_U\sigma_V}$. The choice of this distribution arises because it gave satisfactory results in previous studies (see Lewis & Pedley (2000, 2001), Lewis (2003)). The distribution function is also independent of orientation which reduces the complexity of its usage in equations (4.3.12), (4.3.13) and (4.3.16).

One difficulty in evaluating the predation rates integrals lies in the fact that γ, the angle which the line of sight makes with the vertical is unknown. The procedure for estimating the line of sight is presented in the next sub-section.

4.6.1 Calculation of Line of sight

The vectors $\mathbf{U},\mathbf{V}$ are known (random) and hence $\mathbf{V}_\mathrm{P},\mathbf{V}_\mathrm{H}$ but not $\mathbf{v}_\mathrm{P},\mathbf{v}_\mathrm{H},\mathbf{w}$ individually. It must be emphasised here that $\mathbf{U}$ is not completely random. In generating $\mathbf{U}$, we suppressed the randomness in direction and allowed randomness only in magnitude. From the properties of the flow field the intensity of the turbulent W can be calculated using the following formula (see Yamazaki et al. (1991))

$$W = \left(\frac{\langle\epsilon\rangle}{\aleph}\right)^{\frac{1}{2}} = (\langle\mathbf{w}(\mathbf{x})\cdot\mathbf{w}(\mathbf{x})\rangle/3)^{\frac{1}{2}}. \tag{4.6.2}$$

The angle between the vectors $\mathbf{w}(\mathbf{x}),\mathbf{w}(\mathbf{x}+\mathbf{r})$ can be estimated by

$$\begin{aligned} \cos\omega &= \frac{\langle\mathbf{w}(\mathbf{x})\cdot\mathbf{w}(\mathbf{x}+\mathbf{r})\rangle}{\langle\mathbf{w}(\mathbf{x})\cdot\mathbf{w}(\mathbf{x})\rangle} \\ &= \frac{2\int_0^\infty E(k)(\sin(kr)/kr)dk}{3W^2} \end{aligned} \tag{4.6.3}$$

With these information the procedure used by Lewis (2003) in estimating γ will be adopted. This is based on the assumption that the prey are known swimming and

hence $\mathbf{v}_H = 0$. For each value of $\mathbf{U}, \mathbf{V}$ equations (4.3.8) and (4.3.9) can be used to find $\mathbf{V}_{P,H}$ and hence $\mathbf{w}(\mathbf{x}+\mathbf{r},t)$ from equation (4.2.2). The remaining steps in the calculation is presented below for completeness.

- This involve making a series of random choice of $\mathbf{U}$ and $\mathbf{V}$. For each choice, the corresponding values of $\mathbf{V}_{P,H}(\mathbf{x}+\mathbf{r},t)$ are obtained by means of equations (4.3.8) and (4.3.9). Once $\mathbf{V}_{\mathrm{H}}(\mathbf{x}+\mathbf{r},t)$ is known, $\mathbf{w}(\mathbf{x}+\mathbf{r},t)$ is also determined.

- Given any value of $\mathbf{w}(\mathbf{x}+\mathbf{r},t)$, random vectors of the form

$$\mathbf{w}(\mathbf{x},t) = |\mathbf{w}(\mathbf{x},t)|(\sin\theta\cos\phi, \sin\theta\sin\phi, \cos\theta) \tag{4.6.4}$$

  are generated. The magnitude of the vector are chosen to satisfy

$$|\mathbf{w}(\mathbf{x},t)| = |\mathbf{w}(\mathbf{x}+\mathbf{r},t)|\cos\omega + (1-\cos\omega)\sqrt{3}W. \tag{4.6.5}$$

  The rationale behind the choice of equation (4.6.5) is that, as $r \to \infty$ the correlation between $\mathbf{w}(\mathbf{x}+\mathbf{r},t)$ and $\mathbf{w}(\mathbf{x},t)$ breaks away.

- The angle ϕ is randomly chosen in the $[0, 2\pi]$.

- Random deviate Xdrawn from uniform distribution in [0, 1] was generated and used to generate a random deviate q such that

$$X = \frac{1}{2\pi}\int_{-\infty}^{q} \exp\left(-x^2/2\right)dx. \tag{4.6.6}$$

  The angle θ is then chosen to satisfy $\theta = \omega(1+2q) \bmod \pi$.

The estimation of $\mathbf{w}(\mathbf{x},t)$ as outlined above, enables the calculations of $\mathbf{v}_P$ and hence γ.

4.7 Predation rates for predators following irregular trajectories

The theoretical formulations of the predation rates highlighted in the previous sections are exact assuming a straight line path. Although this is an unrealistic assumption, substantial mathematical simplifications were achieved. Following a convoluted path will affect both the number of contacts and the predation rates.
To estimate the effect of n direction changes after time $\tau < T$, the idea of volume fraction developed by Lewis (2003) which was reviewed in Chapter 1 will be used. As the predation rate formulae (equations (4.3.12), (4.3.13) and (4.3.16)) are directly proportional to the volume mapped out when the predator moves in straight line, multiplying these results by the volume fraction should give a reasonable estimate of the predation rate for a predator following an irregular trajectory.

4.7.1 Capture probability incorporating irregular trajectory

Following an irregular path will imply that the prey particles may take shorter paths traversing the perception field. This in turn means that $\langle t_{TRA} \rangle$ will also be reduced compared to that of straight line path (given by equations (4.5.9) and (4.5.10)). This reduction will make capture more difficult. The question of how straight is the predator's path depends on the relative length of the line segments $U_R(\sigma_P)\tau$ (this reflects both passive advection and swimming motion) compared to $U_R(0)\tau_{\text{LC}}$ (for passive advection by the flow only). It is tempting to suggest an estimate of the form

$$\langle t_{TRA} \rangle_{\text{irr}} = g\Big(\tau/(\chi_{\text{U}}\tau_{\text{LC}})\Big)\langle t_{TRA} \rangle. \tag{4.7.1}$$

Where $g\Big(\tau/(\chi_{\text{U}}\tau_{\text{LC}})\Big) \in [0,1]$ is a non-dimensional function such that

$$g\Big(\tau/(\chi_{\text{U}}\tau_{\text{LC}})\Big) \rightarrow \begin{cases} 1, & U_R(\sigma_P)\tau \gg U_R(0)\tau_{\text{LC}}, \\ \\ 0, & U_R(\sigma_P)\tau \ll U_R(0)\tau_{\text{LC}}. \end{cases} \tag{4.7.2}$$

Numerous mathematical functions might stand for g and a relatively simple one is the standard error function

$$erf(x) = \frac{2}{\sqrt{\pi}} \int_0^x e^{-t^2}\, dt. \tag{4.7.3}$$

So that

$$g\Big(\tau/(\chi_{\text{U}}\tau)\Big) = erf\Big[A\Big(\frac{\tau}{\chi_{\text{U}}\tau_{\text{LC}}}\Big)^{\varsigma}\Big], \tag{4.7.4}$$

where A and ς are non-dimensional constants that may be dependant on the flow field. In this study, the values $A = \varsigma = 0.4$ are found to be suitable because they agree with the output of series of kinematic simulations that will be described presently.

4.8 Kinematic simulation

Numerical simulations are also conducted to study the combined problem of contact and predation rates for predators with restricted field of perception. The numerical model consists of two coupled-modules. One of which is the KS flow field and its turbulent-like characteristics. The second module consists of the individual-based planktonic predator-prey interactions. Altogether a total of seven flow fields were constructed to track the microorganisms in the flow by varying some parameter values (see Tables 4.1 and 4.2). The main parameters varied are the energy dissipation rate and the viscosity values. Using these parameter values the Kolmogorov length, velocity and time scales are calculated. For each flow, these were used to non dimensionalize the remaining variables. For example, all length, time and velocity scales were non-dimensionalised by dividing them with the Kolmogorov length, time and velocity scales respectively.

4.8.1 Model setup and parameters

The basic simulation domain is a cube with varying sides (initial size of each side of the domain is 0.5 m). Making the reasonable assumption that turbulence is homogeneous and isotropic down at scales of the size of individual planktonic predator, the KS flow field (see section 3.4) was constructed within the simulation domain. Into the domain two sets of particles were introduced with one group representing the prey, and the second group the predators. The number of prey and predators introduced into the domain initially were equal (512). This fixes the prey density at a value of $512/0.5^3 \approx 4.3$ per litre a reasonable value for the pelagic marine environment. The particles were initially distributed randomly throughout the domain, with no predator in contact with any prey (all positioned at distance greater than R).

Each group of particles was then assigned a random walk swimming speed drawn from a three dimensional Gaussian distribution with zero mean and standard deviation σ_P, such that the collective swimming speed is $\langle v_{P,H} \rangle = \sqrt{\frac{8}{\pi}}\sigma_{P,H}$. This velocity in essence defines the predators'/prey direction of motion in the absence of any flow. A predator/prey may change its swimming velocity at certain fixed intervals during the simulation. This interval time scale is denoted by τ_{sight}. The simulation has examined two kinds of search patterns. Cruising and saltatory behaviour. For cruising predators, two cases were considered. One of which is the case where the predator never change their direction of motions throughout a run of simulation ($\tau_{\text{sight}} = \infty$). The second is when the predators changes their swimming pattern every $\tau_{\text{sight}} = 2.7$ seconds. To implement this, a number of time steps N_T (equivalent to a time τ_{sight}) was imposed for which the random walk remained unchanged. During a run, questions were asked whether it was time to change the random walk, if yes, new random walk swimming speed was drawn from the appropriate distribution. This results in a change of swimming direction. Otherwise, it was assumed a predator/prey makes no changes to its swimming motion.

For the saltatory predators, the information drawn from the experimental work of Galbraith et al. (2004) were used. The pause travel time (3 seconds) was split into percentage of time spent pausing and travelling as follows (33%, 67%), (50%, 50%), (67%, 33%), (17%, 83%). That is, 33% of the time was spent in pause mode with 33% spent in travel mode and so on. For the simulation in Chapter 6 two more pause-travel modes namely, (100%, 0%) and (0%, 100%) were included. During the travel phases, larval swimming speed was drawn from the appropriate distribution. At the expiration of each travel phase, the predators were given a gliding speed of 0.04 mm s^{-1} and were allowed to change direction. At the end of each pause phase, the larva was allowed to change direction and resume to its travel.

The instantaneous swimming velocity of the predator is the sum of individual swimming and the local turbulent flow velocity. Except for the simulations discussed in

Chapter 6, the prey were assumed to be passively drifting in the flow (non-swimming). This assumption may be true for copepod's prey, it is however not necessarily true for the larval fish prey. However, because of their small sizes and speeds, their individual swimming capability is not so significant and will in general, be dominated by the flow. The new innovation contained in the current model is that the predator's perception field was assumed to be conical in shape with a semi-vertex angle α rather than sphere as was commonly assumed. The restricted perception field is more realistic and it influences the estimates of planktonic contact rates (see Lewis (2003)). The present modelling ideas extends the previous theory and investigated the influence of this kind of perception geometry on planktonic predation rates.

The model parameters were extracted from experimental data (for instance see Galbraith et al. (2004)). Some parameter values such as the contact radius ($R = 12$ mm) have the same value in all the flow fields. Table 4.2 summarises the simulation parameters and their values depending upon the flow fields. Where units are not given, the parameter are dimensionless, and the Kolmogorov scales (length, time and velocity scales) were used in the non-dimensionalising them.

4.8.2 Model execution

Simulations were conducted for four different perception angles $\alpha = \pi/6,\ \pi/4,\ \pi/3$ and $\pi/2$ (hemispherical) with the predators executing two different searching patterns, cruising and saltatory described above. Each run of a simulation involved tracking down of planktonic particles in the domain over a non-dimensional simulation time S_{time} of about 7 min. The non-dimensional simulation time was converted into total number of simulation time steps ($T'_{\text{steps}} = (S_{\text{time}})/(\text{step size})$). The trajectories of the predator and prey $\mathbf{X}_{P,H}$ (where the subscript P and H denote the prey and predator respectively) were obtained using the fourth order Runge - Kutta method to integrate (see Lewis & Pedley (2000))

$$\frac{d\mathbf{X}_{P,H}(t)}{dt} = \mathbf{w}(\mathbf{X}_{P,H}(t), t) + \mathbf{v}_{P,H}(t) \tag{4.8.1}$$

where $\mathbf{v}_{P,H}(t)$ are the swimming motions of the microorganisms and $\mathbf{w}(\mathbf{X}_{P,H}(t), t)$ are the velocity contributions from the flow field. The step sizes (0.02 - 0.08) used in the integration were chosen to be sufficiently small enough to prevent a predator missing a prey in its perception field between two time steps.

Registering an encounter

In these simulations, the act of predation was summarised into two main events viz encounter and capture. The predation events began with the encounter. An encounter was registered whenever a prey microorganism moved to within a distance R in the

Parameter description	Symbolic description	Unit
Average energy dissipation rate	$\langle \epsilon \rangle$	$\mathrm{m}^{2}\ \mathrm{s}^{-3}$
Kolmogorov length scale	η_k	m
Kolmogorov velocity scale	ν_k	$\mathrm{m\ s}^{-1}$
Kolmogorov time scale	τ_k	s
Turbulent intensity	W	
Large eddy size	ℓ	
Kinematic viscosity	ν	$\mathrm{m}^{2}\ \mathrm{s}^{-1}$
Taylor micro scale	λ	
Reynolds number base on micro scale eddy	Re_λ	
Reynolds number base on large eddy size	Re	
Number of Fourier modes	N_k	
Contact radius	R	
Predator's reaction time	$T_R^{'}$	
Non-dimensional simulation time	$\mathrm{S_{time}}$	
Number of time steps	$T_{\mathrm{steps}}^{'}$	

Table 4.1: Kolmogorov scales and parameter values characterizing the kinematic flow field. Where units are not given, the parameters are in non dimensional form.

perception field of the predator. For each encounter that occurred, the distance between the predator and prey were recorded. Those contacts where the distance were less than R are called the close encounters. This feature is a consequence of the restricted perception field and is unavailable in spherical geometry.

We assumed that once a predator encountered a prey, the predator has a particular reaction time $T_R^{'}$ within which it can react, pursue and capture the prey. Detecting an encounter normally requires searching for occurrences when a prey particle moves within the perception field of the predator. Ordinarily this will require checking the relative positions of every prey with every predator at each time step. That is an operation of order $O(N_P \times N_H)$ (number of predators times the number of prey). This is computationally expensive. To circumvent this problem, the simulation domain was further sub-divided into smaller boxes of size R (contact radius) each. The potential prey particle sharing a given box with a predator and also the potential prey in the neighbouring boxes were examined for contact after each time step.

Parameter	Flow 1	Flow 2	Flow 3	Flow 4	Flow 5	Flow 6	Flow 7
$\langle\epsilon\rangle(\mathrm{m}^2\ \mathrm{s}^{-3})$	5.53×10^{-9}	5.53×10^{-8}	5.53×10^{-9}	5.53×10^{-8}	5.53×10^{-7}	5.53×10^{-7}	5.53×10^{-9}
$\nu(\mathrm{m}^2\ \mathrm{s}^{-1})$	1.5×10^{-6}	1.5×10^{-6}	1.2×10^{-6}	1.0×10^{-6}	1.0×10^{-6}	1.5×10^{-6}	1.0×10^{-6}
$\eta_k(\mathrm{m})$	4.97×10^{-3}	2.80×10^{-3}	4.20×10^{-3}	2.06×10^{-3}	1.16×10^{-3}	1.57×10^{-3}	3.67×10^{-3}
$\nu_k(\mathrm{m\ s}^{-1})$	3.02×10^{-4}	5.37×10^{-4}	2.85×10^{-4}	4.85×10^{-4}	8.62×10^{-4}	9.54×10^{-4}	2.72×10^{-4}
τ_k (s)	16.47	5.21	14.73	4.25	1.34	1.65	13.45
W	2.46	4.38	2.61	4.85	8.62	7.79	2.73
ℓ	14.96	84.13	17.69	114.04	641.27	473.12	20.23
λ	9.54	16.97	10.09	18.08	33.39	30.18	10.56
Re_λ	23.5	74.4	26.29	91.08	288.01	235.16	28.8
Re	36.9	368.7	46.1	553	5530	3687	55.3
N_k	96	96	96	96	96	96	64
R	2.40	4.20	2.85	5.69	10.13	7.47	3.2
T_R	0.06	0.19	0.07	0.24	0.74	0.61	0.07
$\mathrm{S_{time}}$	24.16	76.4	27.01	93.6	295.9	241.61	29.6
$\mathrm{T_{steps}}$	1208	1910	1350	2340	7398	6040	1480

Table 4.2: Kolmogorov scales and parameter values characterizing the seven flow fields simulated.

Registering a capture

Every time a prey particle moved into a predator's perception field, contact was registered. From that then, t_{TRA}, the time taken by the prey to traversed predator's perception field was recorded until the prey leaves the perception field. The time was then used to calculate the likelihood of the prey being captured using a capture probability function. The values obtained from these calculations were then compared with random number uniformly generated from [0, 1]. This enables a definitive conclusion to be made as regarding to whether or not the predator has sufficient time to capture the prey. If yes, the prey is removed from calculation and simultaneously a new one is created at a random position out of contact with a predator (this was necessary in order to maintain the constant density). If not, the prey is allowed to continue moving as before. Each simulation was repeated 10 times and the average number of contacts/captures together with their associated standard deviations recorded.
A particular problem is what happens when a predator or prey particle leaves the simulation domain or is eaten. Such a particle was deleted and spontaneously recreated in a random position within the domain and out of contact with a prey or predator. These re-creation processes tend to bias the number of contacts upwards. To this end, each simulation was repeated over three larger domain sizes with corresponding increments in the number of prey to ensure that the prey density remains fixed. The repeated domain sizes are given according to the flow field number in Table 4.3. By considering

Flow field	domain one	domain two	domain three	domain four
1	98.86	123.58	197.73	266.25
2	175.81	219.76	351.62	558.16
3	116.88	146.09	233.75	371.06
4	238.29	297.87	476.59	756.53
5	423.75	529.69	847.5	1345.33
6	312.64	390.80	625.28	992.57
7	134	167.5	268	360.9

Table 4.3: The repeated domain sizes for each of the seven flow fields simulated.

the reciprocal of the domain sizes with the corresponding number of prey, a linear regression line was fitted to the data to obtain the extrapolated average for an infinite domain. These extrapolated results were then compared with the corresponding results for theoretical predictions that was discussed.
The output of the simulation will be later presented as points with corresponding error bars. The error bars represents the standard deviations obtained by repeating the

simulations 10 times.

The simulation code was written in FORTRAN programming language. The summary of the processes involve is represented with a flow chart given as Figure 4.5. As can be seen from the flow chart, the main stages are represented by Mini Charts lettered A - G due to pressure of space. A more detail description of these stages can be found in the appendix.

The summary of the simulation is represented with a flow chart as shown on the next page. To begin with, data were read into the simulation program from an external file. The simulation domain was then split into smaller region (boxes) each of size R (contact radius). This helps one to determine which little region a predator or prey is. As can be seen from the chart, the rest of the simulation process is broken down into mini flow charts denoted by **A** to **G**.

Mini chart A was used to initialize predator and prey positions randomly throughout the domain. All initial contacts were ignored at this stage. That is, all predator and prey in contact at this stage were repositioned.

The actual simulation start in the mini chart **B** where predator-prey moves in the domain. In this chart, the predators were given random walk swimming speeds drawn from three-dimensional Gaussian distributions. The predator's positions were also updated in this chart.

Chart **C** is similar to **B** except that it deals mainly with the prey.

Chart **D** was used to determine whether a given predator was in contact with a prey.

In chart **E** the numbers of prey captures made by the predators were determined based on the time predator-prey pair has spent in contact. Chart **F** was used to determine the number of captures during the last time step.

In chart **G** average number of contacts and the number of captures were calculated together with their associated standard deviations.

More details of these mini charts are given as an appendix. In addition, flow charts for some subroutines are also presented in the appendix. The flow charts keys are as follows:

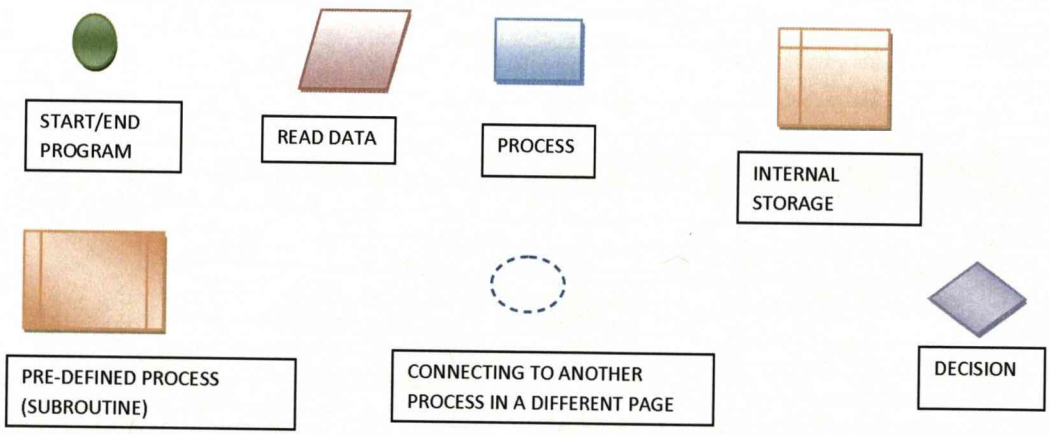

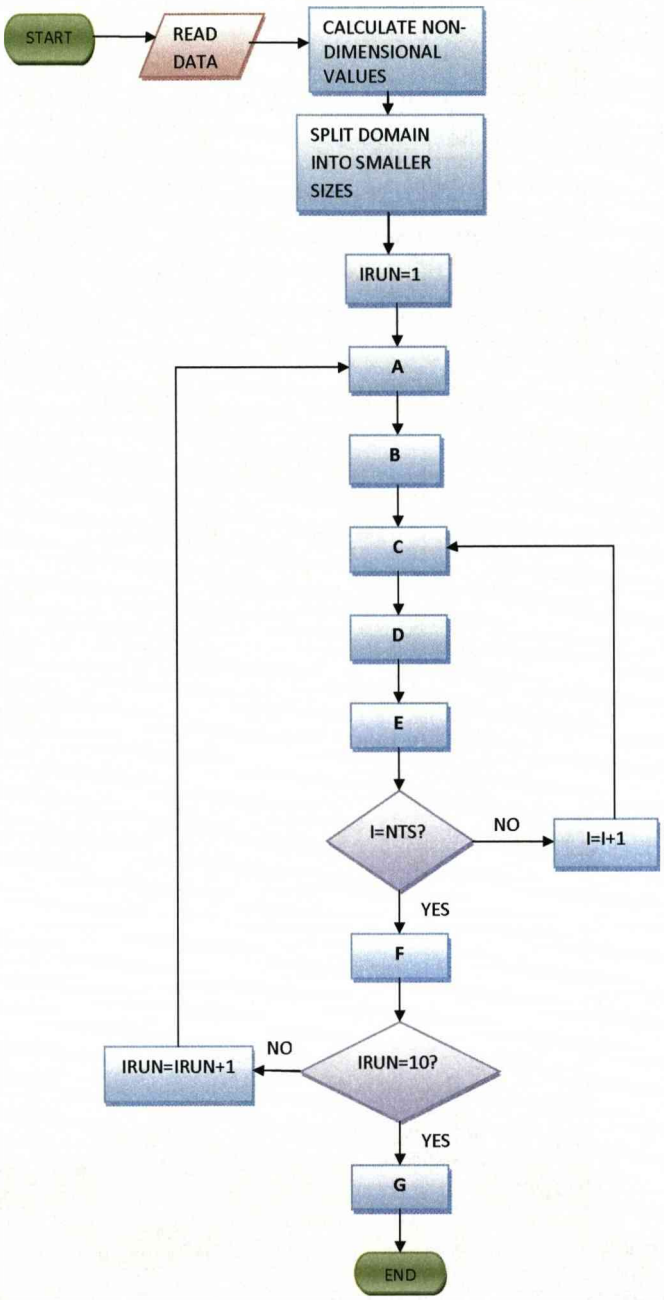

The chart on the left represent the general outline of the simulation procedure conducted in this thesis. This is divided into various stages (**A** to **G**) as shown. Details contents of the stages are given as an appendix. To begin with, data were read into the simulation codes from an external file. These data include the energy dissipation rate, viscosity value, domain size, number of prey and predators, $\sigma_{P,H}$. These were required to run the simulation and also used to non-dimensionalised other parameters. The domain size was then split into smaller regions where each region has size R (contact radius). Ten runs (IRUN=1 to 10) of simulation were carried out with average and standard deviations calculated at the end. The simulation time was divided into NTS number of time steps which was updated in steps of Δt (one time step). The loop beginning with I=1, runs up to the total number of time steps.

Figure 4.5: Flow chart summary of the simulations.

4.9 Preliminary Results

The analyses in the prediction sections give rise to the predation rates for a predator with a hemispherical perception field. However, it is possible to define more general results for arbitrary values of perception angles $\alpha \in [0, \frac{\pi}{2}]$ assuming straight line trajectory. Subsequent modifications can also be made using the volume fraction results to find the actual predation rates for such predators following an irregular trajectory. The general results have been derived but are not presented in this thesis. However, these modelling ideas were used to study the efficiency or otherwise of two types of planktonic foraging strategies namely, cruising and the saltatory feeding behaviours observed in nature. The motivational questions that are being addressed here are

- Is there optimal cruising speed which enhance feeding?
- Is there a relation between saltatory predation and the perception field of the Atlantic cod larvae?
- Can we use theory and simulation to explain field observations?

4.10 Results

In the succeeding sections, results for the average number of captures against predators swimming speeds (for cruising predators) and percentage time spent travelling (for saltatory predators) shall be presented together with corresponding simulation results. Close to each simulation result a number will appear which stand for capture success and is defined by 100(Number of captures)/(Number of contacts). The prediction and simulation results that will be presented in this Chapter correspond to Flow 7 as shown on Table 4.2.

4.10.1 Cruising predators

For cruising predators two forms of motility pattern were looked at. These are cruising with no direction changes ($\tau_{\text{sight}} = \infty$) and cruising with frequent direction changes at different swimming speeds assuming a variety of perception angles $\alpha = \pi/6, \pi/4, \pi/3$ and $\pi/2$. The swimming motions were modelled as random walks with each velocity component drawn from Gaussian distribution with mean zero and standard deviation $\sigma_P = 0.5, 1, 2$ and 3 ($v_P = 0.2 - 1.3$ mm s^{-1}). For cruise swimming with direction changes, $\tau_{\text{sight}} = 0.2$, equivalent to a direction change every 2.7 seconds.
For the results shown on Figures 4.6 and 4.7 the following keys are used. The simulation results for average number of captures are shown with o, * and · together with the corresponding error bars. The output of the theoretical predictions are presented

with solid lines (—, — and —) and the associated uncertainties are represented with dashed lines (- - -, - - - and - - -) . These were derived from the standard error in the calculations of the volume fractions described in Chapter 1. The small numbers beside the error bars represent percentage capture success.

Figure 4.6 shows the results of both the kinematic simulations and the theoretical

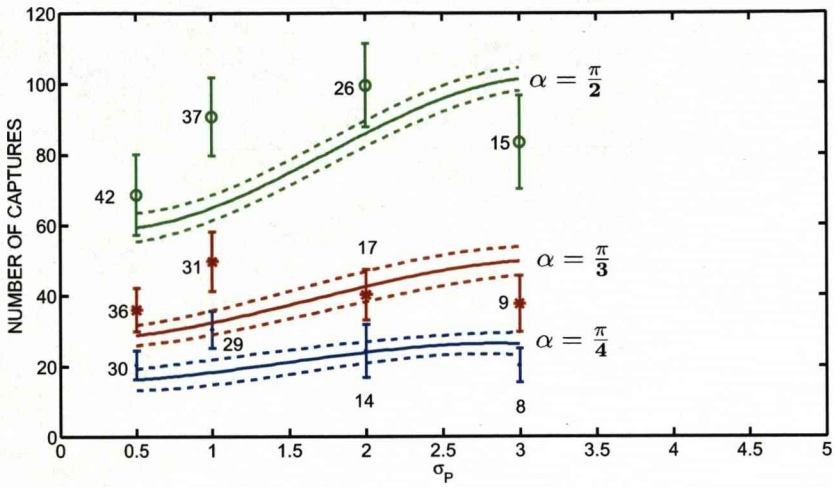

Figure 4.6: Average number of captures made by three groups of cruising predators following a straight line foraging strategy ($\tau_{\text{sight}} = \infty$) with reaction time $T_R = 1.0$. The output of simulation are represented with O, * and · the mean value of prediction results are presented with solid lines (—, — and —) . The associated standard errors are represented with dashed lines (- - -, - - - and - - -) . The small numbers close to the simulation results denote capture success. The prediction results for $\alpha = \frac{\pi}{2}$ are obtained from equations (4.3.12),(4.3.13) and (4.3.16). For the remaining two perception angles, the general form of the predation rates equations (not presented in this thesis) were used.

predictions for the number of captures made by three groups of 512 predators with the different perception angles shown. These results clearly show that as the σ_P increases, capture success, not unexpectedly, decreases. This trend is consistent for all the three groups. However, the overall percentage reduction in capture is more severe in the case of the narrowest perception angle. General observations of both the simulation and the prediction results show that, despite the complexities of the two calculations, very good agreement is achieved especially for the narrow perception fields. The simulation results for the narrow perception fields $\alpha = \frac{\pi}{4}, \frac{\pi}{3}$ are relatively flat with shallow maximum. These suggest that, provided it is within a certain range, a predator capture rate is relatively insensitive to cruising speed. This is consistent with reality, but at odds with the dome shape results of MacKenzie et al. (1994). The dome shape result implies that the predators should move with certain fixed optimum speed. In fact, experimental observations indicate they move with a variety of different swimming speeds.

The capture rates for the two narrow perception fields are almost identical. These are lower than the corresponding captures rates for the wider field of perception ($\alpha = \pi/2$). Looking at these results one is tempted to suggest that cruising predators with narrow perception fields following a straight line strategy, are unlikely to be associated with high cruising speeds. Swimming fast has the potential implications on the predator's energy budget and although increasing the number of potential encounters has a detrimental effect on capture success reducing the predation rate.

Planktonic predators are rarely observed to swim in straight lines for long periods of

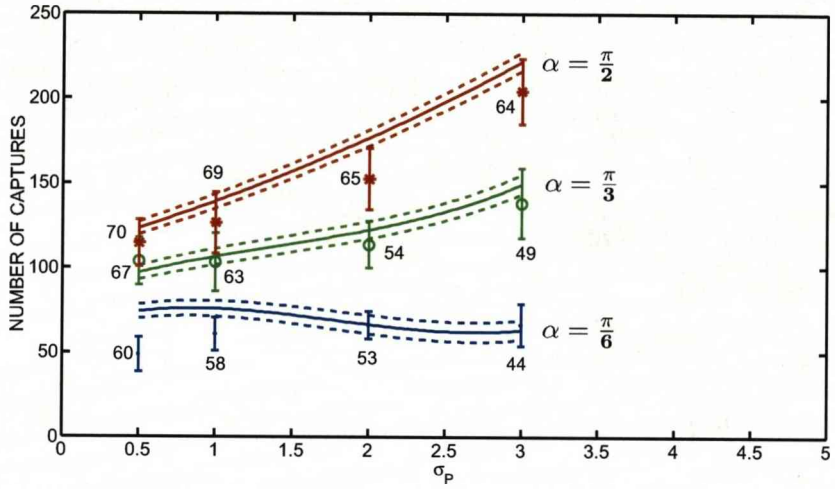

Figure 4.7: Variations in the average number of prey captures made by three groups of cruising predators swimming with direction changes every 10 times steps (2.7 seconds, $\tau_{\text{sight}} = 0.2$) with reaction time $T_R = 0.1$(equivalent to 1 second). Keys as in the previous Figure.

time ($\approx$ 7 min as used for the results in Figure 4.6). A more realistic scenario occurs when the predators are allowed to change directions frequently. Figure 4.7 depicts the result of some such calculations (Figure keys are the same as those on Figure 4.6). In Figure 4.7, the predators adopted a cruising strategy but were allowed to change direction after every 2.7 s. Experimental observation has shown that the reaction time for 6 to 7 mm fish larvae is about 1.3 s (see Werner et al. (2001)). The reaction time for these predators was made 10 times faster than those shown on Figure 4.6 in line with the experimental observations. The first thing to note about the Figure is the excellent agreement between the model predictions and the kinematic simulations. Looking at the Figure we can observe that the capture rate decreases with swimming speed in the line with earlier observations. Decline in capture rate is less severe than the corresponding results for the straight line path, but as T_R is much faster this is to be expected. Once again, there is no clear-cut expected dome-shaped relation between predation rates and swimming speed. Indeed the results for narrowest perception field are ap-

proximately flat. As before this indicates that predators can maximize their capture rates by swimming with a range of speeds. This an important result because it supports experimental findings that the swimming speeds of copepods and fish larvae from different species show considerable variability (see Greene & Landry (1985)). This conclusion fundamentally deviates from the work of MacKenzie et al. (1994) which predicts a distinctive optimal swimming speed for cruising larval fish predators. Mackenzie's (1994) work was based on the idea that perception field of fish larvae predators possessed a spherical symmetry. The fact that their conclusion does not hold when the size of the perception field is reduced has important consequences for the kind of predation strategy such predators are likely to adopt.

4.10.2 Saltatory predators

Atlantic cod larvae (`Gadus morhua`) are an important commercial species in the North Atlantic in both wild fisheries and aquaculture. They are observed to follow saltatory foraging strategy (see section 1.3) which consists of bouts of fast swimming interspersed by pauses. Galbraith et al. (2004) measurements show that during the travelling phases, the larvae swim with a speed in quite a wide ranges 2 -12 mm s^{-1}, with a typical average value of 5 mm s^{-1}. The results from that paper also show that the travelling phases (lasting $\approx 1 - 2$s) are about twice as long as the pausing phases (lasting $\approx 0.5 - 1$s). This is to say that a typical pause-travel cycle lasts for about 3 seconds. This foraging strategy is quite distinctive and cannot have evolved by accident. It must provide quite specific advantages in terms of increased survival maturation rates and must be linked to perception and locomotive capabilities of the larvae as well as the nature of their foraging environment. Consequently it was decided to conduct a series of detailed investigations into why such a strategy might arise, and in particular, the energetic benefits that might accrue.

In order to explore variation in saltatory strategy highlighted above the three seconds (pause-travel time) which equates to about twelve non-dimensional time steps was split into four (pause,travel) fractions (67%, 33%), (50%, 50%), (33%, 67%) and (17%, 83%). That is, 67% of the pause-travel time was spent pausing and 33% of the time spent in travelling etc. During the travel phases, each predator particle was given a random swimming speed drawn from three dimensional Gaussian distribution corresponding to 4.8 mm s^{-1}. Owing to the difficulty in calculating the line of sight when $\sigma_P = 0$, a pausing phase does not actually correspond to stoppage of travel in this thesis. During this time, the predators were allowed to change direction slowly with swimming speed drawn from three dimensional Gaussian distribution with mean $\sigma_P = 0.1$. At the end of this period, the travel phase was resumed.

The formulation of the predation rates calculations discussed earlier is sufficiently flexible to predict the results of both cruising and pause-travel strategies. Saltatory preda-

tion rates can be estimated using the equations by combining the travel phases to form a long single travel sequence. The various pausing phases are also combined in similar manner. The total number of captures is then the sum of the number of captures during travelling and pausing. In a summary, the prediction for the saltatory predation is calculated using the the formula

$$\begin{aligned}\text{prediction} &= \frac{\text{time spent travelling}}{\text{total time}} \times \text{straight line captures} \times \text{volume fraction} \\ &+ \frac{\text{time spent pausing}}{\text{total time}} \times \text{straight line captures} \times \text{volume fraction.}\end{aligned}$$

Figure 4.8 presents the results of both the simulation and the corresponding theoretical results for the number of captures made by 512 saltatory predators swimming in a turbulent flow (Flow 7) for different perception angles $\alpha = \pi/3, \pi/4$ and $\pi/6$. In both the simulation and the prediction, the reaction time of the predators $T_R = 0.1$ (1 second) was used. This is in line with experimental work of von Herbing et al. (2001). In both simulation and prediction, the predator particles were allowed to capture prey during both the travel and pause phases. On Figure 4.8 the prediction results are shown

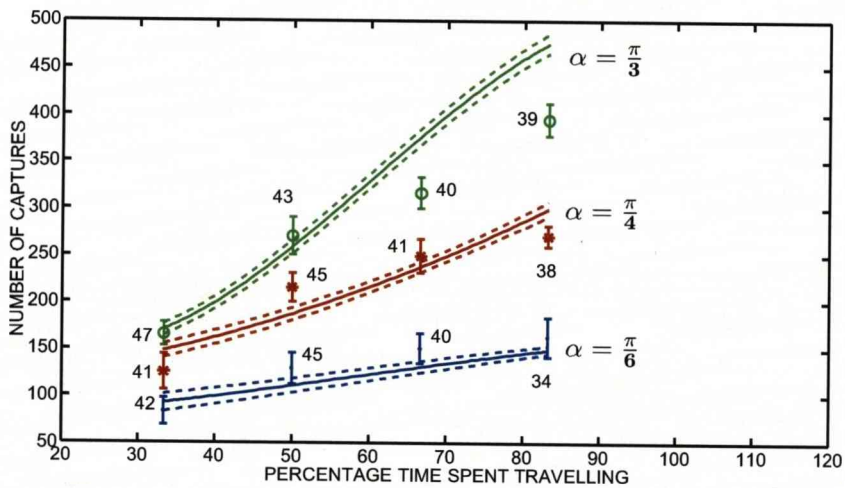

Figure 4.8: Variations in the average number of prey captures by three groups of saltatory predators against the percentage time spent travelling for different perception angles $\alpha = \pi/3, \pi/4$ and $\pi/6$. The prediction results are given with solid lines (—, — and —) and the associated standard deviation are resented with dashed lines (- - -, - - - and - - -) . The o, * and · stand for the corresponding average number of captures from the simulation. Close to the simulation results are small numbers that stand for capture success.

as solid lines (—, — and —) and the corresponding standard deviation are shown as dashed lines (- - -, - - - and - - -) . The signs o, * and · and the error bars are the output of the simulations and the small numbers beside them stand for the capture success. The capture success shown here are generally very good as they lie within the

range observed experimentally. For instance, the report from the experimental work of MacKenzie & Kiørboe (1995) shows that for small cod larvae, the capture success is in the range of 17-68%. The theoretical results are represented with the solid lines enclosed by two dotted lines standing for the corresponding uncertainties. As far as the number of captures is concerned, the results are very clear. Predators can maximize their predation rates if they can maintain the (17%, 83%) pause-travel mode. The wider the perception field the greater the benefit that accrues from pursuing this strategy. As the percentage of travel time decreases the curves for the different perception angles come closer and closer. These trends tend to suggest that continuous swimming is more beneficial to the animals with wide perception field. Travelling fast combined with wide perception angles implies that the predators are benefitting from the extra encounters by making more captures. However, swimming at relatively high speeds during the travel phase places high energy demands upon the larva. The question then is, are the extra captures made during fast swimming sufficient to offset the extra energy expended during the foraging process? This question cannot be answered by merely looking at results shown in Figure 4.8. In order to discern this, one needs to take into consideration the energetic cost of swimming associated with foraging, against the benefit associated with prey capture for the various pause-travel modes. One way to investigate this is to employ energetic demand and supply function in the form of energy gain model.

4.10.3 Net Energy Gain (NEG)

For saltatory foraging to be efficient, it has to be associated with some energetic benefits. In this section, the energy gain function of Galbraith et al. (2004) is employed to track the energy gain or loss per unit time E (measured in cal s^{-1}) for a given pause-travel mode. This energy gain function is basically made up of two competing terms comprising the energy gain in prey capture and a term representing the energy loss due to foraging. Mathematically, the bioenergetic function is expressed as

$$E = E_c PR - E_B M - E_s \langle v_P \rangle M, \tag{4.10.1}$$

where E_c is the energy gain per prey capture and PR is the predation rate. The negative terms represent the overall energy needed for a larva to forage by means of a given pause-travel mode. This depends upon four parameters viz, M typical mass of the larva, E_B is the basal/standard energy required by the larva when resting, E_s is the cost of swimming and $\langle v_P \rangle$ the average swimming speed. The value of E_s is shrouded by uncertainties. The microrespirometry measurement by von Herbing & Boutilier (1996) showed that the value of E_s is about 11.4 J $g^{-1}m^{-1}$, however, von Herbing (2002) reported that the parameter depend on temperature (and hence viscosity). The author reports estimated values at 50 and 70 J $g^{-1}m^{-1}$ for cod larva at temperatures of 10 and

5^0C respectively. Fitting a linear relation through these values, the estimated value for E_s at 20^0C (sea surface temperature for the present simulations and predictions) is 10 J $g^{-1}m^{-1}$ (2.39 $\times 10^{-6}$cal $mg^{-1}mm^{-1}$). One expect that E_s should also depend on turbulence regime, because higher values of $\langle\epsilon\rangle$ would make it more difficult for a fish larva to exercise control over its own motion. Perhaps the most important contribution to E_s and hence the energy gain model is the energetic cost of acceleration out of the low Reynolds number pause regime to the relatively high Reynolds number travel regime (see Weihs (1980)).

For all NEG calculations presented in this Chapter, the parameter values used by Galbraith et al. (2004) will be used. Atlantic cod larvae (`Gadus morhua`), which serves as the representative fish larva in this thesis, feeds on the nauplii of the `Calanus finmarchicus` (see Galbraith et al. (2004)) and the energy gain per capture of this prey is $E_c = 1.97 \times 10^{-3}$cal. Throughout this Chapter, it will be assumed that the typical mass of the template larva is $M = 0.06$ mg. For a fish larva with this mass, the basal energy expenditure is estimated as $E_B = 1.08 \times 10^{-6}$cal $mg^{-1}s^{-1}$ and the corresponding value for cost of move is $E_s = 2.73 \times 10^{-6}$cal $mg^{-1}mm^{-1}$. Using these parameters, NEG calculations were conducted for each group of saltatory predators previously discussed in relation to Figure 4.8.

Figure 4.9 shows the results of the NEG calculations. The results are obtained by

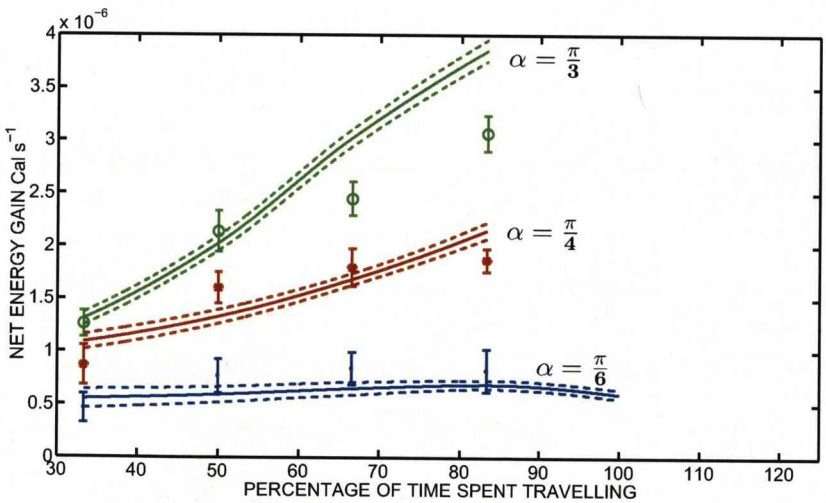

Figure 4.9: Variations in NEG calculations by three groups of saltatory predators with perception angles $\alpha = \pi/4, \pi/3$ and $\pi/6$, with baseline E_s as reported by Galbraith et al. (2004). Otherwise keys are as in the previous Figure. These results are obtained by using the number of captures shown in Figure 4.8 in equation (4.10.1).

using the predation rate equivalent to the number of captures shown in Figure 4.8 and utilising these result in equation (4.10.1). Keys are as before. For predators with wide

perception angles ($\alpha = \pi/4, \pi/3$), both the simulations and the theoretical results show that maximum energy gain is attained by following a (17%, 83%) pause-travel mode. The trends tend to suggest that cruising with no pauses, is to be preferred to saltatory predation in these instances. This however, does not agree with experimental and other observations on cod larvae (they are pause-travellers).

Looking at the results for the group with narrow perception angle $\alpha = \pi/6$, we can see a difference. There exists a shallow maximum of NEG in the vicinity of (33%, 67%) and (17%, 83%) pause travel modes. In other words it benefits a predator with a narrow perception field to spend portion of its foraging time in pause mode. A cruising strategy will be less effective for these predators. This is an important result because it is precisely this type of pause-travel strategy the larvae are seen to adopt experimentally (see Galbraith et al. (2004)).

What is surprising about this is that including any pauses in a foraging strategy would, if there was no flow, reduce the predators encounter rate to zero and be extremely inefficient. However, in the presence of the flow the predator can afford to stop swimming for short periods of time because advection will still ensure suitable prey will be swept into its vicinity. This observation suggests that pause-travel foraging evolved through delicate balance of the scope of larval fishes perception field, its swimming capabilities and crucially, the nature of the background flow to which it is exposed.

We may argue that the uncertainty surrounding the value of E_s has the potential implication that might change the nature of the above conclusions. Using the estimated value of E_s at 20^0C, the NEG result is shown in Figure 4.10(a). This shows that changing the E_s value only affects the numerical value of the results but does not alter the interpretation. Figure 4.10(b) illustrate the case when the value of the baseline E_s is doubled, thus making it more difficult for the predators to swim. For the narrow perception field $\alpha = \pi/6$, the trend in this case is against any sort of travel phase altogether. However, for the other perception angles this change in E_s does not change the interpretation. That is, predators with relatively wide perception fields can maximise their NEG by travelling all the time.

4.11 Conclusions

combined problems of encounter and predation rates for predators with restricted field of perception in a turbulent environment were formulated. The model was initially built under the assumption that predators move in straight lines while searching for prey. This assumption was important in predicting the distance travelled and the time spent by prey in the predator's perception field. The time was then used with a realistic capture probability function to determine whether or not a predator has a sufficient time to capture the prey. Subsequent modifications were incorporated to refine the as-

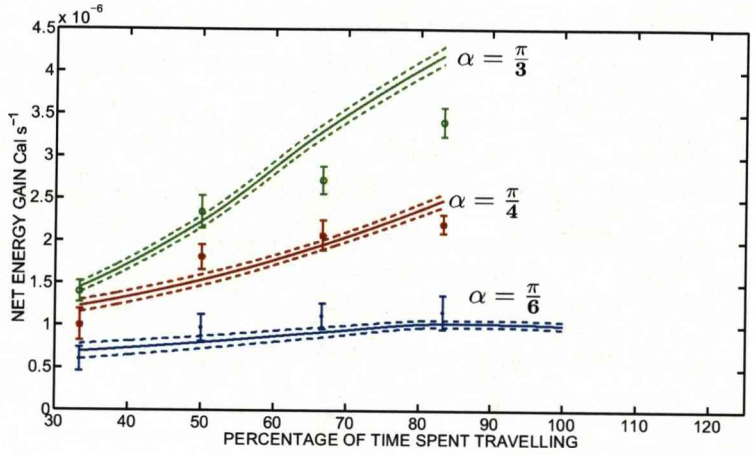

(a) NEG results with the estimated value of $E_s = 2.39 \times 10^{-6}$cal mg^{-1}mm^{-1}

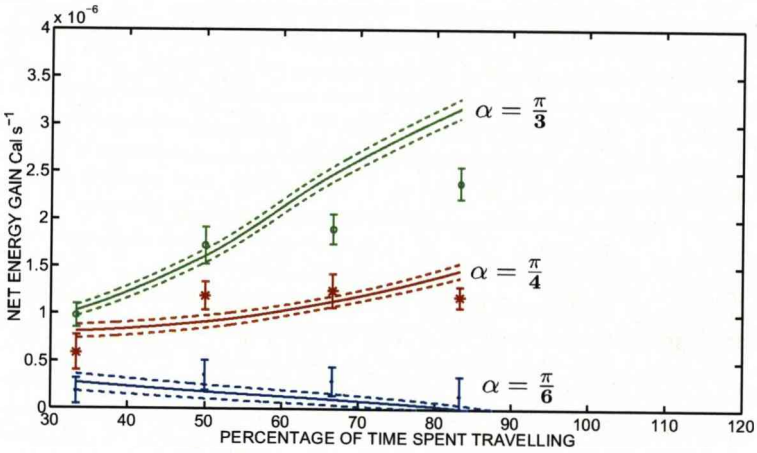

(b) NEG results for doubling the value of E_s

Figure 4.10: Variation in NEG against percentage travelling time by three groups of 512 saltatory predators with perception angles $\alpha = \pi/3, \pi/4$ and $\pi/6$. These results are obtained by using the number of captures shown on Figure 4.8 in equation (4.10.1) with the baseline value of E_s changed. The solid lines (——, —— and ——) are results of theoretical prediction, the corresponding standard deviation are represented with dashed lines (– – –, – – – and – – –) . The signs O, * and · are the results of the simulation. Also shown are the standard deviation.

sumption and to account for more likely scenario when the predator follows an irregular path (either through swimming changes or influenced by the flow). The modifications were done by means of volume fraction estimates. The volume fraction is essentially, the ratio of the volumes a predator will map out when making direction changes to the volume it will mapped out when following a straight line trajectory. The modified model was then used to study the feeding success of cruising and saltatory fish larvae. The results of these applications were compared with the results from a number of KS. Good agreement between model predictions and the simulations were obtained. The main discoveries of this Chapter are as follows:

1. The optimal feeding behaviour of larval fish is strongly connected to the motility pattern, the shape and size of their perception field. The adoption of the pause-travel strategy by the Atlantic cod larvae appears to be directly linked with their narrow perception fields. This strategy is associated with energetic benefits. The simulation results for the perception angle $\alpha = \pi/6$ indicated that optimal predation is attained by remaining close to (33%, 67%) pause-travel mode. The capture success recorded here is in the range 34 - 47%. This is important because it overlaps the ranges of attack success rates observed experimentally. Saltatory searching behaviour is not an optimal strategy for larval fish predators with wide perception field $\alpha > \pi/4$. These predators can maximize their net energy budget by adopting the cruise searching behaviour.

2. There is no distinctive optimal swimming speed for cruising predators with narrow perception fields. This means that the dome-shaped relationship between predation rates and swimming speeds such a feature of the spherically symmetric perception field is much less significant in this instance. For the more realistic narrow perception field, optimal predation rates can be attained by swimming over a range of different speeds. As one would expect, cruising predators with wide perception fields are more efficient in prey capture than those with narrower ones because they have more time to make a capture attempt.

3. The present study have shown that we can indeed use theory and simulations to explain field observations.

4. Environmental factors such as ocean climate may also have a profound effect on the foraging behaviour of cod larvae. Particularly, turbulence is vital to success of pause-travel. Similarly, prey abundance also affects the behaviour of pause-travel searchers. Because of the linearity relation between predation rate and prey density, one can study the effects of variations of the former on the NEG of cod larvae without recourse to new sets of simulations.

5. Other factors which may influence pause-travel searchers are sea surface temperature which influences the viscosity and wind forcing. This means that the optimal pause-travel mode recorded here may be affected in some way by sea surface temperature and wind forcing. The relation between temperature and viscosity suggests that, the influence of the former can be investigated by changing the values of the latter in both simulations and predictions. In principle this is relatively straight forward to do because the basic conceptual framework of the model will not require new derivations. It only boils down to estimating the new model parameters. We would be interested to see how robust the optimal predictions of the best swimming strategies are to changes in these variables.

Chapter 5

Effects of viscosity and turbulent energy dissipation rate changes on saltatory feeding behaviour of fish larvae

5.1 Introduction

Fish larvae typically experience a wide range of temperatures as a result of their vertical and horizontal movements. In addition, the larvae may experience different thermal conditions depending on the part of the spawning season in which they are hatched. Temperature difference influences to a large extent the viscosity of water. For example, a decrease in temperature by 10 ^{o}C can produce a 33% increase in viscosity (see Fuiman & Batty (1997)). This changes have a profound effect on foraging and hence the survival of small fish larvae. This is because low temperatures (high viscosities) hampers their swimming abilities and slow down the rate of growth and development (see von Herbing (2002)). Another detrimental effect of low temperature is that additional energetic cost associated with swimming are incurred.

This Chapter presents the results of theoretical predictions and kinematic simulations of the saltatory feeding strategy of larval fish under varying turbulent dissipation rates and kinematic viscosities. The viscosity values chosen are in the range 1 to 1.5 $\times 10^{-6}$ m^2 s^{-1}. The decision to vary the combination of viscosity and dissipation rate values arises by considering the fact that the temperature in the larval fish habitat is not uniform. For example, the temperature in the North Atlantic (the habitat of Atlantic cod larvae) is roughly in the range -0.5 to 10 ^{o}C (see Guan et al. (2008)). The viscosity values chosen here corresponds to sea surface temperature in the range 5 to 20 ^{o}C . This cover a wide range of habitats associated with the wide distribution of fish larvae. Central to the model is the bioenergetic demand and supply energy gain function which is used to get an insight into the energetic cost of swimming in each turbulent regime

considered. The energy gain calculations will serve a number of purposes. From the results of the calculations, it is possible to estimate the combinations of pause-travel ratio that minimises the energy demands impose on the larva.
A theoretical and numerical frame work for calculating the predation rates and the associated energy gain were established in the previous Chapters. In this Chapter the investigations of the previous Chapter will be extended to look at variety of turbulent energetic regimes, various viscosity conditions at three different larval swimming speeds. Specifically, investigations will be focussed on the robustness or otherwise of pause-travel foraging strategy in various turbulent energetic regimes at different viscosities.

5.2 Simulations parameters

The simulation conducted in this Chapter comprises of six different flow fields. These flow fields were constructed according to the procedure discussed in Chapter 4 in conjunction with the energy spectrum defined by equation (3.3.2). Three representative turbulent and viscosity values were chosen. The values taken for the energy dissipation rates were $\langle\epsilon\rangle = 5.53 \times 10^{-9}, 5.53 \times 10^{-8}$ and 5.53×10^{-7} m^2 s^{-3}. For the kinematic viscosity, the following three values were used $\nu = 1.0 \times 10^{-6}, 1.2 \times 10^{-6}$ and 1.5×10^{-6} m^{2}s^{-1}. These values of viscosity correspond to variation in sea surface temperature of 20^o C, 12^o C and 7^o C (see Batchelor (1967)). Table 4.2 and 4.3 gives more details of the various parameters and domain sizes associated with these flows. The flow fields in this Chapter correspond to Flow 1 to 6. The domain sizes were chosen with two constrain:

1. the smallest value was chosen to exceed the large eddy size (ℓ)

2. each domain size was chosen to ensure that constant prey density was maintained.

During the travel phases, larval swimming speeds were varied from 3, 5 and 10 mm s^{-1}.
Larval fish have a high mortality rate, owing to food limitations or predation, and spend a short time in the larval phase. It is therefore unlikely that an individual fish larva will experience such a diverse range of viscosity regimes during its larval phase, and, consequently, the exact details of the particular saltatory strategy it pursues may be more finely adapted to suit a smaller range of values.

5.3 Simulation description

First feeding Atlantic cod larvae are observed to feed mainly on copepod nauplii, particularly on the nauplii of `Calanus finmarchicus` and this serves as a representative

template for the prey particles. They are considerably less than 1 mm in size, extremely abundant in the North Atlantic and form an important part of the diet of both cod and herring larvae. It will be further emphasis here that by 'particle' here, it means the length scales of both prey and predator are much smaller than the various Kolmogorov length scales, (see Table 4.2), which in turn implies that their presence will have little impact on the general characteristics of the flow field in question. Also, the number of larvae incorporated into each flow (512 per simulation) is at such low densities that we would not expect their presence to materially alter the characteristics of the flow to the extent that the simulated number of prey encounters would differ significantly from those in a real ocean mixed layer. For full account of the simulations see Chapter 4.

5.4 Results

In this section the results of theoretical of formulations and the corresponding KS results for saltatory foraging strategies across a variety of turbulent energy and viscosity regimes are presented along side each other. The various simulations results are plotted as points with their associated error bars. The theoretical predictions were done in the same way as in Chapter 4 with different flow parameters. See Table 4.2 Flow 1-6. The results of theoretical predictions are presented as continuous lines and their associated errors are given in dotted lines. The results are presented in three categories, to examine the effect of variations in predators' swimming speed, energy dissipation rate and viscosity regimes.

5.4.1 Effect of swimming speed

Figure 5.1(a) depicts the average number of prey captures by two groups of 512 saltatory predators moving with the average speeds of $\langle v_P \rangle = 3$ and 10 mm s^{-1}. The $*$, $\cdot$ on the Figure represents the output of the kinematic simulation while the various error bars represent the standard deviations. The small numbers situated next to the error bars give percentage capture success for that pause-travel mode. For instance, consider the group moving with $\langle v_P \rangle = 10$ mm s^{-1} during the travel phase. When travelling 30% of the time a total of 339 number of contacts were registered out of which 111 were captured. So capture success becomes $111 \times 100/339 \approx 33\%$. The —, — (solid lines) are the outputs of the theoretical predictions. These lines are sandwiched in between a pair of dashed lines (- - -, - - -) representing the associated errors corresponding to the theoretical predictions. The results presented in this Figure pertain for $\langle \epsilon \rangle = 5.53 \times 10^{-9}$ m^2 s^{-3} and $\nu = 1.5 \times 10^{-6}$ m^2 s^{-1} (Flow 1).

As far as travelling speed is concerned, the results are a clear cut. The larvae can

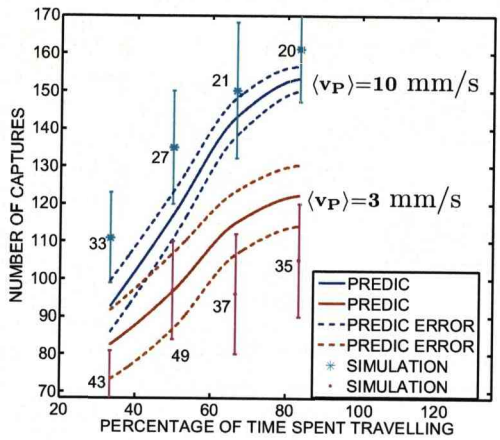

(a) $\langle\epsilon\rangle = 5.53 \times 10^{-9}$ m^2 s^{-3}, $\nu = 1.5 \times 10^{-6}$ m^2 s^{-1}.

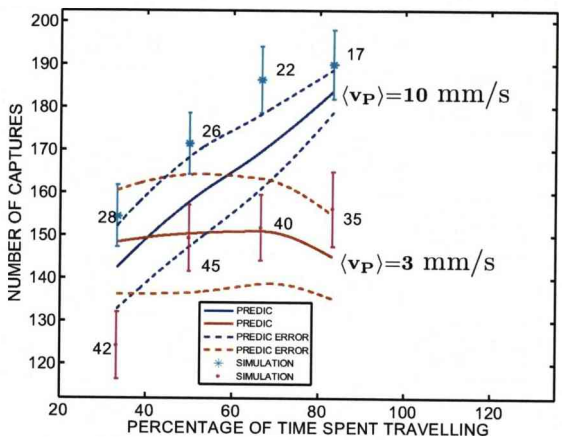

(b) $\langle\epsilon\rangle = 5.53 \times 10^{-8}$ m^2 s^{-3}, $\nu = 1.5 \times 10^{-6}$m s^{-1}.

Figure 5.1: The results of KS and theoretical predictions for the average number of prey captures against the percentage time spent travelling by two groups of 512 saltatory predators with travelling speeds of $\langle v_P\rangle$ = 3 and 10 mm s^{-1}, in the viscosity regime characterised by $\nu = 1.5$ m^2 s^{-1}. (a) With dissipation rates $\langle\epsilon\rangle = 5.53 \times 10^{-9}$m^2 s^{-3}. (b) With $\langle\epsilon\rangle = 5.53 \times 10^{-8}$m^2 s^{-3}. The simulation results are represented by $*$, $\cdot$ and the associated errors are represented with error bars. The numbers close to the error bars represent the capture success, which is obtained as 100×(number captures)/(number of contacts). The theoretical predictions results are represented with ——, —— and the associated errors are represented with - - -, - - - .

maximize their prey captures by travelling continuously with the highest speed ($\langle v_P\rangle$ = 10 mm s^{-1}). This is because travelling fast allow more encounters to be made which results into extra captures in this case. However, one clear revelation from the Figure is that capture success generally decreases with travelling. For example, the group

of saltatory predators which move at an average speed of $\langle v_P \rangle = 10$ mm s^{-1} during their travelling phase, exhibit their highest capture success (33%) when doing the least travelling (30%). A similar trend can be observed for the group with $\langle v_P \rangle = 3$ mm s^{-1} during the travel phase, except for one point, which could be attributed to statistical error. For this group, the highest efficiency in capture is recorded for (50%, 50%) pause-travel mode. Comparison between the two groups reveal that the slow swimmers are more efficient predators. This may be attributed to the fact that predator and prey spend more time in close proximity during pauses, and that swimming fast disturbs the stability of the visual field (see Kramer & Mclaughlin (2001)).

Figure 5.1(b) shows the results of a similar set of simulations and predictions with the dissipation rate changed (see Flow 2). In this set of simulations, the rate of energy dissipation is ten times more rapid than before. In this regime, fast swimmers can maximize their number of captures by remaining in a sustained travelling mode. This is consistent with the previous predictions. However, for the slow swimmers, the result differs from that predicted in Figure 5.1(a). The number of captures drop as the proportion of the time spent in the travel mode increases. The result also shows that to maximize the number of captures, the slow swimmers should maintain about (33%,67%) pause-travel mode. Beyond this capture drops. This might be due to the fact that the combinations of slow swimming and relatively high energetic regimes ensure that prey 'particles' are swept out of the detection zone before they are captured. Comparison of Figure 5.1(a) and Figure 5.1(b) show that higher energetic flow regimes bring about more captures. For instance, the number of captures are bigger than the corresponding lower energetic regime by factors in the range [1.5, 1.9] and [1.2, 1.4] for the prediction and simulation respectively. However, capture success is more in less energetic regimes. This is because the increased relative velocity of the flow reduces the time the predator and prey remain in close proximity, hampering successful capture attempts.

5.4.2 Effect of Energy dissipation

Figure 5.2(a) shows the number of captures by two sets of 512 pause travel predators foraging in two different energy dissipation rates $\langle \epsilon \rangle = 5.53 \times 10^{-8}$ and 5.53×10^{-7} m^2 s^{-3}, with the same average swimming speed $\langle v_P \rangle = 3$ mm s^{-1} during the travel phase. The results are presented in a similar manner to the previous Figure. These corresponds to Flow 4 and 5. Both the predictions and simulations show that high proportion of travel times do not necessarily leads to more captures. Higher captures are achieved by foraging in the flow characterised by $\langle \epsilon \rangle = 5.53 \times 10^{-7}$. The prediction results suggest that maximum number of captures are attained for the pause travel combination (50%, 50%) across both regimes. Beyond this mode capture rate decline. In the $\langle \epsilon \rangle = 5.53 \times 10^{-9}$ m^2 s^{-3} regime, there is a general trend of increasing captures as as the proportion of the travel mode increases. This is borne out by both

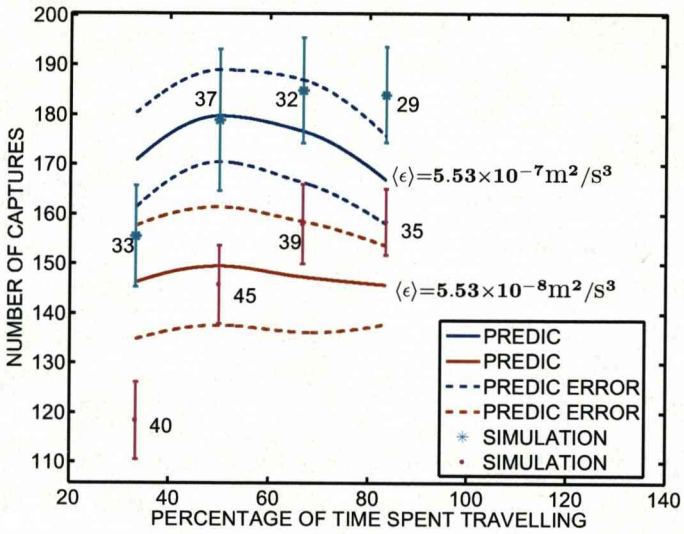

(a) $\langle v_P \rangle = 3$ mm s^{-1}, $\nu = 1.0 \times 10^{-6}$ m^2 s^{-1}

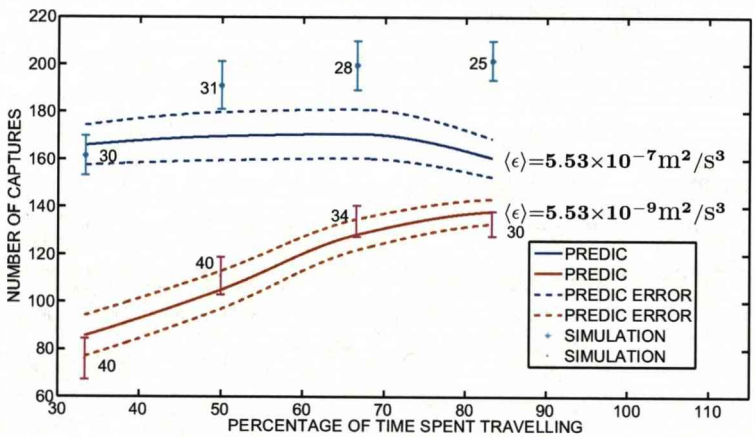

(b) $\langle v_P \rangle = 5$ mm s^{-1}, $\nu = 1.5 \times 10^{-6}$ m^2 s^{-1}

Figure 5.2: The results of KS and theoretical predictions for the average number of prey captures against the percentage of time spent travelling by two groups of 512 saltatory predators in different dissipation rates regime. (a) with $\langle v_P \rangle = 3$ mm s^{-1} and $\nu = 1.0 \times 10^{-6}$ m^2 s^{-1} and (b) $\langle v_P \rangle = 5$ mm s^{-1} and $\nu = 1.5 \times 10^{-6}$ m^2 s^{-1}. Each Figure shows the results for different turbulent regimes characterised by the $\langle \epsilon \rangle$ values shown. The rest of the keys are the same as the same in Figure 5.1.

the predictions and simulations. In the $\langle \epsilon \rangle = 5.53 \times 10^{-7}$ m^2 s $^{-3}$ regime (Flow 6), the simulation predict a continuation of this trend, although at a much slower rate. The predictions tend to highlight the opposite, namely a decrease in capture rate as

the time spent travelling increases. These results brings up a crucial point discernable in both Figures 5.2(a) and 5.2(b), namely that in highly turbulent regimes, spending relatively long periods in the travel mode results in progressively smaller and smaller gains in capture rate. Given that swimming fast for long periods in a highly turbulent regime must impose a significant energy drain on the larva, these results suggest that in highly turbulent regimes, foraging strategies which include a high proportion of pauses will be favoured.

Further observation of the Figure shows that there is a much larger difference in the number of captures across the regimes than those observed in Figure 5.2(a). For example, the pause-travel combination (67%, 33%) in the flow regime $\langle\epsilon\rangle = 5.53 \times 10^{-9}$ m^2 s^{-3}, the simulation result shows that the number of captures is only 47% of the corresponding results in the energetic regime characterised by the dissipation rate $\langle\epsilon\rangle = 5.53 \times 10^{-7}$ m^2 s^{-3}. However, to decide which is the best foraging mode under various regimes can only be properly ascertained through the consideration of the energy expenditure associated with foraging in each regime.

5.4.3 Effect of viscosity

Figure 5.3 shows the KS and predictions results for the average number of captures made by three groups of 512 saltatory predators at two different viscosity regimes. The results are presented in similar fashion to Figure 5.1.

Figure 5.3(a) shows the number of captures by two group of 512 saltatory predators foraging at two different viscosities, $\nu = 1.2, 1.5 \times 10^{-6} m^2/s$ (Flow 3 and 5) in the same turbulent energetic regime $\langle\epsilon\rangle = 5.53 \times 10^{-9} m^2$ s^{-3} with a swimming speed of $\langle v_P \rangle = 5$ mm s^{-1} during the travel phase. The simulation results agree pretty well with the predictions. The trend earlier observed in Figure 5.1 is also reflected here. Capture success remains fairly constant across the two viscosity regimes. This suggests that viscosity has less influence on capture success than $\langle\epsilon\rangle$. It could also be explained by the fact that the predation rates are almost identical.

This is somewhat surprising because one would have thought that lower viscosity will enhance the feeding modes of the larvae in line with observations (see MacKenzie & Kiørboe (1995)). The explanation for this may be attributed to the fact that the effect of viscosity manifests itself more on the physics of the flow field. In other words, when $\langle\epsilon\rangle = 5.53 \times 10^{-9} m^2$ s^{-3} and ν is high the regime is relatively quiescent and so, most of the encounters and hence captures are brought about purely by the larval activities. To investigate this further, the swimming speed is maintained as before with dissipation rate and viscosity regimes changed to $\langle\epsilon\rangle = 5.53 \times 10^{-8} m^2$ s^{-3} and $\nu = 1.0, 1.5 \times 10^{-6} m^2/s$ (Flow 4 and 2) respectively. The effect of these changes are depicted on Figure 5.3(b). These changes in the flow field only make the resultant number of captures more uniform than those observed in Figure 5.3(a). Both Figures

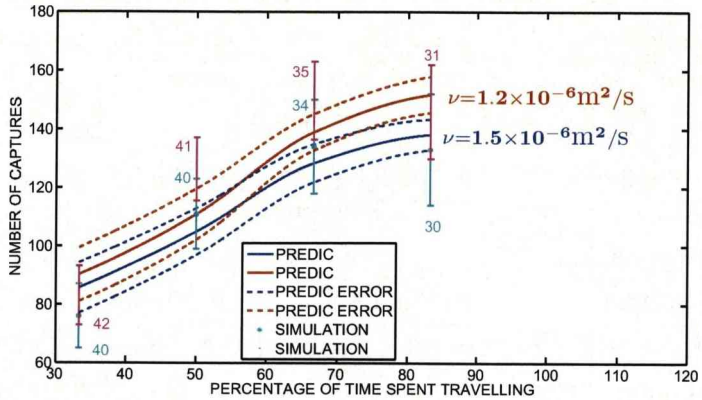

(a) $\langle v_P \rangle = 5$ mm s^{-1}, $\langle \epsilon \rangle = 5.53 \times 10^{-9}$ m^2 s^{-3}

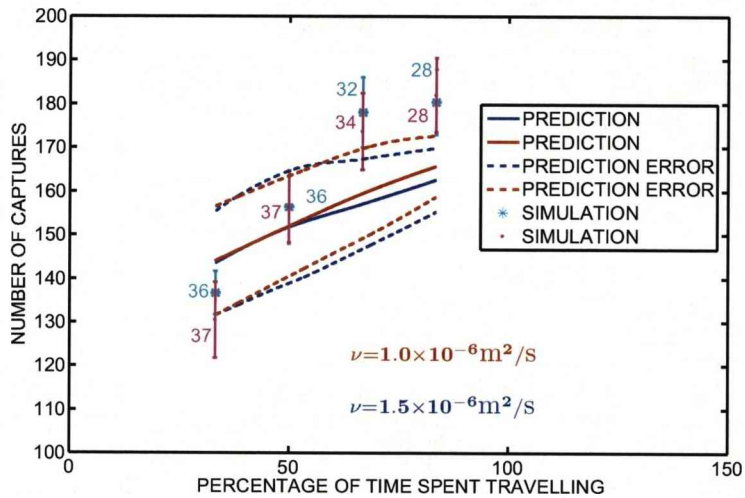

(b) $\langle v_P \rangle = 5$ mm s^{-1}, $\langle \epsilon \rangle = 5.53 \times 10^{-8}$ m^2 s^{-3}

Figure 5.3: The results of KS and theoretical predictions for the average number of prey captures against the percentage of time spent travelling by a group of 512 saltatory predators with travelling speeds of $\langle v_P \rangle = 5$ mm s^{-1} and viscosity regimes characterised by the values of ν shown. (a) Pertains the dissipation rate $\langle \epsilon \rangle = 5.53 \times 10^{-9}$m^2 s^{-3}. (b) Pertains the dissipation rate $\langle \epsilon \rangle = 5.53 \times 10^{-8}$m^2 s^{-3}. The rest of the keys are the same in Figure 5.1.

show no significant effect of viscosity on the number of captures. This further tends to suggest that, for a larva moving with an average speed significantly greater than the strength of the flow field, viscosity levels are relatively insignificant. It may be interesting in the future to investigate the effect of viscosity when the larval speed is dominated by the flow. Further comparisons of Figures 5.3(a) and 5.3(b) reveal only

differences in the number of captures which arise due to the variations in the flow fields (energy dissipation rates). However, implicit in these results is the assumption that a larva can maintain its chosen travel speeds independently with no drain of resources. But swimming in an increasingly viscous flow is in reality bound to impose significant energy demands on the larva, which will impose certain limitations on its optimum predation strategy. To investigate this, these results will be incorporated into NEG model described earlier.

5.5 Net energy gain

In this section the changes on energy budget of a typical larva brought about by the number of captures under varying viscosity and turbulent energetic regimes considered in the previous sections will be studied.

5.5.1 Effects of travel speeds

Figure 5.4 show the NEG calculations for the prediction and KS. These results are obtained by using the predation rates results shown on Figure 5.1 in equation (4.10.1). The results are presented in similar fashion as Figure 5.1. Figure 5.4(a) shows the net energy gain by two groups of 512 saltatory predators foraging in a turbulent regime equivalent to $\langle \epsilon \rangle = 5.53 \times 10^{-9} \mathrm{m}^2\ \mathrm{s}^{-3}$ foraging at average travel speed of $\langle v_P \rangle = 3$ and 10 mm s^{-1} with a flow viscosity $\nu = 1.5 \times 10^{-6}\ \mathrm{m}^2\ \mathrm{s}^{-1}$ respectively. The Figure reveals that the group travelling with $\langle v_P \rangle = 3$ mm s^{-1} can maximize their energy harvest by remaining in the (50%, 50%) pause-travel mode for the simulations and (17%, 83%) for the predictions. For the higher travel speed both the simulation and predictions show that the energy drain associated with moving at such a high speed is far too great for the larva to gain any energetic benefit. The trend shows that for such larva, it is more beneficial to observe (100%, 0%) pause-travel ratio, that is it should behave as an ambush predator. It is energetically too expensive to forage with such speed under these conditions.

Figure 5.4(b) shows the results of similar NEG calculations when $\langle \epsilon \rangle$ is raised to $5.53 \times 10^{-8} \mathrm{m}^2\ \mathrm{s}^{-3}$. The results are similar to those in Figure 5.4(a). For lower travelling speed the larva can optimize its NEG by adopting a (50%, 50%) pause travel mode. For the higher travel speed it is simply unrealistic in energy terms for the predator to do more than act as an ambush predator and sit passively waiting for prey to be advected into its vicinity.

Comparisons of Figures 5.4(a) and 5.4(b) reveal that it is more beneficial for the larva to forage at the higher energetic regime for both swimming speeds. This is because the predators can benefit from extra encounters by making more captures. Also, it is

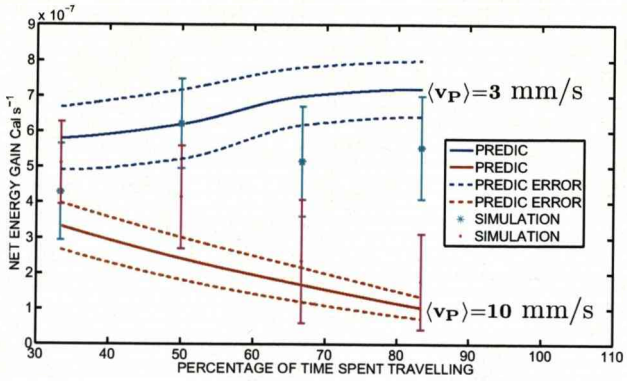

(a) $\langle\epsilon\rangle = 5.53 \times 10^{-9}$ m^2 s^{-3}, $\nu = 1.5 \times 10^{-6}$ m^2 s^{-1}

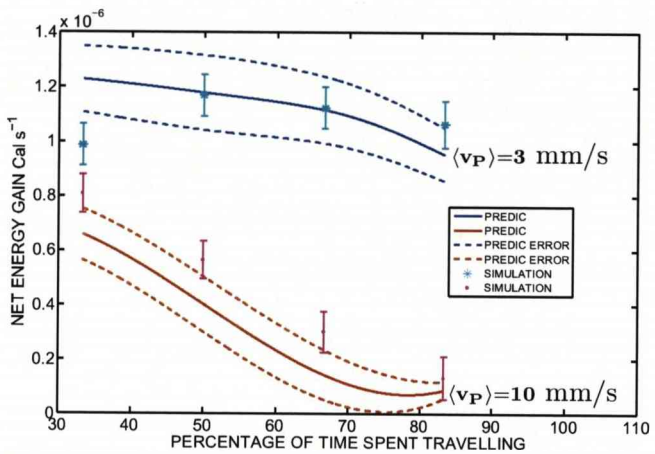

(b) $\langle\epsilon\rangle = 5.53 \times 10^{-8}$ m^2 s^{-3}, $\nu = 1.5 \times 10^{-6}$ m^2 s^{-1}

Figure 5.4: The results of KS and theoretical predictions for NEG against the percentage of time spent travelling by two groups of 512 saltatory predators with two different swimming speeds, $\langle v_P\rangle = 3, 10$ mm/s during their travel phases in the viscosity regime $\nu = 1.5 \times 10^{-6}$ m^2 s^{-1}. (a) Is for the dissipation rate $\langle\epsilon\rangle = 5.53 \times 10^{-9}$m^2 s^{-3} and (b) is for the dissipation rate $\langle\epsilon\rangle = 5.53 \times 10^{-8}$m^2 s^{-3}. Other keys are the same as in Figure 5.1. These results are obtained by using the predation rate results of Figure 5.1 in equation (4.10.1).

more energy efficient to pause more and rely on the high energy of the flow to advect prey to the predators. In summary from the results in this Figure, we can conclude that successful pause-travel foraging will be associated with low travel speeds. This observation is confirmed by conclusions of a number of experimental results such as MacKenzie & Kiørboe (1995), which show that the time average swimming speeds during the travel phase are 1.8 and 2.4 mm s^{-1} for small and large larvae respectively. The present results show that pause-travel is energetically robust for low travel speeds.

The trend of the model predictions $\langle v_P \rangle = 10$ mm s$^{-1}, \langle \epsilon \rangle = 5.53 \times 10^{-7}, 5.53 \times 10^{-8}$ m^2 s $^{-3}$ suggests that cutting out swimming activities altogether would be more beneficial. Any sort of saltatory foraging with relatively high travel speeds is likely to be energetically inefficient whatever the conditions.

The potential discrepancies between simulations and predictions should not be seen as too much drawback. In calculations of complex interactions between planktonic microorganisms such as those carried out here, discrepancies between simulation and predictions are inevitable. One should appreciate that the initial formulation of the predation rate model was based on idealised straight line trajectory. It would be a very difficult task to formulate analytical expressions for the exact path of a prey across predator's perception field. Despite all these, the results are plausible and encouraging.

5.5.2 Effects of Dissipation Rate

Figure 5.5(a) shows the net energy gain by two groups of 512 saltatory predators foraging in two different turbulent energetic ($\langle \epsilon \rangle = 5.53 \times 10^{-7}, 5.53 \times 10^{-8}$ m^2 s $^{-3}$) and the same viscosity regime ($\nu = 1.0 \times 10^{-6}$ m^2 s $^{-1}$) swimming at $\langle v_P \rangle = 3$ mm s^{-1} during the travel phase. These results are obtained by using the number of captures shown on Figure 5.2 into equation (4.10.1). The results show that, it is energetically more beneficial to forage in the higher energetic regime under the given conditions. Simulation results indicate that predators in the lower energy regime can maximize their energy harvest by maintaining (33%, 67%) pause-travel ratio. However, the result (simulation) for the higher energy regime suggest (50%, 50%) pause-travel ratio.

Figure 5.5(b) shows a similar NEG calculation for two groups of 512 saltatory predators foraging in different energetic ($\langle \epsilon \rangle = 5.53 \times 10^{-7}, 5.53 \times 10^{-9}$ m^2 s $^{-3}$) and the same viscosity regime ($\nu = 1.5 \times 10^{-6}$ m^2 s $^{-1}$) with the swimming speeds of $\langle v_P \rangle = 5$ mm s^{-1} during the travel phase. It can be seen that the difference in NEG between the groups is very much pronounced when the travel ratio is small. The difference in NEG narrows as the travel durations increases. The simulation results for the higher energetic regime again show that (50%, 50%) pause-travel maximizes the net energy takings. In the lower energy regime, the results differ slightly. Predators in this regime can maximize their energy gain by foraging at (33%, 67%) pause-travel ratio.

Generally speaking, the Figure show that as $\langle \epsilon \rangle$ increases the maximum value of NEG is shifted backward. Thus, the general trend is that the proportion of time spent travelling should be reduced. This lead to the conclusion that pause-travel foraging would become increasingly uneconomical for larvae in regions where the turbulence levels are high. At high levels of turbulence an individual larva will start to lose the ability to direct and control its movements, or respond effectively to any potential prey entering its perception field.

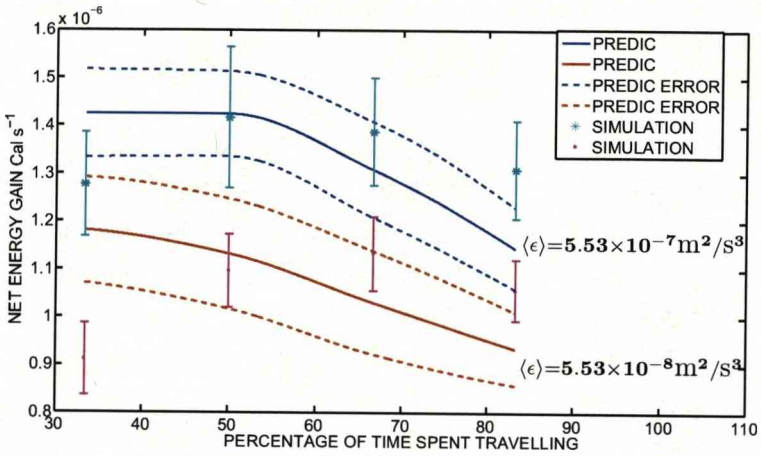

(a) $\langle v_P \rangle$= 3 mm/s, $\nu = 1.0 \times 10^{-6}$ m^2 s^{-1}

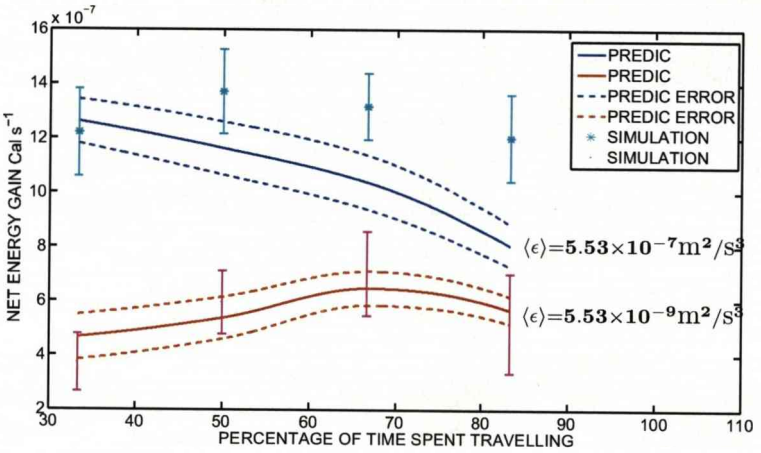

(b) $\langle v_P \rangle$= 5 mm/s, $\nu = 1.5 \times 10^{-6}$ m^2 s^{-1}

Figure 5.5: The results of KS and predictions for the NEG against the percentage of time spent travelling by two groups of 512 saltatory predators in different turbulent dissipation rates regime. (a) With $\langle v_P \rangle$ = 3 mm/s and $\nu = 1.0 \times 10^{-6}$ m^2 s^{-1}. (b) With $\langle v_P \rangle$ = 5 mm/s and $\nu = 1.5 \times 10^{-6}$ m^2 s^{-1}. Each Figure shows the results for two different turbulent regimes characterised by $\langle \epsilon \rangle$ values shown. These results correspond to the number of captures depicted on Figure 5.2. The keys are the same as in Figure 5.1.

5.5.3 Effects of viscosity

It is widely recognised that larval fish swimming energy expenditure depends on viscosity. However the way E_s value from Galbraith et al. (2004) vary with viscosity is not known. We made use of the report by von Herbing (2002) and assumed a linear relation between swimming cost and temperature. This imply that E_s is inversely

proportional to viscosity. Base on this assumption NEG calculations were done to investigate the influence of viscosity on the predation rate results shown on Figure 5.3. For $\nu = 1 \times 10^{-6}\text{m}^2\ \text{s}^{-1}$, value of the baseline swimming energy expenditure ($E_s = 2.73 \times 10^{-6}$ cal mg^{-1} mm^{-1}) is assumed. For $\nu = 1.2$ and $1.5 \times 10^{-6}\text{m}^2\ \text{s}^{-1}$ the values of E_s are assumed to be 3.41 and 4.1×10^{-6} cal mg^{-1} mm^{-1} respectively. These corresponds to 25% and 50% rise in E_s respectively. The NEG results for two groups of 512 predators following the pause-travel search pattern with swimming speed $\langle v_P \rangle = 5$ mm s^{-1} during the travel phase are depicted on Figure 5.6.

Figure 5.6(a) shows the results for the viscosity values shown in turbulent regime characterised by $\langle \epsilon \rangle = 5.53 \times 10^{-9}\ \text{m}^2\ \text{s}^{-3}$. While Figure 5.6(b) show the results when $\langle \epsilon \rangle$ is raised to $5.53 \times 10^{-8}\ \text{m}^2\ \text{s}^{-3}$ in the viscosity regime shown. Once again, the simulations predict that following strategy (33%, 67%) is energetically most favourable in Figure 5.6. This is a significant result because it is exactly what they are observed to be doing experimentally (see Galbraith et al. (2004)). This strategy appears to be robust under various conditions that is why it is commonly observed. However, it can be noted that the difference between this strategy and (50%, 50%) is only marginal. Another point to note is that as a consequence of fact that swimming is more expensive in a more viscous flow, the NEG results differ with viscosity even though the predation rates are almost equal (see Figure 5.3). The results also supports the previous conclusion that pause-travel is more likely to be observed at a relatively low levels of turbulence.

As mentioned earlier, there are overwhelming evidences in literature that the energetic swimming cost is strongly related to viscosity. This has more profound effects on small fish larvae whose crucial activities are performed in viscous hydrodynamic regimes. Larger larvae are more efficient swimmers because of this, they are usually consider to be operating either in the intermediate or the inertial regimes (see Fuiman & Batty (1997)). There is the need to formulate a realistic model of swimming cost that will reflect changes not only in the viscosity of the flow regime, but also on the size and the swimming speed of the animal in question. This formulation is considered in the next section.

5.6 Cost of move for cod larvae

In order to get more insight into the energetic benefits associated with pause-travel an ad-hoc theoretical model for the cost of swimming E_{move} that depends on the kinematic viscosity of the fluid shall be derived. This term should replace $E_s M v_P$ in the Galbraith et al. (2004) formula. Professor Howard Browman (personal communication) states that the value of cost of swim mainly depend on the cost of acceleration out of the low Reynolds number to high Reynolds number regimes as a larva go from pause to travel phase. This work assumes low Reynolds number regime so it is not valid to cover

such accelerations. We shall further assume that larval fish is spherical in shape. This assumption though not correct, will enable us to apply Stokes drag law for a spherical object on the larva.

Consider a neutrally buoyant fish larva swimming in straight line at a constant depth. The forces acting on it are on the horizontal plane which consists of thrust (applied by the larva) and a drag acting in the opposite direction. The drag on a spherical object at low Reynolds number is given by the Stokes' law as

$$D = 6\pi\mu L v_P(t) \tag{5.6.1}$$

where L is a typical length scale of the larva, μ is the dynamic viscosity and v_P is the swimming speed. The drag coefficient written above is an estimate of passive drag and is valid only at low Reynolds number. The drag force on actively swimming body (D_s) is bigger than passive drag force. The ratio of swimming to passive drag coefficients (drag ratio) can be denoted by $\frac{D_s}{D} = \alpha_s > 1$ (see Weihs (1980), Stocker & Weihs (2001), Wu et al. (2007)). The experimental result of Videler & Weihs (1982) show that $\alpha_s = 3.3$ for fish. In terms of α_s the equation of motion for a swimming larvae producing thrust T_{m} is (see Stocker & Weihs (2001))

$$T_{\mathrm{m}} = M\frac{dv_P}{dt} + \alpha_s D, \tag{5.6.2}$$

where M is the mass of the larvae with some added mass of fluid. The required energy to traverse a given distance d over a period of time τ_c can be defined as

$$E = \frac{1}{\beta_c}\int_0^{\tau_c} T_{\mathrm{m}}\left(\frac{d}{t}\right)dt = \frac{1}{\beta_c}\int_0^{\tau_c} T_{\mathrm{m}} v_P dt \tag{5.6.3}$$

where β_c is the mechanical efficiency. In the theoretical work of Videler & Weihs (1982), Visser & Ki⊘rboe (2006) the authors believed that swimming efficiency is a constant, Stocker & Weihs (2001) believe that it is proportional to swimming speed and Verhagen (2004) showed that it depends on body size. In this formulation, the efficiency will be assumed constant. We further assumed that a larva is required to cover the distance d using pause travel such that the distances l_1 and l_2 are covered during the travel and pausing phases respectively within the time specify by t_1 and t_2. With this assumption, $d = l_1 + l_2$ and $\tau_c = t_1 + t_2$. The cost of move (energy per unit time) can be defined as

$$E_{\mathrm{move}} = \frac{1}{\beta_c \tau_c}\int_0^{\tau_c} T_{\mathrm{m}} v_P dt. \tag{5.6.4}$$

Suppose the dependence of v_P on time t is defined as

$$v_P = \begin{cases} v_1, & 0 \le t \le t_1, \\ v_2, & t_1 < t \le \tau_c \end{cases} \tag{5.6.5}$$

where τ_c is the time taken to complete one pause travel cycle. In terms of the unit step function (H(x)) equation (5.6.5) can be written as

$$v_P = v_1 - v_1 H(t - t_1) + v_2 H(t - t_1) - v_2 H(t - \tau_c). \tag{5.6.6}$$

Substituting equation (5.6.6) into (5.6.4) and integrating, the following is obtained

$$E_{\text{move}} = \frac{1}{\beta_c \tau_c} \left(k_c {v_1}^2 t_1 + k_c {v_2}^2 t_2 + M \left({v_1}^2 - 2\, v_1 v_2 + {v_2}^2 \right) \right) \tag{5.6.7}$$

where $k_c = 6\alpha_s \pi \mu L$. It is to be noted that equation (5.6.7) pertains one cycle only. Equation (5.6.7) gives a new model of swimming cost which depends on viscosity, size as well as the swimming speed of the animal. This model can be applied to both cruise and saltatory predators. For cruising animals, the pausing phase can be set zero so that the equation involves only terms with t_1 and v_1.

5.6.1 Application of the new model

In the previous section energetic cost of swim was formulated. This is equivalent to $E_s \langle v_P \rangle M$ in the Galbraith et al. (2004) formula. So the new energy gain model is

$$E = E_c PR - E_B M - E_{\text{move}}. \tag{5.6.8}$$

It will be useful at this juncture to investigate the effects of the new model on the predation rate results presented earlier. In particular, the effect of viscosity and swimming speed will be looked at. In what follows, we shall assumed further that the size of the template larva is $L = 5$ mm and the mass will remain $M = 0.06$ mg. For reason discussed in the previous section the drag ratio $\alpha_s = 2$ will be assumed.

Changes in viscosity

The motion of a fish larva through fluid depends on the propulsive force applied which is temperature dependent. At low temperature, the speeds of contraction of the swimming muscles are extended which results in their lower efficiency (see Videler & Weihs (1982), von Herbing (2002), von Herbing & Boutilier (1996)). This has direct effect of increasing the swimming cost. These findings suggest that major differences exist among the swimming capabilities of larval fish that inhabit cold, temperate waters compared to those that live in warm tropical waters. In studying the relative effect of viscosity it will be assumed that the swimming efficiency will have values $\beta_c = 0.25, 0.3$ and 0.35 at the viscosity values $\nu = 1.5, 1.2$ and 1×10^{-6} m^2 s^{-1} respectively. Based on these assumptions NEG calculations were done by substituting the number of captures shown on Figure 5.3 into equation (5.6.8).

Figure 5.7 show the plot of NEG against percentage travel time for three different viscosity values shown in turbulent flow characterised by $\langle \epsilon \rangle$ with swimming speed $\langle v_P \rangle = 5$ m/s during the travel phase. Other keys are as explained before. Figure 5.7(a) shows a plot of the NEG for two groups of 512 predators in the same energetic regime characterised by $\langle \epsilon \rangle = 5.53 \times 10^{-7}$m^2 s^{-3}. While Figure 5.7(b) shows a similar NEG results for two groups of 512 predators in the energetic regime characterised by

$\langle\epsilon\rangle = 5.53 \times 10^{-8}\text{m}^2\ \text{s}^{-3}$. These results corresponds to those shown on Figure 5.6. The simulation results predicts yet again that the strategies (50%, 50%) and (33%, 67%) are energetically most viable in all cases. We conclude that pause-travel is robust under viscosity regimes. This is just the conclusion got out of Figure 5.6. The only difference between the two is that the present calculation predicts higher energy takings. This imply that the new cost of swim underestimates the value given by Galbraith et al. (2004). This is not surprising because the cost of swim was formulated by assuming that the animals are swimming in a low Reynolds number flow regime.

Changes in swimming speeds

In this section the predation rate results shown on Figure 5.1 will be translated into NEG using the new cost of swim so as to determine whether there are any changes to the conclusions earlier reached. Predators foraging in the same turbulent energy and viscosity regime will be assumed to have the same efficiency. Figure 5.8 shows a plot of NEG for KS and theoretical predictions against the percentage of time spent travelling by two groups of 512 saltatory predators in a turbulent and viscosity regimes characterised $\langle\epsilon\rangle = 5.53 \times 10^{-9}\text{m}^2\ \text{s}^{-3}$ and $\nu = 1.5 \times 10^{-6}\ \text{m}^2\ \text{s}^{-1}$, with two different swimming speeds during the travel phase as shown. The results are obtained by substituting the number of captures shown on Figure 5.1 in equation (5.6.7). These results corresponds to those shown on Figure 5.4, the keys are the same in both Figures.
Figure 5.8(b) shows the result for the efficiency value $\beta_c = 0.3$ while the result for the efficiency $\beta_c = 0.6$ is shown on Figure 5.4(b). Qualitatively, these calculations does not change the predictions got out from Figure 5.4(a). The result indicates that pause-travel is inefficient at high swimming speed but robust under low travel speeds.

5.7 Conclusions

The natural habitat of fish larvae are subject to changes in the turbulent energy dissipation and viscosity values which arises due changes in the flow brought about by differences in wind forcing and solar heating. These animals have instinctively developed the complicated saltatory foraging strategy which increases their chances of survival. Using a series of kinematic simulation, the robustness of saltatory foraging strategies of fish larvae under varying turbulent and viscosity conditions were tested. All together, six flow fields were constructed using some combinations of viscosity and turbulent energy regimes.
Central to the calculations, is the bioenergetic gain function which is adopted to calculate the net energy gains made by successful foraging against the energy expended whilst swimming. One of the input parameters (E_s) to this function is shrouded by

uncertainties. Consequently this parameter was modelled. The new model was then applied on some captures results earlier presented. Using the results of the various energy calculations, a number of conclusions have been drawn:

1. Pause-travel is found to be a robust strategy to adopt by a fish larva with low travel speed. The pause-travel ratio (50%, 50%) and (33%, 67%) have appeared many times as the optimal strategy across many regimes. By looking at the various pause-travel ratios considered, we can say that, no unique optimal strategy across all flow regimes was obtained. We could perhaps consider more pause-travel possibilities. However, the simulations are computationally expensive requiring large amount of computing time.

2. Swimming fast ($\langle v_P \rangle = 10$ mm s^{-1}) appears to be energetically unrealistic for a larva following the saltatory strategy to adopt. Changes in kinematic viscosity affects the energetic benefits associated with pause-travel. Pause-travel is robust across viscosity regimes. The strategy is more energetically beneficial in a less viscous (high temperature) regime than a higher one. This agrees well with experimental observations where larva and adult fish are observed to be less active in colder waters. High viscosity affects the swimming efficiency making it difficult for pause-travel to be observed.

3. Similarly, in a highly turbulent flow pause-travel becomes increasingly difficult to be observed as controlled swimming become difficult.

4. The new energy gain model developed is producing reliable results. This is because results produced by the new model agree well with a published model.

Generally, the results recorded in this and the previous Chapter differ fundamentally from those of predators with spherical perception field. The investigations were carried out base on the fact that larval fish feeds on non-mobile prey. This is not an unrealistic assumption because a large classes of planktonic microorganisms posses no swimming abilities. However, nauplii and later stages of copepods which form the bulk of the diet for fish larvae are known to posses swimming abilities. We would like to know whether pause-travel is robust when larval fish forage on swimming prey. This is investigated in the next Chapter.

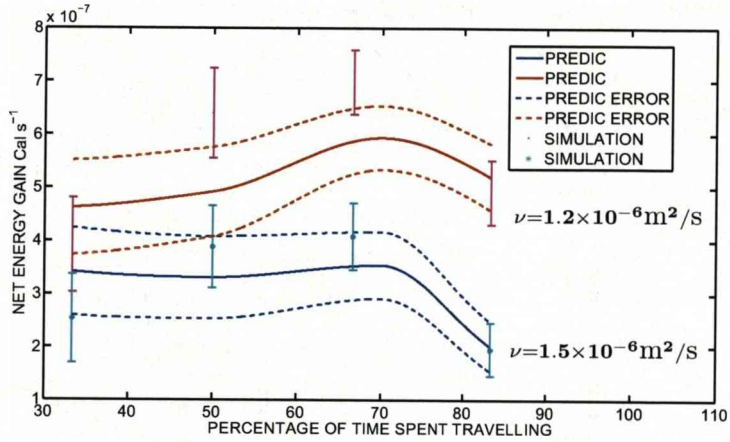

(a) $\langle v_P \rangle = 5$ mm/s, $\langle \epsilon \rangle = 5.53 \times 10^{-9}$ m^2 s^{-3}.

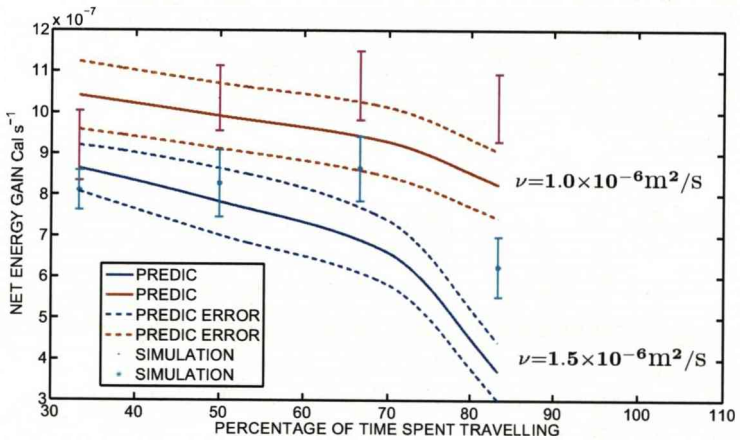

(b) $\langle v_P \rangle = 5$ mm/s, $\langle \epsilon \rangle = 5.53 \times 10^{-8}$ m^2 s^{-3}.

Figure 5.6: The results of KS and theoretical predictions for the NEG against the percentage of time spent travelling by two groups of 512 saltatory predators at two different viscosity regimes shown. These results are obtained by changing the baseline E_s. The value of swimming energy expenditure used for $\nu = 1.5$ m^2 s^{-1} is $E_s = 4.1 \times 10^{-6}$ cal mg^{-1} mm^{-1} this corresponds to a rise in 50% base line swimming cost. (a) With $\langle v_P \rangle = 5$ mm/s, $\langle \epsilon \rangle = 5.53 \times 10^{-9}$ m^2 s^{-3}. The value of swimming energy expenditure used is $E_s = 3.41 \times 10^{-6}$ cal mg^{-1} mm^{-1} for $\nu = 1.2$ m^2 s^{-1}. This corresponds to 25% rise in the baseline E_s value. (b) With $\langle v_P \rangle = 5$ mm/s, $\langle \epsilon \rangle = 5.53 \times 10^{-8}$ m^2 s^{-3}. For $\nu = 1 \times 10^{-6}$m^2 s^{-1}, the swimming energy expenditure is the baseline E_s. All the keys are the same as in Figure 5.1. The results are obtained by substituting the predation rates results shown on Figure 5.3 into equation (4.10.1).

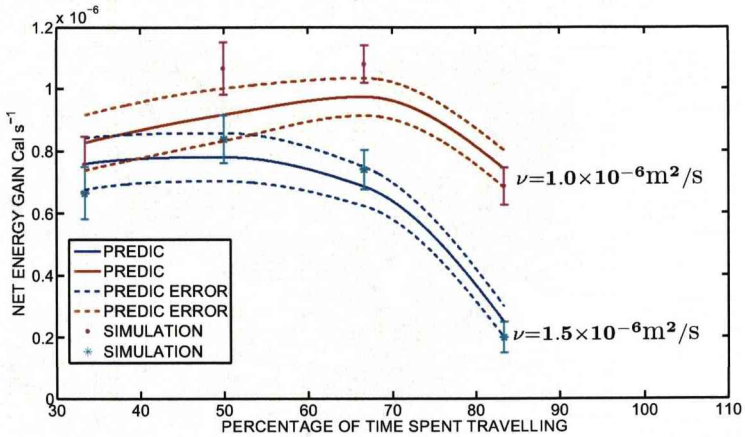

(a) $\langle v_P \rangle = 5$ mm/s,$\langle \epsilon \rangle = 5.53 \times 10^{-9}$ m^2 s^{-3}.

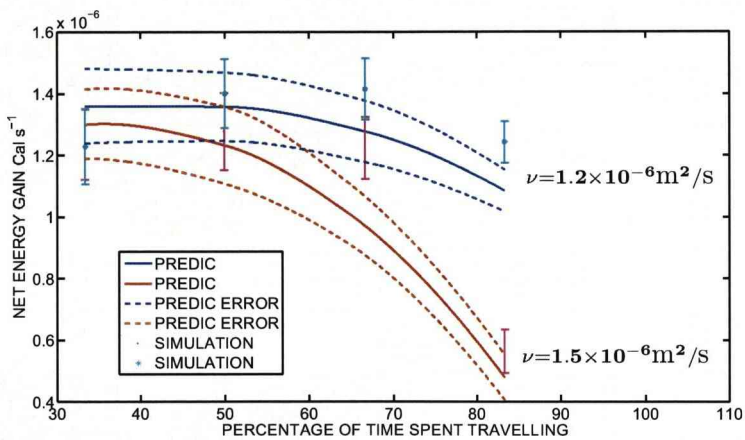

(b) Dissipation rate $\epsilon = 5.53 \times 10^{-8}$ m^2 s^{-3}.

Figure 5.7: The results of KS and theoretical predictions for the NEG against the percentage time spent travelling by two groups of 512 saltatory predators at three different kinematic viscosity regimes shown, in a turbulent flow characterised by $\langle \epsilon \rangle$. These results are obtained using the new energy gain formula. The swimming speed is $\langle v_P \rangle = 5$ mm/s during the travel phase. The value for the drag ratio used is $\alpha_s = 2$. Efficiency values used are $\beta_c = 0.25, 0.3$ and 0.35 at the viscosity values $\nu = 1.5, 1.2$ and 1×10^{-6} m^2 s^{-1} respectively. (a) With dissipation rates $\langle \epsilon \rangle = 5.53 \times 10^{-9}$m^2 s^{-3}. (b) With dissipation rates $\langle \epsilon \rangle = 5.53 \times 10^{-8}$m^2 s^{-3}. The keys are same as in Figure 5.1. The results are obtained by using the number captures shown in Figure 5.3 in equation (5.6.8).

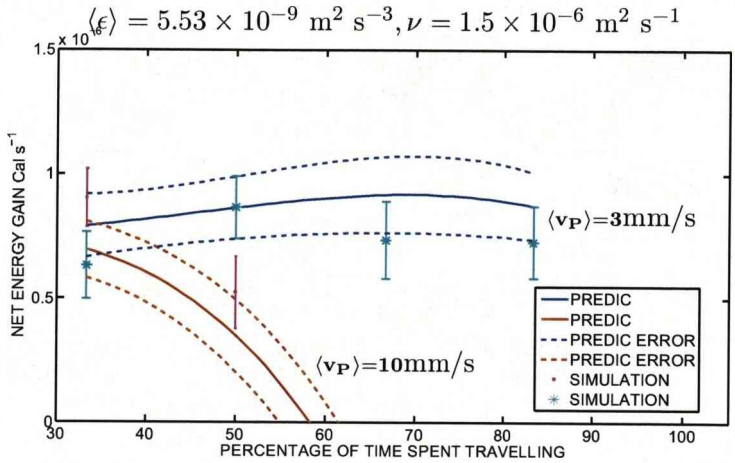

(a) $\langle \epsilon \rangle = 5.53 \times 10^{-9}$ m^2 s^{-3}, $\nu = 1.5 \times 10^{-6}$ m^2 s^{-1}.

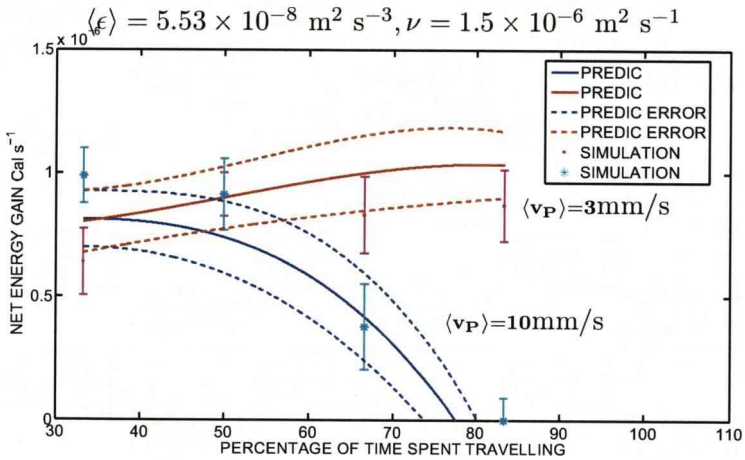

(b) Dissipation rate $\epsilon = 5.53 \times 10^{-9}$ m^2 s^{-3}.

Figure 5.8: The results of KS and theoretical predictions for the NEG against the percentage of time spent travelling by two groups of 512 saltatory predators in a turbulent and viscosity regimes characterised $\langle \epsilon \rangle = 5.53 \times 10^{-9}$m^2 s^{-3} and 1.5×10^{-6} m^2 s^{-1}, with two different swimming speeds during the travel phase as shown. These results are obtained using the new energy gain formula. (a) With efficiency $\beta_c = 0.3$. (b) With efficiency $\beta_c = 0.6$. The keys as in Figure 5.1. The results are obtained by substituting the number of captures shown on Figure 5.1 into equation (5.6.7).

Chapter 6

Incorporating prey swimming into saltatory predation models

6.1 Introduction

Flows of energy in pelagic food webs are to a large extent determined by the ability of the predators to feed on both mobile and non-mobile prey. Because of their small size, swimming speeds of copepod nauplii which forms the major source of protein for cod larvae are usually thought to be negligible. However, cod larvae do not feed on the nauplii only. Moreover, the nauplii are known to spend more than half of their time swimming. It is therefore imperative to conduct a study on saltatory strategy by including components of prey swimming activities. It must be emphasised that a comprehensive theoretical study of planktonic predation rates in a turbulent flow that incorporates swimming prey is a very difficult task.

This Chapter presents the development of both theoretical and simulation models of saltatory strategy in a turbulent flow with swimming prey. Applications of the model will examine the foraging behaviour of Atlantic cod larvae using both theory and simulation. The ideas to be presented form an extension of the methodology presented in Chapter 4 which were based on the assumption that the prey were non-swimmers. Modification of the simulation model to account for prey swimming is relatively straight forward in principle. However, incorporating prey swimming into the prediction model is a much more complicated process. The chief difficulty lies in the calculation of the predators' line of sight. In this work, the line of sight will be estimated by adopting a similar procedure to that described in Chapter 4 when the cod larvae were in their traveling mode. In their pause mode it will be selected randomly. This methodology then allow us to evaluate the multi-dimensional integrals derived in Chapter 4 under the assumption the larva and its prey move in straight line, but now incorporating changes to the larva's line of sight as it moves along. Modification of these results by means of volume fraction estimates to account for non-linear motion then enables one

to predict the actual predation rate. The approach adopted to test the models is based on the use of field and laboratory experimental data obtained from literature studies.

6.2 Model formulation

In this section the details of the simulations performed and the formulation of the prediction model will be presented.

6.2.1 The simulations incorporating prey swimming

The simulation codes developed in the previous Chapters are versatile and require only small set of modifications to incorporate prey swimming. That is, the general formulation of the present simulations differs only slightly with those described previously. For this reason, only a brief summary will be given here.

The major difference between the present simulations and the previous ones is that in this case, the prey were swimming. During a run, the swimming speed of the prey were drawn from three-dimensional Gaussian distribution with mean zero and standard deviation σ_H (see table 6.1). Two kinds of prey motility patterns were considered. First (a) the case when the prey never change their direction of swimming (move with the same speed) throughout the simulation. This is characterised by $t_{\text{sight}} = \infty$. Second (b) the case when the prey are changing their swimming direction every 10 time steps. This is equivalent to changing direction every 2.7 s ($t_{\text{sight}} = 0.2$). In this scenario, new random walk swimming speeds were assigned to each prey particle after every 10 time steps. The other major difference is the adoption of a revised capture function incorporating the prey's swimming speed.

Capture probability function for swimming prey

The capture function used in the previous Chapters does not contain explicit parameters governing the evasive capabilities of the prey. It is widely recognised that prey swimming speed is generally proportional to its size. Consequently, larger prey are more difficult to be captured than smaller ones. For example the experimental report by Buskey (1994) showed that capture success for feeding on Acartia tonsa nauplii lies in the range 10 to 80% depending on age with the smallest being the most vulnerable. Similarly von Herbing et al. (2001) showed that when a cod larva encounter the protozoan Balanion sp, the prey does not attempt to escape but continues to swim slowly. This tends to suggest that smaller prey exhibit little or no escape behaviour. Capture success in the range 62 to 75% for cod larvae feeding on these prey were recorded by the author. Because of the relation between prey size and susceptibility to capture, various authors have used predator-prey size ratio (relative size ratio) as a parameter

in capture probability functions. The relevance of this ratio could be linked to the idea that below a certain threshold value of this ratio, prey are too small to be seen. Above a certain value, prey are too big to be swallowed. The capture probability function used in the previous Chapters is a non-dimensional function involving time variables. Rather than incorporate relative size ratio, we shall use the quotient of prey size to its speed (ss_{quo}). We can define a capture function involving ss_{quo} as

$$p_{\text{cap}} = \frac{\langle t_{\text{TRA}} \rangle^2}{\langle t_{\text{TRA}} \rangle^2 + T_R^2 + (ss_{\text{quo}})^2}. \tag{6.2.1}$$

The introduction of ss_{quo} implies that the new capture function has one more additional parameter to be determined. Values of this parameter can be estimated from experimental results found in literature. This means that the new parameter can be estimated with reasonable accuracy. Greene & Landry (1985), performed some experimental work to study the behaviour of the calanoid copepod Eucheta elongata, feeding on different developmental stages of calanus pacificus. The authors divided the nauplier (N) and the copepodite (C) stages into six (NI to NVI and CI to CVI). The divisions were mainly base on average sizes and speeds. Atlantic cod larvae are known to feed predominantly on these developmental stages of copepods as well. Therefore their experimental data can be used in this study. Representative prey templates were taken from the work of Greene & Landry (1985). This data were then used in calculations of ss_{quo} which is non-dimensionalised using the Kolmogorov time scale. Typical values of ss_{quo} used in this Chapter are presented on Table 6.1. In this Chapter, the capture

Prey stage	Total length (mm)	Mean speed (mm/s)	ss_{quo}	σ_H	t_{sight}
NII	0.27	0.89	0.0226	2.05	$0.2, \infty$
NV	0.53	1.14	0.0346	2.62	$0.2, \infty$
CIV	1.8	3.27	0.0409	7.514	0.2
CIII$^+$	1.7^+	2.5^+	0.051	5.745	0.2

Table 6.1: Typical prey specification used in this Chapter. The prey sizes and swimming speeds are taken from Greene & Landry (1985). ss_{quo} = Total length/(mean swimming speed $\times$ (Kolmogorov time scale)). The entries marked with $^+$ are assumed values different from the corresponding entries given by the authors. Altogether six simulations were conducted for prey sizes/speed shown and for the values of t_{sight} indicated. The Kolmogorov time scale $\tau_k = 13.4473$ for $\langle \epsilon \rangle = 5.53 \times 10^{-9}$ m^2 s^{-3}, $\nu = 1.0$ m^2 s^{-1} were used.

function given by equation (6.2.1) is used. The new capture function was substituted because of the needs to include the characteristics of the prey to reflect their different sizes and speeds. Altogether six different simulations were conducted by varying ss_{quo}, and using two types of motility pattern as shown on Table 6.1. The rest of the simulations are as described in Chapter 4.

6.2.2 The prediction model for prey swimming

The necessary predictions have to estimate the predation rate with prey, swimming at four different prey speeds viz, $\sigma_H = 2.05, 2.62, 5.745$ and 7.514 being are pursued by two different group of larval predators swimming at speeds $\sigma_P = 6.89$ and 11 respectively during their travel phases. The chief difficulty in formulating the predation rate model `when both predator and prey are swimmers` lies in the calculation of the predator's line of sight; more specifically the angle γ which the line of sight makes with the vertical. In the travel phase σ_P is often large, greater than W and σ_H. In that instance $\mathbf{V}_P$ is not so much different from $\mathbf{v}_P$ and hence it is possible to apply the previous methodology of Lewis (2003) to calculate the line of sight (the estimate of W which results provides only a small correction to $\mathbf{V}_P$). In the pause phase things are much more difficult because now σ_P is smallest (although not zero, because the line of sight is defined to be along the predator's swimming direction) of the velocity scales characterising the encounter event. In this situation it is virtually impossible to reconstruct information about the small $\mathbf{v}_P$ from the information contained in the larger velocity scales. So we decided to chose the angle γ randomly for each encounter when estimating the predation rate integrals. Whilst not ideal, as will be seen the good agreement between predictions and simulations justifies making this compromise. In the case when $\sigma_P = 6.89$ in the travel mode, the predator's average travel speed is not significantly different from σ_H, so either of the above methods for choosing γ seems appropriate. In the calculations presented here the former method was adopted, but choosing γ randomly gives only a small, 2%, increase in the prediction results.

One other parameter that needs to be estimated is the relative velocity scale U_R. This scale now must depend on both σ_P and σ_H and may be re-defined as

$$U_R = \begin{cases} \frac{U_R(0,0)}{U_R(0,\sigma_H)}, & \text{when pausing,} \\ \\ \frac{U_R(0,0)}{U_R(\sigma_P,\sigma_H)}, & \text{when travelling.} \end{cases} \tag{6.2.2}$$

However, there is an extra complication in making the predation rate estimates. The volume fraction calculations are designed to predict what happens when the predator follows an irregular trajectory (either by choice by changing swimming heading, or carried along by the flow, or by a combination of the two). The methodology is fine if the prey are non-swimmers, but this no longer applies here. If the prey swim in straight lines ($t_{\text{sight}} = \infty$), actually this is not much of a problem (σ_H is much larger than the flow and so the latter will exert relatively little influence), because we can simply calculate the straight line predation rate from the various multi-dimensional integrals and then estimate the volume fraction modification as before. But if the prey are themselves rapidly `changing direction`, as in some of the simulations here (t_{sight}=0.2), this presents an extra complication. Now calculations of the predator's straight line predation rate will be much too large, because under such circumstances

prey tend to remain in same small region of space for long periods and consequently will be encountered much less frequently. From the predators' viewpoint the effect is as if they are searching for prey which are swimming at a much `slower` speed than they actually are. So in order to take account of this, one needs to modify the straight line calculations by incorporating a reduced prey speed into the calculation. These can then be modified further using the volume fraction estimates, to account for irregularities in the predators' trajectories as before. So the question now arises as to how to define such a reduced prey speed. It obviously should depend on the flow to some extent and the actual values of σ_H and t_{sight}. If t_{sight} is large, no modification is necessary, but if t_{sight} is small, compared to something, then one needs to make a modification. The obvious 'something' is the timescale of the flow, τ_{LC}. So in this work we decided to define

$$\sigma_{\text{HNew}} = \left(\frac{t_{\text{sight}}}{\tau_{LC}}\right)^{\frac{1}{2}} \sigma_H \tag{6.2.3}$$

and replace σ_H by σ_{HNew} in the straight line calculations, when necessary. It must be emphasised that this choice is certainly arbitrary but not unreasonable. Typical calculations of the velocity scale U_R, χ_{U} at different values of $\sigma_{P,H}$ are given in Table 6.2.2. These calculations pertain to two prey motility patterns. Where a value is assigned for σ_{HNew}, it indicates that in this particular calculation the prey are changing their swimming directions rapidly. In summary, the prediction calculations involve the following steps

- Calculate the angle γ. This is calculated following the procedure outlined by Lewis (2003) during the travel phase and is chosen randomly during the pause phase.
- Calculate the straight line predation rates.
- Calculate the velocity scale for both travel and pause phases.
- Calculate the values of χ_{U} and hence τ.
- Estimate the volume fraction.
- Finally, calculate modified estimates of the predation rates.

The capture rates and NEG results are presented in the next section.

6.3 Number of captures and NEG results for saltatory predators feeding on mobile prey

In this section the number of captures and the changes to NEG for saltatory predators foraging for actively swimming prey will be investigated using theory and simulations.

σ_H	σ_{HNew}	σ_P	U_R	χ_U
2.05	-	0.1	1.097	0.7133
	-	11	16.584	0.047
	0.633	0.1	0.8225	0.9510
	0.633	11	16.584	0.047
2.62	-	0.1	1.2373	0.6322
	-	11	17.347	0.045
	0.809	0.1	0.8479	0.9225
	0.809	11	17.347	0.045
5.745	1.773	0.1		
	1.773	6.89	9.5636	0.0818
7.514	2.319	0.1		
	2.319	6.89	9.5463	0.0819

Table 6.2: Typical calculations of U_R, χ_U at different values of $\sigma_{P,H}$. Values of $\sigma_P > 0.1$ denotes the travel phases. The cases where σ_{HNew} has value pertains the simulation with $t_{\text{sight}} = 0.2$. The velocity scales are calculated using equation (1.2.11) and χ_U is calculated in similar manner as was done in (1.2.12).

This is a novel work that is appearing for the first time in literature. To carry out the study, a number of simulations and predictions were conducted separately for two groups of 512 saltatory cod larvae feeding on two different groups of prey with the same size and speed but different motility patterns. One group of prey was changing its heading every 10 time steps ($t_{\text{sight}} = 0.2$) and the second group was moving in straight lines ($t_{\text{sight}} = \infty$). In both cases, the swimming speeds of the prey were drawn from three-dimensional Gaussian distributions with mean zero and standard deviation $\sigma_H = 2.05$. The speeds and the corresponding sizes of the prey are taken from the experimental work of Greene & Landry (1985) as summarise in Table 6.1. The larvae were assumed to be swimming with speed $\sigma_P = 11$ in their travel phase. This corresponds to average swimming speed of about 5 mm/s.

Figure 6.1(a) shows the prediction and simulation results of the number of prey captures obtained when the larvae perform different types of pause-travel foraging strategies (indicated by the percentage on the horizontal axis). The Figure shows the results when foraging for two different prey types, one set which changes direction rapidly as they swim and one set which swim in straight lines. For the case where the prey were frequently changing directions ($t_{\text{sight}} = 0.2$) are given by error bars with ·. For the straight line swimmers ($\tau_{\text{sight}} = \infty$), the simulation results are represented by error

bars with *. The prediction results for straight line swim are represented with with – and the associated standard deviations are given with - -. For $t_{\text{sight}} = 0.2$ the predictions results and the associated standard deviations are respectively represented by – and - -. It can be seen that capture success remain fairly similar irrespective of which type of prey are pursued. This might be explained by the fact that straight line swimmers are easier to encounter but harder to catch, prey swimming randomly are harder to encounter but easier for the predator to catch. The net result turns out the capture rate is much the same.

It is interesting to note that the outputs of the simulations agree well with the predictions. This is encouraging and it shows that the theory upon which the prediction model is built is working fine. As far as the number of captures are concerned, the results show that prey motility pattern does make a difference on the ambush predators (100%, 0%). They find it marginally easier to capture prey that swim in straight lines, a consequence of the fact that they will tend to encounter these prey more frequently. This might mean that the erratic swimming patterns of prey are more efficient means of avoiding predators than the motions in straight lines. This might be one reason why copepod nauplii are never observed swimming in straight lines for any prolonged period of time. It could also be partly explained by the fact that those prey items that follow irregular path will tend to disappear out of predators perception field more quickly.

As the percentage travel time increases, the difference between the numbers of captures narrows. So for cruising predators (that is larvae which spend 100% in the travel-phase), the prey's motility pattern does not seems to make any significant difference. The simulation results show that to maximize the number of captures, the predators should maintain (0%, 100%) pause-travel mode. This is consistent with the capture results obtained previously for non-swimming prey. However, the prediction results show that the number of captures peaks, then falls. The pause-travel mode where the maximum occurs is very close to 100% travel- mode. By traveling most of the time, the predators can cover a lot of ground and in the process encounter many prey. However, the faster the larvae swim, the higher the cost of swimming and hence the higher the drain on the larva's energy resources. This means that as in the case when the larvae forage for non swimming prey, there exists some pause-travel ratio for which the strategy is optimal in terms of the larva's energy budget. To investigate this, the NEG model developed in Chapter 5 is employed.

6.3.1 A NEG model for predators feeding on mobile prey

For a predator feeding on different developmental stages of prey, the energy content of prey is size dependent (von Herbing et al. 2001). Moreover, smaller prey have less developed escape capabilities than larger ones. The energy calculations done in the previous Chapters were based on the assumption that the prey are non-swimming.

Swimming prey will be more difficult to capture. As suggested by Manatunge & Asaeda (1999) the fleeing speed of the prey should be accounted for when calculating the net energy expenditure. To incorporate this into the NEG model, the predators' travelling and pausing speeds v_1 and v_2 that appear in equation (5.6.7) was replaced by $v_{1,2}+\langle v_H\rangle$. If $\langle v_H\rangle = 0$, the original formula is recovered. With the modifications just described, the cost of pursuing a prey and NEG formula can be defined respectively as in equations (6.3.1) and (6.3.2)

$$E_{\text{purs}} = \frac{1}{\beta_c \tau_c}\left(k_c(v_1+\langle v_H\rangle)^2 t_1 + k_c(v_2+\langle v_H\rangle)^2 t_2 + M(v_1 - v_2 + \langle v_H\rangle)^2\right), \quad (6.3.1)$$

$$E = E_c PR - E_B M - E_{\text{purs}}. \quad (6.3.2)$$

The parameter values E_c, E_B and M have the same values reported by Galbraith et al. (2004) (see Chapter 4). Recent studies (see von Herbing & Boutilier (1996)) have shown that the Atlantic cod larvae `Gadus morhua` has shifted its diet from from protozoans Balanion sp to larger copepod nauplii such as canlanus finmarchicus. von Herbing et al. (2001) linked the reason for the shift to the fact that Balanion sp has low energy content (energy content 0.3 mJ) than copepod nauplii (energy content 7 mJ) which are larger. We shall assumed that the energy content of prey depends linearly on size. The capture success (numbers close to the error bars) shown on Figure 6.1(a) are used in place of the swimming efficiency β_c in both theory and simulation. For example, for the pause-travel strategy (100%,0%) $\beta_c = 0.68$ was used for both groups of predators shown on Figure 6.1(b). Having specified the formula, NEG calculations were conducted for two groups of predators feeding on mobile prey with speed $\sigma_H = 2.05$ the results of the calculations for theory and simulations are shown on Figure 6.1(b). Both theory and simulations show the existence of optimal pause-travel ratios which maximize NEG. The optimal pause-travel predicted by theory and simulations are very similar. The results show that the prey group which moves in straight lines yields more energy to predators. This is because they are encountered and get captured more often. This is most apparent for the ambush feeders but applies for all types of pause-travel foraging. The results also show that for cruising predators the differences between foraging for the two sets of prey are least significant. The results recorded here are at odds with the experimental work of Buskey (1994). The author suggested that predators should select those prey items with the most erratic swimming pattern. The present results show that straight lines swimmers are to be preferred. This might also imply that changes in swimming directions by prey are a better means of escaping predators. These conclusions are only based on a single prey size. There is the need for more different prey sizes to be studied before more profound conclusions can be drawn.

Figure 6.2(a) presents the results obtained from theory and simulations when the prey speed was increased to $\sigma_H = 2.62$. The keys are the same as in Figure 6.1(a). The

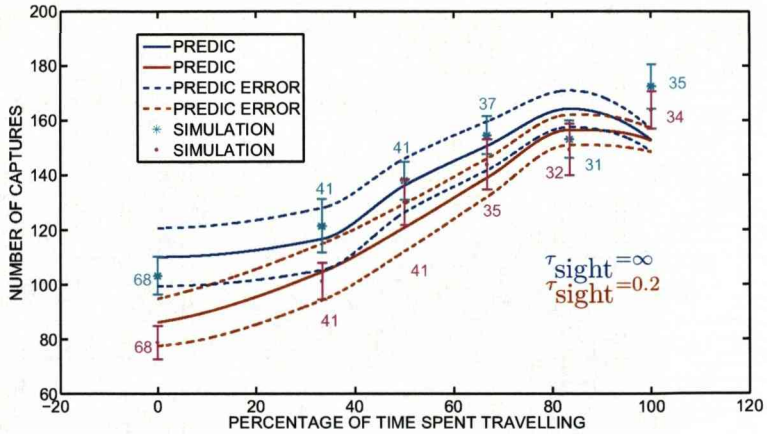

(a) Number of captures by two groups of predators feeding on two groups of prey with swimming speeds $\sigma_H = 2.05$

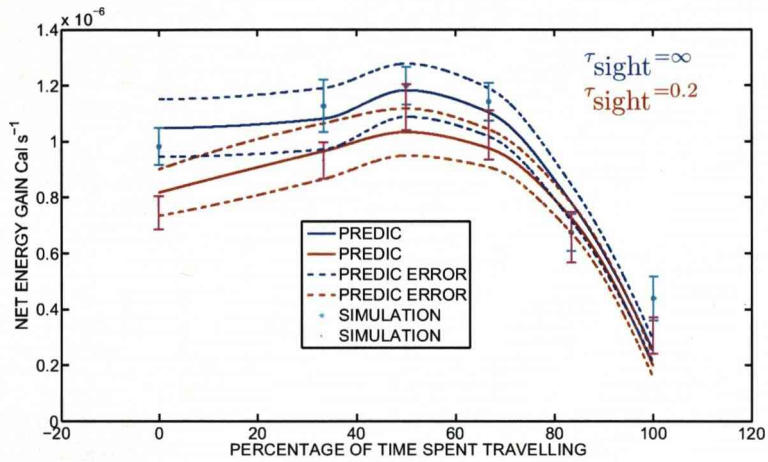

(b) NEG calculations corresponding to the number of captures shown on Figure 6.1(a).

Figure 6.1: Number of captures and NEG calculations for two groups of saltatory predators feeding on two groups of mobile prey with the same speed $\sigma_H = 2.05$ and two different motility patterns. (a) is for the number of captures (b) is the NEG results corresponding to the number of captures shown in (a). The NEG results were calculated using equation (6.3.2). The prediction results are represented with – ($\tau_{\text{sight}} = \infty$) and –($\tau_{\text{sight}} = 0.2$). The associated standard deviations are given with - - and - - respectively. The simulation results are represented with error bars as follows: * ($\tau_{\text{sight}} = \infty$) and · ($\tau_{\text{sight}} = 0.2$).

corresponding size and ss_{quo} are shown in Table 6.1. Similarly, the relative velocity scales and χ_U for this are shown on Table 6.1. Since the prey are bigger than those on Figure 6.1, it is expected that they have higher energy content. So the baseline

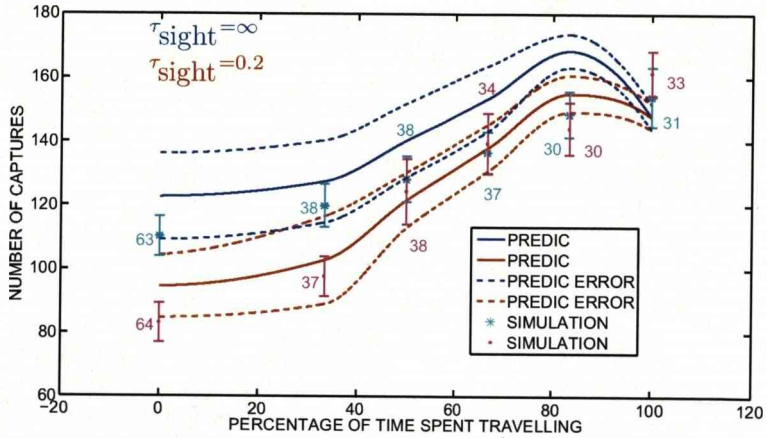

(a) Number of captures by two groups of predators feeding on two groups of prey with swimming speeds $\sigma_H = 2.62$

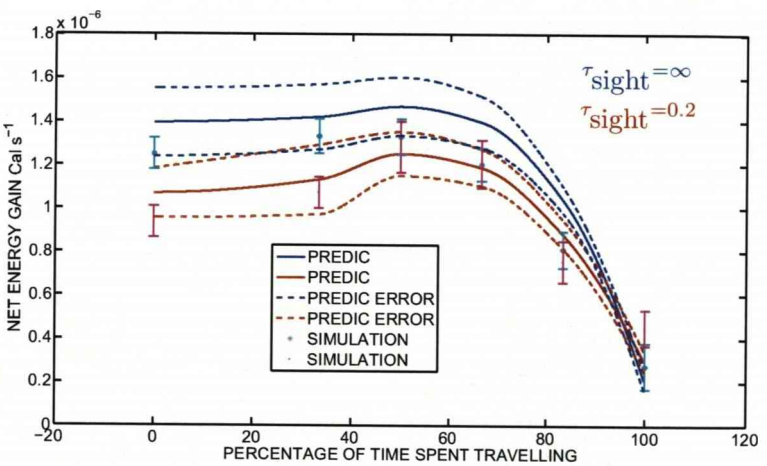

(b) NEG calculations corresponding to the number of captures shown on Figure 6.2(a)

Figure 6.2: Number of captures and NEG calculations for two groups of saltatory predators feeding on two groups of mobile prey with the same speed $\sigma_H = 2.62$ and two different motility patterns. (a) is for the number of captures (b) is the NEG results corresponding to the number of captures shown in (a). Other keys are as described on Figure 6.1

E_c is increased by 20%. The capture success shown on Figure 6.2(a) were used to represent the swimming efficiency β_c. Other parameters are the same as before. The present results do not materially alter the conclusions drawn from Figure 6.1(b). It is significant to notice that the optimal travel ratios are similar. The most noticeable difference between the two NEG calculations is that energy values are higher on Figure

6.2(b). This seems to support the optimal foraging theory, that predators should select the largest (most nutritious) prey available. The natural question become, is there any upper bound in prey size for the optimal foraging theory to hold?

To investigate this new set of simulations were carried out for two different prey sizes and speeds but the same motility pattern ($t_{\text{sight}} = 0.2$). In this case the predators were moving with the swimming speeds $\sigma_P = 6.89$ during the travel phase. This is equivalent to the average swimming speed of 3 mm/s. One group of prey (smaller) were moving with speeds $\sigma_H = 5.745$ and the second group (larger) with speed $\sigma_H = 7.514$. These correspond to swimming speeds of 2.5 and 3.27 mm/s respectively. The corresponding prey sizes are shown on Table 6.1. The E_c values used were obtained by increasing the baseline E_c to 50% and 70% for smaller and larger prey respectively. The results for the number of captures are shown on Figure 6.3(a) and NEG calculations are shown on Figure 6.3(b). The prediction results for the faster (larger) prey are represented with – and the standard deviations are represented with - -. For the slower (smaller) prey the prediction results and the associated standard deviations are given with – and - - respectively. The simulation results are represented with error bars as follows: * for smaller prey and for larger prey. Other keys are the same as in Figure 6.1.

The number of captures follow a similar pattern to those shown on Figure 6.1(a). Both the NEG results for the simulation and the predictions show that there is no significant difference in pursuing either size of prey. However, the smaller prey yields marginally more energy. This is because the larger (faster) prey are swimming slightly faster than the predators while the smaller ones are swimming at a speed slightly less than those of the predators. This tend to suggest that as the speed (size) of the prey increases, it becomes energetically less viable for a given predator to pursue those prey species. This finding supports the results of Greene & Landry (1985) who reported that vulnerability to predation in copepods is a dome shaped function of ontogeny (developmental stage) with peak vulnerability occurring at the copepodite stages.

Remarkably both the optimal travel duration for the prediction and simulation for the different prey sizes are the same. O'Brien et al. (1989) show that for white crappie, longer travel durations are observed when feeding on large prey and shorter move durations are observed when feeding on smaller prey. In this present study, it can be seen that the simulation and prediction results show that the travel durations that produces maximum NEG are similar for both groups of prey. This tends to suggest that the optimum pause-travel durations may be dependent upon larval fish species.

Generally speaking, formulating a working theory for planktonic predation rates when both predator and prey are swimming in a turbulent flow is a remarkable feat. Moreover, the good agreement between the diverse parts of the calculations serves as a good indicator that the underlying ideas upon which the models are built are sound. Given all the complexities involved in the formulations, the results recorded here are very

encouraging.

6.4 Conclusions

In this Chapter, previous theory and simulations codes were extended to study the foraging behaviour of Atlantic cod larvae feeding on mobile prey. The prey items were assumed to be developmental stages of calanus pacificus. The main difficulty in the formulation of the prediction model lies in the calculations of the predators line of sight. This was overcome by assuming that the prey swimming speeds are negligible in comparison with the predators' travel speed. This assumption allows the line of sight to be calculated as was done for non-swimming prey. During the pause-phase, the line of sight were randomly selected.
The models were applied to study the predation rates and NEG for saltatory predators for different prey sizes with a view to determine the effect of prey size and motility patterns on prey selectivity. The main conclusions are as follows:

1. Formulating predation rates models where both the predator and prey (of different sizes) are swimming in a turbulent flow is a very complicated exercise. The joy of it is that this feat has been achieved.

2. Despite the complexities involved in the formulation, the model developed in this Chapter produces reliable and encouraging results. This shows that the principal assumptions upon which it is built are plausible.

3. Saltatory and ambush larval fish predators are more likely to feed on those prey items that moves in a predictable patterns (straight lines).

4. The erratic swimming patterns (changing directions frequently) of prey is more efficient method of avoiding predators than swimming in straight lines.

5. For cruising predators confronted with prey with same sizes and speeds, motility pattern of the prey does not appear to make any significant difference.

6. For a given planktonic predator, there exist optimum prey size for which maximum NEG is attained.

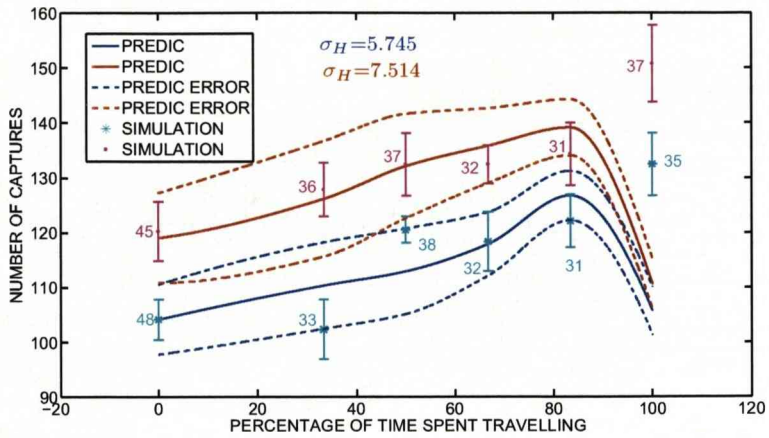

(a) Number of captures by two groups of predators feeding on two groups of prey with different swimming speeds $\sigma_H = 5.745, 7.514$

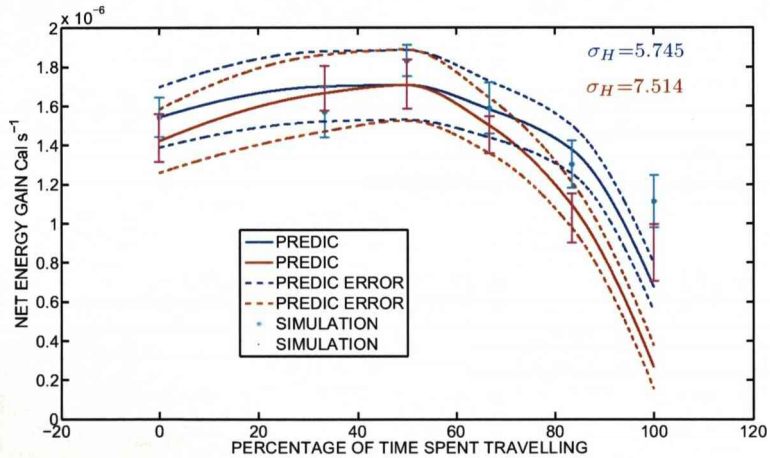

(b) NEG calculations corresponding to the number of captures shown on Figure 6.3(a)

Figure 6.3: Number of captures and NEG calculations for two groups of saltatory predators feeding on two groups of mobile prey with different speeds $\sigma_H = 5.745, 7.514$ and the same motility patterns. (a) is for the number of captures (b) is the NEG results corresponding to the number of captures shown in (a). The prediction results for the faster (larger) prey are represented with – and the standard deviations are represented with - -. For the slower (smaller) prey, the prediction results and the associated standard deviations are given with – and - - respectively. The simulation results are represented with error bars as follows: * for smaller prey and for larger prey. Other keys are the same as in Figure 6.1.

Chapter 7

Energetic advantages of pause-travel at low travel speeds

7.1 Introduction

Experimental observations have shown that larval fish at hatch move through the water by continuous swimming. About three days after hatch they adapt to more efficient motion in water using the pause-travel technique due to evolutionary pressure. Temperature is widely recognised as a factor affecting the age at which the transition occurs from continuous swimming of the newly hatched larvae to the pause-travel swimming pattern of the older larval stage (Hunter 1976). This means that the size of the larva and the viscosity of the flow regime are important parameters that must be taken into account in a model of larval fish energy expenditures.

In Chapter 5 it was shown that foraging using pause-travel swimming technique is robust for low travel speeds. The present Chapter examines the possible advantages of such behaviour over swimming at constant speed. Specifically, a new energy saving function (ratio of the energy required to cover a given distance using pause-travel to the energy require to cover the same distance by swimming continuously) that is valid over a wide range of Reynolds number will be derived analytically. The influence of temperature on the cost of swim will be investigated indirectly through its influence on viscosity. Consequently, the model that will be developed here will be dependent on body size and the water viscosity. By considering the ratio of the energy required to cover a given distance using saltatory strategy to the energy require to cover the same distance using continuous swimming, it is possible to determine theoretically the range of travel speeds over which pause-travel is more advantageous over swimming at constant speed.

7.2 Model formulation

Consider a fish larva moving at constant direction and depth. The larva must overcome resistance due to drag force which can be written (see Weihs (1980)) as

$$D_F = \frac{1}{2}\rho A_w C_D v_P^2, \tag{7.2.1}$$

where A_w is the frontal area, C_D is the drag coefficient and $v_P = v_P(t)$ is swimming speed. This force actually depend upon the Reynolds number regime. Weihs 1986 classify the Reynolds number base on body length (Re_L) into three regimes

- $1 \leq Re_L \leq 30$ is called the viscous region, where viscosity dominate the inertial forcing.
- The inertial regime is defined as the regime where $Re_L > 200$.
- In between the viscous and the inertial regime is refer to as the intermediate regime. In this region there is a gradual transition from viscous to inertial regime as Re_L increases.

In the inertial regime, C_D is approximately constant (see Stocker & Weihs (2001)). However, in the viscous and the intermediate regimes C_D depends upon the Reynolds number (see Fuiman & Batty (1997)). For a 5 mm larva swimming with speed up to 10 mm/s in the viscosity regime of $\nu = 1 \times 10^{-6}$ m^2 s^{-1} $Re_L \leq 50$ which places it into the intermediate Reynolds number regime. During the pausing phase, the combination of the low swimming speed and small size might mean that the larva is within the viscous hydrodynamic regime. It is therefore reasonable to think that its environment is composed of both the viscous and the intermediate regimes. Verhagen (2004) estimated the drag coefficient on a larval fish by representing the head as a sphere with diameter D and the reminder of the body by splitter plate of height D. He arrived at the following result which is valid for $0 < Re_D < 200$

$$C_D = \frac{4}{5} + 24\frac{\nu}{v_P D}, \tag{7.2.2}$$

where Re_D is the Reynolds number base on diameter. This result can be viewed as an estimate of passive drag. Experimental data have shown that the drag on a swimming body is greater than drag on a rigid body by a factor $\alpha_s > 1$. For example, experimental measurement of drag on pause-travel fish larvae by Wu et al. (2007) show that the drag coefficient is 0.242 during the travel phase and 0.06 during the pausing phase. Using equations (7.2.2) and (7.2.1) and the definition of $\rho = M/L^3, A_w = \pi L^2$ for a sphere we can write the drag force on a swimming larva as

$$F = M\left(\lambda_l v_P^2 + v_P \delta_t\right), \tag{7.2.3}$$

Larva size (mm)	Temperature (^{o}C)	U_{crit} m (s^{-1})
9	15	63
	20	78
13	15	73
	20	100
17	15	87
	20	116

Table 7.1: Summary of experimental data for three size classes of larval fish at two temperatures. The table shows the critical swimming speeds at some temperatures. The data are extracted from Table 1 of Wieser & Kaufmann (1998).

where $\lambda_l = \frac{2\pi\alpha_s}{5L}$ and $\delta_t = \frac{6\pi\nu\alpha_s}{L^2}$. This formula is a hybrid comprising of both the viscous and the inertial regimes. If v_P is small the viscous term will dominate. Similarly if v_P is large the inertial term dominate.

The equation of motion of a fish larvae (see equation (5.6.2)) is usually solved during the travel phase with the right hand side replaced by the maximum sustained thrust (see Stocker & Weihs (2001), Videler & Weihs (1982)). The maximum sustained thrust is a function of the critical swimming swimming speed (U_{crit}). It is reasonable to digress slightly and say a little bit about U_{crit}.

7.2.1 Critical swimming speed of fish larvae

Swimming performance is widely accepted as a main character determining survival in many species of fish larvae and other aquatic animals (see Plaut (2001)). It is also assumed that efficient swimming performance is closely related to larval ability to escape predators, find food or mate. The effects of different environmental conditions or pollutants on fish fitness or survival in an ecological system is usually evaluated by its critical (maximum sustained) swimming speed (U_{crit}). The critical swimming speed is measured in the laboratory. To measure this, a larval fish is introduced into a water in which its speed can be controlled by an investigator. The initial speed is then increased at prescribed interval until fatigue sets in and the animal fail to maintain its balance. The time and speed at which this happen are then used to calculate U_{crit} (see Guan et al. (2008), Green & Fisher (2004)). Measurement of these are available in literature. For example Wieser & Kaufmann (1998) reported U_{crit} values for three different size classes of fish larvae (9, 13 and 17 mm) at 15 and 20^o C. The results from Table 1 of that paper are summarised in Table 7.1. For mathematical simplicity, the maximum sustained thrust during the travel phase of saltatory behaviour is usually written in

terms of U_{crit}. In our formulation, the maximum sustained thrust can be written as

$$T_{\text{crit}} = M\left(\lambda_l U_{\text{crit}}^2 + U_{\text{crit}}\delta_t\right). \tag{7.2.4}$$

Using more realistic range of Reynolds number equation (5.6.2) can now be written in terms of U_{crit} as

$$M\frac{dv_P}{dt} + M\left(\lambda_l v_P^2 + \delta_t v_P\right) = T_{\text{crit}}. \tag{7.2.5}$$

7.2.2 Formulation of the energy saving function

In Chapter 5 energetic swimming cost during pause-travel was formulated. However, the formulation was base on Stoke's flow which is valid only when the Reynolds number is less than unity. A more realistic model can be formulated by including higher range of Reynolds number. The energy saving function can be described as the ratio of the energies require to cover a given distance using pause-travel (E_{sal}), to the energy require to cover the same distance by continuous swimming using the same average swimming speed (E_{cru}). More succinctly, the saving function can be defined as

$$E_{\text{ratio}} = \frac{E_{\text{sal}}}{E_{\text{cru}}}. \tag{7.2.6}$$

For pause-travel to be energetically more viable $E_{\text{ratio}} < 1$. If this turn out to be greater than one, then continuous swimming is more benefitting. The ratio is equal to one when the energy expenditure from both modes of swimming are the same. In order to formulate the energy saving function, the energy expenditures during the pause-travel and continuous swimming need to be defined.

Formulation of (E_{sal})

Suppose a larva is required to cover a distance d in time $\tau_c = t_1 + t_2$ by alternating a period of active swimming with powerless glide. In doing so, the distance l_1 is desired to be crossed within a time t_1 which will be assumed to be the travel phase. During the pause phase, the larva is required to cover a distance l_2 in time t_2. In fulfilling this requirement no energy is expended during the pause phase because no thrust is produced (see Stocker & Weihs (2001)). Thus energy is expended during the travel phase only. The net energy expenditure during during pause-travel can be defined as

$$E_{\text{sal}} = \frac{1}{\beta_c \tau_c}\int_0^{t_1} T_{\text{crit}} v_P dt. \tag{7.2.7}$$

Defining the energy in terms of T_{crit} will impose higher energy demand on a larva than defining it in terms of its travel speed. The reason for writing the thrust in terms of the maximum sustained thrust is to reflect the cost of acceleration as a larva moves out

of the low Reynolds number pause phase to the higher Reynolds number travel phase. Equation (7.2.7) can be written as

$$E_{\text{sal}} = \frac{T_{\text{crit}}'}{\beta_c \tau_c} \int_0^{t_1} v_P dt. \tag{7.2.8}$$

Note that the integral term in equation (7.2.9) is just the distance (l_1) covered during the travel phase. So E_{sal} becomes

$$E_{\text{sal}} = \frac{T_{\text{crit}}' l_1}{\beta_c \tau}. \tag{7.2.9}$$

Formulation of (E_{cru})

Suppose now the larva is allowed to take a different course of action to cross the same distance d with a certain constant speed $v_P^c = \frac{l_1+l_2}{t_1+t_2}$. The thrust ($T_c'$) applied can be defined by

$$T_c' = M\left(\lambda_l {v_P^c}^2 + v_P^c \delta_t\right), \tag{7.2.10}$$

we can then write the corresponding energy expenditure as

$$E_{\text{cru}}' = \frac{M}{\beta_c}\left(\left(\frac{l_1+l_2}{t_1+t_2}\right)^3 \lambda_l + \left(\frac{l_1+l_2}{t_1+t_2}\right)^2 \delta_t\right). \tag{7.2.11}$$

Therefore E_{ratio}' can be written as

$$E_{\text{ratio}}' = \frac{A l_1 (t_1+t_2)^2}{(l_1+l_2)^3 \lambda_l + (l_1+l_2)^2 (t_1+t_2)\, \delta_t}, \tag{7.2.12}$$

where $A = T_{\text{crit}}'/M$. To calculate E_{ratio}' numerically, one needs the expressions for t_1, t_2, l_1 and l_2 that appear in equation (7.2.12).

7.2.3 Determination of t_1, t_2, l_1 and l_2

To obtain explicit formulae for t_1, t_2, l_1 and l_2 in terms of the other parameters, we shall use equation (7.2.5) for the travel phase. During the pause phase the thrust applied is zero and the equation can be solved by setting the right hand side equal to zero. It will be assumed further that $v_P = v_1$ during travels and $v_P = v_2$ during the pause phase.

Determination of t_1 and l_1

More compactly, equation (7.2.5) which can be written as

$$\frac{dv_P}{dt} + \left(\lambda_l v_P^2 + \delta_t v_P\right) - A = 0. \tag{7.2.13}$$

This equation has the general form

$$\frac{dy(t)}{dt} = f_0(t) + f_1(t)y(t) + f_2(t)(y(t))^2. \tag{7.2.14}$$

Equations having this general form are called Ricatti equations. The time and distance t_1 and l_1 can then be obtained by solving this equation subject to the condition that at $t = 0, v_P = v_2$. There are many procedures for solving this type of equations. Perhaps the easiest in this case is to use the substitution $y(t) = \frac{du(t)}{dt}/(-u\,(t)\,f_2)$ (see **?**) which reduces the equation into second order linear

$$\frac{d^2}{dt^2}u\,(t) + \delta_t\,\frac{d}{dt}u\,(t) - \lambda_l\,Au\,(t) = 0. \tag{7.2.15}$$

The solution of equation (7.2.15) is

$$u\,(t) = C1\,e^{(-1/2\,\delta_t + p)t} + C2\,e^{(-1/2\,\delta_t - p)t}, \tag{7.2.16}$$

where $C1$ and $C2$ are arbitrary constants and $p = 1/2\,\sqrt{{\delta_t}^2 + 4\,\lambda_l\,A}$. The solution of equation (7.2.13) can now be written as

$$v_P = \frac{(-1/2\,\delta_t + p)\,e^{pt} + C3\,(-1/2\,\delta_t - p)\,e^{-pt}}{(e^{pt} + C3\,e^{-pt})\,\lambda_l}, \tag{7.2.17}$$

where $C3 = C2/C1$. Now at $t = 0, v_P = v_2$. This condition lead to

$$C3 = \frac{-\delta_t + 2\,p - 2\,v_2\,\lambda_l}{\delta_t + 2\,p + 2\,v_2\,\lambda_l}. \tag{7.2.18}$$

Substituting the expression for $C3$ into equation (7.2.17) the solution of equation (7.2.13) becomes

$$v_P = \frac{(p - 1/2\,\delta_t)\,e^{pt}\,(\delta_t + 2\,p + 2\,v_2\,\lambda_l) - (2\,p - \delta_t - 2\,v_2\,\lambda_l)\,e^{-pt}\,(1/2\,\delta_t + p)}{\lambda_l\,((\delta_t + 2\,p + 2\,v_2\,\lambda_l)\,e^{pt} + (-\delta_t + 2\,p - 2\,v_2\,\lambda_l)\,e^{-pt})} \tag{7.2.19}$$

We simplified equation (7.2.19) to get

$$v_P = \frac{\cosh\,(pt)}{b_1\,\sinh\,(pt) + a_1\,\cosh\,(pt)} + \frac{\sinh\,(pt)}{b_2\,\sinh\,(pt) + a_2\,\cosh\,(pt)}, \tag{7.2.20}$$

where $a_1 = 1/v_2, b_1 = \frac{(2\,v_2\,\lambda_l + \delta_t)}{2\,pv_2}, a_2 = \frac{2\,p}{(2\,A - \delta_t\,v_2)}, b_2 = \frac{(2\,v_2\,\lambda_l + \delta_t)}{(2\,A - \delta_t\,v_2)}$. Applying the condition that at $t = t_1, v_P = v_1$ in equation (7.2.20) we obtained the time required to cover the distance l_1 as

$$t_1 = 1/2\,\ln\left(\frac{(2\,v_2\,\lambda_l + \delta_t - 2\,p)\,v_1 + (\delta_t + 2\,p)\,v_2 - 2\,A}{(2\,v_2\,\lambda_l + \delta_t + 2\,p)\,v_1 + (\delta_t - 2\,p)\,v_2 - 2\,A}\right)p^{-1}. \tag{7.2.21}$$

If equation (7.2.20) is integrated with respect to time, the distance travelled l_1 can be obtained. Now (see Alan (2007))

$$\int \frac{\cosh\,(x)}{b\,\sinh\,(x) + a\,\cosh\,(x)}dx = \begin{cases} \frac{ax - b\,\ln\cosh\left(x + \tanh^{-1}\,(b/a)\right)}{a^2 - b^2}, & a > b, \\ \frac{-ax + b\,\ln\sinh\left(x + \tanh^{-1}\,(a/b)\right)}{b^2 - a^2}, & b > a \end{cases} \tag{7.2.22}$$

and

$$\int \frac{\sinh(x)}{b\sinh(x)+a\cosh(x)}dx = \begin{cases} \frac{a\ln\cosh\left(x+\tanh^{-1}(b/a)\right)bx}{a^2-b^2}, & a>b, \\ \frac{bx-a\ln\sinh\left(x+\tanh^{-1}(a/b)\right)}{b^2-a^2}, & b>a. \end{cases} \tag{7.2.23}$$

Comparing a_1 and b_1, a_2 and b_2 it can be seen that $a_1 > b_1$ and $a_2 > b_2$. Integrating equation (7.2.20) from $t = 0$ to $t = t_1$ by means of equations (7.2.22) and (7.2.23) the distance covered (l_1) during the travel phase is

$$\begin{aligned} l_1 &= \left(a_1 pt_1 - b_1 \ln\left(\cosh\left(pt_1 + \tanh^{-1}\left(\frac{b_1}{a_1}\right)\right)\right)\right) p^{-1}\left({a_1}^2 - {b_1}^2\right)^{-1} \\ &+ a_2 \ln\left(\cosh\left(pt_1 + \tanh^{-1}\left(\frac{b_2}{a_2}\right)\right)\right) b_2\, t_1 \left({a_2}^2 - {b_2}^2\right)^{-1} \\ &- 1/2\, b_1 \ln\left(1 - \frac{{b_1}^2}{{a_1}^2}\right) p^{-1}\left({a_1}^2 - {b_1}^2\right)^{-1}. \end{aligned} \tag{7.2.24}$$

Determination of t_2 and l_2

During the pausing, the thrust is zero and the drag coefficient is simply the passive drag. The equation of motion (7.2.5) becomes

$$\frac{dv_P}{dt} + \frac{1}{\alpha_s}\left(\lambda_l v_P^2 + \delta_t v_P\right) = 0. \tag{7.2.25}$$

This is the Bernoulli equation. It is assumed that at the beginning of the pause phase, $v_P = v_1$. The solution of the equation subject to this condition is then

$$v_P = \delta_t\, v_1 \left(-\lambda_l\, v_1 + e^{\frac{\delta_t\, t}{\alpha_s}} \lambda_l\, v_1 + e^{\frac{\delta_t\, t}{\alpha_s}} \delta_t\right)^{-1}. \tag{7.2.26}$$

At the end of the pausing, $t = t_2, v = v_2$. This conditions enable us find the analytic derivation of t_2 as,

$$t_2 = \ln\left(\frac{v_1\,(\delta_t + v_2\,\lambda_l)}{v_2\,(\lambda_l\, v_1 + \delta_t)}\right) \alpha_s {\delta_t}^{-1}. \tag{7.2.27}$$

The distance travelled (l_2) during the pausing phase can be obtained by integrating equation (7.2.26) with respect to time, that is

$$l_2 = \int_0^{t_2} \delta_t\, v_1 \left(-\lambda_l\, v_1 + e^{\frac{\delta_t\, t}{\alpha_s}} \lambda_l\, v_1 + e^{\frac{\delta_t\, t}{\alpha_s}} \delta_t\right)^{-1} dt,$$

which is simplified to give

$$l_2 = \alpha_s \left(\ln\left(\frac{\delta_t\, v_1}{v_2}\right) - \ln\left(\frac{v_1\,(\delta_t + v_2\,\lambda_l)}{v_2\,(\lambda_l\, v_1 + \delta_t)}\right) - \ln(\delta_t)\right) {\lambda_l}^{-1}. \tag{7.2.28}$$

Inserting the expressions for t_1, t_2, l_1 and l_2 into equation (7.2.12) E_{ratio} can be written in terms of speeds, larva size and viscosity.

It now make sense to look at the definition of E_{ratio} when $v_2 = v_1$. From equations (7.2.21), (7.2.27) and (7.2.28) we can see that $t_1 = t_2 = l_2 = 0$ whenever this happen. However, equation (7.2.24) implies that $l_1 = 0$ only when $v_2 = v_1 = 0$. To see this, consider $\left({a_1}^2 - {b_1}^2\right)^{-1} = \frac{4p^2v_2^2}{4p^2-(2v_2\lambda_l+\delta_t)^2} = 0$, together with $t_1 = 0$ implies $l_1 = 0$. However, if $v_2 = v_1 \neq 0$ then

$$l_1 = -b_1 \ln\left(1 - \frac{{b_1}^2}{{a_1}^2}\right) p^{-1}\left({a_1}^2 - {b_1}^2\right) < 0.$$

These conditions means that E_{ratio} is not defined whenever $v_2 = v_1$. This in turn means that the model cannot be applied to ambush (100% pausing) or cruising (100%, travel). However, E_{ratio} can be re-defined to cover these extremes. For ambush, there is no swimming and so $E_{\text{ratio}} = 0$. Now for cruising there is no acceleration from pausing to travel and so U_{crit} should be replaced with v_P^c in the equation of motion and t_2 and l_2 should be equated to zero because there is no pausing phase so that the two modes of swimming are identical. With these definitions E_{ratio} becomes

$$E_{\text{ratio}} = \begin{cases} 0, & v_2 = v_1 = 0, \\ 1, & v_2 = v_1 \neq 0, \\ \frac{Al_1(t_1+t_2)^2}{(l_1+l_2)^3\lambda_l+(l_1+l_2)^2(t_1+t_2)\delta_t}, & v_1 > v_2. \end{cases} \tag{7.2.29}$$

7.3 Results

As stated earlier the numerical value of E_{ratio} indicates the relative efficiency of pause-travel and continues swimming motions. If $E_{\text{ratio}} > 1$ continuous swimming is more efficient. Equation (7.2.29) will now be studied for various parameters involved. One contentious parameter in the equation is the ratio of swimming to pausing drag α_s. Weihs (1980) believed that this parameter cannot be greater than 2 and used $\alpha_s = 2$ in his study of larval anchovy. However Videler & Weihs (1982) believed that this parameter is greater than 2 and that the average value is around 3.3. Just recently, Wu et al. (2007) conducted an experiment on pause-travel koi larva where they determined the drag coefficient during the travel and pausing phases as 0.242 and 0.06 respectively. This put the value of $\alpha_s = 4.3$.

The critical swimming speed is a subject that is receiving well attention. Values of this parameter are readily available and so calculation of E_{ratio} can be done with good accuracy. This parameter is directly proportional to size of the animal as well as the temperature of the flow in question (see Guan et al. (2008), Wieser & Kaufmann (1998)).

The discussion in this Chapter mainly concern small fish larvae and so we are interested in obtaining values of U_{crit} for fish larvae smaller than those listed on Table 7.1. Assuming that the U_{crit} values listed on the Table are linearly related to larval size at a given temperature, we can estimate the critical swimming speeds of fish larva of

length 5 mm at 15 and 20 ^{o}C as 50 and 60 mm/s respectively. For reasons explained earlier it is essential that the travel speed is non-zero. It therefore make sense to set a lower bound for this speed. Newly hatched fish larvae are small in size, about 3.2 mm and swim with an average speed of 0.25 mm/s (see von Herbing & Boutilier (1996), Guan et al. (2008)). This value will be assumed to be the minimum value of the travel speed throughout. During the pausing phase, the larva will be assumed to have a swimming speed of 0.001 mm/s. Variations of E_{ratio} with travel speeds, α_s viscosity and the size of the larva will be discussed below. Figure 7.1 shows the variation in E_{ratio}

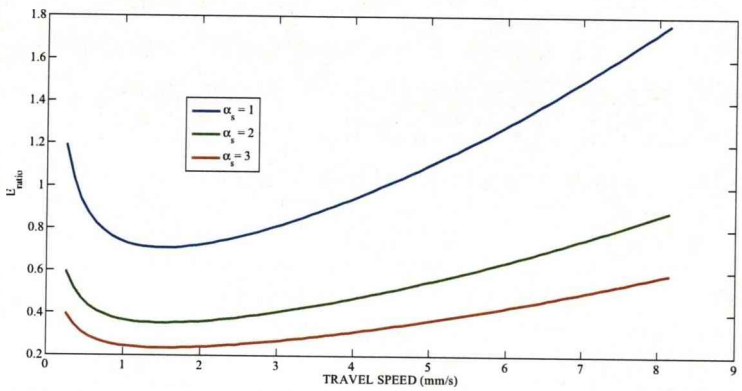

Figure 7.1: Variation of E_{ratio} as a function of travel speed for a fish larva with size $L = 5$ mm, assuming $U_{\text{crit}} = 60$ mm/s, $v_2 = 0.001$ mm/s, with the viscosity value $\nu = 1 \times 10^{-6}$ m^2 s^{-1} and drag ratios as shown. This corresponds to sea surface temperature of 20°C. These results are obtained by using equations (7.2.21), (7.2.24), (7.2.27) and (7.2.28) in equation (7.2.29). The Figure depicts the results for three different drag ratio: $\alpha_s = 1$ (– line), $\alpha_s = 2$ (– line), and $\alpha_s = 3$ (– line).

(energy required per unit distance in pause-travel motion to that required in steady speed swimming at the same average velocity) as a function of the travel speed. The calculations were made for three different drag ratio and viscosity regimes shown. In all the calculations the speed $v_2 = 0.001$ mm/s is assumed during the pausing phase. The viscosity value used is $\nu = 1 \times 10^{-6}$ m^2 s^{-1}. This corresponds to sea surface temperature of 20^{o}C. The critical swimming speed used is $U_{\text{crit}} = 60$ mm/s, this corresponds to a larva with size $L = 5$ mm. General observation of the Figure reveal that when the value of α_s is small, the gains are smaller and the region of travel speed for which this technique is useful becomes more limited. The result for drag ratio $\alpha_s = 1$ is represented with – line, $\alpha_s = 2$ is represented with – line and $\alpha_s = 3$ is shown with – line. It can be seen that even when $\alpha_s = 1$, there is a range of possible travel speeds (about 0.7 to 4 mm/s) that will save energy ($E_{\text{ratio}} < 1$). Outside this range, continuous swimming become more efficient strategy. As for the other values of α_s, pause-travel is most efficient over all range of swimming speeds considered here. However, the trend

show a monotonic decrease in energy saving as the travel speed increases. The conclusion that can be drawn from this is that, for any value of $\alpha_s > 1$ pause-travel is more efficient at certain range of low travel speeds. The range of these speed will increase with increasing α_s. The instinctive question arising here is which travel speed should a larva use, so as to minimize the energy expenditure during each cycle. Looking at the result it can be seen that this minimum exist. Finding the minimum value analytically from equation (7.2.29) will be extremely difficult because of the complex nature of the equation. Figure 7.2 shows the result of similar calculations of E_{ratio} at two different

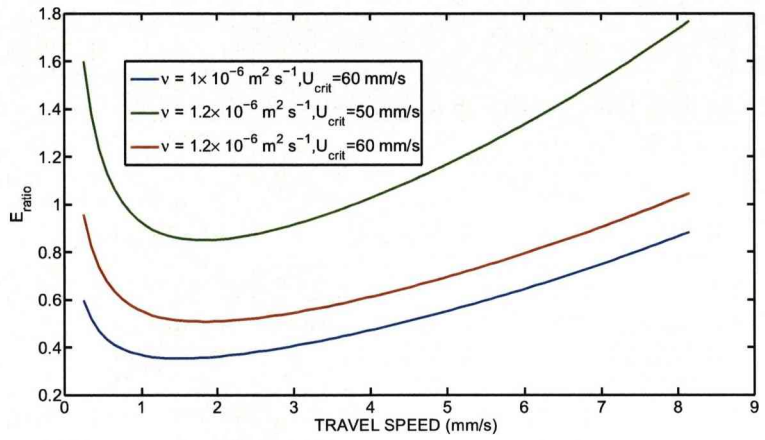

Figure 7.2: Variation of E_{ratio} as a function travel speed for a fish larva with size $L = 5$ mm, assuming a drag ratio $\alpha_s = 2$ at two different viscosity regimes shown. These results are obtained by using equations (7.2.21), (7.2.24), (7.2.27) and (7.2.28) in equation (7.2.29). The results for $U_{\text{crit}} = 60$ mm/s in the viscosity regime $\nu = 1 \times 10^{-6}\text{m}^2\ \text{s}^{-1}$ is the lower curve represented with – line. The middle and upper curves are the results for the same viscosity regimes $\nu = 1.2 \times 10^{-6}\text{m}^2\ \text{s}^{-1}$ and $U_{\text{crit}} = 60$ mm/s (– line), and $U_{\text{crit}} = 50$ mm/s (– line).

viscosity and critical swimming speed values for a 5 mm long fish larva. The results for the viscosity regime $\nu = 1 \times 10^{-6}\text{m}^2\ \text{s}^{-1}$, $U_{\text{crit}} = 60$ mm/s is the lower curve depicted with – curve. The result from this shows that within two decimal places, the minimum value of E_{ratio} is 0.35 with travel speeds in the range [1.45 1.55] mm/s. Also shown are the results for the viscosity regime $\nu = 1.2 \times 10^{-6}\text{m}^2\ \text{s}^{-1}$ at two different $U_{\text{crit}} = 50, 60$ mm/s. These are represented with – and – curves respectively. Comparing the upper (–) and the lower (–) curves we can see that viscosity does make a difference in optimal energy saving. Looking at the upper curve we can see to the left of the minimum point the low travel speeds ensure that viscous effects dominates. Hence continues swimming is more efficient in this region. Gradually, as the travel speed increases up to about 3.5 mm/s pause-travel becomes more effective. The result on the lower curve show that pause-travel is more effective over all range of speeds shown. To the left of the

minimum the low travel speed brings about relatively smaller gain in energy savings. General observations of the results show that pause-travel is more effective at intermediate travel speeds and that more energy is expended in a more viscous regime. We may argue that this conclusion does not hold because of the difference in critical swimming speeds in addition to viscosity. Critical swimming speed is widely recognized as a measure of fitness in both larva and adult fish and its value increases with larval size and decreases with viscosity (see Guan et al. (2008), Wieser & Kaufmann (1998)). Assuming that the U_{crit} is independent of viscosity, more calculations of E_{ratio} were done at $\nu = 1.2 \times 10^{-6}\text{m}^2\ \text{s}^{-1}$ and $U_{\text{crit}} = 60$ mm/s, the result is presented as the middle (–) curve. However, even under this unrealistic assumption the conclusion remain the same as can be seen by looking at the lower (–) and the middle (–) curves. This change in critical swimming speed reduces the difference between the upper and the lower curves by more than 50%, thus influencing the energy saving. For example, the maximum energy saving from the – curve is 15% (corresponding to the minimum value of 0.85) at $v_1 = 1.85$ mm/s. From the – curve the maximum saving is 49% at the same speed. This implies that changing U_{crit} has the effect of increasing the amount of energy savings. At the same temperature (viscosity) larger values of U_{crit} corresponds to increase in larval size. This might be interpreted to mean that larger larvae will be expected to be more efficient in pause-travel motion. In fact this supports the results of Hunter 1976, that at 18 °C three days old larval anchovy with size 4 mm are observed to spend only 20% of their time in pause-travel mode. When they do so, they do it with an average speed of 3.2 mm/s. As they grow older by two days, the are observed to spend 90% of their time in pause-travel mode. These findings support the 'safe harbour hypothesis' (see Muller & Videler (1996)) that fish larvae, instead of devising an optimal strategy for adapting to the viscous flow regime, increases their swimming speeds or sizes to escape into the inertia regime considered as a safe habour.

7.4 Conclusions

In this Chapter a new model of energy saving function was formulated. This function is basically the ratio of energies required to cover a given distance by pause-travel to the energy require to cover the same distance by continues swimming. The function is denoted by E_{ratio} and it serves as a quantitative criterion indicating which mode of motions is more efficient. For values of $E_{\text{ratio}} < 1$ pause-travel is more effective than continues swimming. The expression for E_{ratio} was formulated in terms of times spent in travel and pause modes and the distances covered during these periods. To calculate the numerical values of E_{ratio} explicit formulae for the times and distances are required. To obtain these formulae, modified equation of motion was used. The modified equation was obtained by using drag coefficient that is made up of both the

viscous and the inertial terms. This differs from other formulae in the literature which consist of either the inertial term or the viscous term only. Subsequently, the model was used to study the variation of E_{ratio} with respect to travel speed, ratio of travel to pausing drag coefficient (α_s) and changes in the viscosity of the flow regime. The main conclusions are as follows:

1. Investigations with three different values of α_s show that the higher the value of this parameter, the larger the energy that will be saved by swimming using the pause-travel. The exact value of the parameter appear to be contentious in literature and so more experimental investigations are required to resolve this.

2. The present study indicates that there exist a range of travel speeds over which continues swimming is less effective than pause-travel. The range of these speed will be affected by viscosity.

3. The range of travel speeds over which continues swimming is less effective decreases with viscosity.

4. The combination of size and enhanced swimming speed means that pause-travel is more effective in larger larvae than smaller ones.

In summary, we can say that it is the complex interactions of size, temperature, that will determine to a large extent the survival and growth of small fish larvae. The combination of small size and low temperature will imply a reduce activity which limits the ability of a larva to find food.

The investigations carried out in the previous Chapters were based on the fact that larval fish are visual predators with wedge-shaped perception fields. A large class of planktonic predators are not visual and can perceived their prey by hydromechanical means. The shape of their perception fields are generally unknown as they do not conform to any specific geometry. We would like to know what difference if any, does encounter rate results for these predators makes with those with spherical geometry. This is investigated in the next Chapter.

Chapter 8

Idealised Mathematical model for planktonic Encounter Rates Using Hydromechanical Cues.

8.1 Introduction

When two planktonic microorganisms are in close proximity, the geometry of the surrounding flow field is distorted and this gives rise to hydromechanical disturbances. Certain species of microorganisms can sense these disturbances and utilize them to detect the presence of another microorganisms in the vicinity. Copepods in particular are well adapted to processing these hydrodynamic signals and this enables them to forage for prey or seek out a potential mate. The extent of the disturbance may depend upon parameters such as the separation distance, approach speed, body size as well as the type of foraging strategy employed.

When considering the problem of prey perception or mate tracking by means hydromechanical signals in turbulent flow, the dynamic equations of the surrounding flow field around the two bodies are too complex to solve in detail. In lieu of the actual flow field, a simplified model that is valid at low Reynolds number could be adopted to estimate the signal strength in flows dominated by inertia. Even when swimming in a turbulent flow the dynamics of hydromechanical signalling is likely to be heavily influenced by the viscosity of the fluid, because over small distances (when two spheres get close together) viscosity is the determining characteristic of the background flow. So even though the global Reynolds number might be large, locally (that in the vicinity of the copepod's hydromechanical-receptors) it will be small enough to justify the application of a model based on the Stokes equations. For instance, the size of a sphere representing a predator used in the simulations is 3×10^{-3} m, the largest average swimming speed being 3.7×10^{-4} m s^{-1}. Thus, the Reynolds number (R_e) based on these scales is $R_e = \frac{(3\times10^{-3})\times(3.7\times10^{-4})}{1\times10^{-6}} \approx 1.12$.

The aim of this Chapter is to create a highly simplified model of the flow fields and

forces generated when two microorganisms move within close proximity. The simplest possible analytical model of this scenario is the case of two rigid spheres moving past each other in a viscous incompressible fluid. Using bispherical coordinates, no-slip and far-field boundary conditions, an exact solution of Stokes equations for the translational motion of two spherical bodies of arbitrary size and orientation with respect to their directions of motion will be derived. The various hydrodynamic forces exerted on each sphere will then be calculated.
From these calculations a model will be formulated which will attempt to predict hydrodynamic signal emanating from a small microorganism as it moves through a fluid. The strength and range of this signal (with allowances made for attenuation arising from the presence of the background turbulence which need to be taken into account over larger distances) will then be utilized to estimate the probability that the microorganism can be perceived by a potential predator or mate.

8.2 Encounter Rate Model Using Hydromechanical Cues as means of detection.

In this section, the framework for planktonic predator prey interactions modelled as two rigid spheres moving in a viscous fluid will be set up. These calculations will form the basis for investigations under small scale turbulence typically found in the habitat of planktonic copepods. Consider two planktonic microorganisms of arbitrary size and orientation with respect to the flow field. To characterise the surrounding flow field at a set distance far apart, the following underlying assumptions are made.

Assumptions

- The planktonic particles are spherical in shape. Planktonic particles are not spherical in reality, this assumption is necessary to formulate an analytical framework of the problem on which to base the inevitable heuristic and empirical assumptions required if the model is to incorporate small scale turbulence.
- The microorganisms are not self-propelled. Although a large class of planktonic microorganisms simply drift with flow as they posses no ability to swim, other classes such as copepods and fish larvae have swimming abilities that enable them to move around in the flow. This is not an unreasonable assumption because some copepod species exhibit the ambush behaviour, when they passively drift with flow. The model therefore be best suited to this class of microorganisms.
- The fluid dynamics of their immediate surroundings is governed by the equations of Stokes flow. The Stokes flow equations are only valid for low Reynolds num-

ber regime. Since the flow field immediately surrounding the copepods body is viscous, the Stokes flow approximation is reasonable in this case.

- The no slip boundary conditions are satisfied on the fluid-body interface.

8.2.1 Geometry of the two sphere problem.

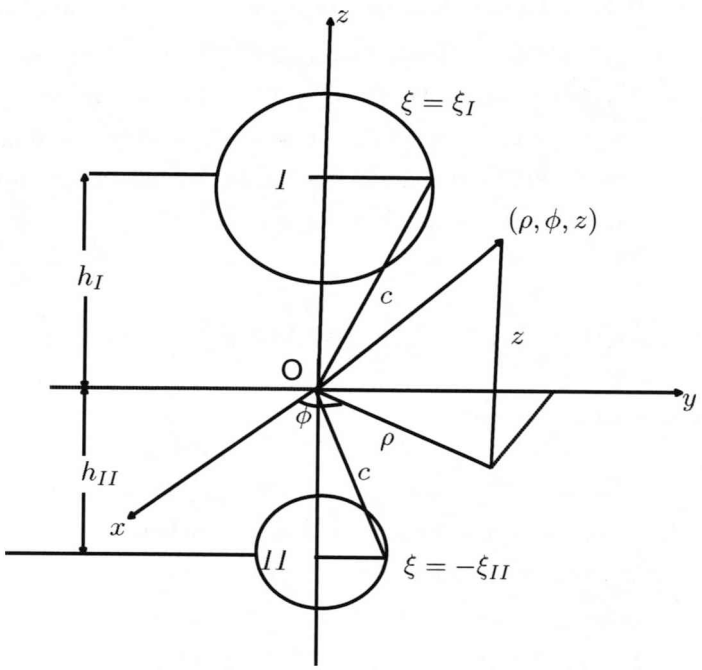

Figure 8.1: Schematic diagram of the geometry of two sphere problem where the top sphere is assumed to be the predator while the lower one the prey.

Suppose that two spheres that are initially positioned at a distant d apart, where d is the closest distance between their surfaces. Geometrically this can be described as in Figure 8.1. The inherent bispherical nature of the problem suggests that it can best be tackled using a bispherical co-ordinate system in which the governing equations and the boundary conditions can be accommodated relatively easily.

8.2.2 Bispherical Coordinates.

In three-dimensional space, a given point can be located by specifying the position vector $\mathbf{r}$ of the point. It is frequently desirable to describe the position of the point by certain coordinates that are more suitable to the problem under consideration. Orthogonal, curvilinear coordinates are the most convenient to employ.

Let

$$f_1 = f_1(x, y, z), \qquad f_2 = f_2(x, y, z), \qquad f_3 = f_3(x, y, z) \tag{8.2.1}$$

be three independent functions with non-vanishing Jacobian. Explicit solution of the system given by equations (8.2.1) can be written in terms of x, y, z as,

$$x = x(f_1, f_2, f_3), \qquad y = y(f_1, f_2, f_3), \qquad z = z(f_1, f_2, f_3). \tag{8.2.2}$$

The set of three numbers (f_1, f_2, f_3) is called the curvilinear coordinates of a point in space. The geometric interpretation of this coordinate system is that $f_i(x, y, z) =$ constant describes a three dimensional surface in space (see Morse & Feshbach (1953)). Examples of these coordinate systems include cartesian, cylindrical, spherical and bispherical coordinates. Given the cylindrical coordinates (ρ, z, ϕ), the parameters ξ and η are taken as the curvilinear coordinates in a meridian plane defined by the conformal transformation (see Morse & Feshbach (1953))

$$\xi + i\eta = \log \frac{\rho + i(z + c)}{\rho + i(z - c)}, \tag{8.2.3}$$

where $c > 0$ is a real number. If the real and imaginary parts of equation (8.2.3) are separated, the bispherical coordinates are given by (Happel & Brenner 1965, Majumdar 1969)

$$\rho = \frac{c \sin \eta}{\cosh \xi - \cos \eta}, \qquad z = \frac{c \sinh \xi}{\cosh \xi - \cos \eta}, \qquad \phi = \phi. \tag{8.2.4}$$

By restricting the range of the coordinates to

$$0 \leq \eta \leq \pi, \qquad -\infty < \xi < \infty, \qquad 0 \leq \phi \leq 2\pi, \tag{8.2.5}$$

the coordinate system is unique (Happel & Brenner 1965). Eliminating η from equation (8.2.4) one has,

$$\rho^2 + \left(z - \frac{c}{\tanh \xi}\right)^2 = \left(\frac{c}{\sinh \xi}\right)^2. \tag{8.2.6}$$

The surfaces $\xi =$ constant are non-intersecting co-axial (having a common axis) spheres with centres along the z-axis at $\rho = 0, \quad z = \frac{c}{\tanh \xi}$. The cases when $\xi = \pm\infty$ corresponds to two spheres each of radius zero with centres at $\rho = 0, z = \pm c$ respectively. These points are called the limiting points of the system. For $\xi > 0$, refers to the sphere lying above the plane $z = 0$ whilst $\xi < 0$ refers to the sphere lying below the z-axis with radius $|\frac{c}{\sinh \xi}|$. In this work, we shall assumed that the sphere above the plane $z = 0$ (see Figure 8.1) corresponds to $\xi = \xi_I$ (the larger sphere) with radius R_I and the sphere in the lower half plane corresponds to $\xi = -\xi_{II}$ (the smaller sphere) with radius R_{II} and that both ξ_I, ξ_{II} are positive. The restrictions imposed by equations (8.2.5) guarante the uniqueness of the bispherical coordinate system that fits a given values of ξ_I, ξ_{II}, c.

The centre to centre separation between the two spherical bodies will be denoted by $D = h_I + h_{II}$ where $h_{I,II}^2 = R_{I,II}^2 + c^2$ (see Figure 8.1). So to specify a particular bispherical coordinate system, three positive numbers c, ξ_I and ξ_{II} that will define the sphere sizes and their centre to centre distance apart are required. These numbers can be obtained through the relations

$$R_I = \frac{c}{\sinh \xi_I}, \tag{8.2.7}$$

$$R_{II} = \frac{c}{\sinh \xi_{II}}, \tag{8.2.8}$$

$$D = \sqrt{R_I^2 + c^2} + \sqrt{R_{II}^2 + c^2}. \tag{8.2.9}$$

After eliminating the square roots from (8.2.9) one obtains,

$$c = \frac{1}{2D}\left(\left(D^2 - (R_I^2 + R_{II}^2)\right)^2 - 4R_I^2 R_{II}^2 \right)^{\frac{1}{2}}, \quad D \geq R_I + R_{II}. \tag{8.2.10}$$

From equations (8.2.7) and (8.2.8) one has,

$$\xi_i = \frac{1}{R_i} \ln\left(c + \sqrt{c^2 + R_i^2} \right) \quad i = I, II. \tag{8.2.11}$$

In addition to bispherical coordinates the cylindrical coordinates (ρ, ϕ, z),

$$x = \rho \cos\phi, \quad y = \rho \sin\phi, \quad z = z \tag{8.2.12}$$

will also be needed. By using equations (8.2.4) and (8.2.12) the bispherical coordinates can also be written as

$$x = \frac{c \sin\eta \cos\phi}{\cosh\xi - \cos\eta}, \qquad y = \frac{c \sin\eta \sin\phi}{\cosh\xi - \cos\eta}, \qquad z = \frac{c \sinh\xi}{\cosh\xi - \cos\eta}. \tag{8.2.13}$$

8.3 Governing Equations.

All fluid flows satisfy the Navier- Stokes equations. On `small` planktonic scales, the dynamics of the ambient fluid is dominated by the viscous terms of the Navier Stokes equations so that the inertia terms can be neglected. Therefore the governing equation of the idealised model of two planktonic microorganisms assumed to be spherical in shape sinking at low Reynolds number in a steady unbounded quiescent fluid in absence of any body forces reduces to the steady Stokes creeping flow equations together with the continuity. These are given by (see Happel & Brenner (1965))

$$\mu \nabla^2 \mathbf{v} = \nabla P, \tag{8.3.1}$$

$$\nabla \cdot \mathbf{v} = 0. \tag{8.3.2}$$

Here $\mathbf{v}$ is the fluid velocity and P is pressure. The creeping flow equations (equations (8.3.1) and (8.3.2)) represent a substantial simplification of the over all flow field and

have a number of advantages: Analytical solutions of the equations are possible for some relatively complex geometries. Also because of their linearity, the superposition principle can be used to add solutions together.

8.4 Exact general solutions of the governing equations.

Solution of the Laplace equation in cylindrical coordinates have a wide applicability in fluid dynamics and other fields of applied mathematics. If the divergence of equation (8.3.1) is taken and equation (8.3.2) is invoked, one has (see Acheson (1990))

$$\nabla \cdot \nabla^2 \mathbf{v} = \nabla \cdot \nabla P \Leftrightarrow \nabla^2 P = 0, \tag{8.4.1}$$

so that the pressure field satisfies Laplace's equation and the velocity field, being a particular solution of (8.3.1), also satisfies Laplace's equation. Laplace's equation can be solved by separation of variables in many coordinate systems such as rectangular, spherical, cylindrical and bispherical coordinates. A natural link provided by equation (8.2.4) between bispherical and cylindrical coordinates allows one to derive the solution to Laplace's equation in terms of the former from the latter. In cylindrical coordinates (ρ, ϕ, z), equation (8.3.1) can be written as (see Goldman et al. (1966))

$$\frac{\partial}{\partial \rho}\left(\frac{P}{\mu}\right) = (\nabla^2 - \frac{1}{\rho^2})v_\rho - \frac{2}{\rho^2}\frac{\partial v_\phi}{\partial \phi}, \tag{8.4.2}$$

$$\frac{\partial}{\rho \partial \phi}\left(\frac{P}{\mu}\right) = (\nabla^2 - \frac{1}{\rho^2})v_\phi + \frac{2}{\rho^2}\frac{\partial v_\rho}{\partial \phi}, \tag{8.4.3}$$

$$\frac{\partial}{\partial z}\left(\frac{P}{\mu}\right) = \nabla^2 v_z, \tag{8.4.4}$$

where the Laplacian operator is defined as

$$\nabla^2 = \frac{\partial^2}{\partial \rho^2} + \frac{1}{\rho}\frac{\partial}{\partial \rho} + \frac{1}{\rho^2}\frac{\partial^2}{\partial \phi^2} + \frac{\partial^2}{\partial z^2}, \tag{8.4.5}$$

and v_ρ, v_ϕ and v_z are the (ρ, ϕ, z), components of the velocity in cylindrical coordinates. Hence the continuity equation (8.3.2) can be written as,

$$\frac{\partial v_\rho}{\partial \rho} + \frac{1}{\rho}v_\rho + \frac{1}{\rho}\frac{\partial v_\phi}{\partial \phi} + \frac{\partial v_z}{\partial z} = 0. \tag{8.4.6}$$

Laplace's equation is separable in cylindrical coordinate system and can be solved by the method of separation of variables. In cylindrical coordinates, the pressure and the components of the velocity field satisfy the following classical form (see Lin et al.

(1970)).

$$P = \frac{\mu}{c}\sum_{k=0}^{\infty}(\overline{W}^0_k \sin(k\phi) + \overline{W}^0_{-k}\cos(k\phi)), \tag{8.4.7}$$

$$v_\rho = \frac{1}{2}\sum_{k=0}^{\infty}\big[(\frac{\rho}{c}\overline{W}^0_k + W^1_k + W^{-1}_k)\sin(k\phi) + (\frac{\rho}{c}\overline{W}^0_{-k} + W^1_{-k} + W^{-1}_{-k})\cos(k\phi)\big], \tag{8.4.8}$$

$$v_z = \frac{1}{2}\sum_{k=0}^{\infty}\big[(\frac{z}{c}\overline{W}^0_k + 2W^0_k)\sin(k\phi) + (\frac{z}{c}\overline{W}^0_{-k} + 2W^0_{-k})\cos(k\phi)\big], \tag{8.4.9}$$

$$v_\phi = \frac{1}{2}\sum_{k=0}^{\infty}\big[(W^{-1}_k - W^1_k)\cos(k\phi) - (W^{-1}_{-k} - W^1_{-k})\sin(k\phi)\big], \tag{8.4.10}$$

where W^i_m expressed explicitly in terms of bispherical coordinates are given by

$$W^i_m = \Delta^{\frac{1}{2}}\sum_{n=|m|+i}^{\infty}\big[A^i_{mn}\cosh((\frac{2n+1}{2})\xi) + B^i_{mn}\sinh((\frac{2n+1}{2})\xi)\big]P^{|m|+i}_n(\cos(\eta)), \tag{8.4.11}$$

and

$$\overline{W}^0_m = \Delta^{\frac{1}{2}}\sum_{n=|m|+i}^{\infty}\big[\overline{A}^i_{mn}\cosh((\frac{2n+1}{2})\xi) + \overline{B}^i_{mn}\sinh((\frac{2n+1}{2})\xi)\big]P^{|m|+i}_n(\cos(\eta)). \tag{8.4.12}$$

$P^m_n(\mu)$ are associated Legendre polynomials of order n and rank m defined by,

$$P^m_n(\mu) = (1-\mu^2)^{m/2}\frac{d^m}{d\mu^m}P_n(\mu) \tag{8.4.13}$$

$$\Delta = (\cosh(\xi) - \cos(\eta)). \tag{8.4.14}$$

Here, i, m and n are integers. The next task is to determine the various constants $A^i_{mn}, \overline{A}^i_{mn}, B^i_{mn}, \overline{B}^i_{mn}$ so that equations (8.3.1) and (8.3.2) are satisfied.

8.4.1 Determination of coefficients from the continuity equation.

Differentiating equations (8.4.8) through (8.4.10) and substituting the appropriate terms into equation (8.4.6) we obtained the following,

$$\sum_{k=0}^{\infty}\Bigg(\Bigg[(\frac{3}{c} + \frac{\rho}{c}\frac{\partial}{\partial\rho} + \frac{z}{c}\frac{\partial}{\partial z})\overline{W}^0_k + (\frac{k+1}{\rho} + \frac{\partial}{\partial\rho})W^1_k + (\frac{\partial}{\partial\rho} + \frac{1-k}{\rho})W^{-1}_k + 2\frac{\partial W^0_k}{\partial z}\Bigg]\sin(k\phi) + \Bigg[(\frac{3}{c} + \frac{\rho}{c}\frac{\partial}{\partial\rho} + \frac{z}{c}\frac{\partial}{\partial z})\overline{W}^0_{-k} + (\frac{k+1}{\rho} + \frac{\partial}{\partial\rho})W^1_{-k} + (\frac{\partial}{\partial\rho} + \frac{1-k}{\rho})W^{-1}_{-k} + 2\frac{\partial W^0_{-k}}{\partial z}\Bigg]\cos(k\phi)\Bigg) = 0. \quad (8.4.15)$$

Equation (8.4.15) will be satisfied if each of the term involving the trigonometric functions is equated to zero. That is

$$(\frac{3}{c} + \frac{\rho}{c}\frac{\partial}{\partial\rho} + \frac{z}{c}\frac{\partial}{\partial z})\overline{W}^0_k + (\frac{k+1}{\rho} + \frac{\partial}{\partial\rho})W^1_k + (\frac{\partial}{\partial\rho} + \frac{1-k}{\rho})W^{-1}_k + 2\frac{\partial W^0_k}{\partial z} = 0, \quad (8.4.16)$$

and,

$$(\frac{3}{c} + \frac{\rho}{c}\frac{\partial}{\partial\rho} + \frac{z}{c}\frac{\partial}{\partial z})\overline{W}^0_{-k} + (\frac{k+1}{\rho} + \frac{\partial}{\partial\rho})W^1_{-k} + (\frac{\partial}{\partial\rho} + \frac{1-k}{\rho})W^{-1}_{-k} + 2\frac{\partial W^0_{-k}}{\partial z} = 0. \quad (8.4.17)$$

In order to simplify the problem, we derived the following relations which are used to transform the equation (8.4.16) into bispherical coordinates

$$\frac{\partial W^i_{\pm k}}{\partial z} = \Bigg(\frac{\partial W^i_{\pm k}}{\partial\eta}\frac{\partial\rho}{\partial\xi} - \frac{\partial W^i_{\pm k}}{\partial\xi}\frac{\partial\rho}{\partial\eta}\Bigg)\Big/\Bigg(\frac{\partial z}{\partial\eta}\frac{\partial\rho}{\partial\xi} - \frac{\partial z}{\partial\xi}\frac{\partial\rho}{\partial\eta}\Bigg), \quad (8.4.18)$$

$$\frac{\partial W^i_{\pm k}}{\partial\rho} = \Bigg(\frac{\partial W^i_{\pm k}}{\partial\xi}\frac{\partial z}{\partial\eta} - \frac{\partial W^i_{\pm k}}{\partial\eta}\frac{\partial z}{\partial\xi}\Bigg)\Big/\Bigg(\frac{\partial z}{\partial\eta}\frac{\partial\rho}{\partial\xi} - \frac{\partial z}{\partial\xi}\frac{\partial\rho}{\partial\eta}\Bigg), \quad (8.4.19)$$

or,

$$\frac{\partial}{\partial z} = \frac{1}{c}\Bigg(-\cosh(\xi)\cos(\eta)\frac{\partial}{\partial\xi} + \frac{\partial}{\partial\xi} - \sinh(\xi)\sin(\eta)\frac{\partial}{\partial\eta}\Bigg), \quad (8.4.20)$$

$$\frac{\partial}{\partial\rho} = \frac{1}{c}\Bigg(\cosh(\xi)\cos(\eta)\frac{\partial}{\partial\eta} - \frac{\partial}{\partial\eta} - \sinh(\xi)\sin(\eta)\frac{\partial}{\partial\xi}\Bigg). \quad (8.4.21)$$

Making use of these results in equations (8.4.16), (8.4.17) we obtained the continuity equation in bispherical coordinates as,

$$3\overline{W}^0_{\pm k} + [(k+1)W^1_{\pm k} + (1-k)W^{-1}_{\pm k}]\Delta\csc(\eta) - \cos(\eta)\sinh(\xi)\frac{\partial\overline{W}^0_{\pm k}}{\partial\xi} - \sin(\eta)\cosh(\xi)\frac{\partial\overline{W}^0_{\pm k}}{\partial\eta} + (\cosh(\xi)\cos(\eta) - 1)\Bigg(\frac{\partial W^1_{\pm k}}{\partial\eta} + \frac{\partial W^{-1}_{\pm k}}{\partial\eta} - 2\frac{\partial W^0_{\pm k}}{\partial\xi}\Bigg) - \sin(\eta)\sinh(\xi)\Bigg(\frac{\partial W^{-1}_{\pm k}}{\partial\xi} + \frac{\partial W^1_{\pm k}}{\partial\xi} + 2\frac{\partial W^0_{\pm k}}{\partial\eta}\Bigg) = 0. \quad (8.4.22)$$

Numerical values of constants satisfying the continuity equation in the form given by equations (8.4.16), (8.4.17) depends upon the value of k. Different values of k will give rise to different continuity equations. Determination of the coefficients requires that equations (8.4.16) and (8.4.17) are simplified to obtain a series of recurrence relations. It is cumbersome for one to go over the simplifications whenever a different value of k is desired. One important contribution made in this Chapter is the derivation of general recurrence relation valid for $k \geq -1$. To achieve this task, a number of recurrence relations involving the Legendre functions are used profusely.

Recurrence relations.

In order to simplify (8.4.22), some basic recurrence relations for Legendre functions from Andrews (1992) are used to derive others. Some of these relations are listed below with the dependence of $P_n^m(x)$ on x omitted. Where m occurs in the denominator, it is further assumed that $m \neq 0$. These relations are as follows:

$$xP_n^m = \frac{1}{2n+1}\Big([n-m+1]P_{n+1}^m + [n+m]P_{n-1}^m\Big). \tag{8.4.23}$$

$$\begin{aligned}(1-x^2)\frac{d}{dx}P_n^m &= \frac{1}{2n+1}\Big([n+1][n+m]P_{n-1}^m \\ &- n[n-m+1]P_{n+1}^m\Big).\end{aligned} \tag{8.4.24}$$

$$x(1-x^2)^{-\frac{1}{2}}P_n^m = \frac{1}{2m}\Big(P_n^{m+1} + [n(n+1) - m(m-1)]P_n^{m-1}\Big). \tag{8.4.25}$$

$$(1-x^2)^{\frac{1}{2}}\frac{d}{dx}P_n^m = \frac{1}{2}\Big(P_n^{m+1} - [n(n+1) - m(m-1)]P_n^{m-1}\Big). \tag{8.4.26}$$

$$\begin{aligned}x(1-x^2)^{\frac{1}{2}}\frac{d}{dx}P_n^m &= \frac{1}{2(2n+1)}\Big([n-m]P_{n+1}^{m+1} + [m+n+1]P_{n-1}^{m+1} \\ &- K\left([n-m+2]P_{n+1}^{m-1} + [n+m-1]P_{n-1}^{m-1}\right)\Big).\end{aligned} \tag{8.4.27}$$

$$(1-x^2)^{-\frac{1}{2}}P_n^m = \frac{1}{2m}\Big(P_{n-1}^{m+1} + [n+m-1][n+m]P_{n-1}^{m-1}\Big). \tag{8.4.28}$$

$$(1-x^2)^{\frac{1}{2}}P_n^m = \frac{1}{2n+1}\Big(P_{n+1}^{m+1} - P_{n-1}^{m+1}\Big). \tag{8.4.29}$$

$$\begin{aligned}(1-x^2)^{\frac{1}{2}}P_n^m &= \frac{1}{2n+1}\Big([n+m][n+m-1]P_{n-1}^{m-1} \\ &- [n-m+1][n-m+2]P_{n+1}^{m-1}\Big).\end{aligned} \tag{8.4.30}$$

Here, $K = n(n+1) - m(m-1)$.

8.4.2 Recurrence relations from the continuity equation

The constants $\overline{A}^0_{\pm kn}, \overline{B}^0_{\pm kn}, A^{-1}_{\pm kn}, B^{-1}_{\pm kn}, A^1_{\pm kn}, B^1_{\pm kn}, A^0_{\pm kn}$ and $B^0_{\pm kn}$
in the auxiliary solutions given in equations (8.4.11) and (8.4.12) are determine explicitly by using the continuity equation and the boundary conditions. To begin with the recurrence relation for general k (see equation (8.4.22)) shall be derived and later use some particular values to calculate the forces and to characterize the resulting flow field. To make the task easier, exponential rather than hyperbolic functions shall be used. Now define,

$$\Lambda_n(A,B,\xi) \;=\; A^i_{\pm kn} e^{(n+\frac{1}{2})\xi} + B^i_{\pm kn} e^{-(n+\frac{1}{2})\xi} \quad i = 0,-1,1. \tag{8.4.31}$$

Making use of the auxiliary function solutions given by equations (8.4.11) and (8.4.12) in equation (8.4.22) we have,

$$\begin{aligned}
0 \;=\; & \left(\frac{\sqrt{\Delta}\left(\Delta\, P_n^{k+1} k + \Delta\, P_n^{k+1}\right)}{\sin(\eta)} + (\cosh(\xi)\cos(\eta) - 1)\left(1/2\, \frac{P_n^{k+1}\sin(\eta)}{\sqrt{\Delta}} \right.\right. \\
+ \; & \left.\left. \sqrt{\Delta}\frac{d}{d(\cos(\eta))} P_n^{k+1} - 1/2\, \frac{(\sinh(\xi))^2 \sin(\eta)\, P_n^{k+1}}{\sqrt{\Delta}} \right) \frac{1}{2}\Lambda_n(A^1_{\pm k}, B^1_{\pm k}, \xi) \right. \\
- \; & \frac{1}{2}\sqrt{\Delta}\sinh(\xi)\sin(\eta)\, P_n^{k+1}\frac{(2n+1)}{2}\Lambda_n(A^1_{\pm k}, -B^1_{\pm k}, \xi) \\
+ \; & \left(3\sqrt{\Delta} P_n^k - 1/2\, \frac{\cos(\eta)(\sinh(\xi))^2 P_n^k(\eta)}{\sqrt{\Delta}} \right. \\
- \; & \left.\left. \sin(\eta)\cosh(\xi)\left(1/2\, \frac{P_n^k \sin(\eta)}{\sqrt{\Delta}} + \sqrt{\Delta}\frac{d}{d(\cos(\eta))} P_n^k \right) \right) \frac{1}{2}\Lambda_n(\overline{A}^0_{\pm k}, \overline{B}^0_{\pm k}, \xi) \right. \\
- \; & \frac{1}{2}\cos(\eta)\sinh(\xi)\sqrt{\Delta}\frac{(2n+1)}{2}\Lambda_n(\overline{A}^0_{\pm k}, -\overline{B}^0_{\pm 1n}, \xi) P_n^k \\
- \; & \left(\frac{(1-k)\Delta^{3/2} P_n^{k-1}}{\sin(\eta)} + (\cosh(\xi)\cos(\eta) - 1)\left(1/2\, \frac{P_n^{k-1}\sin(\eta)}{\sqrt{\Delta}} \right.\right. \\
+ \; & \left.\left. \sqrt{\Delta}\frac{d}{d(\cos(\eta))} P_n^{k-1} \right) - 1/2\, \frac{(\sinh(\xi))^2 \sin(\eta)\, P_n^{k-1}}{\sqrt{\Delta}} \right) \frac{1}{2}\Lambda_n(A^{-1}_{\pm k}, B^{-1}_{\pm k}, \xi) \\
- \; & \frac{1}{2}\sqrt{\Delta}\sinh(\xi)\sin(\eta)\, P_n^{k-1}\frac{(2n+1)}{2}\Lambda_n(A^{-1}_{\pm k}, -B^{-1}_{\pm k}, \xi) \\
+ \; & \left(-\frac{(\cosh(\xi)\cos(\eta) - 1) P_n^k \sinh(\xi)}{\sqrt{\Delta}} \right. \\
- \; & \left.\left. \sinh(\xi)\sin(\eta)\left(\frac{P_n^k \sin(\eta)}{\sqrt{\Delta}} + 2\sqrt{\Delta}\frac{d}{d(\cos(\eta))} P_n^k \right) \right) \frac{1}{2}\Lambda_n(A^0_{\pm k}, B^0_{\pm k}, \xi) \right. \\
+ \; & \left. \sqrt{\Delta}(\cosh(\xi)\cos(\eta) - 1) P_n^k \frac{(2n+1)}{2}\Lambda_n(A^0_k, -B^0_k, \xi). \right.
\end{aligned} \tag{8.4.32}$$

To simplify the task, equation (8.4.32) will now be separated into three equations factored according to P_n^k. This procedure allow easier algebraic simplifications. However,

the equations will be combined together at a later stage to get the overall results.

$$\begin{aligned}
\psi_1 &= (-1/4)\, P_n^k\,(-5+\cosh(\xi)\cos(\eta))\,\Lambda_n(\overline{A}^0_{\pm k},\overline{B}^0_{\pm k},\xi)\\
&- 1/2\, P_n^k\left(\sinh(\xi)\cos(\eta)\,\frac{(2n+1)}{2}\Lambda_n(\overline{A}^0_{\pm k},-\overline{B}^0_{\pm 1n},\xi)\right.\\
&+ 2\cosh(\xi)\cos(\eta)\,\frac{(2n+1)}{2}\Lambda_n(A^0_k,-B^0_k,\xi)+\cos(\eta)\,\Lambda_n(A^0_{\pm k},B^0_{\pm k},\xi)\sinh(\xi)\\
&- \left. 4\,\frac{(2n+1)}{2}\Lambda_n(A^0_k,-B^0_k,\xi)\right)-\sin(\eta)\cosh(\xi)\,\Lambda_n(\overline{A}^0_{\pm k},\overline{B}^0_{\pm k},\xi)\frac{d}{d(\cos(\eta))}P_n^k\\
&- \sinh(\xi)\sin(\eta)\left(\frac{d}{d(\cos(\eta))}P_n^k(\eta)\right)\Lambda_n(A^0_{\pm k},B^0_{\pm k},\xi). \qquad (8.4.33)
\end{aligned}$$

$$\begin{aligned}
\psi_2 &= ((\csc(\eta))/4)\,P_n^{k+1}\Big(\cosh(\xi)-2k\cos(\eta)+2\cosh(\xi)-2\,k\cos(\eta)\\
&+ \cosh(\xi)(\cos(\eta))^2\,)\,\Lambda_n(A^1_{\pm k},B^1_{\pm k},\xi)+(\csc(\eta))/4\,P_n^{k+1}\\
&\times \left(-2\sinh(\xi)+2\sinh(\xi)(\cos(\eta))^2\right)\frac{(2n+1)}{2}\Lambda_n(A^1_{\pm k},-B^1_{\pm k},\xi)\\
&+ \left(\frac{d}{d(\cos(\eta))}P_n^{k+1}\right)(\cosh(\xi)\cos(\eta)-1)\,\frac{1}{2}\Lambda_n(A^1_{\pm k},B^1_{\pm k},\xi). \qquad (8.4.34)
\end{aligned}$$

$$\begin{aligned}
\psi_0 &= ((\csc(\eta))/4\,P_n^{k-1})\Big(\cosh(\xi)+2\,k\cos(\eta)-2k\cosh(\xi)-2\cos(\eta)\\
&+ \cosh(\xi)(\cos(\eta))^2\,\Big)\Lambda_n(A^{-1}_{\pm k},B^{-1}_{\pm k},\xi)+(\csc(\eta))\,\frac{(2n+1)}{4}\,P_n^{k-1}\\
&\times \left(-2\sinh(\xi)+2\sinh(\xi)(\cos(\eta))^2\right)\frac{(2n+1)}{2}\Lambda_n(A^{-1}_{\pm k},-B^{-1}_{\pm k},\xi)\\
&+ \left(\frac{d}{d(\cos(\eta))}P_n^{k-1}(\cosh(\xi)\cos(\eta)-1)\right)\frac{1}{2}\Lambda_n(A^{-1}_{\pm k},B^{-1}_{\pm k},\xi). \qquad (8.4.35)
\end{aligned}$$

Relations between the constants

The recurrence relations (8.4.23)-(8.4.30) can now be used to simplify the above. The aim is to re-write the three equations (8.4.33)-(8.4.35) in a form containing $P_n^k(x)$ for a fixed k. Equation (8.4.35) reduces to,

$$\begin{aligned}
\psi_0 &= \left(-1/2\,\frac{\cosh(\xi)\,(k+n)\,(n+k-1)\,(n+k-2)\,P_{n-1}^{k-2}}{2\,n+1}\right.\\
&+ 1/2\,\frac{\cosh(\xi)\,(-n+k-1)\,P_{n+1}^k}{2\,n+1}+P_n^k\\
&+ 1/2\,\frac{\cosh(\xi)\,(k+n)\,(n-k+3)\,(n-k+2)\,P_{n+1}^{k-2}}{2\,n+1}\\
&+ \left. 1/2\,\frac{\cosh(\xi)\,(-1-k-3\,n)\,P_{n-1}^k}{2\,n+1}+P_n^k\right)\frac{1}{2}\Lambda_n(A^{-1}_{\pm k},B^{-1}_{\pm k},\xi)\\
&- \frac{\Lambda_n(A^{-1}_{\pm k},-B^{-1}_{\pm k},\xi)\,\sinh(\xi)\,(P_{n+1}^k-P_{n-1}^k)}{4}. \qquad (8.4.36)
\end{aligned}$$

$$
\begin{aligned}
\psi_0 &= -1/2\,\Lambda_n(A_{\pm k}^{-1}, B_{\pm k}^{-1}, \xi)\left(P_{n-1}^k + P_{n+1}^k\right)\cosh(\xi) \\
&- \frac{\Lambda_n(A_{\pm k}^{-1}, -B_{\pm k}^{-1}, \xi)\,\sinh(\xi)\left(P_{n+1}^k - P_{n-1}^k\right)}{2} \\
&+ \frac{1}{2}\Lambda_n(A_{\pm k}^{-1}, B_{\pm k}^{-1}, \xi)P_n^k. \qquad (8.4.37)
\end{aligned}
$$

Simplifying (8.4.33) gives

$$
\begin{aligned}
\psi_1 &= \left(\left(\frac{(n+1)\,(n+k)\cosh(\xi)}{2n+1} - \frac{(n+k)\cosh(\xi)}{4n+2}\right)\frac{1}{2}\Lambda_n(\overline{A}_{\pm k}^0, \overline{B}_{\pm k}^0, \xi)\right. \\
&- \left.\frac{(n+k)\sinh(\xi)\,\Lambda_n(\overline{A}_{\pm k}^0, -\overline{B}_{\pm k}^0, \xi)}{4}\right)P_{n-1}^k \\
&+ \left(\left(2\,\frac{(n+1)\,(n+k)\sinh(\xi)}{2n+1} - 2\,\frac{(n+k)\sinh(\xi)}{4n+2}\right)\frac{1}{2}\Lambda_n(A_{\pm k}^0, B_{\pm k}^0, \xi)\right. \\
&- \left.2\,\frac{(n+k)\cosh(\xi)\,\Lambda_n(A_{\pm k}^0, -B_{\pm k}^0, \xi)}{4}\right)P_{n-1}^k \\
&+ \left(\left(-\frac{n\,(n-k+1)\cosh(\xi)}{2n+1} - \frac{(n-k+1)\cosh(\xi)}{4n+2}\right)\frac{1}{2}\Lambda_n(\overline{A}_{\pm k}^0, \overline{B}_{\pm k}^0, \xi)\right. \\
&- \left.\frac{(n-k+1)\sinh(\xi)\,\Lambda_n(\overline{A}_{\pm k}^0, -\overline{B}_{\pm k}^0, \xi)}{4}\right)P_{n+1}^k \\
&+ \left(\left(-2\,\frac{n\,(n-k+1)\sinh(\xi)}{2n+1} - \frac{(n-k+1)\sinh(\xi)}{4n+2}\right)\frac{1}{2}\Lambda_n(A_{\pm k}^0, B_{\pm k}^0, \xi)\right. \\
&- \left.\frac{(n-k+1)\cosh(\xi)\,\Lambda_n(A_{\pm k}^0, -B_{\pm k}^0, \xi)}{2}\right)P_{n+1}^k \\
&+ 1/4\left(5\,\Lambda_n(\overline{A}_{\pm k}^0, \overline{B}_{\pm k}^0, \xi) + 2\,\frac{(2n+1)}{2}\Lambda_n(A_k^0, -B_k^0, \xi)\right)P_n^k. \qquad (8.4.38)
\end{aligned}
$$

Equation (8.4.34) becomes

$$
\begin{aligned}
\psi_2 &= 1/4\,\frac{\cosh(\xi)\,\Lambda_n(A_{\pm k}^1, B_{\pm k}^1, \xi)\,(n-k)\,P_{n-1}^{k+2}}{2n+1} \\
&+ 1/4\,\frac{\cosh(\xi)\,\Lambda_n(A_{\pm k}^1, B_{\pm k}^1, \xi)\,(-n+k)\,P_{n+1}^{k+2}}{2n+1} \\
&+ 1/4\,\frac{\cosh(\xi)\,\Lambda_n(A_{\pm k}^1, B_{\pm k}^1, \xi)\,(n+k+1)\,(n-k+1)\,(n-k)\,P_{n+1}^k}{2n+1} \\
&+ 1/4\,\frac{\cosh(\xi)\,\Lambda_n(A_{\pm k}^1, B_{\pm k}^1, \xi)\,(n+k)\,(3n+1-k)\,(n+k+1)\,P_{n-1}^k}{2n+1} \\
&- \frac{\Lambda_n(A_{\pm k}^1, -B_{\pm k}^1, \xi)\,\sinh(\xi)\,(n+k)\,(n+k+1)\,P_{n-1}^k}{4} \\
&+ \frac{\Lambda_n(A_{\pm k}^1, -B_{\pm k}^1, \xi)\,\sinh(\xi)\,(n-k)\,(n-k+1)\,P_{n+1}^k}{4} \\
&- \frac{1}{2}\Lambda_n(A_{\pm k}^1, B_{\pm k}^1, \xi)\,(n+k+1)\,(n-k)\,P_n^k. \qquad (8.4.39)
\end{aligned}
$$

$$
\begin{aligned}
\psi_2 &= \Big(1/2\,\cosh(\xi)\,\frac{1}{2}\Lambda_n(A^1_{\pm k},B^1_{\pm k},\xi)\,(n-k)\,(n-k+1)\\
&+ \frac{\Lambda_n(A^1_{\pm k},-B^1_{\pm k},\xi)\,\sinh(\xi)\,(n-k)\,(n-k+1)}{4}\Big)P^k_{n+1}\\
&+ \Big(1/4\,\cosh(\xi)\,\Lambda_n(A^1_{\pm k},B^1_{\pm k},\xi)\,(n+k)\,(n+k+1)\\
&- \frac{\Lambda_n(A^1_{\pm k},-B^1_{\pm k},\xi)\,\sinh(\xi)\,(n+k)\,(n+k+1)}{4}\Big)P^k_{n-1}\\
&- \frac{1}{2}\Lambda_n(A^1_{\pm k},B^1_{\pm k},\xi)\,(n+k+1)\,(n-k)\,P^k_n. \qquad (8.4.40)
\end{aligned}
$$

Adding equations (8.4.37), (8.4.38) and (8.4.40) multiplying through by P^k_n simplifying and integrating from -1 to 1 we obtained followings,

$$
\begin{aligned}
0 &= \Big[\left(-1/2\,n^2-1/2\,n+1/2\,k^2+1/2\,k\right)A^1_{\pm kn}\\
&+ \left(1/4\,k-1/2\,kn-1/4\,n+1/4\,k^2+1/4\,n^2\right)A^1_{\pm kn-1}\\
&+ \left(1/4\,k^2+3/4\,n+1/2+3/4\,k+1/4\,n^2+1/2\,kn\right)A^1_{\pm kn+1}\\
&+ (n+1/2)\,A^0_{\pm kn}-1/4\,A^{-1}_{\pm kn+1}+5/4\,\overline{A}^0_{\pm kn}+(-1/2\,n+1/2\,k)\,A^0_{\pm kn-1}\\
&+ (-1/2-1/2\,k-1/2\,n)\,A^0_{\pm kn+1}-1/4\,A^{-1}_{\pm kn-1}+1/2\,A^{-1}_{\pm kn}\\
&+ (1/4\,n+1/4\,k+1/4)\,\overline{A}^0_{\pm kn+1}+(-1/2\,n+1/2\,k)\,\overline{A}^0_{\pm kn-1}\Big]e^{1/2\,\xi\,(2\,n+1)}, \qquad (8.4.41)\\
0 &= \Big[(-1/2\,n+1/2\,k)\,\overline{B}^0_{\pm kn-1}+(1/4+1/4\,n+1/4\,k)\,\overline{B}^0_{\pm kn+1}\\
&+ (1/2\,n-1/2\,k)\,B^0_{\pm kn-1}+(1/2+1/2\,n+1/2\,k)\,B^0_{\pm kn+1}+(-n-1/2)\,B^0_{\pm kn}\\
&+ \left(1/2+3/4\,n+3/4\,k+1/4\,k^2+1/4\,n^2+1/2\,kn\right)B^1_{n+1}\\
&+ \left(1/4\,n^2-1/4\,n-1/2\,kn+1/4\,k+1/4\,k^2\right)B^1_{\pm kn-1}-1/4\,B^{-1}_{\pm kn+1}\\
&+ 1/2\,B^{-1}_{\pm kn}-1/4\,B^{-1}_{\pm kn-1}+5/4\,\overline{B}^0_{\pm kn}\\
&+ \left(-1/2\,n^2+1/2\,k+1/2\,k^2-1/2\,n\right)B^1_{\pm kn}\Big]e^{-1/2\,\xi\,(2\,n+1)}. \qquad (8.4.42)
\end{aligned}
$$

Equating the coefficients of the exponential functions in equation (8.4.42) to zero, we obtained the following two sets of equations involving the various constants

$$\begin{aligned}
0 &= 5\,\overline{A}^{0}_{\pm kn} + 2\,(k-n)\,\overline{A}^{0}_{\pm kn-1} + (n+1+k)\,\overline{A}^{0}_{\pm kn+1} + 2\,A^{-1}_{\pm kn} \\
&- A^{-1}_{\pm kn+1} - A^{-1}_{\pm kn-1} + 2\,(n+1+k)\,(-n+k)\,A^{1}_{\pm kn} \\
&+ (n+2+k)\,(n+1+k)\,A^{1}_{\pm kn+1} + 2\,(1+2\,n)\,A^{0}_{\pm kn} + 2\,(k-n)\,A^{0}_{\pm kn-1} \\
&- 2\,(n+1+k)\,A^{0}_{\pm kn+1} + (k-n+1)\,(-n+k)\,A^{1}_{\pm kn-1}, \qquad (8.4.43)
\end{aligned}$$

$$\begin{aligned}
0 &= 5\,\overline{B}^{0}_{\pm kn} + 2\,(k-n)\,\overline{B}^{0}_{\pm kn-1} + (n+1+k)\,\overline{B}^{0}_{\pm kn+1} + 2\,B^{-1}_{\pm kn} - B^{-1}_{\pm kn+1} \\
&- B^{-1}_{\pm kn-1} + 2\,(n+1+k)\,(-n+k)\,B^{1}_{\pm kn} + (k-n+1)\,(-n+k)\,B^{1}_{\pm kn-1} \\
&+ (n+2+k)\,(n+1+k)\,B^{1}_{\pm kn+1} - 2\,(2\,n+1)\,B^{0}_{\pm kn} + 2\,(n-k)\,B^{0}_{\pm kn-1} \\
&+ 2\,(n+1+k)\,B^{0}_{\pm kn+1}. \qquad (8.4.44)
\end{aligned}$$

Equations (8.4.43) and (8.4.44) are the general recurrence relations involving the constants that most be satisfied to ensure (8.3.2) holds. However, by themselves they are insufficient to determine the actual values of the constant $A's$ and $B's$. In order achieve that we must examine the additional constraints that arise from the no slip boundary conditions acting on the surfaces of the spheres.

8.5 Boundary Conditions

For the problem consider here (translational motion of two spheres in an unbounded quiescent fluid), it is necessary to fragment the problem into a number of cases viz: the $k = 1$ and $k = 0$ modes. The $k = 1$ mode corresponds to an arbitrary translational motion along the x and y plane whilst $k = 0$ mode is for translation motion along the line of centre (z axis). Thus, in this formulation, the required solution takes the form

$$P = \frac{\mu}{c}\sum_{k=0}^{1}(\overline{W}^{0}_{k}\sin(k\phi) + \overline{W}^{0}_{-k}\cos(k\phi)), \qquad (8.5.1)$$

$$\begin{aligned}
v_\rho &= \frac{1}{2}\sum_{k=0}^{1}\left[(\frac{\rho}{c}\overline{W}^{0}_{k} + W^{1}_{k} + W^{-1}_{k})\sin(k\phi)\right. \\
&+ \left.(\frac{\rho}{c}\overline{W}^{0}_{-k} + W^{1}_{-k} + W^{-1}_{-k})\cos(k\phi)\right], \qquad (8.5.2)
\end{aligned}$$

$$\begin{aligned}
v_z &= \frac{1}{2}\sum_{k=0}^{1}\left[(\frac{z}{c}\overline{W}^{0}_{k} + 2W^{0}_{k})\sin(k\phi)\right. \\
&+ \left.(\frac{z}{c}\overline{W}^{0}_{-k} + 2W^{0}_{-k})\cos(k\phi)\right], \qquad (8.5.3)
\end{aligned}$$

$$\begin{aligned}
v_\phi &= \frac{1}{2}\sum_{k=0}^{1}\left[(W^{-1}_{k} - W^{1}_{k})\cos(k\phi)\right. \\
&- \left.(W^{-1}_{-k} - W^{1}_{-k})\sin(k\phi)\right]. \qquad (8.5.4)
\end{aligned}$$

It is desired to find the coefficients such that equations (8.5.2) - (8.5.4) satisfy both the Laplace equation (which means they must satisfy (8.4.43) and (8.4.44) above) and the no slip conditions on the surface of the spheres. In addition the velocity field should tend to zero as we moves far away from the spheres.

8.6 Recurrence Relations Arising From the Boundary Conditions

Consider the $k = 1$ first.

8.6.1 Recurrence Relations for the k=1 mode

In cylindrical coordinates, the velocity field is given by (see Tritton (1988))

$$\mathbf{v} = i_\rho v_\rho + i_\phi v_\phi + i_z v_z. \tag{8.6.1}$$

Here i_ρ, i_ϕ and i_z are units vectors in the ρ, ϕ and z directions respectively. A particular solution satisfying the boundary condition can be written in terms of the x, y and z components of the velocity fields as,

$$\begin{aligned} v_\rho &= U_x^N \cos(\phi) + U_y^N \sin(\phi), && (8.6.2)\\ v_\phi &= -U_x^N \sin(\phi) + U_y^N \cos(\phi), && (8.6.3)\\ v_z &= 0, && (8.6.4) \end{aligned}$$

where, $U^N = (U_x^N, U_y^N, U_z^N)$ are the translational velocities of sphere $N = I, II$ in the x, y and z-directions respectively. The linearity of these equations implies that the recurrence relations involving the x and y velocity components can be treated separately. In view of this, the formal treatment of translational motion along the y direction is presented below. The translational motion along the x direction can be treated in an entirely analogous fashion. For a sphere translating with only y component of the velocity, the no slip condition on its surface implies that

$$\begin{aligned} U_y^N &= \frac{1}{2}\left(\frac{\rho}{c}\overline{W}_1^0 + W_1^1 + W_1^{-1}\right), && (8.6.5)\\ U_y^N &= \frac{1}{2}\left(W_1^{-1} - W_1^1\right), && (8.6.6)\\ 0 &= \frac{1}{2}\left(\frac{z}{c}\overline{W}_1^0 + 2\,W_1^0\right). && (8.6.7) \end{aligned}$$

Note that equations (8.6.5) to (8.6.7) gives 6 sets of equations when evaluated on both spheres. Determination of a recurrence relation for the $k = 1$ mode from the boundary conditions can be done in a number of ways. One of these is to obtain explicit formulas for each of the constants in equations (8.6.5) to (8.6.7) in terms of A_{1n}^0 and B_{1n}^0 and

substitute the resulting expression into equations (8.4.43) and (8.4.44) to get two sets of recurrence relation involving A_1^0 and B_1^0 only. This procedure will be adopted here. To this end, the main equations ((8.6.5) to (8.6.7)) from the boundary conditions will be simplified. From equation (8.6.7) we have,

$$\overline{W}_1^0 = \frac{-2c}{z} W_1^0. \tag{8.6.8}$$

Similarly from equation (8.6.6) we have,

$$W_1^{-1} = 2\,U_y^N + W_1^1. \tag{8.6.9}$$

Making use of equations (8.6.8) and (8.6.9) in (8.6.5) yields,

$$W_1^1 = \frac{\rho}{z} W_1^0. \tag{8.6.10}$$

Using equations (8.6.10) in (8.6.9) the following relation is obtained

$$W_1^{-1} = 2\,U_y^N + \frac{\rho}{z} W_1^0. \tag{8.6.11}$$

Equation (8.6.8) is equivalent to

$$\Delta^{\frac{1}{2}} \sum_{n=1}^{\infty} \Lambda_n(\overline{A}_1^0, \overline{B}_1^0, \xi) P_n^1(\cos(\eta)) = -\frac{2\Delta^{\frac{3}{2}}}{\sinh(\xi)} \sum_{n=0}^{\infty} \Lambda_n(A_1^0, B_1^0, \xi) P_n^0(\cos(\eta)) \tag{8.6.12}$$

.

With the help of equation 8.4.23, (8.6.12) can be written as,

$$\begin{aligned} \sum_{n=1}^{\infty} \Lambda_n(\overline{A}_1^0, \overline{B}_1^0, \xi) P_n^1(\cos(\eta)) &= -\frac{2}{\sinh(\xi)} \Bigg[\cosh(\xi) \sum_{n=1}^{\infty} \Lambda_n(A_1^0, B_1^0, \xi) P_n^1(\cos(\eta)) \\ &- \frac{n P_{n+1}^1(\cos(\eta))}{2n+1} - (n+1) P_{n-1}^1(\cos(\eta)) \Bigg]. \end{aligned} \tag{8.6.13}$$

Simplifying equation (8.6.13) in terms of Legendre functions we obtained an expression for coefficients of $\overline{W}_1^0$ in terms of coefficients of W_1^0 as,

$$\begin{aligned} \Lambda_n(\overline{A}_1^0, \overline{B}_1^0, \xi) &= \frac{2}{\sinh(\xi)} \Bigg[-\cosh(\xi)\, \Lambda_n(A_1^0, B_1^0, \xi) \\ &+ \frac{(n-1)}{2n-1} \Lambda_{n-1}(A_1^0, B_1^0, \xi) + \frac{(n+2)}{2n+3} \Lambda_{n+1}(A_1^0, B_1^0, \xi) \Bigg] \quad n \geq 1. \end{aligned} \tag{8.6.14}$$

Similarly, equation (8.6.11) can be written as,

$$\Delta^{\frac{1}{2}} \sum_{n=0}^{\infty} \Lambda_n(A_1^{-1}, B_1^{-1}, \xi) P_n^0(\cos(\eta)) = 2\,U_y^N + \frac{\sin(\eta)\,\Delta^{\frac{1}{2}}}{\sinh(\xi)} \sum_{n=0}^{\infty} \Lambda_n(A_1^0, B_1^0, \xi) P_n^0(\cos(\eta)). \tag{8.6.15}$$

Using recurrence relation and the identity (see Goldman et al. (1966))

$$(\cosh(\xi) - \cos(\eta))^{-\frac{1}{2}} = \sqrt{2} \sum_{n=0}^{\infty} \kappa_n P_n^0(\cos(\eta)),$$

where

$$\kappa_n = \sqrt{2}e^{-(n+\frac{1}{2})|\xi|},$$

and simplifying in terms of Legendre functions an expression for coefficients of W_1^{-1} in terms of coefficients of W_1^0 are obtained

$$\begin{aligned}\Lambda_n(A_1^{-1}, B_1^{-1}, \xi) &= 2U_y^N + \frac{1}{\sinh(\xi)}\left[\frac{(n+1)(n+2)}{2n+3}\Lambda_{n+1}(A_1^0, B_1^0, \xi)\right. \\ &- \left.\frac{(n-1)n}{2n-1}\Lambda_{n-1}(A_1^0, B_1^0, \xi)\right] \quad n \geq 0. \end{aligned} \tag{8.6.16}$$

In an entirely analogous fashion, it can be shown that the expression for coefficients of W_1^1 in terms of coefficients of W_1^0 is

$$\Lambda_n(A_1^1, B_1^1, \xi) = \frac{1}{\sinh(\xi)}\left[\frac{\Lambda_{n-1}(A_1^0, B_1^0, \xi)}{2n-1} - \frac{\Lambda_{n+1}(A_1^0, B_1^0, \xi)}{2n+1}\right] \quad n \geq 2. \tag{8.6.17}$$

Equations (8.6.14), (8.6.16) and (8.6.17) are the three key relations for calculating the numerical values of the coefficients.

8.6.2 Numerical Calculations of the Constants

The problem now is the determination of the sets of coefficients $\{A_{1n}^0\}, \{A_{1n}^{-1}\}, \{A_{1n}^1\}$, $\{\overline{A}_{1n}^0\}, \{B_{1n}^0\}, \{B_{1n}^{-1}\}, \{B_{1n}^1\}$, and $\{\overline{B}_{1n}^0\}$ such that the boundary conditions on the spheres and at infinity together with the continuity equations are satisfied. Since the functions W_1^0,W_1^{-1},W_1^1 and $\overline{W}_1^0$ are non-singular for $-1 \leq \mu \leq 1$, then the boundary conditions far away from the spheres are satisfied. For $\xi = \xi_I$ and $\xi = -\xi_{II}$, equations (8.6.5) - (8.6.7) are evaluated on both spheres to give six equations. These equations were combined with two equations ((8.4.43) and (8.4.44)) from continuity, to get a total of eight linear equations that can be solved numerically. Calculations of the coefficients were carried out using `FORTRAN` programming language. To achieve that, the infinite series solution given by (8.4.11) and (8.4.12) were first truncated and retain only the leading N terms. For each N, algebraic system of equations in the unknowns A_{1n}^0, A_{1n}^1, A_{1n}^{-1}, $\overline{A}_{1n}^0$, B_{1n}^0, B_{1n}^1, B_{1n}^{-1}, and $\overline{B}_{1n}^0$ $n = 0, 1, 2...N$ were solved. In order to achieve good accuracy when the two spheres are in close proximity, a greater number of terms has to be retained in the series. This number depends on the machine precision. The largest value of N used is 125 equivalent to a 1000×1000 array.

An alternative procedure for obtaining the numerical values for the constants involved derivation of explicit relations for each of the six sets of coefficients $\{A_{1n}^{-1}\}$,$\{A_{1n}^1\}$,$\{\overline{A}_{1n}^0\}$, $\{B_{1n}^{-1}\}$, $\{B_{1n}^1\}$ and $\{\overline{B}_{1n}^0\}$ in terms of A_{1n}^0 and B_{1n}^0. Substituting these relations into (8.4.43) and (8.4.44) yields, system of equations of the form $\mathbf{MX} = \mathbf{B}$ involving A_{1n}^0 and B_{1n}^0 only were obtained. In view of the unwieldy character of the equations, they

are omitted from this write up. Here $\mathbf{X}$ is the matrix of the unknowns (A^0_{1n} and B^0_{1n}), $\mathbf{B}$ represent the right hand side of the system of equations and $\mathbf{M}$ is the matrix of coefficients whose entries are described by equation (8.6.18). Matlab code were written to carry out the numerical calculations using this method. To do that, the coefficients A^0_{-1}, B^0_{-1} were set to zero and the resulting matrix of coefficients conform to the following general pattern.

$$\mathbf{M} = \left(\begin{array}{ccccc|ccccc} \alpha_n & \alpha_{n+1} & 0 & 0 & \dots & \beta_n & \beta_{n+1} & 0 & 0 & \dots \\ \alpha_{n-1} & \alpha_n & \alpha_{n+1} & 0 & \ddots & \beta_{n-1} & \beta_n & \beta_{n+1} & 0 & \ddots \\ 0 & \alpha_{n-1} & \alpha_n & \alpha_{n+1} & \ddots & 0 & \beta_{n-1} & \beta_n & \beta_{n+1} & \ddots \\ 0 & 0 & \alpha_{n-1} & \alpha_n & \ddots & 0 & 0 & \beta_{n-1} & \beta_n & \ddots \\ \vdots & \ddots & \ddots & \ddots & \ddots & \vdots & \ddots & \ddots & \ddots & \ddots \\ \hline \alpha^*_n & \alpha^*_{n+1} & 0 & 0 & \dots & \beta^*_n & \beta^*_{n+1} & 0 & 0 & \dots \\ \alpha^*_{n-1} & \alpha^*_n & \alpha^*_{n+1} & 0 & \ddots & \beta^*_{n-1} & \beta^*_n & \beta^*_{n+1} & 0 & \ddots \\ 0 & \alpha^*_{n-1} & \alpha^*_n & \alpha^*_{n+1} & \ddots & 0 & \beta^*_{n-1} & \beta^*_n & \beta^*_{n+1} & \ddots \\ 0 & 0 & \alpha^*_{n-1} & \alpha^*_n & \ddots & 0 & 0 & \beta^*_{n-1} & \beta^*_n & \ddots \\ \vdots & \ddots & \ddots & \ddots & \ddots & \vdots & \ddots & \ddots & \ddots & \ddots \end{array}\right) \tag{8.6.18}$$

where the α_i and α^*_i are coefficients of A^0_{1n} while β_i and β^*_i are the corresponding coefficients of B^0_{1n}. The procedure runs very fast on windows and the largest system solved being 140×140 size. In other words a 140 by 140 system of equations is not as computationally expensive as it seems because $\mathbf{M}$ had a sparse tridiagonal structure to make the computation easier (most of the elements in the matrix $\mathbf{M}$ are zero).

It is ostensibly difficult also to say anything about the convergence of the coefficients A^0_{1n} and $B^0_{1n}, n = 0, 1, 2, 3 \dots N$ by inspecting the equations. Perhaps the only method of establishing convergence is by numerical means.

As suggested by Davis (1969) a very useful check for the convergence is that

$$sum_1 = \sum \left[2\,n(n+1)A^0_{1n} + (2\,n+1)A^{-1}_{1n}\right], \tag{8.6.19}$$

$$sum_2 = \sum \left[2\,n(n+1)B^0_{1n} - (2\,n+1)B^{-1}_{1n}\right], \tag{8.6.20}$$

should vanish for N sufficiently large. Figure 8.2 shows typical calculations of sum_1 and sum_2 for sphere sizes R_I, and $R_{II} = 0.5 \times 10^{-3}, \times 10^{-4}$m respectively against the number of equations. In this case, the larger sphere is assumed to be translating along the y-direction only at a speed $U^I_y = 3 \times 10^{-3}$ m s^{-1}. The smaller sphere is assumed to be passively drifting. The separations was kept at $2R_{II}$. From these calculations it can be discerned that not only do the coefficients converge, but but they do so relatively quickly. The magnitude of the sums also depend upon the sphere size ratios and their separation. Next, the equations for the case $k = 0$ mode must be examined which give the corresponding boundary conditions along the z direction.

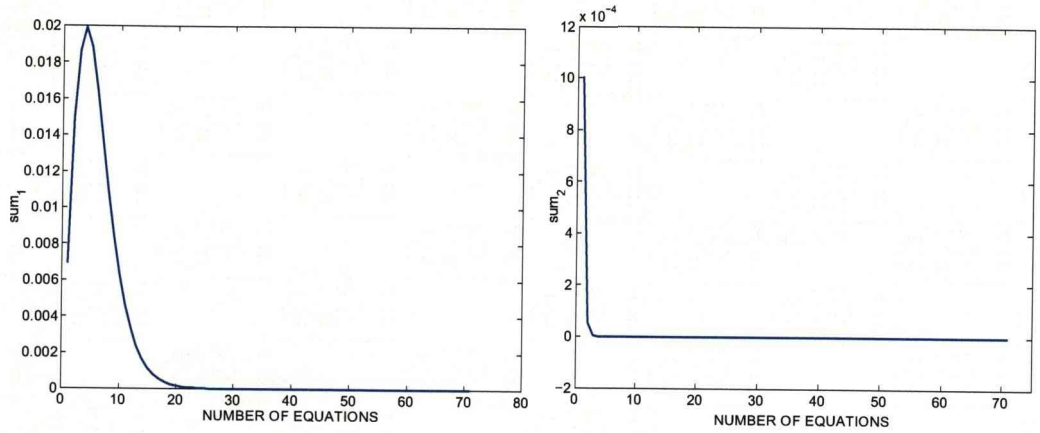

(a) Calculation of the sums from equation (8.6.19). (b) Calculation of the sums from equation (8.6.20).

Figure 8.2: A plot of the convergence test using equations (8.6.19) and (8.6.20) against the number of equations for sphere sizes R_I, and $R_{II} = 0.5 \times 10^{-3}, \times 10^{-4}$m respectively, with the following translational velocities $U_y^I = 3 \times 10^{-3}$ m s^{-1}, $U_y^{II} = 0$ m s^{-1}. (a) Represent the calculation of the sum of the coefficients using equation (8.6.19). (b) Represent the calculation of the sum of the coefficients using equation (8.6.20).

8.6.3 Recurrence Relations for the k=0 mode

All two dimensional flows of incompressible fluid can be encapsulated by using Stoke's stream function. In such cases, the solution of the equations of motion is reduced to the search of one single scalar function (see Acheson (1990)). In general, three-dimensional fluid flows are not amenable to treatment in this way. However, there do exist certain classes of three-dimensional flow that can be characterised by means of a stream function. Examples include the streaming past a body of revolution parallel to its axis of symmetry (see Acheson (1990), Happel & Brenner (1965)). This type of flow is an example of what is termed axisymmetric flow. In such a flow, the velocity field is independent of the azimuthal angle (ϕ).

The $k = 0$ mode corresponds to an axisymmetrical flow arising from the translational motion of the two spheres along their line of centres with constant velocity in an otherwise quiescent and unbounded fluid. The no slip boundary condition requires that

$$v_\rho = 0, \tag{8.6.21}$$

$$v_\phi = 0, \tag{8.6.22}$$

$$v_z = U_z^N. \tag{8.6.23}$$

In view of equations (8.5.2)-(8.5.4), these conditions imply that

$$0 = \frac{1}{2}\left(\frac{\rho}{c}\overline{W}_0^0 + W_0^1 + W_0^{-1}\right), \tag{8.6.24}$$

$$0 = \frac{1}{2}\left(W_0^{-1} - W_0^1\right), \tag{8.6.25}$$

$$U_z^N = \frac{1}{2}\left(\frac{z}{c}\overline{W}_0^0 + 2\,W_0^0\right). \tag{8.6.26}$$

From which the following relations are obtained,

$$\overline{W}_0^0 = \frac{-2c}{z}\left(W_0^0 - U_z\right),. \tag{8.6.27}$$

$$W_0^{-1} = \frac{\rho}{z}\left(W_0^0 - U_z\right), \tag{8.6.28}$$

$$W_0^1 = \frac{\rho}{z}\left(W_0^0 - U_z\right). \tag{8.6.29}$$

The procedure is entirely analogous to $k = 1$ mode. We need to obtain explicit result for all the coefficients in terms of A_{0n}^0 and B_{0n}^0. To obtain these relations equation (8.6.27) is written as,

$$\begin{aligned}\Lambda_n(\overline{A}_0^0, \overline{B}_0^0, \xi)P_n^0(\cos(\eta)) &= \frac{2\Delta^{\frac{1}{2}}}{\sinh(\xi)}U_z \\ &- \frac{2}{\sinh(\xi)}\left[\cosh(\xi) - \cos(\eta)\right]\Lambda_n(A_{0n}^0, B_0^0, \xi)P_n^0(\cos(\eta)).\end{aligned} \tag{8.6.30}$$

Using the identity (see Davis (1969))

$$(\cosh(\xi) - \cos(\eta))^{\frac{1}{2}} = \sum_{n=0}^{\infty}\lambda_n P_n^0(\cos(\eta)), \tag{8.6.31}$$

where

$$\lambda_n = -\frac{1}{\sqrt{2}}\left(\frac{e^{-\left(n-\frac{1}{2}\right)|\xi|}}{2n-1} - \frac{e^{-\left(n+\frac{3}{2}\right)|\xi|}}{2n+3}\right),$$

in conjunction with equation (8.4.23) and simplifying in terms of Legendre functions we obtained

$$\begin{aligned}\Lambda_n(\overline{A}_0^0, \overline{B}_0^0, \xi) &= \frac{2}{\sinh(\xi)}\left(\lambda_n U_z - \cosh(\xi)\,\Lambda_n(A_0^0, B_0^0, \xi)\right. \\ &+ \left.\frac{n\Lambda_{n-1}(A_0^0, B_0^0, \xi)}{2n-1} + \frac{(n+1)\Lambda_{n+1}(A_0^0, B_0^0, \xi)}{2n+3}\right), \quad n \geq 0.\end{aligned} \tag{8.6.32}$$

Using a similar procedure to that used in obtaining equation (8.6.32) it can be shown that,

$$\begin{aligned}\Lambda_n(A_0^1, B_0^1, \xi) &= \frac{1}{(2n-1)\sinh(\xi)}\left(\Lambda_{n-1}(A_0^0, B_0^0, \xi) - \lambda_{n-1}U_z\right) \\ &- \frac{1}{(2n+3)\sinh(\xi)}\left(\Lambda_{n+1}(A_0^0, B_0^0, \xi) - \lambda_{n+1}U_z\right), \quad n \geq 1.\end{aligned} \tag{8.6.33}$$

$$\sum_{n=-1}^{\infty} \Lambda_n(\overline{A}_0^0, \overline{B}_0^0, \xi) P_n^{-1}(\cos(\eta)) = -\frac{\sin(\eta)}{\sinh(\xi)} \left(\Delta^{\frac{-1}{2}} U_z - \sum_{n=0}^{\infty} \Lambda_{n+1}(A_0^0, B_0^0, \xi) P_n^0(\cos(\eta)) \right). \quad (8.6.34)$$

To simplify equation (8.6.34), the definition (see Andrews (1992))

$$P_n^{-m}(\cos(\eta)) = (-1)^m \frac{(n-m)!}{(n+m)!} P_n^m(\cos(\eta)), \quad (8.6.35)$$

is needed. In addition we need the identity (see Andrews (1992)) $P_n^{-1}(\cos(\eta)) = -\frac{1}{(n+1)n} P_n^m(\cos(\eta))$. Using this definition and relation (8.4.29), simplifying in terms of Legendre functions we obtained,

$$\begin{aligned} \Lambda_n(A_0^{-1}, B_0^{-1}, \xi) &= \frac{-n(n+1)}{(2n-1)\sinh(\xi)} \left(\Lambda_{n-1}(A_{0n}^0, B_{0n}^0, \xi) - \lambda_{n-1} U_z \right) \quad (8.6.36) \\ &+ \frac{n(n+1)}{(2n+3)\sinh(\xi)} \left(\Lambda_{n+1}(A_0^0, B_0^0, \xi) - \lambda_{n+1} U_z \right) \quad n \geq 1. \end{aligned}$$

Equations (8.6.32), (8.6.33) and (8.6.36) are the equations used in obtaining the coefficients for $k = 0$.

8.7 Force field

Given any translational velocity, torques and forces are parameters of great significance in hydrodynamic analysis. A rigid particle in a fluid may undergo both translational and rotational motion. The linearity of the Stokes equation allows the consideration of these modes of motion separately and the results can be combined together by superposition. However, the present analysis will be restricted to translational motion only.

Consider a body with constant translating velocity in an unbounded fluid. Then the hydrodynamic force on the body is as given by (Happel & Brenner 1965)

$$\mathbf{F} = \int_{\text{body}} \prod \cdot d\vec{S}, \quad (8.7.1)$$

where $\prod$ is the pressure stress tensor given by

$$\prod = -p\mathbf{I} + 2\mu\mathbf{\Delta}. \quad (8.7.2)$$

Here $\mathbf{I}$ is a tensor and $\mathbf{\Delta}$ is the rate of deformation tensor. Using equation (8.7.1), one can derived formulas for calculating the forces on the two spheres in the x, y, and z directions. However, following the analysis of Lin et al. (1970) one can write the

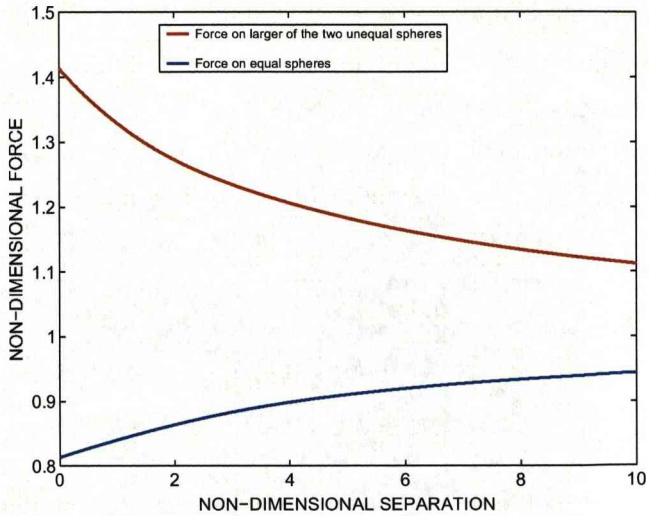

Figure 8.3: A plot of the calculated y–component of the forces for some sphere sizes against the separation distances. The – line show the forces on the sphere with size $R_I = 5 \times 10^{-3}$ and speed $U_y^I = 1 \times 10^{-3}$. This sphere is interacting with another sphere which is ten times smaller and non-swimming. The – lines shows the corresponding force calculations on one of the spheres when two spheres of equal sizes, $R_I = R_{II} = 5 \times 10^{-3}$ m and speeds $U_y^I = U_y^{II} = 1 \times 10^{-3}$ m s^{-1} are interacting. The Figure is plotted using equation (8.7.4).

equations for the force field in this formulation as

$$F_x' = -2^{\frac{3}{2}}\pi\mu c \sum_{n=0}^{\infty} \left(A_{-1n}^{-1} \pm B_{-1n}^{-1}\right), \tag{8.7.3}$$

$$F_y' = -2^{\frac{3}{2}}\pi\mu c \sum_{n=0}^{\infty} \left(A_{1n}^{-1} \pm B_{1n}^{-1}\right), \tag{8.7.4}$$

$$F_z' = -2^{\frac{5}{2}}\pi\mu c \sum_{n=0}^{\infty} \left(A_{0n}^{0} \pm B_{0n}^{0}\right), \tag{8.7.5}$$

where μ is the dynamic viscosity of the fluid. It is to be noted that $(+)$ is to be used for the sphere I while $(-)$ is to be used for sphere II. All the force calculations in what follows are non-dimensionalised using the Stokes formula (see Acheson (1990))

$$F' = 6\pi\mu a U, \tag{8.7.6}$$

where a is the radius of the sphere and U is the sinking speed. The separations distances (the minimum distance between the spheres surface) are non dimensionalised by the smaller sphere radius.

A particular problem associated with the force calculations is that the results are quite erratic as the spheres get very close. Accuracy can be improved by addition of more terms in the system of linear equations (that is by increasing N). Figure 8.3 shows the computed y-component of the forces for spheres of equal and unequal sizes and speeds. The equal spheres have sizes $R_I = R_{II} = 5 \times 10^{-3}$ m and speeds $U_y^I = U_y^{II} = 1 \times 10^{-3}$

m s^{-1}. The sizes of the unequal spheres are $R_I = 5 \times 10^{-3}, R_{II} = 5 \times 10^{-4}$ m, and speeds $U_y^I = 1 \times 10^{-3}, U_y^{II} = 0$ m s^{-1}. The calculations were done 1 separation distance. Subsequently, extrapolation was carried out to estimate the results at close distances. Two contrasting behaviour are demonstrated. For spheres of equal sizes, the force exerted on each sphere as they come closer, gets smaller. It is predicted that, the limiting value of the forces on either sphere is 82% of the corresponding result from Stokes formula (single sphere). However, when the spheres are unequal in size, the force on the larger sphere get bigger as the separations decreases. The prediction in this case, is that the limiting force is about 141% of the corresponding force on a solitary sphere calculated using the Stokes formula. From the point of view of prey perception the interest here is mainly in the case when the spheres are moving head on towards each other. Because in that scenario the various forces on the spheres (or cell bodies) will be greatest. In that case the line along which the spheres are moving towards each other will be taken as the z-axis and limit out investigation to the k=0 mode.

8.8 Prey perception by hydromechanical means

8.8.1 Introduction

In this section, planktonic encounter rates involving planktonic particles which perceive prey by hydromechanical means shall be studied. When considering prey perception by hydromechanical means, the perception field of the predator is determined by its ability to detect small changes in the characteristics of the local flow field brought about by a body close by. This depends not just on the characteristics of the flow field, but also the relative distance and orientation of the microorganisms and their respective swimming directions. It also depends on the predator's sensory capabilities to distinguish the signal produced by a potential prey from the background noise.

Idealised spherical bodies are used to represent both the predator and prey interacting in turbulent flow. The resulting interaction may cause velocity differences over the bodies of both the predator and its prey. These velocity differences are referred to as the signal strength (see Visser (2001)). Detection is triggered when the signals strength exceeds certain threshold value. The magnitude of the threshold signal, effectively determines the reaction distance.

The situation where the predator swims constantly in a straight line will be considered by employing two forms of signal mechanism; rate of deformation and velocity magnitude. Planktonic microorganisms rarely move in straight lines for long. Consequently, the encounter rates for predators exhibiting direction changes in swimming pattern will also be considered. Frequently, the motion of planktonic microorganisms consist of a number of different swimming patterns in combination and the resulting encounter rate

will depend upon the specific combination of these simplified movements. The surface surrounding the predator where the signal strength equals the critical signal, is assumed to define the boundary of the effective perception field of the predator. This kind of surface will present a wide range of perceptive distances from which average value can be found.

8.8.2 Formulation of the encounter rate problem

The two sphere problem discussed above will now be adopted to study planktonic predator-prey interactions in turbulent flow. The larger sphere will henceforth be termed "predator" and the smaller one "prey." The present calculations will linked the KS flow field and the two sphere problem.

Planktonic copepods are primary grazers on phytoplankton which are mostly non-motile. Because these predators are non-visual, they use their highly sensitive antennae to detect the presence of potential food in their vicinity. To formulate a potential encounter rate model based on hydrodynamic perception, the position of the antenna must be determined exactly. However, to try and augment the two sphere problem discussed above by adding in some antennae to the larger sphere introduces complications that are much too difficult to estimate analytically. It is essential that our model should be analytic because the ultimate aim is to describe the forces and signals interacting on the planktonic bodies in a turbulent flow, the generation of which is extremely expensive in CPU time. To attempt to calculate the forces and signals numerically in such a flow would require the computational resources well beyond those that are currently available. In order to use the two sphere problem to estimate the hydrodynamic forces experienced by the planktonic predator/prey in a turbulent simulation, we shall assumed that the predator has antennae which are always aligned perpendicular to its swimming direction. We shall also be assumed that the relevant hydromechanical signals are detected at the tip of one of the antennae. To set up the model, the position of the antenna will be formulated first.

Let the position vector of the prey and predator from some reference point **ó** be given by $\mathbf{y}_H$ and $\mathbf{y}_P$ respectively. This set up is depicted on Figure 8.4. Then **oó** can be defined by

$$\mathbf{oó} = \mathbf{y}_P - h_I \mathbf{u}_{\hat{PH}}, \tag{8.8.1}$$

where $\mathbf{u}_{\hat{PH}}$ is a unit vector in the direction of $\mathbf{y}_P - \mathbf{y}_H$ and it lies along the $z-$ axis. From Figure 8.4 the antenna position ($\mathbf{A}_{pos}$) can be defined as

$$\mathbf{A}_{pos} = h_I \hat{\mathbf{u}}_{PH} + R_I \hat{\mathbf{u}}_s + l_a \hat{\mathbf{u}}_{ant}, \tag{8.8.2}$$

where l_a is the length of the antenna and $\hat{\mathbf{u}}_{ant}$ and $\hat{\mathbf{u}}_s$ are unit vectors. Having specify the antenna position, the relevant signal strength at its tip can be found. The unit

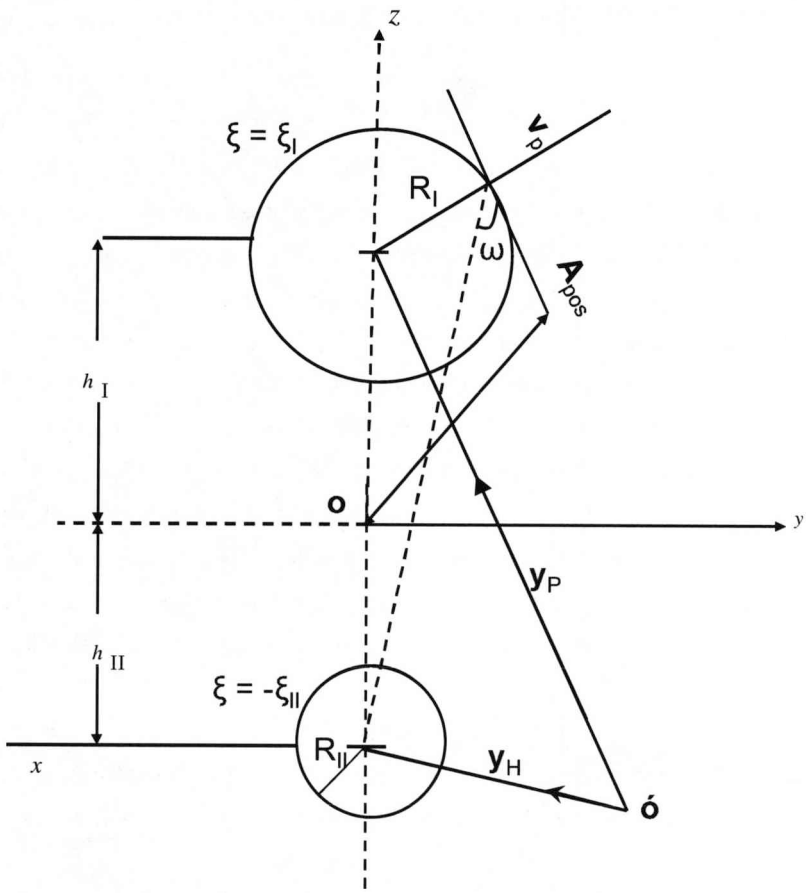

Figure 8.4: Geometry of the encounter situation between a predator and prey showing typical antenna position and the contact angle (ω). The contact distance is defined as $d = h_I + h_{II} - (R_I + R_{II})$, where R_I and R_{II} are the predator and prey sizes respectively, $\mathbf{y}_P$ and $\mathbf{y}_H$ are the position vectors of the of the predator and prey from some reference point ó respectively.

vector $\hat{\mathbf{u}}_{ant}$ can be defined in spherical coordinates as

$$\hat{\mathbf{u}}_{ant} = (\sin\theta\cos\phi, \sin\theta\sin\phi, \cos\theta)\,, \tag{8.8.3}$$

where ϕ, θ are the azimuthal and zenith angles respectively. To calculate the unit vector numerically, the azimuthal angle is randomly generated. Because the antenna is perpendicular to the swimming direction, we must have $\mathbf{v}_P \cdot \hat{\mathbf{u}}_{ant} = 0$. If $\mathbf{v}_P = \left(v_P^x, v_P^y, v_P^z\right)$, then using equation (8.8.3) a relation for θ can be written as

$$\theta = \arctan\left(\frac{-v_P^z}{v_P^x\cos\phi + v_P^y\sin\phi}\right). \tag{8.8.4}$$

Now the cylindrical coordinates ρ and z can be written in terms of the antenna position as follows. Let $\mathbf{A}_{pos} = \left(A_{pos}^x, A_{pos}^y, A_{pos}^z\right)$. Then From equation (8.2.12)

$$\rho = \sqrt{x^2+y^2} = \sqrt{\left(A_{pos}^x\right)^2 + \left(A_{pos}^y\right)^2} \tag{8.8.5}$$

$$z = A_{pos}^z. \tag{8.8.6}$$

Given any predator-prey separation d, the parameters c, h_I, h_{II} can now be calculated. From equation (8.2.4) we can write

$$\rho^2\left(\cosh^2\xi - 2\,\cosh\xi\cos\eta + \cos^2\eta\right) - c^2\left(\cosh^2\xi - 1\right) = 0. \tag{8.8.7}$$

After simplification equation (8.8.7) reduces to

$$\cosh\xi = \frac{\rho\cos\eta \pm c\sin\eta}{\rho}. \tag{8.8.8}$$

From equation (8.2.4) we have

$$\left(z^2 - c^2\right)\cosh^2\xi - 2\,z^2\cosh\xi\cos\eta + z^2\cos^2\eta + c^2 = 0. \tag{8.8.9}$$

Substituting equation (8.8.8) into (8.8.9) an expression for η is obtained as

$$\eta = \pm\arctan\left(2\,\frac{\rho\,c}{\rho^2 + z^2 - c^2}\right). \tag{8.8.10}$$

Using equation (8.8.10) the following relations are obtained

$$\begin{aligned}\sin\eta &= \frac{2c\rho}{\sqrt{\left(c^2-\rho^2-z^2\right)^2 + 4\,c^2\rho^2}},\\ \cos\eta &= \frac{\left(c^2-\rho^2-z^2\right)}{\sqrt{\left(c^2-\rho^2-z^2\right)^2 + 4\,c^2\rho^2}}.\end{aligned} \tag{8.8.11}$$

Using equation (8.8.11) in (8.8.8) a formula for calculating ξ is obtained as

$$\xi = \cosh^{-1}\left(\frac{c^2\left(1+4\rho^2\right) - \rho^2 - z^2}{\sqrt{\left(c^2-\rho^2-z^2\right)^2 + 4\,c^2\rho^2}}\right). \tag{8.8.12}$$

8.8.3 Relevant hydromechanical stimuli

When a predator and prey are in close proximity, the flow-field geometries are distorted, the extent of the distortion depending upon how far they are apart. The hydrodynamic disturbances can cause a deformations of the streamlines around the antennae of the predator, which can be perceived as hydromechanical signals. The signals generated by a passively sinking or self-propelled copepod depends on the sum of forces it exerts on the ambient fluid, the Reynolds number regime, the boundary conditions imposed on the moving object, its size and speed (see Kiørboe & Visser (1999)). The efficiency of the signals depend upon the amount of information it conveyed to the recipient (predator, prey or mate). Various components of the fluid disturbance can potentially serve as a mechanical cue eliciting a reaction. In this thesis, the signal strength due to velocity magnitude and the rate of deformation will be considered.
In cylindrical coordinates, the components of the rate of strain tensor are given by the following equations (see Tritton (1988)),

$$\begin{aligned} e_{\rho\rho} &= \frac{\partial v_\rho}{\partial \rho}, \\ e_{\phi\phi} &= \frac{1}{\rho}\frac{\partial v_\phi}{\partial \phi} + \frac{v_\rho}{\rho}, \\ e_{zz} &= \frac{\partial v_z}{\partial z}, \\ 2e_{\phi z} &= \frac{1}{\rho}\frac{\partial v_z}{\partial \phi} + \frac{\partial v_\phi}{\partial z}, \\ 2e_{z\rho} &= \frac{\partial v_\rho}{\partial z} + \frac{\partial v_z}{\partial \rho}, \\ 2e_{\rho\phi} &= \rho\frac{\partial}{\partial \rho}(\frac{v_\phi}{\rho}) + \frac{1}{\rho}\frac{\partial v_\rho}{\partial \phi}. \end{aligned} \tag{8.8.13}$$

The deformation rate and the velocity magnitude will be calculated using

$$\Delta = \sqrt{e_{\rho\rho}^2 + e_{\phi\phi}^2 + \frac{1}{2}e_{\rho\phi}^2 + e_{zz}^2 + \frac{1}{2}e_{\rho z}^2 + \frac{1}{2}e_{\phi z}^2}, \tag{8.8.14}$$

$$s = \sqrt{v_\rho^2 + v_z^2 + v_\phi^2}, \tag{8.8.15}$$

respectively (see equations (8.4.8)-(8.4.10)). Following Caparroy et al. (2000) the signal strength s^* due to deformation can be defined by

$$s^* = l_a \Delta, \tag{8.8.16}$$

where l_a is the length scale of the antenna. From equation (8.8.16), it is clear that the length of the antenna will determine the sensitivity of the animal to changes in local velocity gradients brought about by nearby objects. Long antenna appear to be advantageous but could potentially mean the animal is excessively sensitive to fluid

disturbances, resulting in unnecessary response behaviour.
In what follows, the threshold signal due to rate of deformation and velocity magnitude are respectively set as 0.2 and 0.04 mm/s.

8.9 Model execution

The turbulent kinematic simulations are similar to those described in Chapter 4. The most significant differences will be highlighted here.
Input data to the simulation program include the predator and prey sizes, antennae length and the threshold signal strength. These and other parameters were non-dimensionalised using the Kolmogorov scales. As before, the simulation domain is a cube initially with sides 0.5 m. Initially 512 prey and predators were introduced into the domain. The same number of predators was maintained throughout. We assumed that the prey particles were non-motile phytoplankton with size 3×10^{-4}m. For planktonic predator-prey interactions, the suggested predator-prey size ratio is about 10:1 (see Greene (1988)). Consequently, the second group with length scale 3×10^{-3}mm was chosen to represent the predators. The length of the mechanoreceptive structures involved in detection is an important parameter governing the predator's perception capabilities. In this work, we assume that antenna length of the template predator was 2×10^{-3}m. The predators and prey were initially positioned at distances greater than 12 mm. This was base on the assumption that the signal strength at these distances are not sufficiently high for any prey to be detected. This is a reasonable assumption as can be seen from Figure 8.7(b). Predator-prey pairs that were initially within a distance $\leq$ 12 mm away were repositioned. The swimming speeds of the predators were drawn from three-dimensional Gaussian distribution with mean zero and standard deviation σ_P.
The total simulation time was 7 minutes which was divided into a number of time steps (simulation time /step size). Each predator swims in a given direction over a prescribed time steps. Specifically, two sets of simulations were conducted. One of these involve the case where the predators never change their swimming directions throughout the simulation. The second encapsulates the situation where the predators were changing their swimming direction every 10 time steps (equivalent to 2.7 seconds). During the simulation predators and prey were brought together by the combined effects of the predators' speed and the flow. The current positions of predators and prey were recorded for later processing. The KS flow field, the predator-prey interactions and the two-sphere problems were linked together in a subroutine called `Conthresh`. It was in this routine that the decisions were made as to whether or not a predator was in contact with a prey. Altogether four sets of simulations were conducted using two forms signal modalities viz, the deformation rates and the velocity magnitude. For each of these

signal modalities two sets of simulations were conducted, that is case where predators never change their swimming directions and the case where they are changing their swimming directions every 2.7 seconds.

8.9.1 Registering contacts

Deciding whether a prey in the vicinity of a predator would actually be detected by the latter (and hence registered as a 'contact') requires that the signal generated by the former which propagates to the antenna tip should exceed the appropriate detection threshold. This decision making process was done in a subroutine called `Conthresh`. Input to this routine includes predators and prey current positions and random walk swimming speeds, predator's identification number, antenna length and predator-prey sizes. It returns a single character CC ='YES' or 'NO' indicating whether to register contact or not.

In this work we shall assumed that there exists some background signals (noise) irrespective of whether a prey is in the vicinity of a predator or not. This means that for detection to occur, the signal created by a nearby prey must be large enough to be discernible above the background noise. To this end, registering a contact between a predator and a nearby prey requires that the signal strength was calculated twice. Initially the signal strength was calculated by using the actual distance $d = d_1$ (calculated using their current positions) between predator and prey. Secondly, the signal was recalculated on the assumption that the predator and prey were very far apart ($d = d_2 = 12$ mm). This constitutes the background signal. If the difference between these two signals is greater than the designated threshold, then contact was registered as having occurred. Whenever a contact has been designated, the angle (ω) formed by the line joining the centre of the prey to the base of the predator's antennae was measured (see Figure 8.4). This is called the contact angle. Similarly, the distance (along the line of centres) between the surfaces of the predator and prey was also measured. This is called the contact distance.

The main difference between the present and the previous simulations are

1. The subroutine `CONECONE` is replaced with a different routine `Conthresh`. The procedures described by E and F in the Flow chart summary (see Chapter 4) do not apply for hydromechanical signals.

`Conthresh` is the main routine where the decisions were made as to whether contact was made or not. In summary, the determination of a contact using this routine involves the following steps.

1. Using the predator and prey positions (inputs to the routine) the predator-prey separation ($d = d_1$) was calculated. This was followed by the calculation of a unit

vector $\mathbf{u}_{ant}$ (see equation (8.8.3)). The angle ϕ was the generated randomly in $[0, 2\,\pi]$ from Gaussian distribution with mean zero. This enables the calculation of the angle θ.

2. Using d_1 the parameter values $h_{I,II}, c, \xi_{I,II}$ were calculated and hence the antenna position.

3. The cylindrical coordinates ρ and z were then calculated from equations (8.8.5) and (8.8.6) respectively and hence ξ, η.

4. The angles ξ and η were then calculated from equations (8.8.12) and (8.8.10) respectively.

5. Steps 1 to 5 five describes a modified (because of the antenna) two sphere problem. The two sphere problem was then solved in a subroutine within `Conthresh` called `twosphere`.

6. Inputs to `twosphere` are $c, \xi_{I,II}, \xi, \eta,$ and v_P^z.

7. The subroutine `twosphere` is where the numerical evaluation of equations (8.6.32), (8.6.33) and (8.6.36) were done. It returns the coefficients, the forces, the torques and importantly the signal strength s_1 to the subroutine `Conthresh`.

8. Steps 1 to 5 were then repeated with distance $d = d_2$ to obtain the signal s_2 (when the spheres are along way, 12 mm apart).

9. The signal $S = |s_1 - s_2|$ was then compared with the threshold value (Th). If $S > Th$, then CC='YES' is returned to the main routine and contact was registered otherwise no contact and CC='NO' is returned.

This summary is represented with a flow chart on Figure 8.5.

8.10 Results

Figures 8.6(a) and 8.7(a) shows the number of contacts made by two groups of 512 predators. One group swim in straight lines ($\tau_{\text{sight}} = \infty$). These are represented with the blue errorbar. The second group is for random walk swimmers ($\tau_{\text{sight}} = 0.2$) and is represented with red errorbar. Figure 8.6(a) is for velocity magnitude while Figure 8.7(a) is for signal due to deformation. It is clear from the Figures that encounter rate by hydromechanical perception does not materially alter the conclusions drawn in the case when the predator's perception field was assumed to be a simple sphere.
As $\sigma_P \to 0, \tau \to \tau_{\text{LC}}$ (see Chapter 1) and the contact rate results arising from both classes of motility, do not differ so much. However as σ_P increases, the contact rate

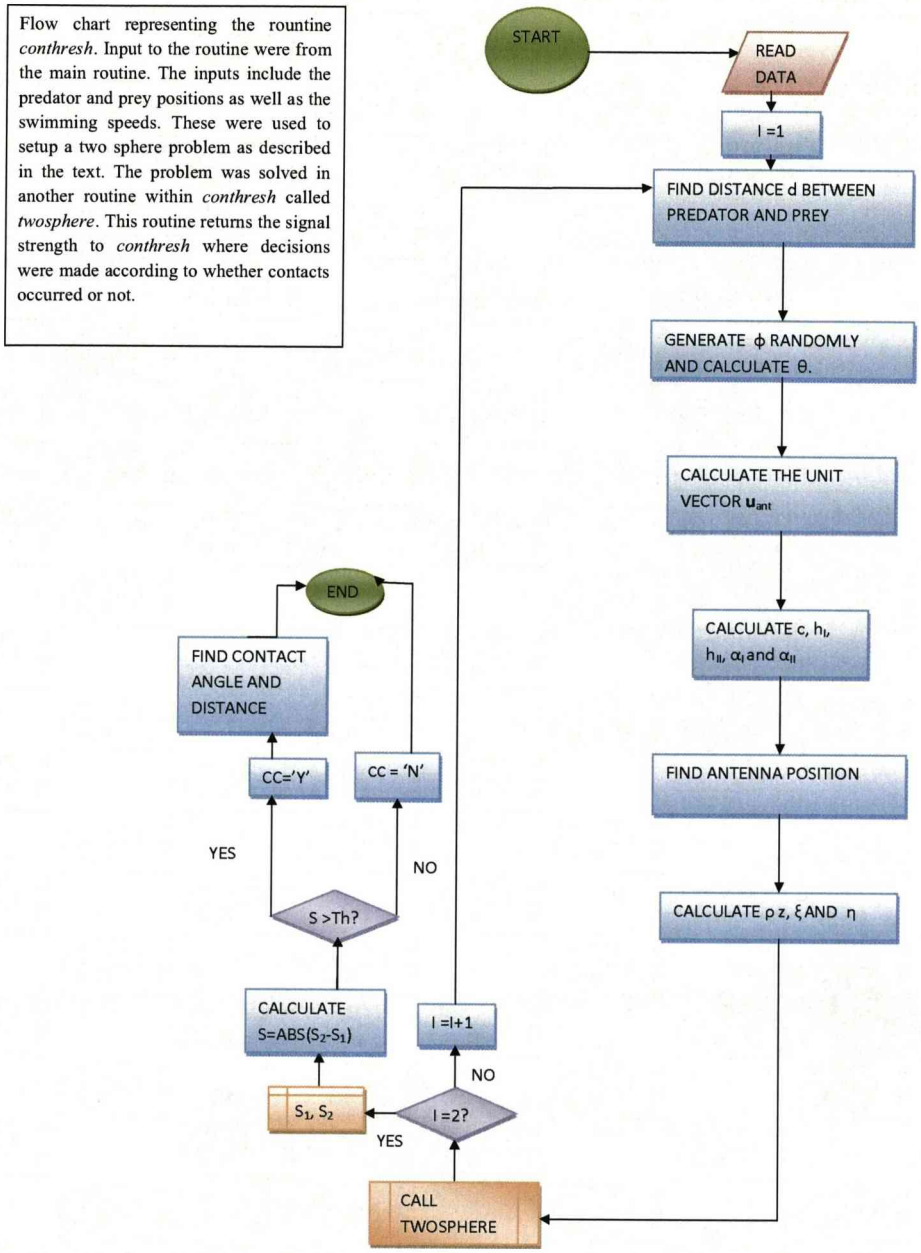

Figure 8.5: Flow chart summary of the major changes made to the previous simulation codes in order to study hydromechanical signalling.

results diverges. These serves to illustrate that as the predators moves slowly (low σ_P

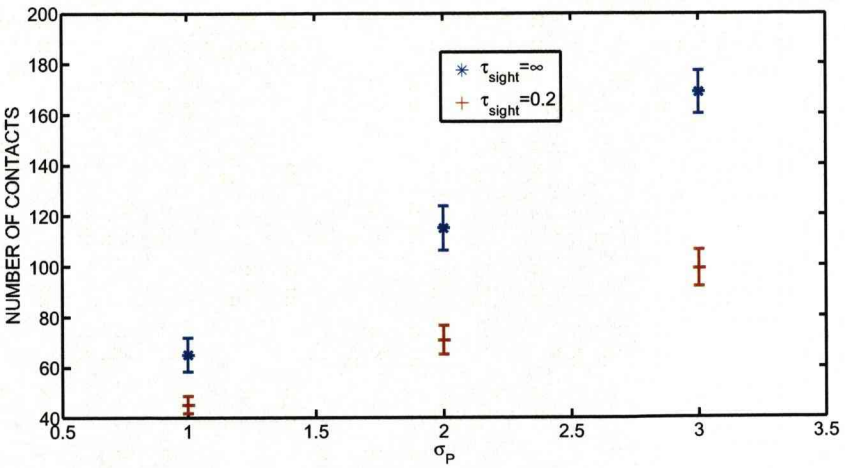

(a)

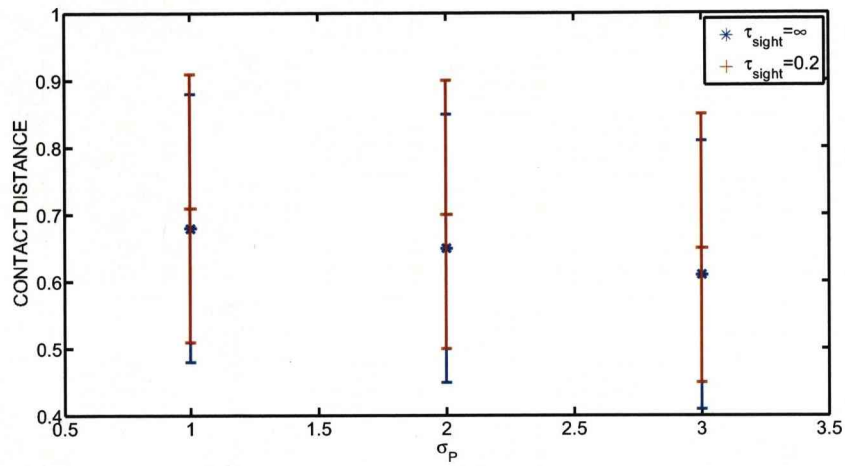

(b)

Figure 8.6: Number of contacts, average contact distances, recorded for 2 groups of 512 predators against the swimming speeds for a signal based on the differences between velocity magnitudes. (a) Depicts the number of contacts for straight line swimmers (blue errorbar $\tau_{\text{sight}} = \infty$) and random walk swimmers (red errorbar $\tau_{\text{sight}} = 0.2$). (b) Depicts the average contact distances recorded during the simulation against the predators' swimming speeds. The contact distances are the separation between the predator and prey on contact.

values), the two motility patterns do not differ much. As a result, the contact rates for straight line and random walk swim do not differ significantly. As σ_P increases, the trajectories of the predators undergoing random walk become more and more convoluted as more time was spent re-tracking the same volume of fluid. Hence, the divergence of contact rate for the two motility patterns.

Figures 8.6(b) and 8.7(b) show the average contact distances against the variances of

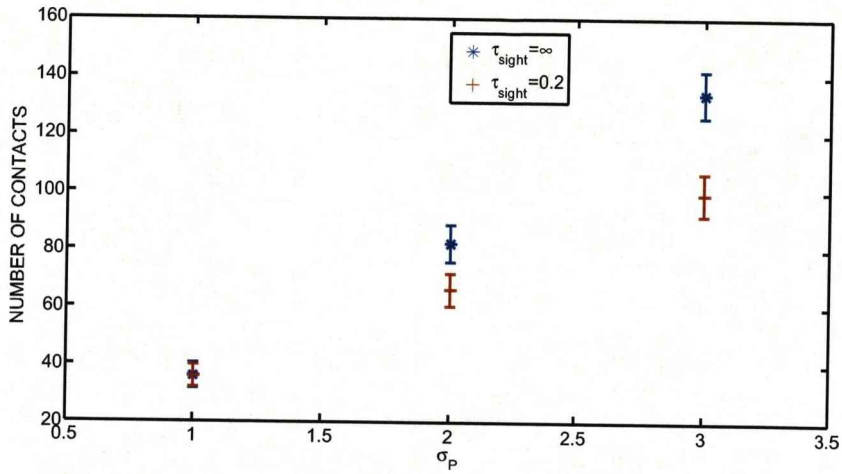

(a)

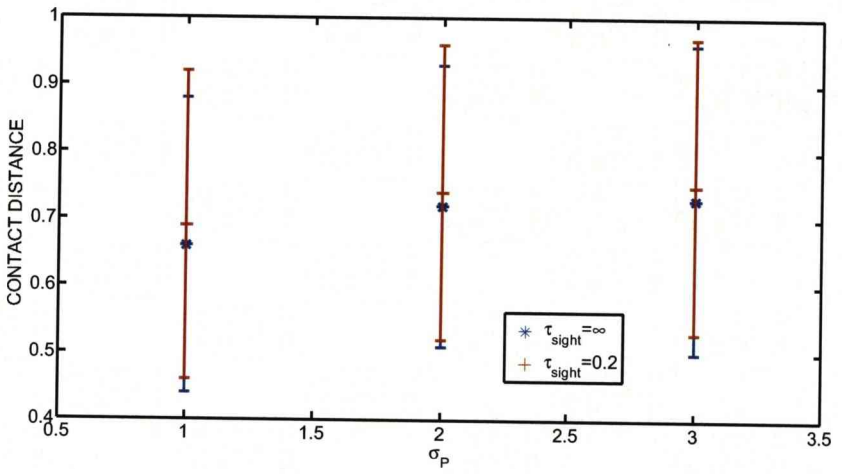

(b)

Figure 8.7: Number of contacts, average contact distances, recorded for two groups of 512 predators against the variance of swimming speeds for a signal based on the difference between deformation rates. (a) Depicts the number of contacts (b) Depicts the average contact distances. The keys are the same as in Figure 8.6

swimming speed. Consistent features of these Figures are that for predators which follow a random walk swimming pattern tend to perceive objects at greater distances. However, the extent of the error bars restrict further discussion in this direction. Comparison of the two Figures also shows that the average contact distances do not differ so much when the different types of flow signal are employed.

The contact distance results are somewhat surprising. When swimming randomly predators can perceive prey at marginally greater distances than when they swim in straight lines. Perceptual benefits accrue because pauses aids the sensory systems to

detect the relevant stimuli (see Kramer & Mclaughlin (2001)). This might explain why they tend to perceive further away when random walking. Despite these perceptual benefits, the random walk swimmers were still making less encounters. However, this type of motility pattern is much more closer to reality than sustained straight line swimming. Whenever any contact was designated to have occurred, the contact an-

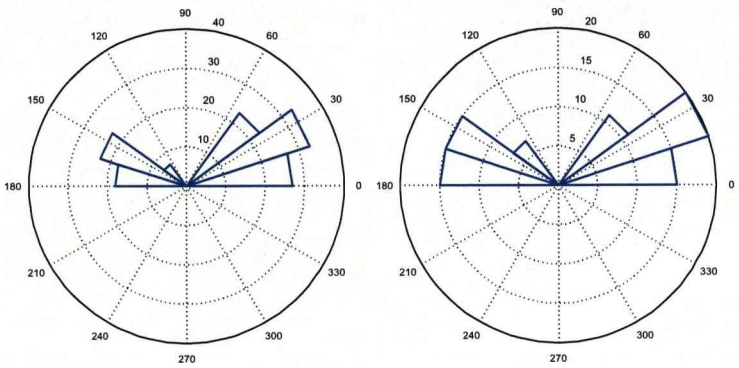

(a) (b)

Figure 8.8: Frequency histogram for contact angles arising from signals due to velocity magnitude in one run of simulations. These results are obtained by recording the angle ω (see Figure 8.4) whenever contact occur between a predator and prey and using them to form the frequency histogram. (a) Depicts the results for the straight line swimmers (b) Shows the results for the random walk swimmers

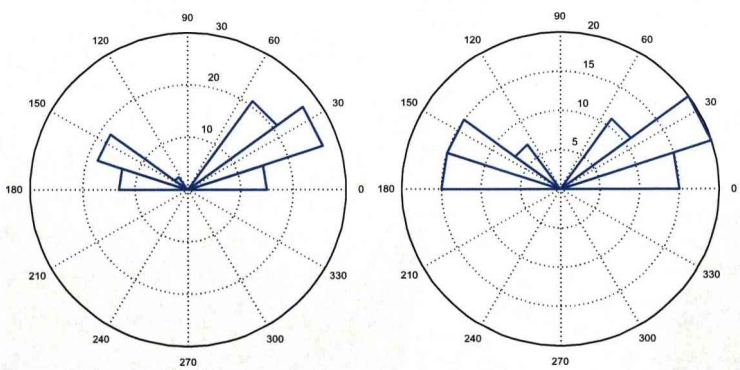

(a) (b)

Figure 8.9: Frequency histogram for contact angles arising from signal strength due to rate of deformation, in one run of simulations. Other keys are the same as in Figure 8.8. (a) Depicts the results for the straight line swimmers (b) Shows the results for the random walk swimmers

gle (see Figures 8.4 and 8.10) was recorded. When the antenna is perpendicular to the line of centres and the predator is moving in the direction of decreasing $z, \omega = 0$. However, when the antenna is perpendicular to the line of centres and the predator

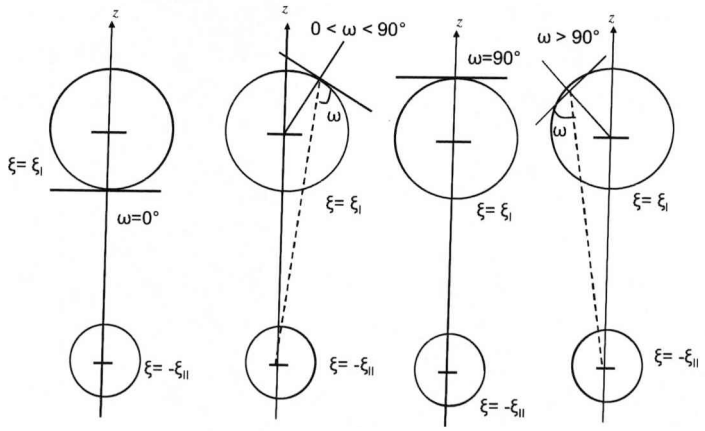

Figure 8.10: Schematic diagram showing some possible range of the contact angle ω which depend on the position of the antenna. When the antenna is perpendicular to the line of centres and the predator is moving in the direction of decreasing $z, \omega = 0$. However, when the antenna is perpendicular to the line of centres and the predator is moving in the direction of increasing $z, \omega = 90^o$.

is moving in the direction of increasing $z, \omega = 90^o$. The angles were used to form a frequency histogram as shown on Figures 8.8 and 8.9. These further serve to illustrate that planktonic particles perceived their prey at a range of different orientations. Except for the sizes of the histograms, the angular distributions show similar trend. When a predator and prey approaches each other head on, the angle ω is defined to be 0^o. In all the Figures, more contacts were recorded in the range [20, 40^o] than any other relative orientation. Note that no contacts were recorded at 90^o. As the relative orientation $\rightarrow 90^o$ from either direction, the antennae moved further away from the scene of disturbance (see Figure 8.10). One observation that we can make from these results is that the number of contacts drops off to zero in the range [60, 120^o]. This does not necessarily means that contacts cannot occur in those orientations. It is merely indicates that the net signals generated were not sufficient to rise above the threshold. Lack of sufficient signal strength could be attributed to a number of factors such as prey sizes and speeds. The prey were assumed to be non-swimming organisms in these simulations and were therefore not likely to cause detectable disturbances in those relative orientations. Figures 8.11 and 8.12 shows the stem plot illustrating the range of distances at which prey particles were perceived for the two different motility patterns during one set of the simulations. The results were obtained by recording the

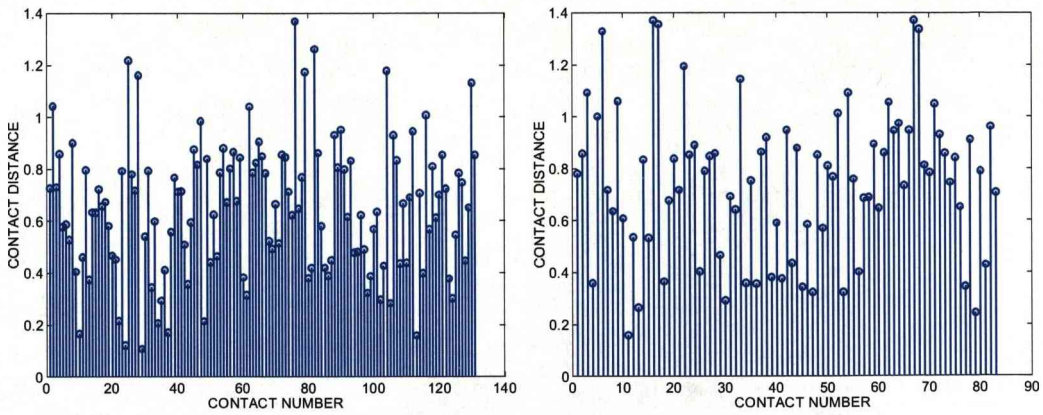

(a) (b)

Figure 8.11: Stem plot for contact distance against the contact number. For example, the first contact in (a) occurred at a distance of 0.76 approximately. This is for signal strength due to velocity magnitude, in one set of the simulations. (a) Is for straight line swimmers while (b) is for random walk swimmers.

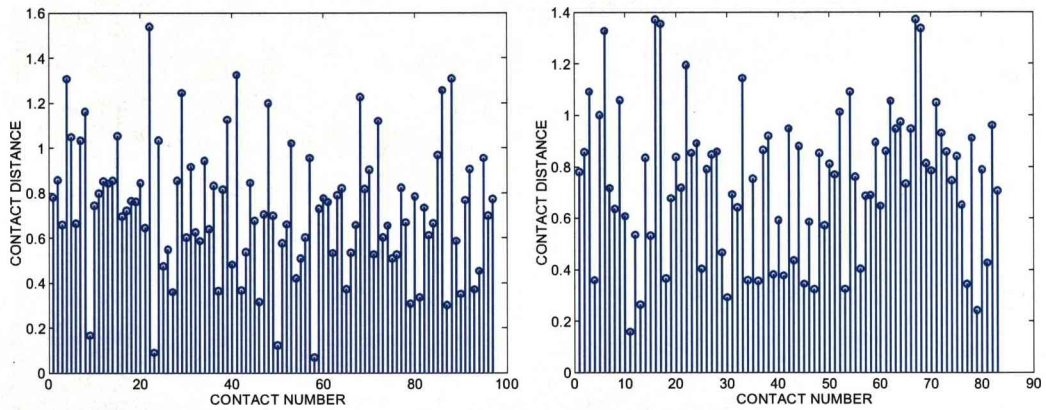

(a) (b)

Figure 8.12: Stem plot for contact distance against the contact number. For example, the first contact in (a) occurred at a distance of 0.8 approximately. This is for signal strength due to deformation rate, in one run of simulations. (a) Is for straight line swimmers while (b) is for random walk swimmers.

first contact and the distance at which it occurred, the second contact and the distance at which it occurred and so on. The large variation across the distances suggest the existence of large error bars. The variations of the distances occur due to the differences in the strength of the signal as predator and prey move towards each other. Small distances are associated with low signals. In those cases predator and prey have got very close before perception occurs. On the other hand, when the signal strength is very high, the predator can detect the presence of the prey some considerable distance

away. The averages of these distances over 10 runs of simulations at various speeds are depicted in Figures 8.7(b) and 8.6(a).

8.11 Conclusions

In this chapter, encounter rates for predators perceiving prey by hydromechanical signals in a turbulent flow were studied. The model framework for determining the signal generated by a small prey microorganism in the vicinity of a predator was constructed by employing methods originally designed to study the classical problem of two spheres of arbitrary sizes and speeds falling in Stokes flow. Even when swimming in a turbulent flow the dynamics of the two sphere problem is likely to be heavily influenced by the viscosity (because of the sphere sizes) of the fluid, because over small distances (when two organisms get close together) viscosity is the determining characteristic of the background flow. So even though the global Reynolds number might be large, locally (that in the vicinity of the copepod's hydromechanical-receptors) it will be small enough to justify the application of a model based on the Stokes equations. Extensions to the classical problem were made by adding sensory structures (antennae) to one of the spheres (predator). The new setting was then introduced into a small scale turbulent flow. The rate at which a group of such predators encounter their prey was then investigated using two forms of signal modalities. The main conclusions are as follows:

1. The first conclusion that can be drawn is that, accuracy of the calculated forces on the spheres increases by addition of more terms to the system of equations when the two spheres are in close proximity.

2. Prey perception tend to occur when the relative orientation between the predator and prey were in the range $[20, \quad 40^o.]$

3. Predators swimming by changing directions tend to perceives prey marginally further away than those swimming constantly in straight lines.

4. Predators can perceive prey over wide range of separation distances.

5. In almost all encounter rates studies in literature the perception field of planktonic predators is automatically assumed to be spherical. Here, more evidence were presented that the perception field of predators perceiving prey by hydromechanical signals is not spherical.

6. The final conclusion is that predators perceiving prey by hydromechanical means are more sensitive to signals due to velocity magnitude than the deformation rates counterparts.

One potential drawback in the encounter rate formulation is that the predators were not self propelled. Planktonic predators are capable of localize motion in real life. It would be interesting to see what the results might be under such circumstances.
Despite the drawbacks the results are plausible and encouraging. The ad-hoc arrangement might still be applied to planktonic copepods, such as `Oithona similis` that perceives inert particles by hydromechanical means.

Chapter 9

Conclusions and Further Work

In this dissertation, a combined investigation into encounter and predation rates in turbulent flows for predators with non spherical perception fields were undertaken for the first time. The work involved two distinct parts: visual and non-visual predators. In the first scenario (the case of visual predators) the predator was assumed to have a particular perception field which is conical in shape. From this assumption a theoretical model that predicted the likely encounter and capture rates for such a predator in the presence of a turbulent flow was formulated. These predictions were tested against kinematic simulations (KS). In the second scenario (the case of non-visual predators) we looked at the specific case of a predator which perceives its prey by means of hydromechanical signals. The limits of the perception field for a predator using this method of perception are poorly defined, particularly when this foraging methodology is employed in a turbulent regime. So part of the thesis was set aside to try and formulate a better understanding of this means of prey perception and its limitations. The method of investigations consisted of both theoretical predictions and kinematic simulations (KS). The summary of the thesis is given below.

A new model that combined the problem of both encounter and predation rates for planktonic predators with non-spherical geometry was formulated. To achieve this, it was initially assumed that the perception field of fish larval predator is conical in shape with a semi-vertex angle α. This kind of geometry offers various possibilities for prey entry points into the perception field. Based on these possibilities, encounter rate formulae were derived. By assigning a capture probability to each encounter that could possibly occur, predation rate formulae for predators following straight line trajectories were obtained. Subsequent modifications to the model were made so as to obtain estimates of the predation rates for predators following irregular trajectories. One species of larval fish `Atlantic Herring` are known to forage by swimming continuously. This foraging strategy is known as cruise searching. Another species of fish larvae, the `Atlantic cod, Gadus morhua` is known to forage by travelling at discrete units of time intersperse with pauses when they search their surroundings for prey.

This feeding behaviour is known as pause-travel or saltatory. The model so developed was then applied to study the cruising and the saltatory strategies of fish larvae.
In addition to the theoretical model developed, KS were conducted to test the theoretical model. The KS flow fields were constructed using large number of Fourier modes within cubic domain. The results from the KS were then compared with outputs from the theoretical predictions. Over all, good agreements were achieved. The results for the number of captures from both theory and simulations were then used in conjunction of net energy gain (NEG) model to determined the energetic benefits associated with pause-travel.
The investigation conducted above were based on the assumptions that prey are non-swimming. A novel model was formulated to study the combine problems of encounter and predation rates for planktonic predators swimming in a turbulent flow, pursuing mobile prey. This was also done using both theory and simulations. It was relatively straight forward in principle to incorporate prey swimming components into the simulation codes. However, incorporating prey swimming into the prediction model was much more complicated process. The main interest here was to formulate for the first time a working model for planktonic predators pursuing swimming prey in a turbulent flow.
A new model of energy saving function was also formulated. This function is basically the ratio of energy required to cover a given distance by pause-travel to the energy require to cover the same distance by continues swimming. It serves as a quantitative criterion indicating which mode of motion is more efficient. The model was formed using drag coefficient that is made up of both the viscous and the inertial terms. This differs from other formulae in the literature, which consist of either the inertial term or the viscous term only.
In Chapter 8 attention was devoted to non-visual planktonic predators perceiving their prey by means of hydrodynamic disturbances. The model was based on two spheres in Stokes flow where one spheres was assumed to be the prey and the other the predator. Using the no-slip boundary conditions on the surface of the spheres, a system of partial differential equations was transformed into a system of linear equations involving truncated infinite series. These systems were solved with a good accuracy to determine the coefficients so that the solution satisfied the governing equations and the boundary conditions. The resulting coefficients were then used to calculate the hydrodynamic drag forces on each of the spheres. A modification to the classical problem was made by introduction of antennae to one of the spheres (predator). It was also assumed that the predators can perceived the hydrodynamic disturbances produced by a prey using the antennae tip. Detection of nearby prey depends upon proximity and sensitivity to particular signal modality. Hence, two forms of signal modalities were used to calculate the encounter rates, contact distances and the orientation angles over which contacts

occurred.

To put it more compactly, the following are the main main achievements of this work:

1. The followings new models were formulated
   (a) Predation rate model for planktonic predators with restricted perception fields in a turbulent flow, where the prey are non-swimming.
   (b) Model for calculating the swimming cost for a fish larva.
   (c) Predation rate model for planktonic predators with restricted perception fields in a turbulent flow for swimming prey.
   (d) Energy saving function model for larval fish.
   (e) An encounter rate model for planktonic predators perceiving prey by hydromechanical signals.
2. The difficulties encountered during the course of the study have been overshadowed by the joy of counting what have achieved most especially in terms of personal development.

The main conclusions of the thesis are as follows;

1. Pause-travel strategy is energetically beneficial and is strongly linked to the shape of the larval fish perception field. Narrow perception field is intimately bound up with saltatory behaviour. The perception field $\alpha = \pi/6$ is close to the actual sensory field of cod larvae observed in real life.
2. The results from both theory and simulations for the perception angle $\alpha = \pi/6$ showed that pause-travel did indeed prove to be a robust strategy for the larvae to adopt under low travel speed.
3. There is no well defined optimal strategy. However, (50%, 50%) and (33%, 67%) pause-travel strategies appeared marginally more than others and might be taken as the energetically most favourable. These results are backed up by experimental findings, in fact they `explain` the experimental results. Saltatory predators forage in these specific pause-travel ratios because it is mathematically optimum for them to do so. Very strong selection pressure means that only those larvae which foraged in this way are likely to have survived to adulthood and have the opportunity to pass on their genes. Hence it is entirely to be expected that the descendants of these survivors are also observed to forage in a similar manner.
4. Planktonic predators with large perception field can maximise their net energy gain by adopting the cruise searching behaviour.

5. For pause-travel predators, the present calculation shows that the capture rate is about 30- 50%. These capture rates results overlap the ranges observed experimentally.

6. There appear to be no distinctive optimal swimming speed for cruising fish larvae with narrow perception field. The implication of this is that the dome-shape relationship between predation rates and swimming speeds no longer holds.

7. For both cruising and saltatory feeders, capture efficiency decreases with swimming speeds.

8. The combination of size and enhanced swimming speed means that pause-travel is more effective in larger larvae than smaller ones.

9. Formulating predation rates models where both the predator and prey (of different sizes) are swimming in a turbulent flow is a very complicated exercise. The joy of it is that this feat has been achieved. Despite the complexities involved in the formulation, the model developed produces reliable and encouraging results. This shows that the principal assumptions upon which it is built are plausible.

10. The erratic swimming patterns (changing directions frequently) of prey are more efficient method of avoiding predators than swimming in straight lines.

11. The contact radius for planktonic predators is a dynamical entity rather than a fixed number. This supports experimental results.

12. The perception fields of planktonic predators are not isotropic as previously assumed. Prey perception is biased towards certain relative orientations.

13. Threshold signal strength required to elicit a reaction depends on signal modality. Signals higher than neurophysiological threshold are required to perceived prey using the deformation rates. A relatively lower signal is required to perceive velocity magnitude than the deformation rate.

14. The distances over which contact occur depend on the signal modality and swimming behaviour. Predators swimming by changing directions tend to perceives prey marginally further away than those swimming constantly in straight lines.

15. Fast swimming in straight line leads to more prey encounters than frequent direction changes.

16. Given that one of the goals of the fish farm industry is domesticate an edible fish like the cod. If fish such as this could be raised commercially from egg to adult rather than in the manner of cattle or sheep, the implications to the world's fishing industries (both financial and ecological) would be enormous. There would

no longer be any need for large fleets to scour the world's oceans trawling for the ever dwindling stocks of marketable fish. Instead they could be raised for the market at local fish farms. Prices would go down whilst many species would be saved from extinction. But to achieve that we need to understand everything about how they live and survive in the ocean, and the most important observation about the ocean is that it is turbulent. Hence the need to try and understand how species have adapted their behaviour to survive in such conditions.

17. To answer the question that `Can we use theory and simulations to explain experimental and field observations?` The answer is `Yes we can.`

It must be emphasised that the formulations of encounter rates by hydromechanical signals was highly simplified. For example, the assumption that the predators are not self propelled is an over simplification. Planktonic predators such as copepods are known to posses the ability to move actively in the flow. This potential problem could be overcome if squirming motion can be incorporated to mimic the predators swimming capabilities. Given that the contact rates were calculated by simulation only, it would be interesting if the corresponding analytical model can be formulated. The chief difficulty is that the perception field is a dynamic entity rather than a fixed volume of space. The fact that distances between predator and prey in the flow are randomly distributed might imply that the analytical formulations are amenable to treatment using the theory of stochastic geometry.
It might be useful in the future to conduct simulations and possibly to formulate a working model that investigates the process of prey selection by planktonic predators. That is, for a predator confronted with different prey sizes and speeds, what factors will determined the choice of a suitable prey?

Bibliography

Acheson, D. J. (1990), *Elementary Fluid Dynamics*, Oxford University Press.

Alan, J. (2007), *Table of Integrals, Series, and Products.*, Burlington, MA, USA: Academic Press.

Andrews, L. C. (1992), *Special functions of mathematics for engineers*, McGraw-Hill, New York.

Baird, M. E. & Emsley, S. M. (1999), 'Towards mechanistic model of plankton population dynamics', *Journal of Plankton Research* **21**, 85–126.

Batchelor, G. K. (1967), *The theory of Homogeneous turbulence.*, Cambridge University Press.

Bolton, T. F. & Havenhand, J. N. (2005), 'Physiological acclimation to decreased water temperature and the relative importance of water viscosity in determining the feeding performance of larvae of a serpulid polychaete', *Journal of Plankton Research* **27**(9), 875–879.

Browman, H. I. & O'Brain, W. J. (1992), 'Foraging and prey search behviour of golden shiner (`Notemigonus crysoleucas`) larvae.', *Can. J. Fish Aquat. Sci.* **49**, 813–819.

Bundy, M. H., Gross, T. F., Vanderploeg, H. A. & Strickler, J. R. (1998), 'Perception of innert particles by calanoid copepods: behavioral observations and a numerical model.', *Journal of Plankton Research.* **20**(11), 2129–2152.

Buskey, E. J. (1994), 'Factors affecting feeding selectivity of visual predators on the copepod acartia tonsa: locomotion, visibility and escape responses', *Hydrobiologia* **292/293**, 447–453.

Caparroy, P., Thygesen, U. H. & Visser, A. W. (2000), 'Modelling the attack success of planktonic predators: patterns and mechanism of prey selectivity.', *Journal of Plankton Research* **22**(10), 1871–1900.

Chatwin, P. C. & Paul, J. S. (1993), 'The structure and magnitude of concentration fluctuations.', *Boundary-Layer Meteorology* **62**, 269–280.

Davis, M. H. (1969), 'The slow translation and rotation of two unequal spheres in a viscous fluid.', *Chemical Engineering Science.* **24**, 1769–1776.

Fields, D. M. & Yen, J. (1997), 'The escape behavior of marine copepods in response to a quantifiable fluid mechanical disturbance', *Journal of Plankton Research* **19**, 1289–1304.

Fuiman, L. A. & Batty, R. S. (1997), 'What a drag it is getting cold: Partitioning the physical and physiological effects of temperature on fish swimming', *The Journal of Experimental Biology* **200**, 1745–1755.

Fung, J. C. H., Hunt, J. C. R., Malik, N. A. & Perkins, R. J. (1992), 'Kinematic simulation of homogeneous turbulence by unsteady random fourier modes', *Journal of Fluid Mechanics* **236**, 281–318.

Fung, J. & Perkins, R. (2008), 'Dispersion modeling by kinematic simulation: Cloud dispersion model', *Fluid Dynamics Research* **40**, 273–309.

Galbraith, P. S., Browman, H. I., Racca, R. G., Skftesvik, A. B. & Saint-Pierre, J.-F. (2004), 'Effect of turbulence on the energetics of foraging in atlantic cod gadus morhua larvae', *Marine Ecology Progress Series* **281**, 241–257.

Gerritsen, J. & Strickler, J. R. (1977), 'Encounter probabilities and community structure in zooplankton: a mathematical model.', *J. Fish Res. Board Can.* **34**, 73–82.

Goldman, A. J., Cox, R. G. & Brenner, H. (1966), 'The slow motion of two identical arbitrarily oriented spheres through a viscous fluid.', *Chemical Engineering Science.* **21**, 1151– 1170.

Green, B. S. & Fisher, R. (2004), 'Temperature influences swimming speed, growth and larval duration in coral reef fish larvae', *Journal of Experimental Marine Biology and Ecology* **299**, 115–132.

Greene, C. H. (1988), 'Foraging tactics and prey-selection patterns of omnivorous and carnivorous calanoid copepods', *Hydrobiologia* **167/168**, 295–302.

Greene, C. H. & Landry, M. R. (1985), 'Patterns of prey selection in the cruising calanoid predator euchaeta elongata', *Ecological Society of America* **66**(5), 1408–1416.

Guan, L., Snelgrov, P. V. R. & Gamperl, A. K. (2008), 'Ontogenetic changes in the critical swimming speed of gadus morhua (atlantic cod) and myoxocephalus scorpius (shorthorn sculpin) larvae and the role of temperature', *Journal of Experimental Marine Biology and Ecology* **360**, 31–38.

Happel, J. & Brenner, H. (1965), *Low Reynolds number Hydrodynamics.*, Prentice-Hall.

Hays, G. C., Richardson, A. J. & Robinson, C. (2005), 'Climate change and marine plankton', *Trends in Ecology and Evolution.* **20**(6), 337–344.

Hinze, J. O. (1959), *Turbulence An Introduction to its Mechanism and Theory*, McGraw-Hill.

Hwang, J. & Strickler, R. (2001), 'Can copepods differentiate prey from predators hydromechanically?', *Zoological Studies.* **40**(1), 1–6.

Jiang, H., Meneveau, C. & Osborn, T. R. (1999), 'Numerical study of the feeding current around a copepod.', *J. Plankton Res.* **21**, 1391–1421.

Ki⌀rboe , T. & Saiz, E. (1995), 'Planktivorous feeding in calm and turbulent environments with emphasis on copepods.', *Mar. Ecol. Prog. Ser* **122**, 135–145.

Ki⌀rboe , T., Saiz, E. & Visser, A. W. (1999), 'Hydrodynamic signal perception in the copopod acartia tonsa.', *Mar. Ecol. Prog. Ser* **179**, 97–111.

Ki⌀rboe , T. & Visser, A. W. (1999), 'Predator perception in copepods due to hydromechanical signals.', *Mar. Ecol. Prog. Ser.* **179**, 81–95.

Kraichnan, R. H. (1970), 'Diffusion by a random velocity field', *The Physics of Fluids* **13**(1), 22–31.

Kramer, D. L. & Mclaughlin, R. L. (2001), 'The behavioral ecology of intermittent locomotion.', *AMER. ZOOL.* **41**, 137–153.

Lalli, C. M. & Parsons, T. R. (2002), *Biological Oceanography An Introduction*, Butterworth Heinemann.

Lesieur, M. (2008), *Turbulence in Fluids.*, Oxford Science Publications.

Lewis, D. (2003), 'Planktonic contact rates in in homogeneous isotropic turbulence: case of predator with limited sensory field of perception.', *J.Theor.Biol.* **234**, 73–97.

Lewis, D. M. & Bala, S. I. (2006), 'Plankton predation rates in turbulence: A study of the limitations imposed on a predator with a non-spherical field of sensory perception', *Journal of Theoretical Biology* **242**, 44–61.

Lewis, D. M. & Pedley, T. J. (2000), 'Planktonic contact rates in homogeneous isotropic turbulence: theoretical predictions and kinematics simulations.', *J. Theor. Biol.* **205**, 377–408.

Lewis, D. M. & Pedley, T. J. (2001), 'The influence of turbulence on plankton predation strategies.', *J.Theor. Biol.* **210**, 347–365.

Lin, C. J., Lee, K. J. & Sather, N. F. (1970), 'Slow motion of two spheres in a shear field', *J. Fluid Mech.* **43**, 35–47.

MacKenzie, B. & Leggett, W. (1991), 'Quantifying the contribution of small-scale turbulence to the encounter rates between larval fish and their zooplankton prey: effects of wind and tide', *Mar. Ecol. Prog. Ser.* **73**, 149–160.

MacKenzie, B. & Leggett, W. (1993), 'Wind-based models for estimating the dissipation rates of turbulent energy in aquatic environments: empirical comparisons', *Mar. Ecol. Prog. Ser.* **94**, 207–216.

MacKenzie, B., Miller, T.J. Cyr, S. & Leggett, W. (1994), 'Evidence for a dome shaped relationship between turbulence and larval fish ingestion rates.', *Limnol. Oceanogr.* **39**, 1790–1799.

MacKenzie, B. R. & Kiørboe , T. (1995), 'Encounter rates and swimming behavior of pause-travel and cruise larval fish predators in calm and turbulent environments.', *Limnol. Oceanogr.* **40**(7), 1278–1289.

Majumdar, S. R. (1969), 'On the slow motion of viscous liquid in space between two eccentric spheres.', *Journal of the Physical society of Japan* **26**(3), 827–840.

Malik, N. A. & Vassilicos, J. C. (1999), 'A langrangian model for turbulent dispersion with turbulence -like flow structure: Comparison with direct numerical simulation for two- particle statistics', *The physics of Fluids* **11**(6), 1572–1580.

Manatunge, J. & Asaeda, T. (1999), 'Optimal foraging as the criteria of prey selection by two centrarchid fishes', *Hydorbiologia* **391**, 223–240.

Martinez, D. O., Chen, S., Doolen, G. D., Kraichnan, R. H., Wang, L. P. & Zhou, Y. (1997), 'Energy spectrum in the dissipation range of fluid turbulence', *J. Plasma Physics* **57**, 195–201.

Mathieu, J. & Scott, J. (2000), *An introduction to Turbulent Flow*, Press syndicate of the university of Cambridge.

McComb, W. (1991), *The physics of Fluid Turbulence*, Oxford Science Publications.

Mei, R. & Adrian, R. J. (1995), 'Effect of reynolds number on isotropic turbulent dispersion.', *Trans. ASME I: J. Fluids Eng.* **117**, 402–409.

Mei, R. & Hu, K. C. (1999), 'On the collision rate of small particles in turbulent flows', *J. Fluid Mech.* **391**, 67–89.

Müller, U. K., van den Boogaart, J. G. M. & van Leeuwen, J. L. (2008), 'Flow patterns of larval fish: undulatory swimming in the intermediate flow regime', *The Journal of Experimental Biology* pp. 196–205.

Morse, P. M. & Feshbach, H. (1953), *Methods of theoretical physics*, McGraw- Hill, New York.

Muller, U. K. & Videler, J. J. (1996), 'Inertia as a 'safe harbour' : do fish larvae increase length growth to escape viscous drag?', *Rev. Fish Biol. Fish* **6**, 353–360.

O'Brien, W. J., Evans, B. I. & Browman, H. I. (1989), 'Flexible search tactics and efficient foraging in saltatory searching animals', *Oecologia* **80**, 100–110.

Pao, Y.-H. (1965), 'Structure of turbulent velocity and scalar fields at large wavenumbers', *The Physics of Fluids* **8**(6), 1063–1075.

Peck, M. A., Buckeley, L. J. & Bengtson, D. A. (2006), 'Effects of temperature and body size on the swimming speed of larval and juvenile atlantic cod (gadus morhua): implications for individual-based modelling', *Environmental Biology of fishes* **75**, 419–429.

Plaut, I. (2001), 'Critical swimming speed: its ecological relevance', *Comparative Biochemistry and Physiology Part A* **131**, 41–50.

Podolsky, R. D. & Emlet, R. B. (1993), 'Separating the effects of temperature and viscosity on swimming and water movement by sand dollar larvae (dendraster excentricus)', *J. exp. Biol.* **176**, 207–221.

Roemmich, D. & McGowan, J. (1995), 'Climatic warming and the decline of zooplankton in the california current.', *Science* **267**, 1324–1326.

Rothschild, B. J. & Osborn, T. R. (1988), 'Small-scale turbulence and plankton contact rates', *J. Plankton Res.* **10**, 465–474.

Saiz, E., Calbet, A. & Broglio, E. (2003), 'Effect of small-scale turbulence on copepods: the case of oithina davisae.', *Limnol. Oceannogr.* **48**(3), 1304–1311.

Smagorinsky, J. (1963), 'General circulation experiments with the primitive equations', *Monthly weather review* **91**, 99–162.

Speziale, C. G. (1991), 'Analytical methods for the development of reynolds-stress closures in turbulence', *Annu. Rev. Fluid Mech* **23**, 107–157.

Stefan., S., Hopmans, E. C., Breugel, Y. v., Kuypers, M. M. M. & Damste, J. S. S. (2003), 'Extremely high sea-surface temperature at low lattitudes during the middle cretaceous as revealed by archael membrane lipids', *Geology* **31**(12), 1069–1072.

Stimson, M. & Jeffery, G. B. (1926), 'The motion of two spheres in a viscous fluid.', *Proc. Royal. soc. A.* **A**, 110–116.

Stocker, S. & Weihs, D. (2001), 'Optimization of energetic advantages of burst swimming of fish', *Math. Meth. Appl. Sci.* **24**, 1387–1400.

Suga, T. & Hanawa, K. (1990), 'The mixed layer climatology in the northwestern part of the north pacific subtropical gyre and the formation area of subtropical mode water', *Journal of Marine Research* **48**, 543–566.

Sundby, S. & Fossum, P. (1990), 'Feeding conditions of arcto-norwegian cod larvae compared with the rothschild-osborn theory on small-scale turbulence and plankton contact rates.', *J. Plankton Res.* **12**(6), 1153–1162.

Svensen, C. & Kiørboe , T. (2000), 'Remote detection in `Oithona similis`: hydromechanical versus chemical cues.', *Journal of Plankton Research.* **22**(6), 1155–1166.

Tennekes, H. & Lumley, J. (1972), *A first course in Turbulence.*, MIT press, Cambridge, MA, USA.

Thorpe, S. A. (2004), 'Recent developments in the study of ocean turbulence', *Annu. Rev. Earth Planet. Sci.* **32**, 91–109.

Tritton, D. J. (1988), *Physical Fluid Dynamics*, Oxford Science Publications.

Verhagen, J. H. G. (2004), 'Hydrodynamics of burst swimming fish larvae, a conceptual model approach', *Journal of Theoretical Biology* **229**, 235–248.

Videler, J. & Weihs, D. (1982), 'Energetic advantages of burst- and- coast swimming of fish at high speeds', *J. exp. Biol.* **97**, 169–178.

Visser, A. W. (2001), 'Hydromechanical signals in plankton.', *Mar. Ecol. Prog. Ser.* **222**, 1–24.

Visser, A. W. & Kiørboe , T. (2006), 'Plankton motility pattern and encounter rates.', *Oecologia* **148**, 538–546.

von Herbing, I. (2002), 'Effects of temperature on larval fish swimming performance: the importance of physics to physiology.', *Journal of Fish Biology* **61**, 865–876.

von Herbing, I. & Gallager, S. (2000), 'Foraging behaviour in early atlantic cod (`Gadus morhua`) feeding on a protozoan (balanion sp.) and a copepod nauplius (`Pseudo-diaptomus sp.`).', *Mar. Biol.* **136**, 591–602.

von Herbing, I., Gallager, S. & Halteman, W. (2001), 'Metabolic costs of pursuit and attack in early larval atlantic cod.', *Mar. Ecol. Prog. Ser.* **216**, 201–212.

von Herbing, I. H. & Boutilier, R. G. (1996), 'Activity and metabolism of larval atlantic cod (`Gadus morhua`) from scotian shelf and newfound land source populations.', *Mar. Biol.* **124**, 607–617.

Weihs, D. (1980), 'Energetic significance of changes in swimming modes during growth of larval anchovy, engraulis mordax', *Fishery Bulletin* **77**(3), 597–604.

Werner, F. E., Mackenzie, B. R., Perry, R. I., Lough, R. G., Naimie, C. E., Blanton, B. O. & Quinlan, J. A. (2001), 'Larval trophodynamics, tubulence, and drift on georges bank: A sensitivity analysis of cod and haddock', *SCI. MAR* **65 (suppl 1)**, 99–115.

Wieser, W. & Kaufmann, R. (1998), 'A note on interaction between temperature, viscosity, body size and swimming energetics in fish larvae', *The Journal of Experimental Biology* **201**, 1369–1372.

Wu, G. G., Yang, Y. & Zeng, L. (2007), 'Kinematics, hydrodynamics and energetic advantages of burst-and-coast swimming of koi carps (cyprinus carpio koi)', *The Journal of Experimental Biology* **210**, 2181–2191.

Yamazaki, H., Osborn, T. R. & Squires, K. D. (1991), 'Direct numerical simulation of planktonic contact rate in turbulent flow', *J. Plankton Res.* **10**, 629–643.

Yen, J., Lenz, J., Gassie, J. & Hartline, J. (1992), 'Mechanoreception in marine copepods: Electrophysiological studies on the first antennae.', *J. Plankton Res.* **14**, 495–512.

APPENDIX

Mini Chart A

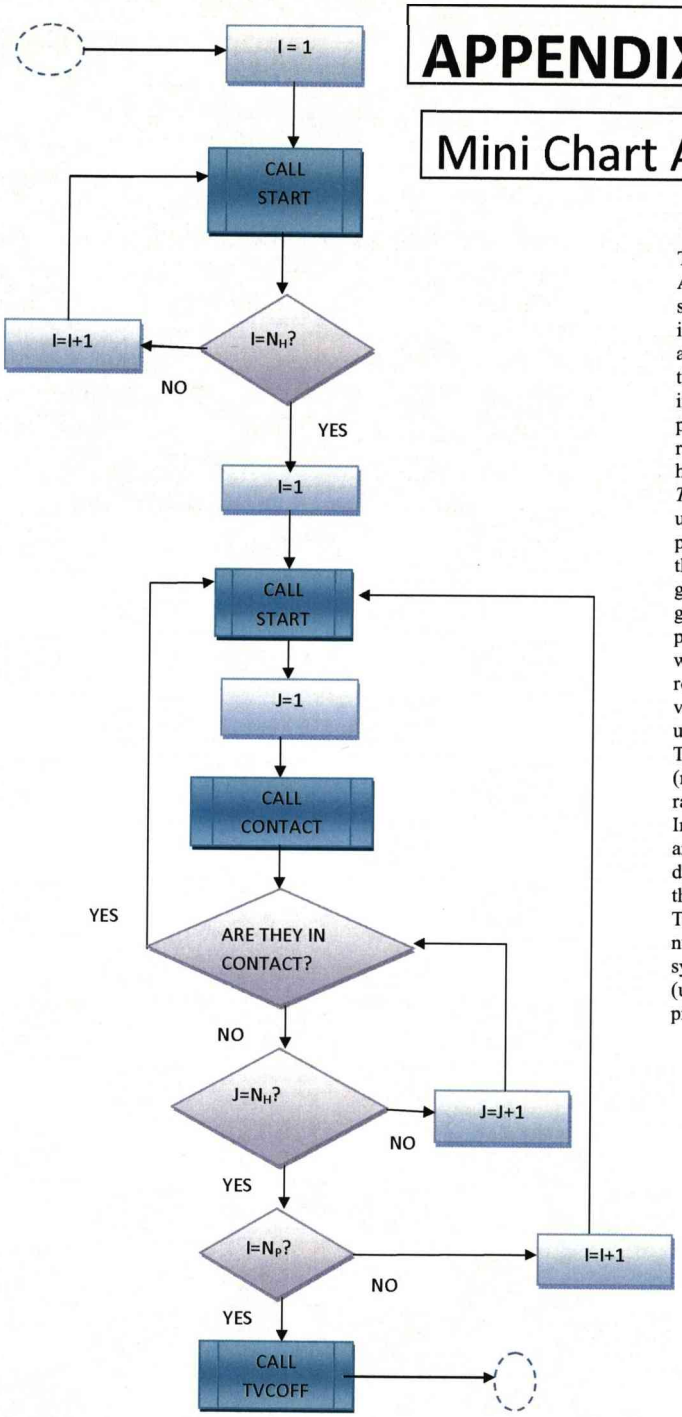

This is the flow chart represented by **A** on the general outline of the simulation. It was mainly used to initialize predator and prey positions and keep them at distance greater than the contact radius. To begin with all initial contacts were ignored. So a predator in contact with a prey was repositioned. Three subroutines used here are; *START, CONTACT* and *TVCOFF*. The routine *START* was used to assign random positions to predators and prey. *CONTACT* was then used to determine whether a given predator was at a distance greater than the contact radius from a prey. If not, the predator and prey pair was repositioned. *TVCOFF* is the routine for calculating the turbulent velocity field. This remained unchanged during the simulation.

The first loop started from 1 to N_H (number of prey) was used to assign random positions to all the prey. Initially the prey were positioned anywhere in the domain. This was done first because there were a lot of them.

The second loop started from 1 to the number of predators (N_P) systematically positioned predators (usually only 512) out of contact with prey.

Figure 9.1: Mini Chart represented by **A** on the simulation summary.

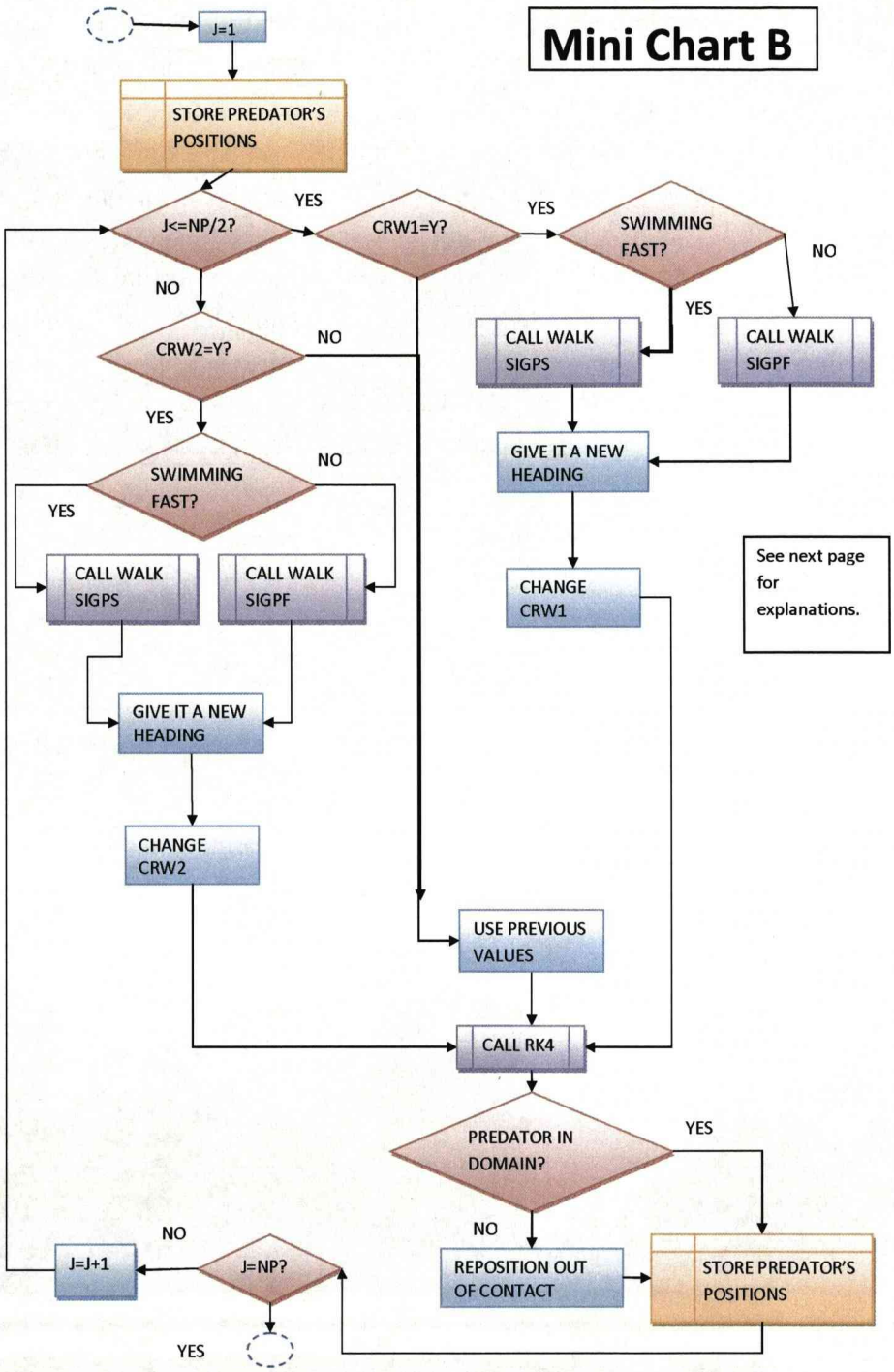

Figure 9.2: Mini Chart represented by **B** on the simulation summary.

Figure 9.2 is the block represented by **B** in the simulation summary. This has to do with predators. The saltatory predators were divided into two groups (1 to $N_P/2$ and $N_P/2$ +1 to N_P). Initially, one group of predators was travelling and the second remained in pause-mode. The character strings `CRW1, CRW2` were used to determine the time duration during which the 2 groups of predators should change their random walk. The routine `WALK` was used to assign random walk swimming speed to each predator. Changing random walk could be from travel to pause as indicated by calling `WALK` with `SIGPS` or from pause to travel (calling `WALK` with `SIGPF`). Whenever random walk changes, a new heading (swimming direction) was given to each predator. The routine `RK4` was used to advance particle position forward in time using fourth order Runge-Kutta method. This process occasionally led the predators to move out of the simulation domain and so the affected predator were repositioned out of contact with any prey.

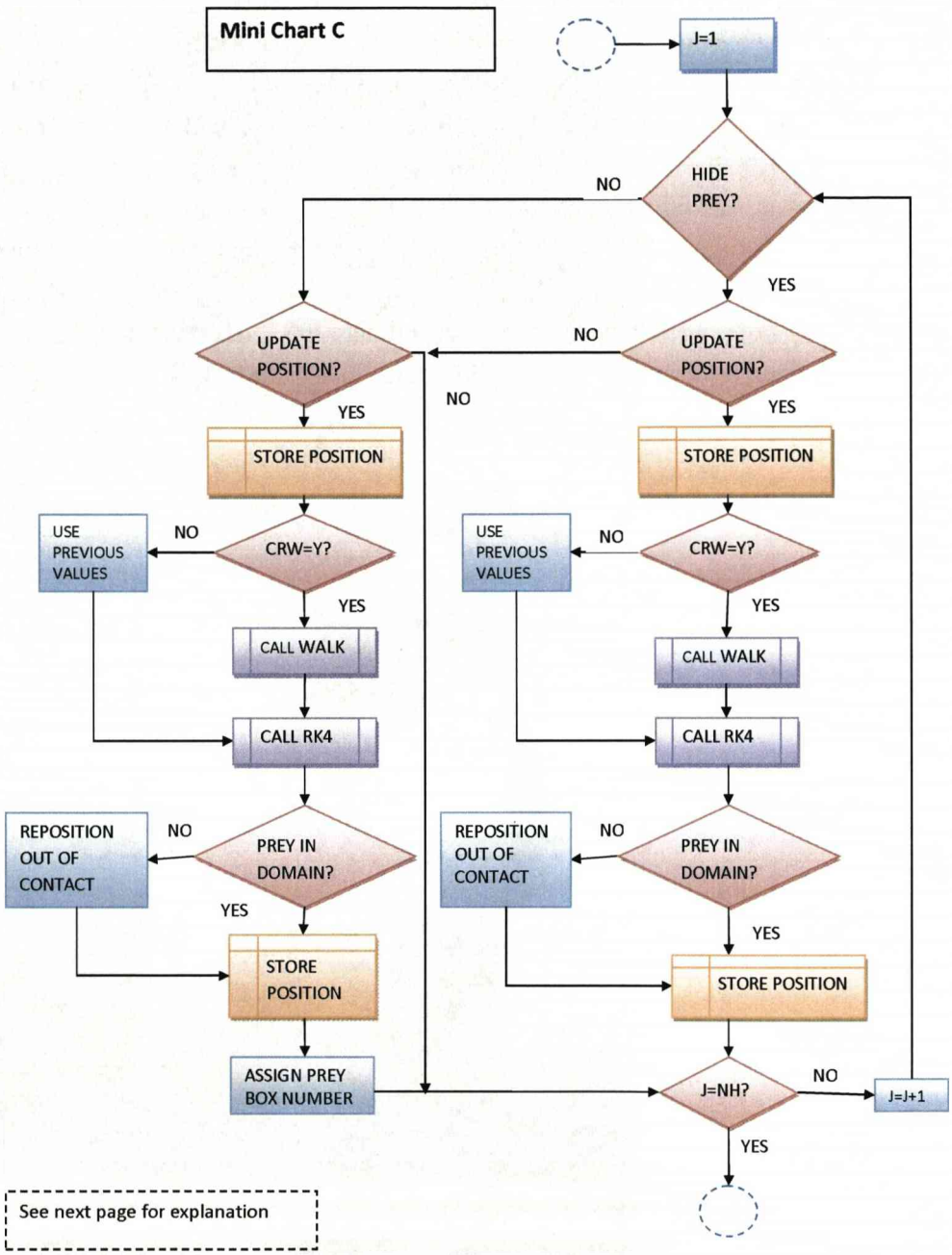

Figure 9.3: Mini Chart represented by **C** on the simulation summary.

Figure 9.3 is the prey loop and is represented with the letter **C** on the summary. It runs from J=1 to the number of prey. Consumed prey were taken out of the simulation. So initially question was asked whether a given prey is to be hidden or not. For those prey in the simulation, we made decisions as to whether time was due to change their random walk or not. The subroutine `WALK` was used to assign random walk swimming speeds to both predators and prey. The routine `RK4` was used to advance prey position forward in time using fourth order Runge-Kutta method. This process occasionally sent prey out of the simulation domain. The affected prey were repositioned out of contact with any predator. Every prey in the simulation domain was assigned a box number which essentially specified its localised position. Each box was a cube of size R, and the whole domain was split up into these (thousands) of different boxes. As the prey particles moved their positions after each time step was recorded, as is the box number in which they reside. This made the process for checking for new contacts easier.

Figure 9.4 is the Mini Chart represented by **D** on the simulation summary. It was mainly used to check for contacts between predator and prey. The basic procedures followed to check for new contacts were: First the array containing occupied prey box numbers was sorted, so that IBOX(1)=gives lowest occupied prey box number, IBOX(2)=second lowest occupied prey box number etc.

A loop was started looking at each predator in turn. The box number of an individual predator (where it resides) and numbers of all the boxes that directly surrounded it were recorded. Then each of these box numbers containing the predator and those that surrounded it were compared directly with the sorted array of occupied prey box numbers. Because the latter was sorted it was easy to pin down which two occupied prey box numbers lie below and above the number of a box containing, or surrounding the predator. At that stage a further check was then run to see if the two boundaries occupied prey box numbers coincide with the number of the box containing or surrounding the predator. If yes, then we have found a prey in close proximity to this particular predator (there may be more than one). The routine `CONECONE` was then used to determine definitively if this particular predator and this particular prey (determined from its box number) have actually come into contact. For all new contacts the number of contacts was raised by one. In addition the numbers of the predator-prey contact pair were recorded. For 'old' contacts (that is this particular pair were in contact on the previous time step, which was done by checking through to see if this predator was already in contact with this prey on the previous step) then no actions were taken. When there was no contact, all the box numbers containing or surrounding the predator were searched by checking with the sorted array of prey boxes.

When all the boxes containing or surrounding this predator have been checked against the inventory of occupied prey box numbers, we moved on to the next predator and the procedures mentioned above were repeated. This procedure has the advantage that we only had to carry out detailed calculations of whether a predator has come into contact with a prey in its locality. Those prey (the vast majority) that were nowhere near the predator at that time were essentially ignored in the checking process. Otherwise this becomes an $N_P \times N_H$ checking process which is very inefficient in CPU time.

Figure 9.5 is the Mini Chart represented by **E** on the main simulation summary. It was mainly used to determine whether a predator in contact with a prey has sufficient time to capture it. Once a predator was in contact with a prey, the prey was monitored (recording the time they spend in contact) until it disappear from the predator's perception field. The numbers of captures were determined by checking all previous contacts which have ceased to be contacts during this time step.

The procedures followed to determine whether a prey was captured or not were as follows; For a given predator pair in contact during the previous time step, we determined whether they are still in contact during this time step or not. If not, we calculated the likelihood of the prey being captured using the capture function (P_{CAP}) and generated a uniform random number R_{CAP}. If $P_{\mathrm{CAP}} > R_{\mathrm{CAP}}$ then the prey was captured otherwise the prey has escaped. Whenever capture occurred, the number of captures was updated, spontaneously a new prey was recreated elsewhere out of contact with any predator, to avoid prey density dropping. These procedures were repeated for all the number of contacts during the previous time steps (LPC).

Figure 9.6 is the Mini Chart represented by **F** and **G** on the main simulation summary. It was mainly used for tidying up process. Figures 9.7 to 9.10 are the flow charts for some of the subroutines used in the simulations.

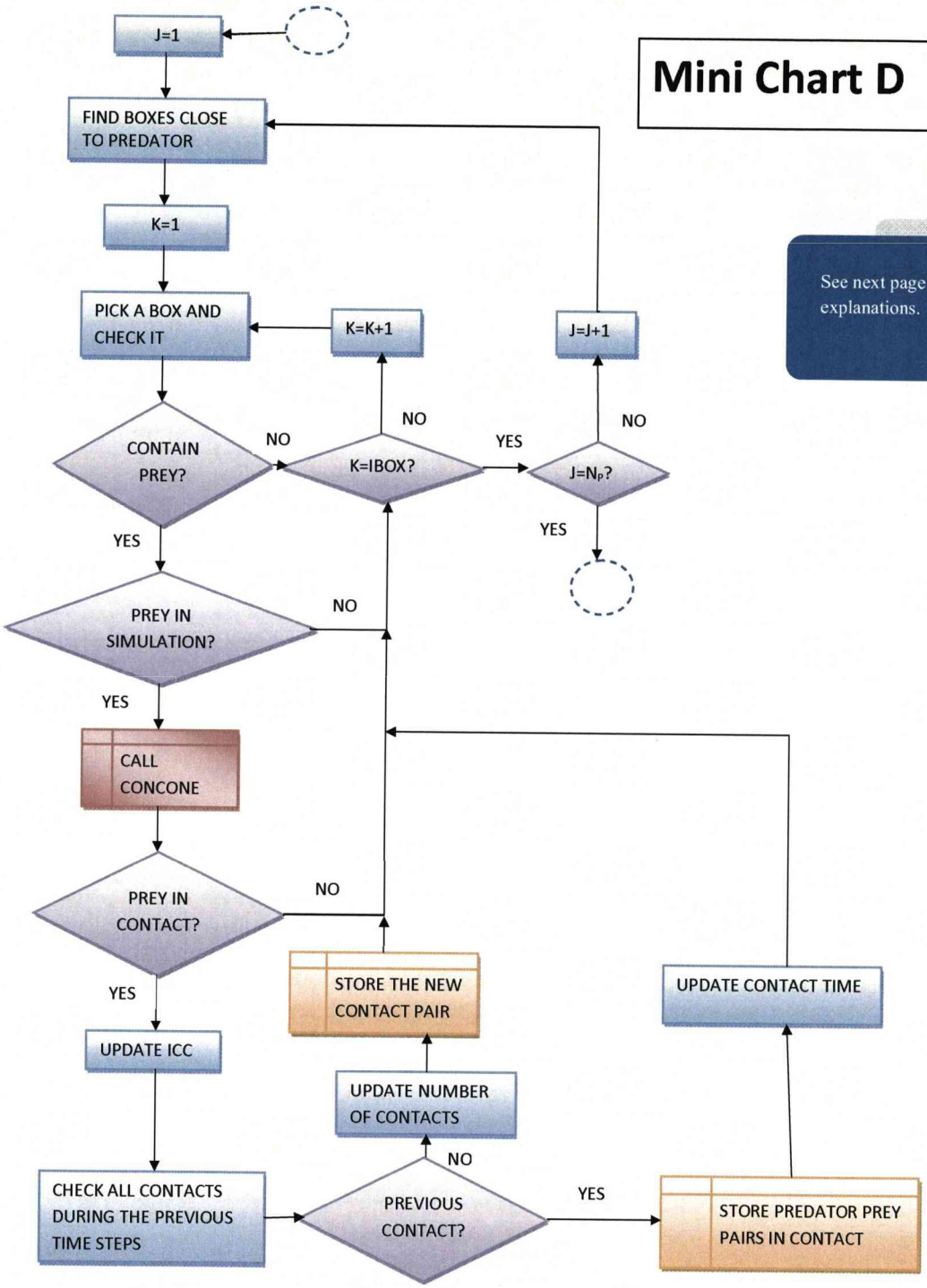

Figure 9.4: Mini Chart represented by **D** on the simulation summary.

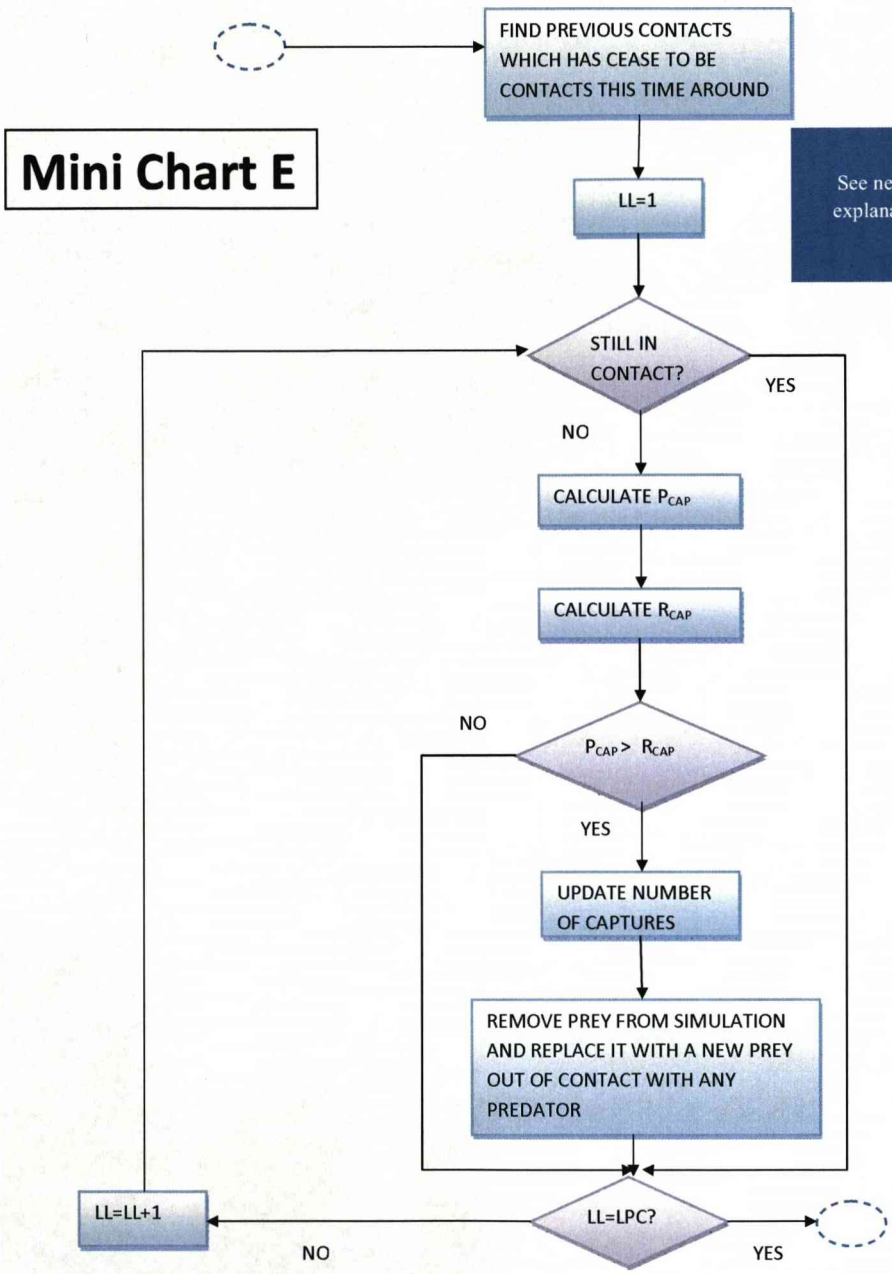

Figure 9.5: Mini Chart represented by **E** on the simulation summary.

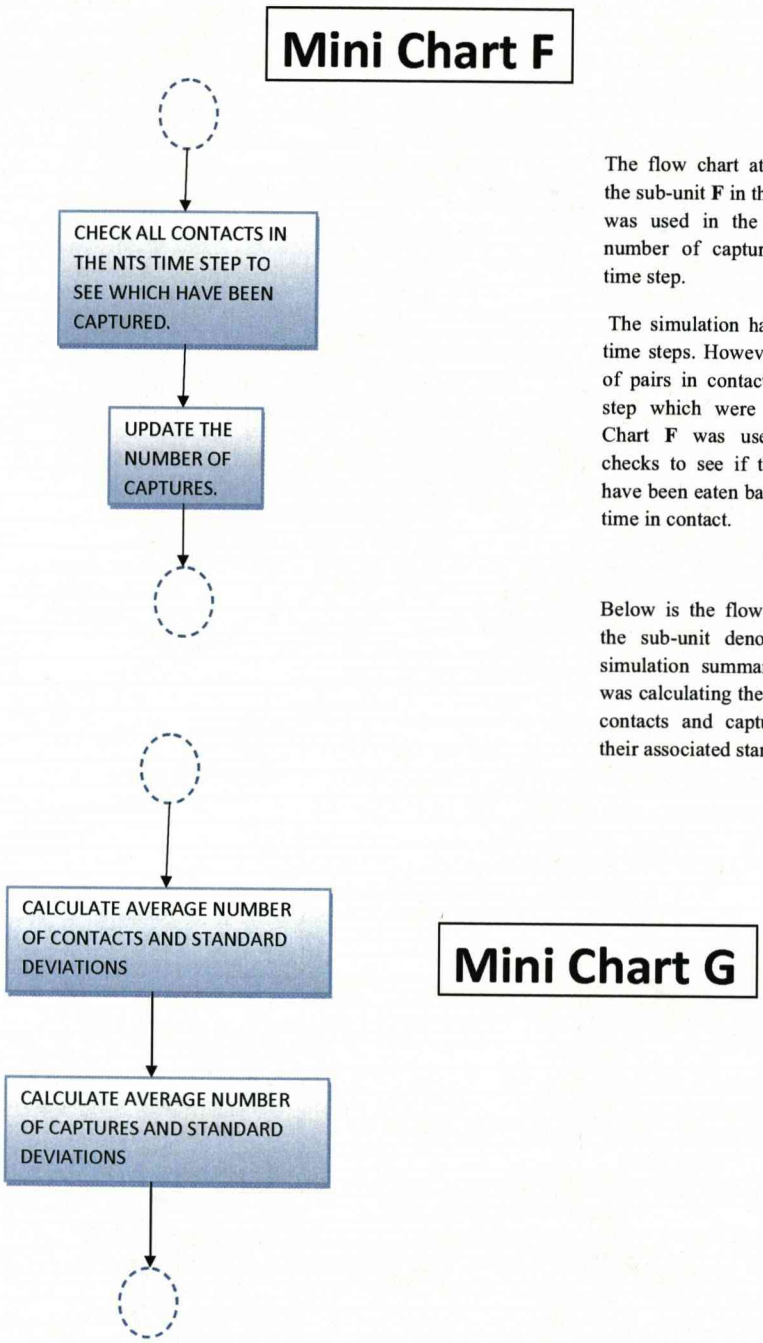

The flow chart at the top represents the sub-unit **F** in the main summary. It was used in the calculation of the number of captures during the last time step.

The simulation has ended after NTS time steps. However, there were a lot of pairs in contact on the NTS time step which were not tested. Mini Chart **F** was used for tidying up checks to see if they were likely to have been eaten based on their current time in contact.

Below is the flow chart representing the sub-unit denoted by **G** in the simulation summary. The main task was calculating the average number of contacts and captures together with their associated standard deviations.

Figure 9.6: Mini Chart represented by **F** and **G** on the simulation summary.

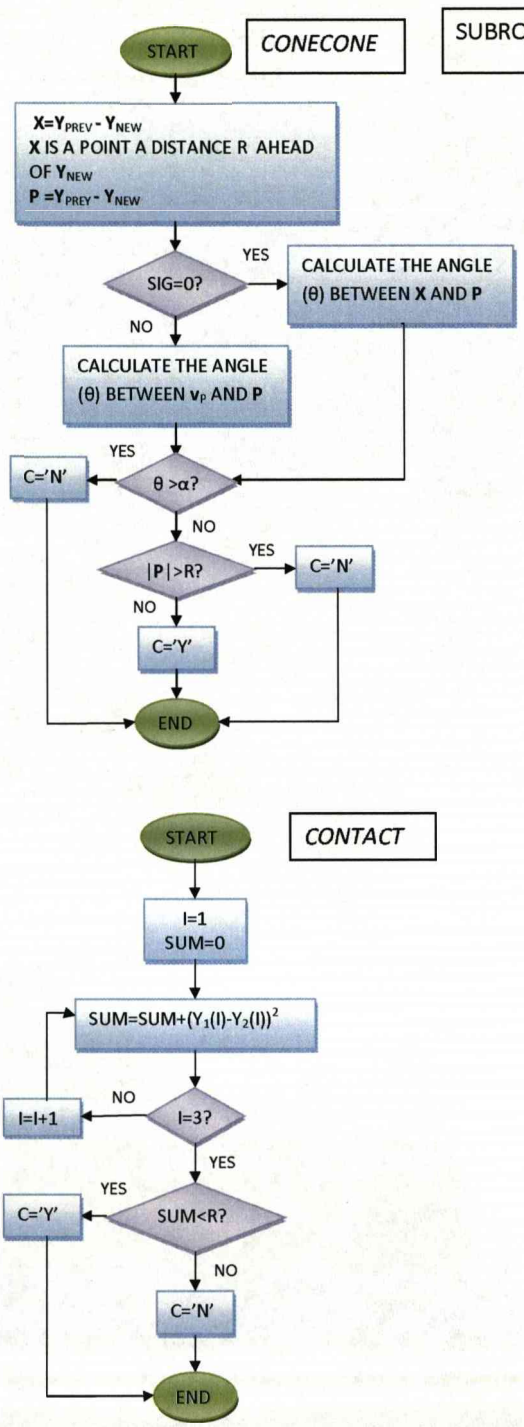

The flow charts on the right represent two subroutines *CONECONE* (top) and *CONTACT* (bottom) used many times in the simulation. Inputs to *CONCONE* are the contact radius, R, the perception angle α, prey position $\mathbf{Y}_{PREY}$, current and previous predator positions $\mathbf{Y}_{NEW}$ and $\mathbf{Y}_{PREV}$. It returns a character C which indicates whether a predator and prey are in contact (C='Y') or not (C='N'). To arrive at a conclusion, the angle between $\mathbf{v}_P$ (line of sight) and the vector **P** is compared with the predator's perception angle (which is known) and the predator-prey separation is compared with R (contact radius). If predator is non-swimming, the line of sight is defined as $\mathbf{Y}_{PREV}$-$\mathbf{Y}_{NEW}$. In this case a point **X** a distance R ahead of $\mathbf{Y}_{NEW}$ is calculated. The angle is then calculated as the angle between **X** and **P**. This routine supersedes the routine below (contact) which was used mainly to positioned predators and prey at distances greater than R.

The routine *CONTACT* checks to see if two particles are in 'contact'. That is if particle 1 with position **Y**1 and particle 2 with position **Y**2 are a distance *R* from each other. Input to *CONTACT* are the contact radius *R* and the *x,y,z* coordinates of the predator and prey positions contain in the arrays $\mathbf{Y}_1$,$\mathbf{Y}_2$. It returns a character C ('Y' or 'N').

Figure 9.7: Flow chart of the subroutine `CONECONE`, mainly used to determined contacts between predator and a nearby prey.

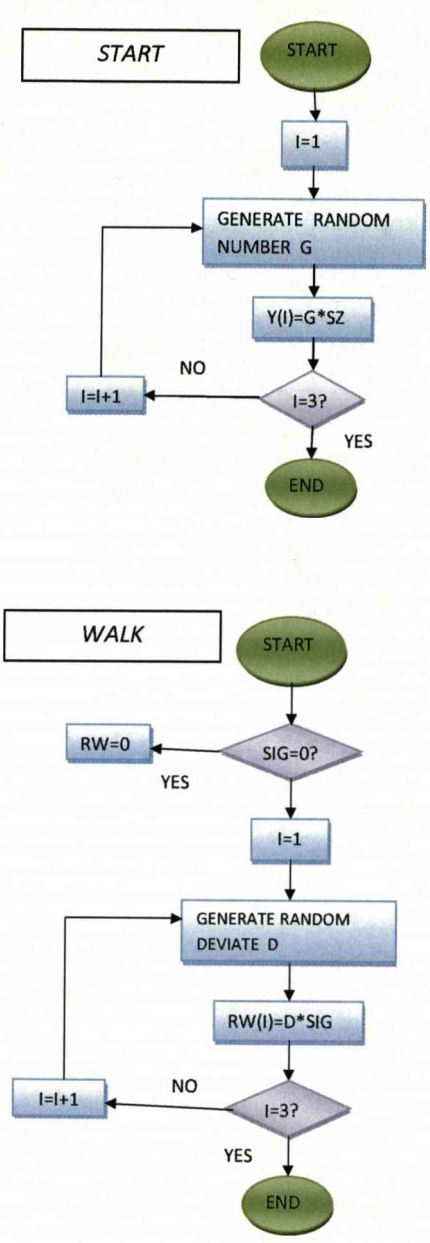

SUBRUTINE *(START, WALK)*

The flow charts on the left are two routines used in the simulation. At top left is subroutine START. This was used to initialize the positions (**Y**) of predator and prey randomly throughout the simulation domain SZ. It uses a random number generator. Inputs to the routine are the seed of the random number and the domain size. It returns the *x,y* and *z* coordinates of the particle's position in the array **Y.**

At the bottom left is another subroutine call WALK. It generates a random walk velocity to mimic the predator/prey swimming. The components of the random walk are drawn from three dimensional Gaussian distribution with mean zero and standard deviation SIG. Inputs to the routine are the seed of the random number and SIG. It return the *x,y* and *z* components of the random walk velocity in the array **RW**.

Figure 9.8: Flow chart of the subroutines `START`, `WALK`, mainly used to initialise positions and to assign random walk swimming speeds to predators and prey.

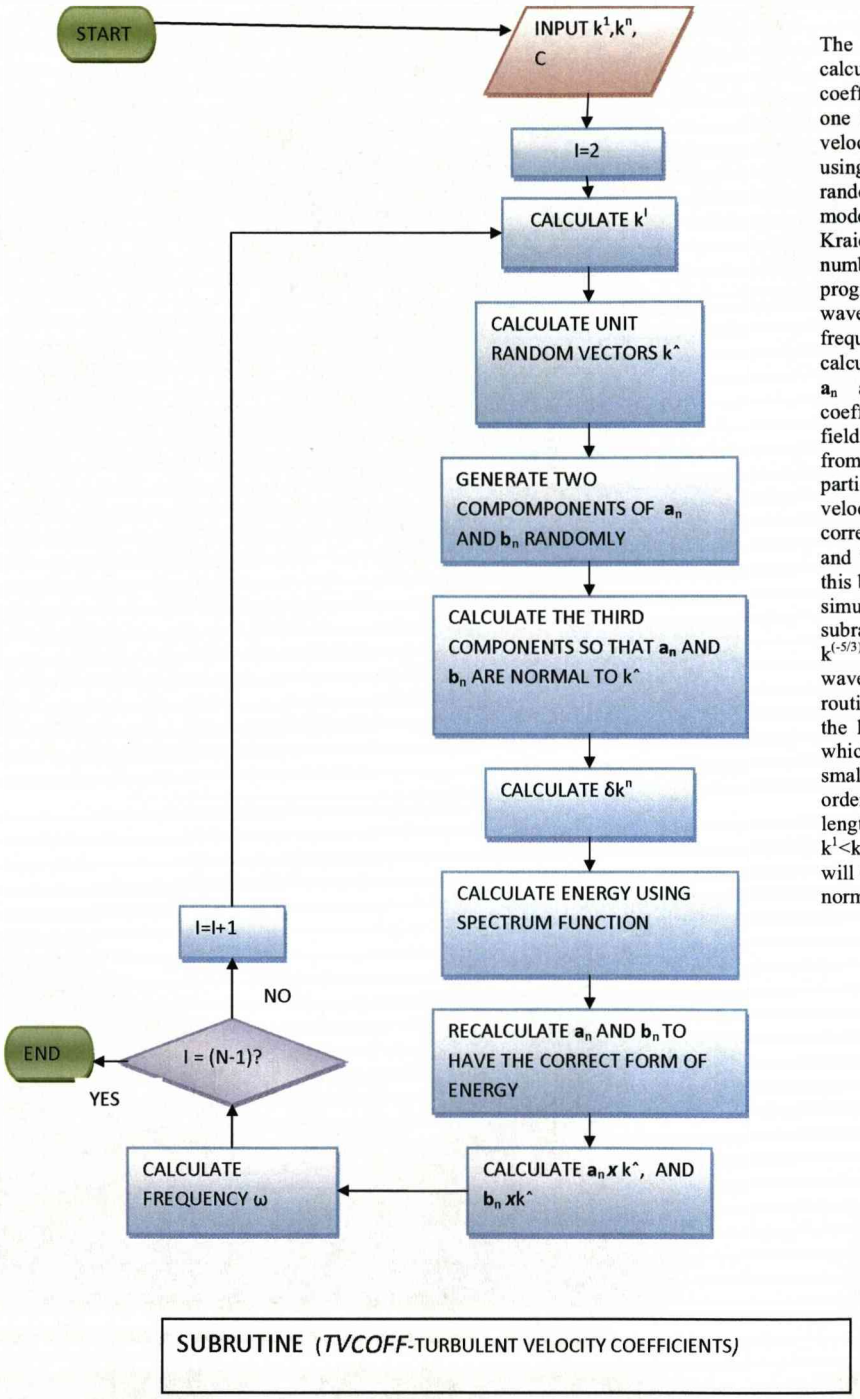

The following routine calculates a whole series of coefficients that will enable one to calculate the turbulent velocity field. It does this using the method of randomly selected Fourier modes developed by Kraichnan 1970. Here N is the number of modes used. The program calculates N wavevectors and N angular frequencies ω. It also calculates two sets of vectors $\mathbf{a}_n$ and $\mathbf{b}_n$ which act as coefficients in the velocity field. These are calculated from the wavevectors in a particular way to ensure the velocity field has prescribed correlation statistics. Malik and Vassilicos have modified this basic method to produce a simulated flow with an inertial subrange type spectrum of $k^{(-5/3)}$ between two fixed wavenumbers $k^1<k<k^n$. In this routine k1=1/ (L the size of the largest eddies) and k^n=1 which is equivalent to the smallest eddies being of the order of the Kolmologorov length scale. Outside the range $k^1<k<k^n$ the energy spectrum will be zero. C represents the normalization constant.

Figure 9.9: Flow chart of the subroutine `TVCOFF`, mainly used to calculate series of coefficients that will enable one to calculate the velocity fields.

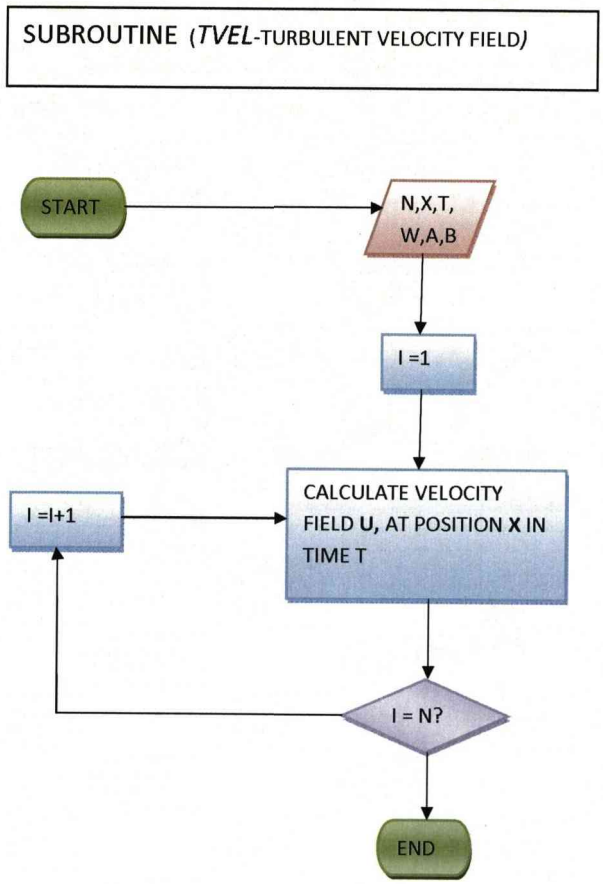

This routine uses the coefficients calculated in TVCOF to calculate the turbulent velocity **U** (**X**,T) at position **X** and time t. The result is stored in **U**.

Figure 9.10: Flow chart of the subroutine `TVEL`, mainly used to calculate the turbulent velocity fields.

EBUS302 Total Quality Management (from the Management School) (7.5 credits)